

Diss. ETH No. 27438

Optimal Design of HF Inductors and Universal EV Charger Mains Interfaces

A thesis submitted to attain the degree of

DOCTOR OF SCIENCES of ETH ZURICH
(Dr. sc. ETH Zurich)

presented by

PANTELEIMON PAPAMANOLIS

MSc ETH

born on 19.07.1989

citizen of Greece

accepted on the recommendation of

Prof. Dr. Johann W. Kolar, examiner

Prof. Dr. Paolo Mattavelli, co-examiner

2021

ETH Zurich
Power Electronic Systems Laboratory
Physikstrasse 3 | ETL H23
8092 Zurich | Switzerland

<http://www.pes.ee.ethz.ch>

© 2021, Panteleimon Papamanolis

To Elli and Michalis, my parents.

Στους αγαπημένους μου γονείς.

To Manos, my brother.

Στον αδερφό μου.

Acknowledgments

I left this chapter last, because I knew it was going to be the most challenging to write.

The last four years have been a journey of personal and professional growth, filled with laughter, stress, confidence, doubt, courage, and fear. I will forever be grateful for all the experiences gained and, thus, I would like to use these pages and appreciate all the people who contributed to it. I want to be reminded of them and of this particular moment, every time I read these lines (again).

First and foremost, I would like to thank Prof. Johann W. Kolar. I would like to thank you for the opportunity and honor to be a member of your laboratory, and to work under your guidance. You are a committed researcher and a real visionary, probably the first one I had the chance to meet in my life; it is because of this, that PES was, is, and will continue to be among the power electronics leading research institutes worldwide.

Secondly, I would like to express my gratitude to Prof. Paolo Mattavelli, for accepting to be the co-examiner of my PhD defense and for taking the time to read my thesis. Hopefully, it was a smooth and interesting read.

I would like to sincerely thank my supervisor all these years, Dr. Florian Krismer. I hope you see this work as part of yours, and I am very grateful of your contribution. Thank you for the trust you put on me and for providing me with the opportunity to be the Teaching Assistant of your wonderful course. Teaching at ETH has been an unforgettable experience for me.

The most special thanks go to my friend and office-mate Dr. Thomas Guillod. I was very lucky to share all these years with you and to get the chance to know you and collaborate with you. I will forever be grateful of the things you taught me, your support, and our friendship. I wish you the best of success to your next steps.

Dr. Michalis Antivachis, my gratitude towards you belongs to all life aspects, as you have been a flatmate, a colleague, and most importantly a friend. I could not have been luckier with our decision of becoming flatmates 6.5 years ago.

Dr. Jon Azurza, (soon to be) Dr. Piotr Czyz and Dr. Mattia Guacci, I am most grateful of all our moments. The laughter, the support (technical and emotional), and the discussions among us, have been the best medicine during this long journey. I learned a lot from you and I witnessed our common growth on every level personal and professional. I believe and hope that these bonds will keep strong for many years to come.

A big thank you to my office-mates during these four years, starting from Dr. Daniel Rothmund. You are the kindest (and fittest) friend I will ever have and an exceptional engineer. Thank you for all the things you taught me. To the talented and funny Dr. Oliver Knecht. And, finally, to the gifted Ms. Neha Nain, whose growth I have witnessed since her first day in Zurich, when I accepted to be her supervisor, until now, where we came to share the same office.

I would like to thank all the students that entrusted me, by choosing me as their supervisor for their projects during their MSc studies, i.e., Bima Sanusi, Etta Shyti, Joel Arnold, Marc Herzog, Simon Wyss, Simon Hobi, and Francesc Trunas.

Of course many thanks go to all PES members. Our endless discussions on the whiteboards, our struggles and our jokes will stay forever with me. The supervisor of my master's thesis and then colleague, Dr. Dominik Neumayr, a hatching visionary and a great engineer. The out-of-the-box thinker Dr. Dominik Bortis, with whom I had the pleasure to work during my last project and for which I am very thankful. The practical, Julian Böhler. The humble genius, Michael Haider. The loud genius, Morris Heller. The calm, Dr. Huber Jonas. The musician and very caring, Emanuel Hubmann. The kind, Gustavo Knabben. The, recently, co-author, David Menzi and the always eager to learn, Dr. Spasoje Miric. The HF guy, Pascal Niklaus. The work-efficient, Dr. Jannik Schäffer. And of course our newest members, Ivana Bagaric, Reto Bonetti, Rosario Giuffrida, Yunni Li, Gwendolin Rohner, Marc Röthlisberger, and Daifei Zhang.

I would like to further express my gratitude to all PES alumni, with whom I had the pleasure to work with during these four years. The amazing and funny, Dr. Mario Maurerer, my magnificent friend, Dr. Arda Tuysuz, the genius and always smiling, Dr. Lukas Schrittwieser, the extreme-sports guy, Dr. Christoph Gammeter, the co-supervisor of my master's thesis, Dr. Matthias Kasper, the always polite and (soon to be) Dr. Pedro Bezerra, Dr. Michael Leibl, Dr. David Boillat, Dr. Michael Flankl, Dr. Thomas Holenstein, Dr. Johann Miniböck, Dr. Andreas Müsing, Dr. Marcel Schuck, Dr. Pascal Püntener, Dr. Tobias Wellerdieck.

Finally, the backbone of our institute. Our four amazing secretaries who always make sure that we have everything we need and who treat us more like family than employees. Mrs. Monica Kohn, Mrs. Maurantonio Prisca, Mrs. Roswitha Coccia, and Mrs. Yvonne Schnyder. Our technician Mr. Peter Seitz, and our IT specialist Mrs. Marina Eisenstaat. And our former employees, Dr. Beat Seiler, Mr. Peter Albrecht, and Ms. Claudia Stucki.

Since I moved to Zurich, I had the blessing to create lifelong friendships with some of the most beautiful and capable people. Our trips, drinks, dinners, and discussions mean the world to me. I would like to thank my friend, ex-flatmate, and co-investor Spiros Daglas, and his amazing girlfriend, my friend Yasmine Priore. My cousin and great friend Gerasimos Kallivokas. And, of course, Thanos Kontis, Giorgos Zinas, and Anastasia Dimitriadou. My dear friend, Dr. Fotini Pashalidou, and my loved friend Francesca Meyer. And finally my three classmates during my MSc studies, Dr. Orçun Caraca, Berkin Kalay and Harsoveet Singh.

None of this would have been true, had I not been a member of the Prometheus Team of the National Technical University of Athens, under the guidance of Prof. Antonios Kladas. This is where my love for power electronics and electric motion began. To all my friends and team members, I will forever be grateful to our experiences and memories. Anastasia Sampani, Stefanos Spanomitsos, Nikos Apostolopoulos, Konstantinos Bourchas, Konstantina Nikolaou, Stavros Yiayiannos, Dr. Charalampos Patsios, Dimitris Gyparakis, Konstantinos Anagnostopoulos, Dr. Achilleas Tsitsimelis, Dr. Georgios Sfakianakis, Dr. Minos Beniakar, Dr. Kostantinos Laskaris, Dr. Ilias Papastamatiou, Anastasia Skolariki.

My lifelong best friends, whom I love and respect with all my heart, Dr. Kiriakos Amiridis, Alexandros Anagnostopoulos, Spiros Floropoulos, Dionisis Galiatsatos, Romanos Mavroudis, and Giorgos Varnelis. I want to thank you for your invaluable support, even while being 1600 km away.

To my close family, Vasilis Pantelakis and his family, and his mother Korina Leoutsakou, my beloved uncle Dinos Limnidis, my aunt Aggeliki Stergiopoulou, my cousins Marios and Markella, and to my two grandmothers, Markella and Evangelia, thank you for everything.

Last but not least, I would like to thank my lucky charm, my girlfriend Özge Hatiboğlu, for her immense support and love. And of course my family, my inspiration and support, my parents, Michalis Papamanolis and Elli Limnidou, my brother, Manos Papamanolis, his wife, Eleni Aggelatou, my impeccable nephew, Michelangelo, and my niece, Eliza, who will be born within the next 1 - 2 days. I love you with all my heart.

*Danke. Thank you. Σας ευχαριστώ.
Pantelis, Zurich, 13.01.2021*

“No man ever steps in the same river twice.”

HERACLITUS, 544 - 484 BC

“Ποταμῷ γὰρ οὐκ ἔστιν ἐμβῆναι δις τῷ αὐτῷ.”

Ἡράκλειτος, 544 - 484 π.Χ.

*“One of the greatest discoveries a man makes,
one of his great surprises,
is to find he can do what he was afraid he couldn't do.”*

HENRY FORD, 1863 - 1947

Abstract

By the end of the year of 2030, and even after taking into consideration the impact of the Covid-19 pandemic into the global economy, the ambitious Sustainable Development Scenario predicts that Electric Vehicles (EV) will occupy 30 % share of the global market, representing 12 % of all cars worldwide. In addition, 87 % of the times these vehicles will be charged at home, typically using the on-board chargers, with a maximum allowed power delivery of 22 kW for European countries (3-phase mains) and 19.2 kW for the USA (1-phase mains). This renders the need of technological advancements in this field mandatory, in order to realize compact, efficient, and economical EV chargers.

The arrival of Wide Bandgap (WBG) semiconductors contributed significantly towards this direction, rendering magnetic components the bottleneck of power electronic systems. On the other hand, WBG semiconductors feature lower losses, which allows converters to operate at higher frequencies, something, typically, beneficial for magnetic components.

In this regard, this thesis focuses on two important aspects of EV charging, i.e., magnetic components, specifically power inductors, and universal applicability. In a first step, optimal operation of power inductors, employed in typical power electronics applications, e.g., buck/boost converters, is analyzed with respect to fundamental system parameters, i.e., switching frequency and current ripple. This analysis provides a better insight into the design of inductors and their optimal operating regions. Moreover, due to the substantially flat region around the global optima, many opportunities related to secondary objectives, e.g., partial load efficiency and manufacturing cost, are identified, and shown to result only in a minor, i.e. 15 - 20 %, increase in losses at rated power. The analysis is conducted in two steps, starting from simple analytical models and continuing with more accurate semi-numerical models. As a result of this comparison between the two models, better insight with respect to fundamental non-linearities is gained, e.g., core saturation, and, moreover, a simple two-equation design guide is derived, that directly leads to quasi-optimal inductor designs. The findings of this work are verified with calorimetric measurements for frequencies between 150 - 750 kHz and for three different inductors.

From the previous work, the need for accurate core loss data was identified, since the operation of inductors is optimum at frequencies near the peak of the Performance Factor (PF) of the employed core material. Nevertheless, to the author's knowledge, no existing method achieves accurate enough measurements (e.g., measurement uncertainty < 25 %) at very high

frequencies, i.e., in the MHz range. Hence, as a second step of this work, a transient calorimetric measurement method of core losses is developed, whose accuracy is largely independent of the excitation frequency and current shape, and, moreover, it is simple and fast to implement. Furthermore, a thorough sensitivity analysis of the different uncertainties of the method leads to simple guidelines for its optimal application. Accordingly, core loss data of the NiZn 67 material from Fair-Rite for frequencies between 5 - 50 MHz is measured; during these measurements the maximum and average worst-case uncertainties are estimated to be equal to 19.8 % and 13.3 %, respectively. The calculated PF based on the measured losses reveals a performance peak at 34 MHz, which highlights the great potential of NiZn magnetic core materials at such frequencies.

As a last challenge of this thesis, an AC/DC PFC rectifier topology is presented that allows operation at rated power for both 3-phase and 1-phase mains supply. Such topology constitutes a universal solution for the mains interface of an on-board EV charger, and, as a result, can lead to interoperability, and also simpler and more cost-efficient production lines. The topology is based on the conventional two-level six-switch (2LB6) 3-phase PFC rectifier, extended by the addition of a diode bridge-leg for the return current during 1-phase operation, and a novel EMI filter that effectively attenuates the generated noise for both operations. The stresses on the main power components (semiconductors, boost inductors, DC-link capacitors) are analyzed and design guidelines are provided. Furthermore, the conducted EMI is analyzed and the effectiveness of each component of the EMI filter is discussed, leading to a design guideline of the EMI filter. The proposed concept is validated by realizing a 22 kW hardware prototype that achieves a power density of 6.4 kW/dm^3 , a peak efficiency of 98.2 % during 3-phase operation at 15 kW, and an efficiency of 97.9 % at 19.5 kW. The operation at 19.5 kW confirms the thermal feasibility of the converter at full load. Furthermore, successful compliance with the CISPR 11 Class B QP EMI regulations is achieved for both operations, while measured at an operating power of 4.5 kW due to power limitation of the employed Line Impedance Stabilization Network (LISN) device. An extension of the concept to multilevel converters is proposed, e.g., flying capacitor PFC rectifiers and T-type PFC rectifiers, in case increased efficiency and/or power density is desired.

Finally, the main findings of this thesis are summarized in the conclusion. Based on the gained knowledge/experience during this work, alternative approaches on the analyzed topics are proposed, together with possible exten-

sions. Related scientific topics that lack deep understanding are highlighted, and, accordingly, thoughts for future projects are shared.

Kurzfassung

AUFGRUND aktueller Schätzungen ist, auch bei Berücksichtigung der negativen Auswirkungen der aktuellen Covid-19 Pandemie auf die Wirtschaft, davon auszugehen, dass bis Ende 2030 elektrisch betriebene Fahrzeuge einen Marktanteil von 30 % erreichen werden. Hinzu kommt, dass die Batterien dieser Fahrzeuge zu 87 % der Zeit zu Hause unter Verwendung privater – meist fahrzeugintegrierter – Ladegeräte mit einer maximalen Ladeleistung von 22 kW in den Ländern Europas (3-phasiger Netzanschluss) bzw. 19.2 kW in den USA (einphasiger Anschluss mit 240 V / 80 A) aufgeladen werden. Entsprechend steigen die Anforderungen an die Ladeelektronik hinsichtlich Kompaktheit, Effizienz und Kosten auch zukünftig weiter an.

Ein wesentlicher Schritt, leistungselektronische Schaltungen in diese Richtung zu verbessern, ist unter Verwendung moderner SiC und GaN Leistungshalbleiter möglich, welche geringere Verluste und höhere Schaltfrequenzen erlauben. Folglich ermöglicht der Einsatz solcher Leistungshalbleiter auch eine Verringerung der Baugröße und der Verluste magnetischer Komponenten.

Der Schwerpunkt dieser Dissertation liegt auf zwei zentralen Aspekten der technologischen Weiterentwicklung von Ladegeräten für elektrische Fahrzeuge. Der erste Aspekt ist die Optimierung magnetischer Komponenten, v.a. von Spulen mit Magnetkern, da sich zunehmend zeigt, dass magnetische Komponenten die Verbesserung der Performance leistungselektronischer Schaltungen limitieren. Der zweite Aspekt betrifft die universelle Einsetzbarkeit der Ladegeräte für dreiphasige und einphasige Netze.

In einem ersten Schritt erfolgt die Analyse des optimalen Betriebs einer Induktivität in einer typischen leistungselektronischen Anwendung, z.B. einem Tief- oder Hochsetzsteller, hinsichtlich der Schaltfrequenz und der Amplitude des Stromrippels. Diese Analyse erlaubt eine detaillierte Beschreibung der Zusammenhänge, welche in Spulen zwischen den verschiedenen beteiligten physikalischen Größen vorliegen (z.B. elektrischem Strom, magnetischer Flussdichte, Temperatur), sowie eine Charakterisierung optimaler Betriebsbereiche. Das globale Verlustminimum stellt sich als vergleichsweise flach heraus, d.h. um das globale Verlustminimum herum sind die minimal erreichbaren Verluste einer Induktivität in einem weiten Bereich der Schaltfrequenz und der Stromrippelamplitude nur geringfügig erhöht. Aufgrund dieser Eigenschaft sind weitere Optimierungen möglich, sofern eine geringfügige Erhöhung der Verluste im Bereich von 15 % bis 20 %, zulässig ist, z.B. eine Verbesserung der Teillasteffizienz oder die Verringerung der Herstellkosten. Die hierfür durchgeführte Analyse erfolgt unter Verwendung eines einfachen analytischen Modells und eines detaillierten semi-numerischen Modells. Die

mit diesen Modellen berechneten Ergebnisse erlauben die Untersuchung fundamentaler Parameterabhängigkeiten, z.B. im Zusammenhang mit nicht-linearen Eigenschaften wie magnetischer Sättigung. Außerdem lässt sich daraus eine einfache Entwurfsvorschrift – bestehend aus zwei Gleichungen – für die nahezu optimale Auslegung von Induktivitäten ableiten. Die in dieser Arbeit berechneten Ergebnisse sind experimentell für drei verschiedene Induktivitäten und im Frequenzbereich zwischen 150 kHz und 750 kHz mittels kalorimetrischer Messungen verifiziert.

Im Rahmen der Durchführung des ersten Teils der Arbeit hat sich herausgestellt, dass die optimale Betriebsfrequenz einer Spule vergleichsweise hoch ist und in der Nähe der Frequenz liegt, bei welcher der Performance Factor (PF) des Kernmaterials das Maximum aufweist. Damit resultiert das Erfordernis, die Kernverluste auch bei hohen Frequenzen genau zu messen. Nach Kenntnisstand des Autors sind zur Zeit dieser Arbeit keine Messmethoden dokumentiert, welche bei hohen Frequenzen bis in den MHz-Bereich eine ausreichende Genauigkeit (z.B. eine Messunsicherheit kleiner als 25 %) erreichen. Daher wird im zweiten Teil dieser Arbeit eine transiente kalorimetrische Messmethode für Kernverluste entwickelt, welche einerseits genau und andererseits einfach und schnell implementierbar ist. Die entwickelte Messmethode wird einer detaillierten Sensitivitätsanalyse unterzogen und die daraus gewonnen Erkenntnisse ermöglichen die Erstellung einer einfachen Richtlinie zur optimalen Anwendung der Methode. Die Arbeit präsentiert gemessene Kernverluste des NiZn 67 Ferritmaterials (Fair-Rite) im Frequenzbereich zwischen 5 MHz und 50 MHz. Die bei diesen Messungen auftretende maximale Messunsicherheit beträgt 19,8 %, die mittlere Messunsicherheit 13,3 %. Der auf Basis der gemessenen Kernverluste berechnete PF weist ein Maximum bei 34 MHz auf. Im Zusammenhang mit den Ergebnissen des ersten Teils der Arbeit wird damit das große Potential von NiZn Ferritmaterialien für zukünftige, mit sehr hohen Schaltfrequenzen betriebene leistungselektronische Schaltungen deutlich.

Im letzten Teil dieser Arbeit wird eine Gleichrichtertopologie mit sinusförmiger Stromaufnahme untersucht, welche sowohl am dreiphasigen wie auch am einphasigen Netz mit derselben Ausgangsleistung betrieben werden kann. Ein solches Gleichrichtersystem stellt eine universelle Lösung für ein Ladegerät zur bordseitigen Integration in ein Elektrofahrzeug dar, da es sich in vielen Ländern der Erde betreiben lässt und auch die Herstellung einfacher und kosteneffizienter werden kann. Die Schaltungstopologie basiert auf einer gesteuerten dreiphasigen Gleichrichter-Brückenschaltung (3 Halbbrückenzweige bestehend aus je 2 MOSFETs) mit sinusförmigem Eingangsstrom.

Diese Schaltung wird um eine Dioden-Halbbrückenschaltung ergänzt, welche den Anschluss eines Rückleiters für den Strom im einphasigen Betrieb ermöglicht. Außerdem wird das EMV Filter geeignet angepasst, damit sowohl im dreiphasigen wie auch im einphasigen Betrieb eine effektive Filterwirkung gewährleistet ist. Im Zusammenhang mit der Auslegung des Gleichrichtersystems beinhaltet die Arbeit die zur Berechnung der Belastungen der wichtigsten Komponenten des Leistungsteils (Halbleiterschalter, Hochsetzstellerinduktivitäten, Zwischenkreiskondensator) benötigten analytischen Ausdrücke und fasst, darauf aufbauend, den Entwurf des Leistungsteils in einem Leitfadens zusammen. Hinzu kommen Überlegungen bezüglich der leitungsgebundenen elektromagnetischen Störungen und der Wirksamkeit der einzelnen Filterkomponenten in Abhängigkeit des Betriebsmodus (dreiphasig oder einphasig) und der Störsignalkomponente (Gegentakt oder Gleichtakt). Die experimentelle Überprüfung des vorgeschlagenen Konzepts erfolgt anhand eines realisierten Prototypen mit einer Nennleistung von 22 kW, welcher eine Leistungsdichte von 6.4 kW/dm^3 und, bei dreiphasigem Betrieb, eine maximale Effizienz von 98.2 % bei einer Ausgangsleistung von 15 kW sowie eine Effizienz von 97.9 % bei einer Ausgangsleistung von 19.5 kW erreicht. Der Betrieb mit einer Ausgangsleistung von 19.5 kW bestätigt, dass die Leistungskomponenten des Konverters auch bei Volllast nicht thermisch begrenzt sind. Außerdem wird der experimentelle Nachweis erbracht, dass der realisierte Gleichrichter die CISPR 11 EMV Grenzwerte (Klasse B, QP) sowohl im dreiphasigen wie auch im einphasigen Betrieb bei einer Ausgangsleistung von 4.5 kW einhält (die reduzierte Ausgangsleistung ist auf den begrenzten maximal zulässigen Strom der verwendeten Netznachbildungen zurückzuführen). Das vorgeschlagene Konzept lässt sich mit geringfügigen Modifikationen auch auf Multilevelkonvertertopologien, z.B. Flying Capacitor Konverter oder T-Type Konverter, anwenden, falls eine höhere Effizienz und/oder eine höhere Leistungsdichte erforderlich sein sollte.

Im letzten Kapitel werden zunächst die in dieser Arbeit gewonnenen Erkenntnisse zusammengefasst. Im Anschluss daran erfolgt, auf Basis des im Rahmen dieser Dissertation hinzugewonnenen Wissens bzw. der erarbeiteten Erfahrung, eine Beschreibung verschiedener Vorschläge für alternative Ansätze und möglicher Erweiterungen der hier untersuchten Themen. In diesem Zusammenhang werden verwandte wissenschaftliche Themenbereiche hervorgehoben, für deren tiefes Verständnis noch weitere Forschung erforderlich ist, und Gedanken im Hinblick auf zukünftige Projekte beschrieben.

Abbreviations

2D	Two-Dimensional
2LB6	Two-Level Six-Switch PFC Rectifier
3D	Three-Dimensional
3T2C	Three-Level T-type PFC Rectifier
AC	Alternating Current
CM	Common Mode
CUT	Core Under Test
DC	Direct Current
DM	Differential Mode
DSC	Differential Scanning Calorimeter
DUT	Device Under Test
EMI	Electromagnetic Interference
EMT	Electromagnetic Thermal
EV	Electric Vehicle
FEM	Finite Element Method
FoM	Figure of Merit
GaN	Gallium Nitride
GSE	Generalized Steinmetz Equation
HF	High Frequency
HT	Heat Transfer
ICE	Internal Combustion Engine
IGBT	Insulated Gate Bipolar Transistors
iGSE	improved Generalized Steinmetz Equation
IPT	Inductive Power Transfer
LISN	Line Impedance Stabilization Network
LMS	Least Mean Square
LF	Low Frequency
MF	Magnetic Field
MOSFET	Metal-Oxide-Semiconductor FET
NTC	Negative Temperature Coefficient
OP	Operating Point
PCB	Printed Circuit Board
PE	Protective Earth
PF	Performance Factor
PFC	Power Factor Correction
PWM	Pulse-Width Modulation
QP	Quasi-Peak

Abbreviations

rms	Root-Mean-Square
RTD	Resistance Temperature Detector
SE	Steinmetz Equation
Si	Silicon
SiC	Silicon Carbide
WBG	Wide Bandgap

Contents

Acknowledgments	v
Abstract	xi
Kurzfassung	xv
Abbreviations	xix
1 Introduction	1
1.1 Motivation	1
1.2 Aims & Contributions	4
1.3 Outline of the Thesis	12
1.4 Publications	14
2 Minimum Loss Operation of High-Frequency Inductors	19
2.1 Introduction	20
2.2 Analytical Model and Basic Design Principles	25
2.3 Semi-Numerical Analysis	40
2.4 Validation with Further Designs	54
2.5 Fast Design Guideline	57
2.6 Design Space Diversity	59
2.7 Experimental Verification	62
2.8 Conclusion	66
3 Transient Calorimetric Measurement of Core Losses	69
3.1 Introduction	70
3.2 Experimental Setup and Operating Principle	73
3.3 Measurement Accuracy	78
3.4 FEM Simulation	94
3.5 Experimental Verification	99
3.6 Conclusion	105
4 Universal 3-Phase / 1-Phase PFC Rectifier System	111
4.1 Introduction	112
4.2 Modifications for 1-Phase Operation	115
4.3 Design of Main Power Stage	122
4.4 Generated EMI Noise and Filtering	126
4.5 Experimental Results	141
	xxi

4.6	Conclusion	148
5	Conclusion and Outlook	151
5.1	Results of the Thesis	151
5.2	Future Trends and Research Areas	155
	Appendices	161
A	Transient Calorimetric Measurement of Core Losses	163
A.1	Derivation of Total Measurement Uncertainty	163
A.2	Derivation of Optimal Measurement Times	164
B	Universal 3-Phase / 1-Phase PFC Rectifier System	167
B.1	Asymmetric Construction of the 4-Phase CM Choke	167
B.2	Power Components' Stresses in 3-Phase Operation	169
B.3	Power Components' Stresses in 1-Phase Operation	175
B.4	Power Components' Stresses in 1-Phase Operation at Half DC-link Voltage	177
B.5	Extension to Three-Level Converters with Inherent Utiliza- tion of the DC Midpoint	179
	Bibliography	181
	Curriculum Vitae	199



Introduction

1.1 Motivation

According to [1], between the period of 2014-2019 the number of Electric Vehicles (EVs) expanded by an annual average of 60 %, leading to a total number of 7.2 millions, i.e., 1 % of the global market share. Even during 2020, where the Covid-19 pandemic had a substantial impact on the vehicle market, the sales of EVs remained broadly at 2019 levels, compared to Internal Combustion Engine vehicles (ICEs), which contracted by 15 %. According to the same data and the ambitious Sustainable Development Scenario, EVs are expected to occupy 30 % of the global market share by the end of 2030.

Targeting a net zero emissions future, EVs represent an essential solution, since the transportation sector accounted in 2015 for 18 % of the global CO₂ emissions [2]. In support of that, governments worldwide, either in the form of purchase subsidies (in the range of € 4,000 - 6,000) and/or tax exemption, promote the EV market and stimulate its development [1]. However, even after such governmental promotion, consumers need to deal with their range anxiety and the lack of widespread charging stations, which both constitute great concerns. Car manufacturers address such issues by increasing the installed battery capacity of EVs, nevertheless, leading to increased costs. In this regard, charging of EVs is essential, not only for practical reasons, but also in order to boost the confidence of future consumers. The IEC 62196 European standards [3] define four different charging modes. Modes 1 - 3 correspond to AC supplies, private or public, that incorporate the on-board EV charger. Each of the three modes features different power levels (commonly up to 22 kW), and different control/safety features. On the contrary, Mode 4, corresponds

to high-power off-board chargers (commonly up to 250 kW), that feature a DC output and are found only in public spaces [4].

Apart from the above standardized solutions, another solution represents the battery swapping initially started by *Better Place* in 2013, and currently adopted by the Chinese car manufacturer *Nio* [5]. Battery swapping allows for a replacement of the empty battery pack with a fully charged one, within less than 4 minutes, while parked at the dedicated stations. This can decrease the short-term EV value, since the possibility of purchase without bearing the cost of the battery pack is provided. Finally, *VW* has introduced the robot-charger which is located in parking lots and does not require dedicated infrastructures. Upon a call through the dedicated phone application, the robot brings a portable battery next to the respective EV, connects it to the car, and initiates the charging procedure [6]. This can be substantially beneficial also in terms of grid performance, since the individual charging of the portable batteries can take place outside the grid rush hours.

Even though DC fast chargers (Mode 4) are expected to expand in the future [7], this comes with many challenges, namely the increased cost of the infrastructures, the grid limitations with respect to the peak delivered power, the management of the generated heat (for a 250 kW charger, even an efficiency of 99 % requires the dissipation of 2.5 kW), the stress on the batteries and the need for a reliable battery management system [8–10]. According to [11], DC fast chargers of 50 kW will be the dominating technology of fast charging in the future, since it represents a good trade-off between charging speed and the above limitations, and allows for full charging during a 20 minutes break from driving, e.g., a refreshment stop, while traveling. Nevertheless, the same article considers the low power solutions (Modes 1 - 3), as the dominating solutions in general. This is mostly based on the fact that in Europe, cars travel in average approximately 10 km/day [12], ¹ which corresponds to home/work commute. As a result, slow charging at home and/or at work, which allows for slow, yet cheap and less stressful, with respect to the battery, charging, is sufficient. Additionally, access to DC fast chargers in rural areas is significantly limited. The same finding is also supported by [1], according to which currently 90 % of the installed chargers globally are low power chargers corresponding to 6.4 million units. Moreover, this number will increase to 210 million units by 2030. The same source, predicts that by 2030 the share of charging for passenger vehicles will be 87 % from private chargers (i.e., off-board installed at home, or on-board chargers),

¹The same number for the USA is approximately 64 km/day.

3 % public chargers of low power, and a limited 10 % from high power DC fast chargers. ²

All of the above indicate the need for continued advancements on private off-board, as well as, on-board low power EV chargers. In this context, this thesis addresses two main challenges, split into two parts. Part I focuses on possibilities of reduction of the volume of on-board chargers, by volume minimization of the magnetic components, and Part II on the conceptualization of a universal topology that allows for a single production line of EV chargers addressed worldwide.

1.1.1 Part I: Optimal Design of HF Inductors

Fundamentally, the volume reduction of an on-board charger can be achieved by employing multilevel topologies [13]. Moreover, with the arrival of WBG semiconductors, this can be further advanced, due to the reduced semiconductor losses, which lead to less cooling requirement, and, furthermore, allow operation at increased switching frequencies, hence, reduction of the size of the required EMI filter and the magnetic components. The latter is of great importance, since magnetic components constitute a substantial share of the total system volume.

Even though, magnetics are fundamental components of the total system, for many engineers they are frequently treated as black boxes and their full potential is not exploited. This applies also to the boost inductor, which is a key component of PFC rectifiers. An understanding of the behavior of such components, with respect to key system parameters, will allow for system designers to better utilize their resources and, as a result, achieve more compact and efficient designs. On this subject, optimization results show that operation at higher frequency is desirable, especially with respect to power density [14]. However, proper design is sensitive to accurate magnetic core data, especially at high frequencies.

1.1.2 Part II: Universal EV Charger Mains Interfaces

Since private chargers will dominate the charging share in the near future, universal solutions are mandatory. Typically, home appliances are of limited power, hence, single-phase power electronics, up to 7 kW, represents a universal solution. However, in case high power private charging is desired,

²The sharing prediction for China and Japan is 73 % private, 7 % public low power, 20 % public high power, due to increased population density.

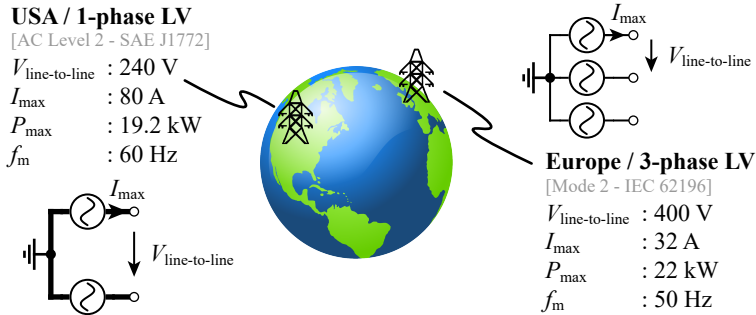


Fig. 1.1: Low Voltage (LV) mains for two different geographical regions, i.e., USA and Europe. The power distribution infrastructure in the USA features a split-phase 1-phase mains at 240 V line-to-line, and Europe features a 3-phase mains at 400 V line-to-line.

i.e., approximately 20 kW, such solution cannot be universally applied. The main reason for this are the existing low voltage (LV) grid infrastructures, which differ between different regions. Focusing on the USA and Europe (cf. **Fig. 1.1**), the power distribution infrastructure in the USA features a split-phase 1-phase grid at 240 V and 60 Hz, that allows for a maximum power delivery of 19.2 kW, whereas European countries feature a three-phase grid at 400 V and 50 Hz, that allows for a maximum power delivery of 22 kW, i.e., 7.3 kW per phase.

As a result, manufacturers of on-board EV chargers, or low-power off-board chargers, hold separate production lines between the products delivered to Europe and to the USA, which results in increased complexity and cost. Moreover, an after market purchase of an EV between the two continents results in limited charging capabilities, unless, DC fast charging is employed. Hence, there is a clear need for a universal solution.

1.2 Aims & Contributions

1.2.1 Part I: Optimal Design of HF Inductors

Aims

With the emergence of modern wide bandgap semiconductors, the performance barriers of power electronics are pushed further, and the main trend is led by designs that feature continuously increasing switching frequencies,

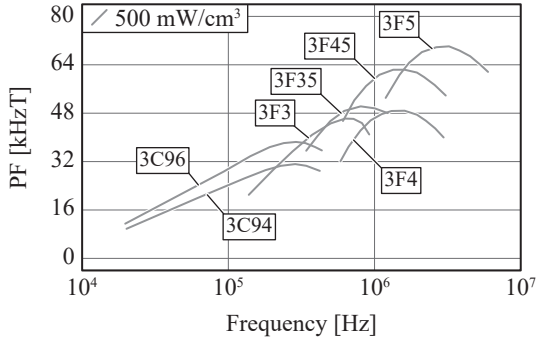


Fig. 1.2: Performance factor of different MnZn ferrites (adapted from Ferroxcube data [20]).

even into the MHz range [15–17]. As a result, the volume and, potentially, the cost of the realized systems is decreased, and at the same time reasonable efficiency values are achieved. Such trend can be significantly beneficial for many applications, including on-board EV battery chargers. According to [18], magnetic components are the bottleneck of common power electronic systems, especially with respect to the volume and the weight. Nevertheless, they seem to benefit from the increasing switching frequencies, as can be seen from the quick assessment provided by the Performance Factor (PF) plot of **Fig. 1.2**, where the value of the PF increases for different materials [19]. The PF corresponds to a typical figure of merit of magnetic core materials, commonly defined as:

$$PF = f\hat{B}, \text{ for } p = \text{constant}, \quad (1.1)$$

where f is the frequency, \hat{B} the peak flux density, and p the core-loss density. In other words, the PF represents the amount of electromagnetic induction that can be obtained from the analyzed material, for a fixed loss density.³

In this regard, the first part of this work focuses on a better understanding of the performance of magnetic components, and specifically inductors. This is done in two steps:

³The considered PF represents a simplified figure of merit that does not take other HF effects, such as the winding losses, into consideration.

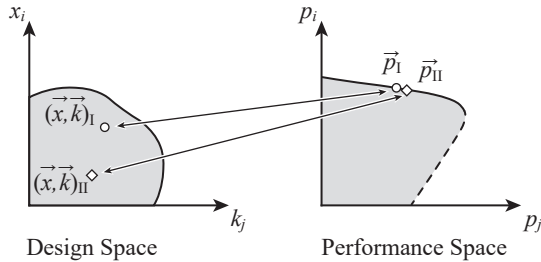


Fig. 1.3: Example of the design space diversity (figure adapted from [21]).

1. Investigating and understanding the optimal performance of inductors with respect to key system parameters, i.e., switching frequency and current ripple.
2. Investigating different methods for the measurement of core losses in the MHz range, in order to acquire accurate data, since HF ferrites are extremely promising at such frequencies.

Contributions

It is commonly known from literature, that converter designs with significantly different design parameters can result in similar overall performance values (cf. **Fig. 1.3**). This effect arises from different trade-offs and is referred to as the design space diversity [18]. Because of that, understanding of individual components, while conducting a complete system optimization, becomes difficult and, furthermore, typical optimization algorithms (e.g., brute force, genetic) bring results, nevertheless, with little understanding regarding the underlying mechanisms. As a result, an individual component investigation is required.

Since the goal is to analyze the component's performance from a system's perspective, main design parameters, such as core material/shape/size and type of coil are considered fixed, and only main system parameters, i.e., the switching frequency, and the current ripple are modified (cf. **Fig. 1.4**); for each analyzed point, the number of turns is optimized with respect to the generated total losses.

Based on this, optimal operating regions of the analyzed magnetic component and important trends are identified and further opportunities, with respect to secondary objectives, are highlighted. The latter becomes feasible, due to the significantly flat behavior of the optimal region and, eventually, is

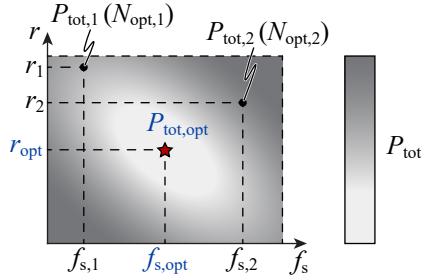


Fig. 1.4: Example of an $f_s - r$ plane contour plot, that reveals the optimal operating region of a power inductor. For the analysis, only the two fundamental system parameters, i.e., the switching frequency, f_s , and the current ripple, r , are modified, whereas the number of turns is always optimal. The remaining parameters are considered fixed.

thoroughly analyzed using a brute force optimization. For the verification of the theoretical results, a steady-state calorimeter is built, that achieves for measurements up to 5 W a maximum uncertainty of 54 mW. Finally, a simple two-equation design guideline for quasi-optimal inductor designs is proposed.

From the previous analysis, it becomes clear that core loss data is critical, since it largely determines the optimal operating region of the magnetic components. Theoretical models of the core losses cannot be used for engineering purposes due to their lack of quantitative accuracy, hence, state-of-the-art loss estimation models rely on semi-empirical equations and measured data, e.g., the Steinmetz Equation (SE), the Generalized Steinmetz Equation (GSE), or the improved Generalized Steinmetz Equation (iGSE) [22–27]. Nevertheless, acquiring such data is challenging, especially at very HF, i.e., > 1 MHz.

State-of-the-art methods are depicted in **Fig. 1.5**. The electrical measurement (electrical method 1) of the induced losses on the Core Under Test (CUT) of **Fig. 1.5(a)** features compensation of the reactive power, by series connection of a resonant capacitor, C_{res} , and, ideally, is insensitive to potential phase discrepancies of the measurement equipment, due to the proposed extraction method of the core losses [28]. It is, nevertheless, limited to sinusoidal excitations, which is the case only for resonant inductors and, occasionally, transformers. Unfortunately, for frequencies in the MHz range, the values of C_{res} are in the range of pF, hence, parasitics of the PCB, CUT and the complete setup, impact substantially the measurement's accuracy. **Fig. 1.5(b)**

Tab. 1.1: State-of-the-art measurement methods of core losses.

Parameter	Elec.	Elec.	Steady-state	Trans.
	Method 1	Method 2	Calor.	Calor.
	[28]	[29]	[31, 32]	[33]
Accur. [$f \rightarrow$ MHz]	✓	✓	✓✓✓	✓✓
Complexity	XX	XX	XXX	X
Post-process	X	XX	X	XX
Meas. time	Tens of sec.	Tens of sec.	Tens of min.	Tens of sec.

corresponds as well to an electrical measurement (electrical method 2) of the induced core losses and features (partial) compensation of the reactive power, by series connection of an air-core inductor, of similar inductance value. The compensation is achieved by 180° phase-shift at the outputs of the transformers as explained in [30]. This method is independent of the type of excitation, nevertheless, it can be impacted by the accuracy of the measurement equipment, and is subject to complex post-process calculations [29]. Finally, the proposed method of Fig. 1.5(c) corresponds to a steady-state calorimetric measurement of the induced core losses, that is independent of the type of excitation [31, 32]. Realization of such setup can be complex, however, experimental verification of its accuracy can be done simply by using a resistive device under test. The main drawback of such method is the measurement time, which is in the order of several minutes/hours.

In this work, a transient calorimetric measurement method of the core losses is developed that features a combination of the benefits of the above-mentioned state-of-the-art methods, i.e., time-efficiency, accuracy, and simplicity. **Tab. 1.1** depicts a qualitative comparison between the discussed methods and the proposed one. The method relies on the thermal monitoring of the CUT during the first seconds of its excitation. For this, a simple Negative Temperature Coefficient (NTC) thermistor can be employed. Based on a thorough sensitivity analysis of the uncertainty parameters for a given CUT, the proposed method achieved a worst-case uncertainty $< 30\%$ for a total range of measured losses between 20 mW - 20 W; and by using it, experimental core loss data of the NiZn 67 material from Fair-Rite was acquired for frequencies ranging between 5 MHz - 50 MHz. **Fig. 1.6** depicts the PF of the measured material, in comparison to the PF of the MnZn N87 material from EPCOS-TDK, both materials were measured during the course of this work.

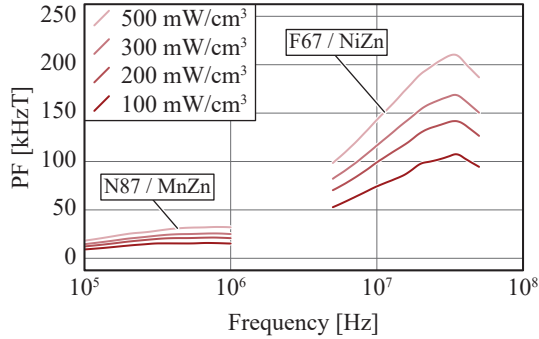


Fig. 1.6: Comparison between the PF of N87 MnZn ferrite from EPCOS-TDK and 67 NiZn ferrite from Fair-Rite (measurements from [33] - Chapter 3).

1.2.2 Part II: Universal EV Charger Mains Interfaces

Aims

At the moment, nearly no reasonable concept is known of a mains interface that allows full/rated power delivery of an EV charger, when employed in a 1-phase mains supply (e.g., USA) or a 3-phase mains supply (e.g., Europe) (cf. Fig. 1.1). Such concept requires that the employed system is able to deliver the same power and at the same time complies with the EMI noise regulations, while operating with different numbers of phases, voltage ratings and frequencies. Conventional 3-phase PFC rectifiers are limited to approximately 1/3 of the rated power in case of 1-phase operation.

Potential solution results from the utilization of isolated single-phase modules in adapted connection, either in parallel, in case of 1-phase grid, or in star (or delta), in case of 3-phase grid (cf. Fig. 1.7). Nevertheless, such a solution is complex and potentially expensive, since it requires three transformers and three individual DC/DC stages.

Contributions

In this work, a universal mains interface is proposed, that is based on the conventional two-level six-switch (2LB6) 3-phase boost-type PFC rectifier, featuring simple and cost-effective modifications, that allow both, 1-phase and 3-phase operation, at rated power (e.g., 22 kW). These are namely, a diode bridge-leg for the return current, a novel EMI filter that involves a 4-phase

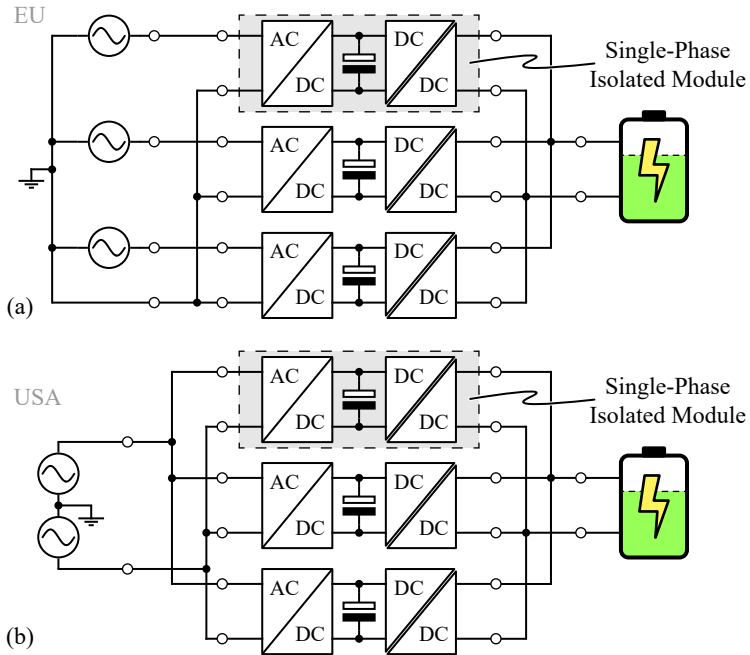


Fig. 1.7: Possible realization of an EV charger power circuit topology that allows full power delivery, both in a 3-phase (e.g., Europe) and a 1-phase (e.g., USA) LV mains, using 1-phase PFC rectifier modules and subsequent isolated DC/DC converter modules.

Common Mode (CM) choke, and a relay on the DC side that ensures proper attenuation of the generated CM noise, depending on the type of operation.

A 22 kW prototype confirms the proposed concept. The hardware achieves in 3-phase operation a measured efficiency of 97.9 % at 19.5 kW and a power density of 6.4 kW/dm³. Moreover, it successfully complies with the CISPR 11 Class B Quasi-Peak (QP) EMI regulations for both operating modes, i.e., 3-phase and 1-phase, while running at 4.5 kW.⁴ Compliance with the Class B limits of the CISPR 11 regulations is critical, since the final application corresponds to private charging in domestic environment. The concept can be extended also to multilevel topologies, which is beneficial, in case increased power density and/or efficiency is required.

1.3 Outline of the Thesis

The core of this thesis is structured in two parts (three chapters), whose content is summarized herein. In particular:

PART 1 - High-Frequency Inductors

► **Chapter 2**

The loss-optimal design of a power inductor employed in a 2 kW, 400 V DC/DC converter is analyzed in this chapter, for a given core and type of coil, i.e., litz wire with fixed strand diameter. First, analytical models are employed in order to identify certain trends and investigate the impact of critical non-linearities, e.g., core saturation. Further, a more accurate semi-numerical model is employed in order to confirm the initial findings. The main results are extended to different core size, different strand diameter, and distributed air-gap. A simple "two-equation" guideline that leads to quasi-optimal designs is proposed, and the design space diversity that may open design opportunities, with respect to secondary objectives, is discussed. The above are verified experimentally using three quasi-optimal Devices Under Test (DUTs) and an accurate steady-state calorimetric setup.

► **Chapter 3**

In this chapter, a transient calorimetric measurement method of core losses is presented. The main principles of the proposed method are

⁴During the EMI measurements, the power was limited to 4.5 kW, due to the power limitations of the employed Line Impedance Stabilization Network (LISN) in 1-phase operation.

discussed and a thorough analysis of the measurement uncertainties is presented. This is done based on two different approaches, i.e., a worst-case consideration, and a more realistic one, according to which, each uncertainty follows a Gaussian distribution. The main findings are verified through Finite Element Method (FEM) simulations, as well as, experimentally, by comparison with a state-of-the-art electrical measurement method (cf. Fig. 1.5(a)). Furthermore, measurements of a HF NiZn ferrite material up to 50 MHz are presented and a step-by-step description of the workflow is provided.

PART 2 - Universal EV Charger Mains Interfaces

► Chapter 4

A universal boost-type PFC rectifier topology that allows for operation at full/rated power in case of a 3-phase and a 1-phase mains is proposed. The topology is based on the conventional two-level six-switch (2LB6) 3-phase PFC rectifier which features simple and economical modifications. All required modifications are discussed in detail. Moreover, the stress on the main power components, i.e., semiconductors, boost inductors, and DC-link capacitors, is evaluated for both operating modes, i.e., 3-phase / 1-phase and a simple design guideline is presented. All sources of conducted Electromagnetic Interference (EMI), i.e., Differential Mode (DM) and Common Mode (CM), are analyzed for both operating modes and the dominating ones are considered for the design guideline of the EMI filter. The findings are experimentally verified by means of a 22 kW hardware prototype. Finally, an extension of the proposed concept to multilevel topologies is provided.

Conclusion and Outlook

► Chapter 5

The most significant findings of this thesis, i.e., optimal operation of magnetic components, accurate and fast measurement of magnetic core losses, and the proposed universal mains interface, are summarized in the conclusion. All challenges encountered along the way are discussed and potential improvements are proposed. Finally, poorly understood related topics are highlighted and, accordingly, future projects are proposed.

1.4 Publications

The most relevant documents created as part of this thesis, or in the scope of related projects, are listed in this section in chronological order.

1.4.1 Journal Papers

The main findings presented in this thesis have been published in international refereed journals. In particular:

- ⑤ T. Guillod, **P. Papamanolis**, and J. W. Kolar, “Artificial Neural Network (ANN) Based Fast and Accurate Inductor Modeling and Design,” *IEEE Open Journal of Power Electronics*, vol. 1, pp. 284–299, 2020.
- ④ **P. Papamanolis**, T. Guillod, F. Krismer, and J. W. Kolar, “Minimum Loss Operation and Optimal Design of High-Frequency Inductors for Defined Core and Litz Wire,” *IEEE Open Journal of Power Electronics*, vol. 1, pp. 469–487, 2020.
- ③ **P. Papamanolis**, T. Guillod, F. Krismer, and J. W. Kolar, “Transient Calorimetric Measurement of Ferrite Core Losses up to 50MHz,” *IEEE Transactions on Power Electronics*, vol. 36, no. 3, pp. 2548–2563, 2021.
- ② J. Azurza, G. Zulauf, **P. Papamanolis**, S. Hobi, S. Miric, and J. W. Kolar, “Three Levels Are Not Enough: Scaling Laws for Multi-Level Converters in AC/DC Applications,” *IEEE Transactions on Power Electronics*, vol. 36, no. 4, pp. 3967–3986, 2021.
- ① **P. Papamanolis**, D. Bortis, F. Krismer, D. Menzi, and J. W. Kolar, “New EV Battery Charger PFC Rectifier Front-End Allowing Full Power Delivery in 3-Phase and 1-Phase Operation,” *MDPI Electronics*, vol. 10, no. 17, pp. 2069, 2021.

1.4.2 Conference Papers

Core achievements presented in this thesis and other research results have been published in the proceedings of international conferences. In particular:

- ⑥ **P. Papamanolis**, D. Neumayr, and J. W. Kolar, “Behavior of the Flying Capacitor Converter Under Critical Operating Conditions,” in *Proc. of the 26th International Symposium on Industrial Electronics (ISIE)*, Edinburgh, Scotland, UK, 2017.

- ⑤ **P. Papamanolis**, F. Krismer, and J. W. Kolar, “Minimum Loss Operation of High-Frequency Inductors,” in *Proc. of the 33rd Applied Power Electronics Conference and Exposition (APEC)*, San Antonio, TX, USA, 2018.
- ④ **P. Papamanolis**, F. Krismer, and J. W. Kolar, “22 kW EV Battery Charger Allowing Full Power Delivery in 3-Phase as well as 1-Phase Operation,” in *Proc. of the 10th International Conference on Power Electronics (ICPE - ECCE Asia)*, Busan, Korea, 2019.
- ③ P. Czyz, F. Krismer, **P. Papamanolis**, T. Guillod, and J. W. Kolar, “New 40 kV / 300 kVA Quasi-2-Level Operated 5-Level Flying Capacitor SiC “Super-Switch” IPM,” in *Proc. of the 10th International Conference on Power Electronics (ICPE - ECCE Asia)*, Busan, Korea, 2019.
- ② **P. Papamanolis**, T. Guillod, F. Krismer, and J. W. Kolar, “Transient Calorimetric Measurement of Ferrite Core Losses,” in *Proc. of the 35th Applied Power Electronics Conference and Exposition (APEC)*, New Orleans, LA, USA, 2020.
- ① J. W. Kolar, J. Azurza, S. Miric, M. Haider, M. Guacci, M. Anti-vachis, G. Zulauf, D. Menzi, P. Niklaus, J. Miniboeck, **P. Papamanolis**, G. Rohner, N. Nain, D. Cittanti, and D. Bortis, “Application of WBG Power Devices in Future 3-Phase Variable Speed Drive Inverter Systems “How to Handle a Double-Edged Sword”,” in *Proc. of the 66th International Electron Devices Meeting (IEDM)*, San Fransisco, CA, USA, 2020.

1.4.3 Patents

The most innovative and original outcomes of the research of the author and others, which could offer a competitive advantage if commercially exploited, have led to the filing of national and international patents. In particular:

- ③ J. W. Kolar, J. E. Huber, F. Krismer, D. Neumayr, and **P. Papamanolis**, “Wechselrichter,” Patent Application (Austria), 2017.
- ② J. W. Kolar, **P. Papamanolis**, and F. Krismer, “Mehrphasige Umrichter-topologie für mehrphasigen und einphasigen Betrieb,” Patent Application (Switzerland), 2018.

- ① P. Czyz, **P. Papamanolis**, F. Krismer, T. Guillod, V. Lazarevic, J. W. Kolar, “Voltage Source Converter Configured to Transition Between at Least Two Voltage Levels,” Patent Application (Sweden), 2020.

1.4.4 Workshops, Seminars, Keynotes

Main results of the research activity of the author have been as well disseminated in the form of oral presentations at international academic and industrial workshops. In particular:

- ③ J. W. Kolar, F. Krismer, and **P. Papamanolis**, “General Properties / Scaling Laws & Inherent Limitations of Energy Electronics,” *Keynote Presentation at the 20th European PhD School Workshop*, Gaeta, Italy, 2019.
- ② J. W. Kolar, F. Krismer, P. Czyz, T. Guillod, and **P. Papamanolis**, “Emerging MV Applications - Data Centers & Superfast EV Charging,” *Presentation at the ECPE Workshop on Power Semiconductors in Medium Voltage Applications – SiC vs. Silicon*, Freiburg, Germany, 2019.
- ① **P. Papamanolis**, F. Krismer, and J. W. Kolar, “Minimum Loss Operation of High Frequency Inductors,” *Presentation at the ECPE Workshop on Magnetic Components in Power Electronics*, Grenoble, France, 2020.

PART 1

**Optimal Design
of HF Inductors**

2

Minimum Loss Operation of High-Frequency Inductors

This chapter summarizes most relevant research findings also published in:

- ▶ **P. Papamanolis**, T. Guillod, F. Krismer, and J. W. Kolar, “Minimum Loss Operation and Optimal Design of High-Frequency Inductors for Defined Core and Litz Wire,” *IEEE Open Journal of Power Electronics*, vol. 1, pp. 469–487, 2020.
- ▶ **P. Papamanolis**, F. Krismer, and J. W. Kolar, “Minimum Loss Operation of High-Frequency Inductors,” in *Proc. of the IEEE Applied Power Electron. Conf. and Expo. (APEC)*, San Antonio, TX, USA, 2018.

Motivation

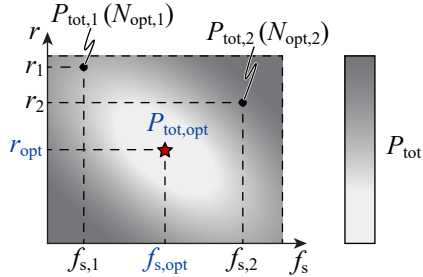
With the emergence of WBG semiconductors, power inductors have become the bottleneck of power electronic converters. However, the low losses of these devices allow for increased switching frequencies, which seem to be beneficial with respect to magnetic components. In order to understand such potential, this work focuses on a systematic analysis of the performance of power inductors, with respect to key system operating parameters, i.e., the switching frequency and the current ripple amplitude.

Executive Summary

This chapter studies the loss-optimal design of a power inductor employed in a 2 kW, 400 V input DC/DC converter. The design of an inductor is subject to a large number of design parameters and the implications of the different parameters on the losses are often not clearly traceable in a full optimization, e.g., different current ripple amplitudes can lead to designs with similar losses, as larger ripple amplitudes lead to increased AC core and winding losses but lower DC losses in the winding due to lower inductance values and/or lower numbers of turns. In an effort to achieve a comprehensible description of the implications of the key design parameters (switching frequency, f_s , current ripple, r , number of turns, N) on the losses, the remaining parameters, e.g., core (E55/28/21 N87) and type of conductor (litz wire), are considered to be given. In a first step, the investigation is based on a simplified analytical model, which is refined in a step-by-step manner, e.g., to consider core saturation. In a second step, the implications of further critical aspects on the losses, e.g., temperatures of core and coil, are examined using a comprehensive semi-numerical model. Surprisingly, the evaluation of the losses calculated in the f_s - r domain reveals that nearly minimum inductor losses are obtained for a current ripple that is inversely proportional to the frequency, i.e., for a constant inductance, within a wide frequency range, from 200 kHz to 1 MHz. Furthermore, the investigation reveals a decrease of the losses for increasing frequencies up to 375 kHz, e.g., from 4.32 W at 80 kHz ($r = 110\%$) to 2.37 W at 375 kHz ($r = 18\%$). The detailed analysis related to these results enables the compilation of a simple two-equation guideline for the design of an inductor that achieves close to minimum losses. In a next step, interesting trade-offs are identified based on a study of the design space diversity, e.g., with respect to low cost and increased partial-load efficiency. The findings of this work are experimentally verified, i.e., the losses of three different inductors are measured with an accurate calorimetric method and at four different frequencies, ranging from 150 kHz to 700 kHz.

2.1 Introduction

Wide-bandgap semiconductors have led to unprecedented switching frequencies, f_s , for power converters up to several MHz, commonly using modulation strategies that allow for soft transitions of the semiconductors (e.g., Triangular Current Modulation, TCM) [18, 34]. This is motivated by the expected increase in the power density on the system level, mainly due to the decrease of the volume of the magnetic components and/or the filtering requirements, e.g., with respect to EMI CISPR regulations. Literature confirms this trend [35], nevertheless, only from a system-level perspective. Applicability of this expectation on the magnetic components directly is not evident, and common



System parameter (for provided specifications)

- **Switching frequency - f_s**

Inductor design parameters

- **Current ripple - r**
 - **Number of turns - N**
 - **Air-gap length**
- } **Modified for each pair of (f_s, r)**
Condition: achieve r for given f_s
Goal: minimize total losses - P_{tot}
- **Core geometry:** shape, volume, aspect ratios, single/distributed gap
 - **Core material:** MnZn ferrite, NiZn ferrite etc.
 - **Coil type:** solid wire, litz wire (diff. strand diam.), foil, flat wire, conventional/optimized turn place.
 - **Coil material:** copper, aluminum
- } **Considered fixed**

Fig. 2.1: Compilation of typical degrees of freedom available in an inductor design. This work focuses on the choice of two key parameters, namely, switching frequency and current ripple, while ensuring an optimal choice of the number of turns and the air gap length. Further design parameters, e.g., magnetic core and type of conductor, are considered given.

potential misconceptions, according to which magnetic components represent the bottleneck of the complete systems, or that increasing frequency always leads to smaller components, and/or that 50 % of allowed relative peak-to-peak current ripple, r , is approximately optimal, remain unanswered. Investigations on a system level are less suitable to clarify the above, since designs with significantly different design parameters can map to nearly same overall performance values (e.g., efficiency, power density). This effect arises from different trade-offs and is referred to as design space diversity [18]; by way of example, increased switching frequencies may lead to smaller magnetic components but larger cooling systems, due to increased switching losses. Hence, individual component investigations are mandatory.

Such type of analysis has been previously conducted in literature, but mostly with respect to the operation of medium-frequency transformers. Specifically, using the Performance Factor ($PF = B_{\text{tot}} f_s$), the optimal region of operation of a transformer, with respect to the applied level and frequency of the magnetic flux density is defined [24, 36–38]. This is further improved in [19], where the impact of the High-Frequency (HF) copper losses is also considered. A more systematic and detailed approach is presented in [39, 40]. However, these considerations are not directly applicable to inductors, since critical key design parameters differ. Specifically, inductor designs feature an additional Low-Frequency (LF) core premagnetization component and also a different distribution of the magnetic field inside the winding window, due to the fringing-field caused by the air gap. The value of the inductance components of an inductor related to the stray field and the field in the magnetic core is more critical compared to transformers and, depending on the choice of f_s and L , the rms value of the AC current component varies, whereas in the case of the transformer it remains constant. Therefore, individual analysis of power inductors is required.

Multiple references exist in literature solely focusing on inductor optimization, divided into simple analytical models [41–44], semi-numerical and data-based models [45], the most recent convex optimization geometric program formulation [46] and finite element optimizations [47, 48]. Nevertheless, all the above focus on the modeling and optimization procedures and not on understanding the actual optimal operation of power inductors, which serves the main motivation behind this analysis. Such knowledge is critical for the evaluation of the validity of different optimization results, and also for the parametrization of the optimization algorithms, in order to become more computationally efficient, by accurately focusing the main objectives and the investigated region and parameter ranges of the design space [49].

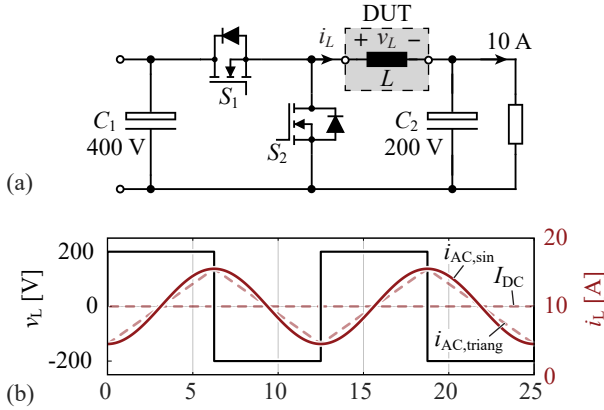


Fig. 2.2: (a) Considered topology of a DC/DC buck converter; (b) example of the considered sinusoidal waveform of the current ripple instead of a triangular shape, for $f_s = 80$ kHz switching frequency and $r = 110\%$ relative peak-to-peak current ripple.

As the following considerations should allow to gain insight into key parameter dependencies, the number of parameters that take influence on the inductor losses are reduced to a minimum, cf. **Fig. 2.1**. Specifically, the magnetic core (N87 TDK - E55/28/21) and the type of conductor (litz wire with single strand diameter, d_r , of $100\ \mu\text{m}$) are assumed as given. Moreover, the simple topology of a 2 kW DC/DC buck converter, cf. **Fig. 2.2(a)** is considered, that is operated with constant input and output voltages, and a sinusoidal instead of a triangular shape of the AC current ripple, with the same peak value, is assumed (cf. **Fig. 2.2(b)**), which typically results in a slight overestimation of the core losses [50].

Moreover, the above considerations do not have an impact on the generality of the findings, since similar magnetic excitations apply to typical AC/DC and DC/AC topologies, i.e., triangular voltage-imposed flux density waveform and LF current-imposed premagnetization. The implications of different core shapes on the core losses can be considered by a constant shape factor [51]. Finally, different ferrite materials exhibit similar loss characteristics, in different frequency ranges, as shown in the performance factor graphs presented in [20, 52].

With this, the analysis can emphasize on the implications of the remaining three design degrees of freedom, i.e.,

1. switching frequency, f_s

2. relative peak-to-peak current ripple (or inductance, assuming 50 % duty cycle),

$$r = \frac{2I_{AC,pk}}{I_{DC}} \quad \text{with} \quad I_{AC,pk} = \frac{V_o}{4f_s L}, \quad (2.1)$$

3. number of turns, N ,

on the losses. In **Section 2.2**, the impact of critical non-linearities, i.e., saturation of the magnetic core and varying Steinmetz parameters for different magnetic flux waveform characteristics (e.g., frequency, amplitude), is investigated using simple analytical equations. In addition, the optimal $f_s - r$ operating area with regard to minimal inductor losses is inspected in detail, revealing a flat characteristic around the minimum. In a second step, **Section 2.3** proposes and evaluates a detailed semi-numerical model in order to take the following aspects, which have been omitted in Section 2.2, into account:

- ▶ More accurate calculation of the copper AC resistance (e.g., by detailed calculation of the magnetic field in the core window);
- ▶ Impacts of f_s , AC and DC flux densities, and core temperature on the core losses;
- ▶ Detailed thermal model;
- ▶ Placement of each turn in the coil (turn packaging).

Based on this, the initial findings from the analytical models are confirmed. The results presented in Section 2.3, which are obtained for given core and single strand diameter, denote the basis for further evaluation in **Section 2.4**, where different design considerations are analyzed, i.e., distributed air gap, different strand diameter of the litz wire, and different core size. **Section 2.5** presents a simple "two-equation" guideline that directly leads to quasi-optimal designs, and in **Section 2.6** the design space diversity of inductors is investigated, which reveals further design opportunities, with respect to quasi-optimal designs (i.e., up to +20 % losses from the global optima $P_{gl,opt}$, but at lower manufacturing cost and improved partial load efficiency) [18, 39]. Finally, in **Section 2.7**, all the above-mentioned findings are further confirmed through experimental verification.

Tab. 2.1: Main specification.

Parameter	Value
Topology	DC/DC buck converter
Nominal power (P_{nom})	2 kW
Input voltage (V_i)	400 V
Output voltage (V_o)	200 V
Considered frequencies (f_s)	[40, 1000] kHz
Efficiency profile	Euro weighted efficiency [55]
Ambient temperature (T_{amb})	60 °C
Cooling mechanism	Natural convection

2.2 Analytical Model and Basic Design Principles

Tab. 2.1 lists the specifications of the considered DC/DC buck converter, which have their origin in typical specifications of commercial solar inverters; the output to input voltage ratio of 0.5 has been selected in order to consider maximum current ripple. The considered ambient temperature, T_{amb} , at 60 °C corresponds to a commonly considered maximum case temperature of a converter [53]. In addition, in **Tab. 2.2**, the main geometrical and electrical parameters of the considered inductor are presented. The N87 ferrite core material of TDK-EPCOS is a commonly used low-cost material that features minimum losses for core temperatures between 80 °C and 90 °C and achieves a high performance factor [52] in the considered operating range. The chosen E55/28/21 core allows for a thermally valid operation in an wide range of f_s and r . For this model, a distributed air gap on the centered limb is considered, since, for this special case, an analytical solution exists for the magnetic field distribution inside the core window [54]. Finally, the selected litz wire with a single strand diameter of $d_r = 100 \mu\text{m}$ is a good compromise between low losses and cost in the investigated ranges of f_s and r .

2.2.1 Nonsaturable Core, Constant Steinmetz Parameters

In a first step, the analysis neglects the presence of magnetic flux density saturation, the frequency and flux density dependence of the Steinmetz parameters, and the influence of the core DC premagnetization on the core

Tab. 2.2: Main design parameters.

Parameter	Value
Ferrite core	MnZn N87 E 55/28/21
Type of coil	Round litz wire, $d_r = 100 \mu\text{m}$
Core volume (V_c)	44000 mm^3
Core cross-section (A_c)	353 mm^2
Winding window area (A_w)	250 mm^2
Winding window width (w_w)	10.2 mm
Average turn length (l_{avg}) ¹	116 mm
Copper fill factor (k_f) ¹	30%
Copper conductivity (σ) ¹	$50 \cdot 10^6 \text{ S/m}$
Mag. flux density sat. (B_{sat})	360 mT
Steinmetz par. ($k_{\text{SE}}, \alpha, \beta$) ¹	$9.66, 1.30, 2.59$
Core temperature (T_{core}) ¹	$80 \text{ }^\circ\text{C}$

¹This value applies only to the analytical model, discussed in Section 2.2.

losses. Even though this approach is of limited accuracy, its results enable the deduction of first conclusions with regard to suitable values of f_s , r , and N .

The inductor losses are split into copper and core losses. The copper losses feature DC and AC components,

$$P_{\text{Cu,tot}} = \underbrace{R_{\text{DC}} I_{\text{DC}}^2}_{P_{\text{Cu,DC}}} + \underbrace{c_0 R_{\text{DC}} \frac{I_{\text{AC,pk}}^2}{2}}_{P_{\text{Cu,AC}}}, \quad R_{\text{DC}} = \frac{N l_{\text{avg}}}{\sigma k_f \frac{A_w}{N}}, \quad (2.2)$$

where c_0 considers skin and proximity effects [54],

$$c_0 = \begin{cases} 1 + \frac{1}{12} \left(\frac{k_f w_w d_r}{\delta^2} \right)^2 & \forall d_r < 3.17\delta, \\ \frac{1}{\delta} \left(\frac{d_r}{4} + \frac{8(k_f w_w)^2}{3d_r} \right) & \forall d_r \geq 3.17\delta. \end{cases} \quad (2.3)$$

In (2.3), δ and w_w denote the skin depth and the width of the core window, respectively.

The magnetic flux density can be separated into a current-imposed DC component and a voltage-imposed AC component,

$$B_{\text{DC}} = \frac{L I_{\text{DC}}}{N A_c}, \quad B_{\text{AC}} = \frac{V_o}{4 f_s N A_c}. \quad (2.4)$$

Since the implications of B_{DC} on the core losses are neglected in this Section, only B_{AC} contributes to the core losses, which, for sinusoidal waveforms, are

calculated with the Steinmetz Equation (SE) [23],

$$P_{\text{core}} = V_c k_{\text{SE}} f_s^\alpha B_{\text{AC}}^\beta = V_c k_{\text{SE}} f_s^{\alpha-\beta} \left(\frac{V_o}{4N A_c} \right)^\beta. \quad (2.5)$$

With (2.2) and (2.5) the total inductor losses are

$$P_{\text{tot}} = P_{\text{Cu,tot}} + P_{\text{core}} = c_1 N^2 + c_2 N^{-\beta} \quad (2.6)$$

with

$$c_1 = \frac{P_{\text{Cu,tot}}}{N^2} = \frac{(32 f_s^2 I_{\text{DC}}^2 L^2 + c_0 V_o^2) l_{\text{avg}}}{32 \sigma A_w k_f f_s^2 L^2}, \quad (2.7)$$

$$c_2 = \frac{P_{\text{core}}}{N^{-\beta}} = V_c f_s^{\alpha-\beta} k_{\text{SE}} \left(\frac{V_o}{4A_c} \right)^\beta. \quad (2.8)$$

For $dP_{\text{tot}}/dN = 0$, the optimal number of turns,

$$N_{\text{opt}} = \left(\frac{\beta c_2}{2 c_1} \right)^{\frac{1}{2+\beta}}, \quad (2.9)$$

results, which enables the derivation of the optimum ratio between core and copper losses, with respect to minimum total losses, as often stated in literature [56, 57],

$$\left. \frac{P_{\text{core}}}{P_{\text{Cu,tot}}} \right|_{N=N_{\text{opt}}} = \frac{2}{\beta}. \quad (2.10)$$

The minimum total losses for given inductance and switching frequency are

$$P_{\text{tot,opt}} = P_{\text{tot}}(N_{\text{opt}}) = c_3 \left(\frac{c_4 f_s^2 L^2 + 1}{L^2} \right)^{\frac{\beta}{2+\beta}} f_s^{\frac{2(\alpha-2\beta)}{2+\beta}}, \quad (2.11)$$

with

$$c_3 = (2 + \beta) \left[\left(\frac{k_{\text{SE}} V_o^{2\beta} V_c}{2A_c^\beta} \right)^2 \left(\frac{c_0 l_{\text{avg}}}{512 A_w k_f \sigma \beta} \right)^\beta \right]^{\frac{1}{2+\beta}}, \quad (2.12)$$

$$c_4 = \frac{32 I_{\text{DC}}^2}{c_0 V_o^2}. \quad (2.13)$$

According to (2.11) and for constant frequency, the total losses for $N = N_{\text{opt}}$ monotonically decrease for increasing inductance and, for $L \rightarrow \infty$,² converge to

$$P_{\text{tot,opt}}(f_s)|_{L \rightarrow \infty} = P_{\text{conv}}(f_s) = c_3 c_4^{\frac{\beta}{2+\beta}} f_s^{\frac{2(\alpha-\beta)}{2+\beta}}. \quad (2.14)$$

The resulting non-zero value of $P_{\text{conv}}(f_s)$ is related to the fact that both, copper losses and core losses, cannot approach zero, since I_{DC} and B_{AC} are constant (independent of L - assuming constant N) and greater than zero. In addition, the copper losses increase for increasing N and the core losses decrease for increasing N , cf. (2.2) and (2.5). Thus, for $L \rightarrow \infty$, the optimal number of turns converges to a finite value greater than zero, too, in order to maintain $P_{\text{core}}/P_{\text{Cu,tot}} = 2/\beta \approx P_{\text{core}}/P_{\text{Cu,DC}}$,

$$\lim_{L \rightarrow \infty} N_{\text{opt}} = N_{\text{conv}} = c_5 f_s^{\frac{\alpha-\beta}{2+\beta}}, \quad (2.15)$$

$$c_5 = \left(\frac{2^{-1-2\beta} \sigma A_w k_f k_{\text{SE}} \beta \left(\frac{V_o}{A_c} \right)^\beta V_c}{I_{\text{DC}}^2 l_{\text{avg}}} \right)^{\frac{1}{2+\beta}}. \quad (2.16)$$

In contrast, the value of $P_{\text{conv}}(f_s)$ monotonically decreases for increasing frequency, given that $\alpha < \beta$ applies, and converges to zero for $f_s \rightarrow \infty$, cf. (2.14). The reason for this result can be explained based on the decrease of the voltage time area due to the increase of f_s , which enables a decrease of the core losses. This, in turn, is accompanied by a decrease of the copper losses in order to maintain $P_{\text{core}}/P_{\text{Cu,tot}} = 2/\beta$. Accordingly, also N_{opt} approaches zero for $f_s \rightarrow \infty$ (to approach zero copper losses).³

Fig. 2.3(a) depicts an f_s - r contour plot of the total losses (including losses due to skin and proximity effects) for the parameters listed in Tab. 2.2 and an extended range of operating points, i.e.,

$$50 \text{ kHz} \leq f_s \leq 1 \text{ MHz} \quad \text{and} \quad 1\% \leq r \leq 500\%, \quad (2.17)$$

to obtain a more complete picture.⁴ Fig. 2.3(a) confirms the findings described above:

² $L \rightarrow \infty$ is theoretically evaluated by assuming infinite permeability of the ferrite core and an air gap that approaches zero.

³For the analysis, a non-integer number of turns is allowed.

⁴The maximum ripple in a practical system with MOSFET semiconductors may not exceed the value needed for quasi-lossless switching, i.e., approximately 200%.

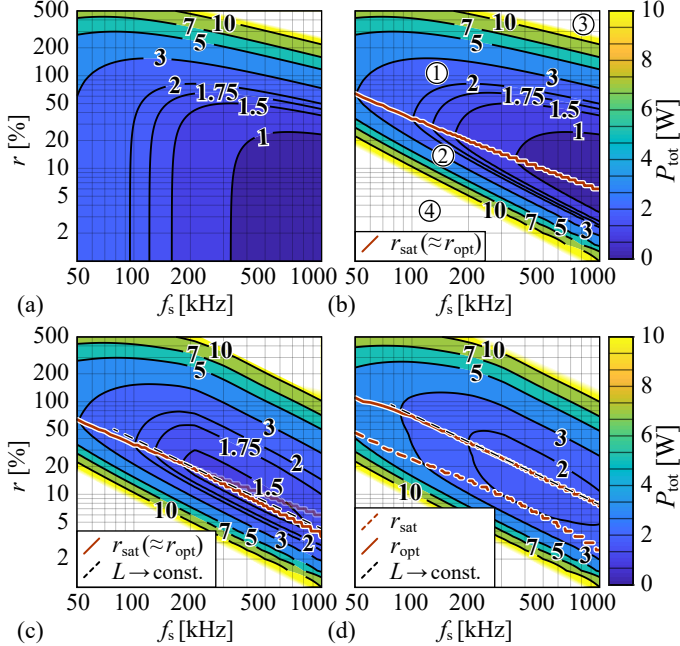


Fig. 2.3: Contour plots of the total losses, for the f_s - r -plane defined with (2.17) and four distinct cases: (a) no saturation limit, constant Steinmetz parameters; (b) saturation limit of 360 mT, constant Steinmetz parameters; (c) and (d) saturation limit of 360 mT, operating-point dependent Steinmetz parameters; (c) only considers the implications of B_{AC} and f_s on k_{SE} , α , and β ; (d), in addition, takes the impact of B_{DC} on the Steinmetz parameters into account.

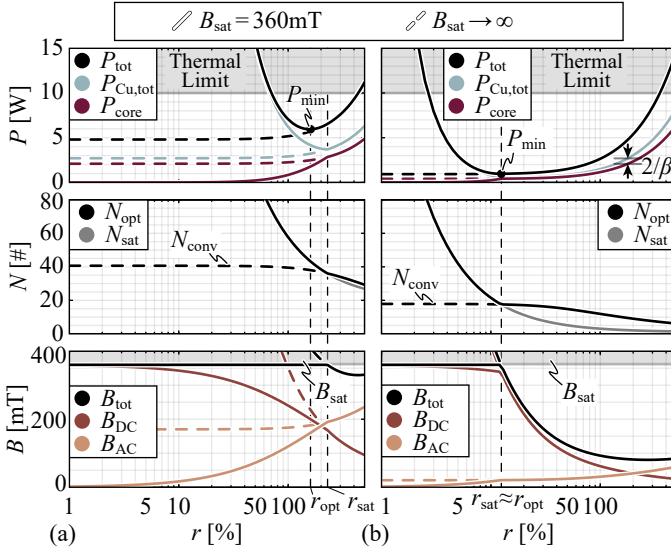


Fig. 2.4: Investigation of the optimal ripple (or inductance), r_{opt} (or L_{opt}), for two different frequencies, i.e., (a) 20 kHz, and (b) 375 kHz. For both frequencies, the cases of magnetic flux density going to infinity and limited at 360 mT are depicted.

1. For a given frequency, minimum total losses result for $L \rightarrow \infty$ (corresponding to $r \rightarrow 0$);
2. The value of $P_{\text{conv}}(f_s)$, i.e., the total losses for $r \rightarrow 0$, decreases for increasing frequency.

2.2.2 Saturable Core, Constant Steinmetz Parameters

For L approaching infinity and N approaching the finite value N_{conv} , the current-imposed DC flux component approaches infinity, cf. (2.4). This is not realistic, due to saturation of the magnetic core. In the following, the magnetic flux density saturation limit of the considered ferrite core, B_{sat} , is set to 360 mT.

In order to get an understanding of the implications of the magnetic flux density saturation limit on the optimal ripple value, **Fig. 2.4** presents the characteristics of the losses, the optimal number of turns for given r and f_s , and the flux densities with respect to ripple and for two different frequencies

of 20 kHz and 375 kHz.⁵ It can be observed that, due to $B_{DC} + B_{AC} \leq B_{sat}$, a clear loss minimum, P_{min} , results for a given frequency, which appears at a ripple r_{opt} that is slightly less but close to r_{sat} , i.e., the ripple where the theoretically calculated magnetic flux density is equal to the saturation magnetic flux density. Below this ripple there is a steep increase of N , in order to limit the magnetic flux density. The difference between r_{opt} and r_{sat} arises, because in this limited interval the decrease of the AC copper losses, $P_{Cu,AC}$, for decreasing r , together with the decrease of P_{core} due to the increase of N , outweigh the increase of the DC resistance, R_{DC} . A theoretical verification of the impact of $P_{Cu,AC}$ on r_{opt} has been conducted by applying $P_{Cu,AC} = 0$ in (2.2), which yields

$$P_{tot} = P_{min} \quad \forall r \geq r_{sat} \quad \Leftrightarrow \quad P_{Cu,AC} = 0. \quad (2.18)$$

Even though this result is mainly of theoretical value, it confirms that $r_{opt} < r_{sat}$ can only result for $P_{Cu,AC} > 0$.⁶ With increasing frequency, the values of r_{sat} and r_{opt} decrease and, in addition, r_{opt} approaches r_{sat} , e.g., at 375 kHz, $r_{opt} \approx r_{sat}$ applies.

The f_s - r contour plot of the total losses that considers the saturation limit is shown in **Fig. 2.3(b)**. Four regions are highlighted. Region ① corresponds to thermally valid designs that are not limited by saturation and can acquire their corresponding optimal number of turns. Region ② corresponds to designs that are limited by saturation. The trajectory of r_{sat} , which is approximately equal to the trajectory of r_{opt} , delimits the two regions. Regions ③, ④ correspond to thermally invalid designs due to excessive AC copper/core losses and DC copper losses, respectively.

No analytical solution has been found for r_{opt} , however, an analytical expression can be derived for r_{sat} and, using (2.1), for L_{sat} . Subsequently, $L_{opt} \approx L_{sat}$ is considered, based on the assumption that r_{opt} is close to r_{sat} . Starting with (2.4),

$$B_{tot} = B_{DC} + B_{AC} = B_{sat} \Rightarrow N = \frac{4f_s L I_{DC} + V_o}{4f_s A_c B_{sat}} \quad (2.19)$$

applies for N . Furthermore, N needs to be equal to N_{opt} , cf. (2.9), in order to obtain minimum losses. The equation $N = N_{opt}$ can be solved with respect

⁵The frequency value of 20 kHz is considered only in this section for better understanding of the analysis, nevertheless, it is a non-optimal frequency for the considered core material and, thus, for the rest of the analysis is omitted.

⁶In addition, and in anticipation of the results discussed in Section 2.3, the finding (2.18) will contribute to the reason why the loss optimum computed with the detailed inductor model is rather flat within a relatively wide range of r .

to L based on the assumption that $B_{DC}^2 \gg B_{AC}^2$ applies,⁷ which is a valid assumption in the considered frequency range. With this,

$$N_{opt} \approx \left(\frac{\sigma A_w k_f k_{SE} \beta \left(\frac{V_o}{A_c} \right)^\beta V_c f_s^{\alpha-\beta}}{2^{1+2\beta} I_{DC}^2 I_{avg}} \right)^{\frac{1}{2+\beta}} \quad (2.20)$$

and

$$L_{sat} \approx \underbrace{c_6 f_s^{\frac{\alpha-\beta}{2+\beta}}}_{L_{sat,a}} - \underbrace{\frac{V_o}{4 f_s I_{DC}}}_{L_{sat,b}} \approx L_{opt}, \quad (2.21)$$

$$c_6 = \frac{A_c^{\frac{2}{2+\beta}} B_{sat} \left(2^{-1-2\beta} \sigma A_w k_f k_{SE} \beta V_o^\beta V_c \right)^{\frac{1}{2+\beta}}}{I_{DC}^{\frac{4+\beta}{2+\beta}} I_{avg}^{\frac{1}{2+\beta}}} \quad (2.22)$$

result.

Compared to the numerically derived value of L_{sat} , (2.21) results in a maximum deviation of 0.64 % at $f_s = 100$ kHz and converges to zero for increasing frequency. At higher frequencies, the first term, $L_{sat,a}$, becomes dominant and, in a double-logarithmic representation,

$$\log(L_{sat,a}) = \log(c_6) + \frac{\alpha - \beta}{2 + \beta} \log(f_s), \quad (2.23)$$

$\log(L_{sat,a})$ is directly proportional to $\log(f_s)$. By way of example, for the settings listed in Tab. 2.2 ($\alpha = 1.30$, $\beta = 2.59$), $(\alpha - \beta)/(2 + \beta) = -0.28$ results, which, in terms of decibel (dB), corresponds to a change of $L_{sat,a}(f_s)$ by -5.6 dB/decade.

According to the findings related to (2.18), $L_{opt} \approx L_{sat}$ is valid if the AC copper losses have a negligible impact on the DC losses, i.e., for a low ratio of AC to DC copper losses. At $L = L_{sat}$, this ratio is obtained based on (2.2) and (2.20),

$$\frac{P_{Cu,AC,sat}(f_s)}{P_{Cu,DC,sat}(f_s)} 100\% \approx \frac{c_0}{32} \left(\frac{V_o}{f_s L_{sat} I_{DC}} \right)^2 100\%. \quad (2.24)$$

For the considered specifications, the result, marked with (i) in **Fig. 2.5**, shows

⁷By applying (2.4) to $B_{DC}^2 \gg B_{AC}^2$, the inequality $16(f_s L I_{DC})^2 \gg V_o^2$ results. With this, and for the assumption of a negligible impact of high-frequency losses due to skin and proximity effects ($c_0 = 1$), the expression $32(f_s L I_{DC})^2 + c_0 V_o^2$, which appears in the course of the derivation of (2.20), can be replaced by $32(f_s L I_{DC})^2$.

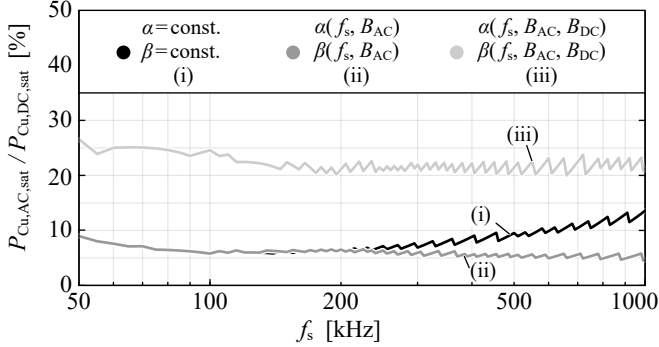


Fig. 2.5: Ratio of AC to DC copper losses with respect to switching frequency and for $L = L_{\text{opt}}$. Three distinct cases are depicted, (i) for constant Steinmetz parameters, (ii) for Steinmetz parameters that take into consideration the impact of f_s , B_{AC} , and (iii) for Steinmetz parameters that take into consideration the impact of f_s , B_{AC} , B_{DC} .

that the AC copper losses are less than 15 % of the DC copper losses within the complete range of considered frequencies, and the calculated relative error between P_{\min} and $P_{\text{tot}}(r_{\text{sat}})$ is less than 1 %. Nevertheless, even for the extreme case of 20 kHz, considered above, evaluation revealed that the relative error between P_{\min} and $P_{\text{tot}}(r_{\text{sat}})$ drops below 8 % already for an AC to DC copper loss ratio equal to 50 %.

Finally, since the condition $P_{\text{Cu,AC}} \ll P_{\text{Cu,DC}}$ at L_{sat} for $f_s \in [50 \text{ kHz}, 1000 \text{ kHz}]$ is validated, the optimal losses and number of turns, that correspond to each $L_{\text{opt}} - f_s$ pair can be directly calculated using (2.15) and (2.14), respectively. Comparison between the estimated ones through (2.15) and (2.14) and the ones using a brute-force evaluation approach returns an absolute maximum error below 1 % that converges towards zero with increasing frequency, for both values.

2.2.3 Steinmetz Parameters Dependent on f_s and B_{AC}

Since the Steinmetz parameters are obtained from an exponential fitting to measured core losses of the employed material, they are only valid within a limited range of operation. In order to increase the accuracy of the computed core losses, the employed Steinmetz parameters need to be adapted to the operating point, which, with regard to core losses, is mainly characterized by the magnetic flux density (frequency, amplitude of AC component, DC

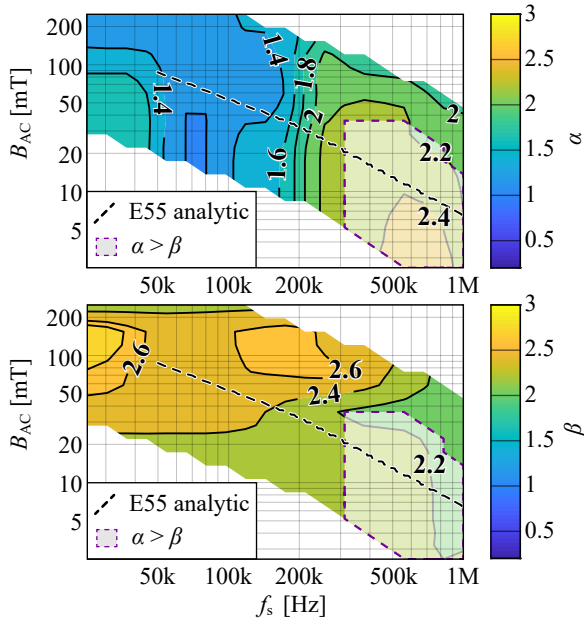


Fig. 2.6: Contour plot of the values of the Steinmetz parameters α , β with respect to the amplitude and the frequency of the applied AC magnetic flux density. The values are extracted using local Least Mean Square (LMS) fitting of the Steinmetz Equation on measured loss-data at 80 °C and a DC premagnetization equal to 0 mT (cf. Section 2.3). Additionally, a trajectory is highlighted that corresponds to the optimal designs, L_{opt} , of E55/28/21 core depicted in Fig. 2.3(c), Fig. 2.7.

bias) and the core temperature. **Fig. 2.6(a), (b)** depicts the values of α and β with respect to f_s and B_{AC} for the N87 material, $T_{core} = 80^\circ\text{C}$, and $B_{DC} = 0\text{ T}$. The values are obtained with local Least Mean Square (LMS) fittings of the Steinmetz Equation (SE) to measured losses (cf. Section 2.3). It can be seen that $\alpha < \beta$ applies for most combinations of f_s and B_{AC} , except for high frequencies, where the two parameters show approximately equal values; for $f > 350\text{ kHz}$ even $\alpha > \beta$ applies at some regions. The white regions in Fig. 2.6 correspond to regions where the resulting loss density is outside the limits of interest, i.e., $0.5\text{ kW/m}^3 < p_{core} < 1000\text{ kW/m}^3$. It should be noted that that these two maps change for different values of T_{core} and B_{DC} .

Fig. 2.3(c) shows a contour plot of the losses that results for (2.6) if the impact of the frequency and the AC magnetic flux density on the Steinmetz parameters is considered. The contour plot reveals a significantly flat region of low losses between 200 kHz and 1000 kHz. Since the characteristic properties of the losses along the minimum-loss trajectory marked with L_{opt} are of particular interest, **Fig. 2.7** presents a direct comparison of P_{tot} , L , N , B_{DC} , B_{AC} , and B_{tot} along these trajectories in Fig. 2.3(b) and Fig. 2.3(c), i.e., for constant and for operating-point dependent Steinmetz parameters (with respect to f_s, B_{AC}). In addition, the minimum-loss trajectory of Fig. 2.3(c) is also plotted in Fig. 2.6. According to Fig. 2.7, deviations between the results appear for $f_s > 200\text{ kHz}$. There, the minimum losses are nearly constant with respect to frequency if the Steinmetz parameters are adapted to the operating point. A view on Fig. 2.6(a) reveals that the characteristic of α along the optimal trajectory experiences a sharp rise from 1.6 to 2.2 (approaching the value of β) around 200 kHz, and, at 300 kHz, enters the region where $\alpha \approx \beta$ applies. With this, Fig. 2.7 confirms the findings related to (2.14), (2.20), and (2.21), that the minimum losses, the optimal inductance, and the optimal number of turns are independent of frequency given that $\alpha = \beta$ applies. Moreover, the result confirms that the optimal designs are all limited by saturation.

2.2.4 Steinmetz Parameters Dependent on f_s, B_{AC}, B_{DC}

DC flux premagnetization has, potentially, a strong impact on the core losses of commonly employed magnetic core materials [27]. **Fig. 2.3(d)** depicts the contour plot of the core losses for DC premagnetization being considered. Compared to Fig. 2.3(c), an increase of the losses is observed in low-loss regions, e.g., at $f_s = 500\text{ kHz}$ and $r = 10\%$. Furthermore, for given frequency, the minimum-loss trajectory, r_{opt} , yields a higher ripple than the trajectory r_{sat} . In order to investigate the reason for this result, **Fig. 2.8** details the characteristics of losses, inductance, and flux densities along the two tra-

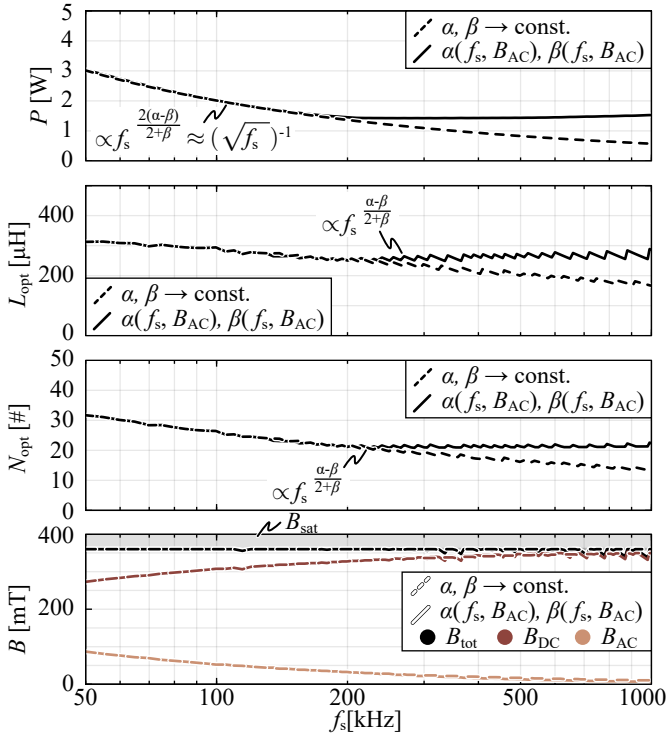


Fig. 2.7: Loss-optimal designs over frequency using the analytical model for two distinct cases, i.e., i. with AC proximity losses and constant Steinmetz parameters, ii. with AC proximity losses and Steinmetz parameters that take into consideration the impact of AC magnetic flux density and switching frequency for a constant temperature of 80 °C and $B_{DC} = 0$ mT.

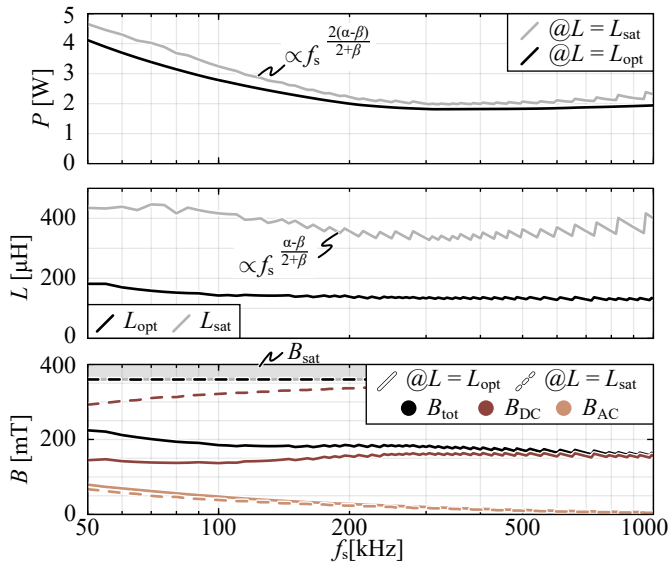


Fig. 2.8: Comparison of the main performance characteristics of the two trajectories L_{opt} and L_{sat} depicted in Fig. 2.3(d).

jectories, which reveals a substantial decrease of B_{DC} , from approximately 300 – 350 mT at $L = L_{sat}$ to 150 mT at $L = L_{opt}$. Furthermore, the losses increase only slightly when L increases from L_{opt} to L_{sat} , with a maximum deviation of 23.4 % at 1 MHz and an average deviation of 12.6 %. Accordingly, also the core losses and the total copper losses remain approximately similar, in order to maintain a loss ratio of z over β . Since the AC copper losses even increase for increasing ripple (the ratio $P_{Cu,AC}/P_{Cu,DC}$ reaches values between 20 % and 30 %, as shown with curve (iii) in Fig. 2.5), the loss reduction achieved by decreasing the inductance from L_{sat} to L_{opt} only stems from the reduction of the DC premagnetization, B_{DC} , that enables a reduction of the core losses.

2.2.5 Main Observations and the Three Quasi-Optimal Ranges

According to the above findings, optimal inductor designs feature a monotonically decreasing current ripple amplitude with increasing frequency that leads to an approximately constant inductance value. Moreover, designs with peak flux densities near saturation feature losses that are close to the optimum (for given frequency). The total losses decrease for increasing frequency, reaching a global loss minimum approximately at the point where the Steinmetz parameters α and β are equal. Around this point the total losses are relatively flat, with respect to all three design degrees of freedom: N , r , and f_s . In this regard, a range can be defined for each of the three degrees of freedom in order to identify inductor designs that feature almost minimum losses.

Flat range A – number of turns

In case of flat range A, the ripple and the switching frequency are kept constant, and N is changed, starting from the optimal value, N_{opt} . The derivation starts with the total losses (2.6), which can be expressed as a function of the optimal number of turns (2.9), and while assuming already a loss ratio of z over β ,

$$\frac{P_{tot}(N)}{P_{tot,opt}} = \frac{2}{2 + \beta} \left[\frac{\beta}{2} \left(\frac{N}{N_{opt}} \right)^2 + \left(\frac{N}{N_{opt}} \right)^{-\beta} \right]. \quad (2.25)$$

Expression (2.25) enables the calculation of N for a defined acceptable increase of the total inductor losses (with respect to the minimum inductor losses). However, no closed form solution is found and (2.25) needs to be solved numerically, instead. **Fig. 2.9** presents the boundaries of flat range A for an

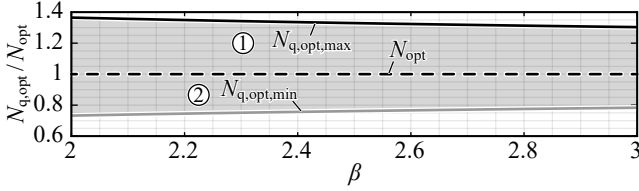


Fig. 2.9: Relative deviation from the optimal number of turns as a function of β . The gray area denotes the range of N that leads to an increase of the total losses of less than 20%. The lower and upper boundaries are directly calculated using (2.26) and (2.27), respectively.

accepted loss increase of 20%, i.e., $P_{\text{tot}}(N)/P_{\text{tot}}(N_{\text{opt}}) = 1.2$, and $2 < \beta < 3$. The region enclosing the applicable range of N , $N_{\text{q,opt,min}} < N < N_{\text{q,opt,max}}$, is split into the two regions ① and ②. Region ① results in better performance at partial load and region ② results in better performance in case of overload operation. This will be further discussed in Section 2.6, where the design space diversity of the inductor is investigated. The depicted boundaries can be approximated by means of LMS fitting,

$$N_{\text{q,opt,min}} \approx (0.6343 + 0.0505\beta) N_{\text{opt}}, \quad (2.26)$$

$$N_{\text{q,opt,max}} \approx (1.4835 - 0.0610\beta) N_{\text{opt}} \quad (2.27)$$

(the error between numerical and approximated results is less than 0.2% for $2 < \beta < 3$). Note that (2.26) and (2.27) are of universal character, i.e., not limited to the settings listed in Tables 2.1 and 2.2.

Flat range B – ripple

This flat range considers changing ripple, constant frequency, and optimal number of turns (at each individual operating point); the corresponding trajectories are vertical lines in the contour plots shown in Fig. 2.3. Fig. 2.4 illustrates respective examples for $f = 20$ kHz and $f = 375$ kHz and, in case of $f = 375$ kHz, reveals low total losses, close to the respective minima, within a relatively wide range of r . In addition, the impact of the DC bias on the core losses increases this range towards higher ripple values, due to the decreasing core losses, which provides a certain compensation of the increasing AC copper losses, cf. Section 2.2.4.

Flat range C – along L_{opt} trajectory

The last flat range is along the trajectory of optimal inductance, L_{opt} , highlighted in Fig. 2.3, and depends entirely on the relationship between α and β . For ferrite N87, this trajectory can be split into the two ranges listed below, cf. Fig. 2.8.

- ▶ 50 kHz $< f_s < 150$ kHz: $\alpha \in [1.3, 1.6]$, $\beta \in [2.6, 2.7]$; with (2.14), $P_{\text{tot,opt}} \propto f_s^{-0.60} \dots f_s^{-0.43} \approx 1/\sqrt{f_s}$ results;
- ▶ 250 kHz $< f_s < 850$ kHz: $\alpha \approx \beta \approx 2$ applies, i.e., with (2.14), $P_{\text{tot,opt}}$ remains approximately constant.

The second range corresponds to flat range C and is an unchanged optimal design, since the inductance value and the number of turns remain approximately constant as well. This can be particularly beneficial for conventional TCM operation, where different frequencies are applied to the same magnetic component.

2.3 Semi-Numerical Analysis

This Section revisits the analysis of Section 2.2, using a detailed semi-numerical model in order to clarify that the drawn conclusions remain true if previously disregarded effects, in particular due to elevated temperatures of core and coil, are taken into consideration. For this, the analyzed range is slightly modified to the more practical range

$$40 \text{ kHz} \leq f_s \leq 1 \text{ MHz} \quad \text{and} \quad 2\% \leq r \leq 200\%. \quad (2.28)$$

The employed ElectroMagnetic-Thermal (EMT) coupled inductor model is entirely implemented in MATLAB [58] and provides the capabilities listed below.

- ▶ *Core losses* are calculated with the improved General Steinmetz Equation (iGSE) [25]. The Steinmetz parameters are extracted by means of interpolation, using pre-measured loss values, that take the implications of AC magnetic flux density, frequency, core temperature, and DC premagnetization into consideration [21]. The losses of the employed core material, N87, have been measured using the method proposed in [59].

- ▶ *AC copper losses* in the HF litz wire are determined according to [60] with the magnetic field in the core window being computed with the mirroring method [45].
- ▶ *The thermal model*, which is based on [56] and extended according to [21], considers the heat dissipation mechanisms of conduction, convection, and radiation in order to compute the surface temperatures of coil and core and the hot-spot temperature inside the coil.

The EMT model implements an iterative procedure to take the implications of elevated temperatures on core and copper losses into account, i.e., the losses and the temperatures are computed in a subsequent manner until both, losses and temperatures, reach convergence. The employed EMT modeling approach has been experimentally verified in several converter designs, e.g., [61, 62].

For the analysis, and unless otherwise specified, the following considerations apply:

1. The cooling of the component is entirely based on natural convection and no forced air-flow is considered.
2. The core has a single air gap per core limb (instead of the distributed air gap assumed in Section 2.2 to simplify the analysis), since this denotes a more common type of realization.

2.3.1 Optimization with Respect to N

For each operating point characterized with f_s and r , the number of turns is optimized with respect to the losses and, under the assumption of a constant fill factor, this is expected to lead to an approximately equal share between the core and copper losses. **Figs. 2.10, 2.11** reveals air-gap lengths, flux densities, and losses with respect to N for the two selected operating points $f_s = 80$ kHz, $r = 110$ % and $f_s = 375$ kHz, $r = 18$ % (the global loss minimum); these two operating points serve as basis for the further analysis and are referred to with OP_1 and OP_2 , respectively.

The designs are limited by saturation in case of low N and by impractically large air gap values at high N , whereas the maximum air-gap lengths are limited to 30 % of the height of the core window. Due to the varying fill factor, which results from the packaging of the turns, local optima exist.

Despite the varying fill factor, the applicability of (2.25) and (2.26), (2.27) is also confirmed by direct comparison with the peaks of the bars. Specifically,

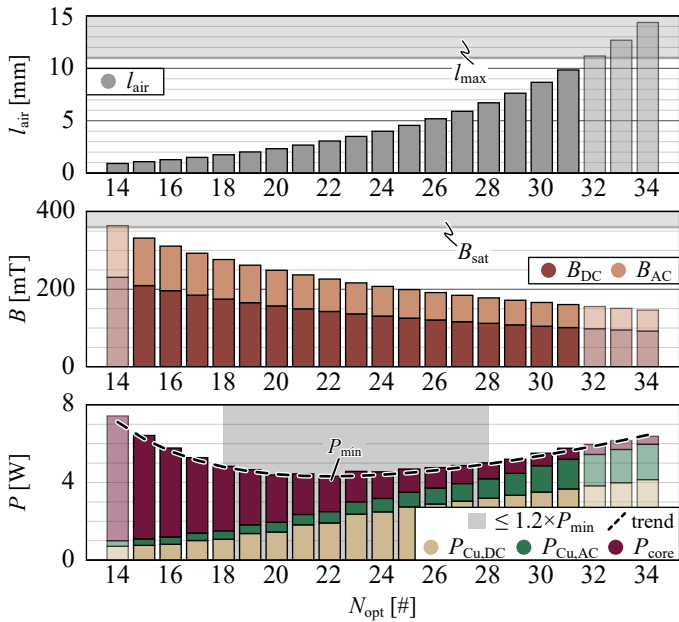


Fig. 2.10: Air-gap length, flux density, and losses for different numbers of turns for the following operating point: $f_s = 80$ kHz, $r = 110\%$. Local minima, P_{min} , and flat ranges A (cf. 2.2.5) are marked for both cases. The dashed trajectory denoted as trend corresponds to application of (2.25).

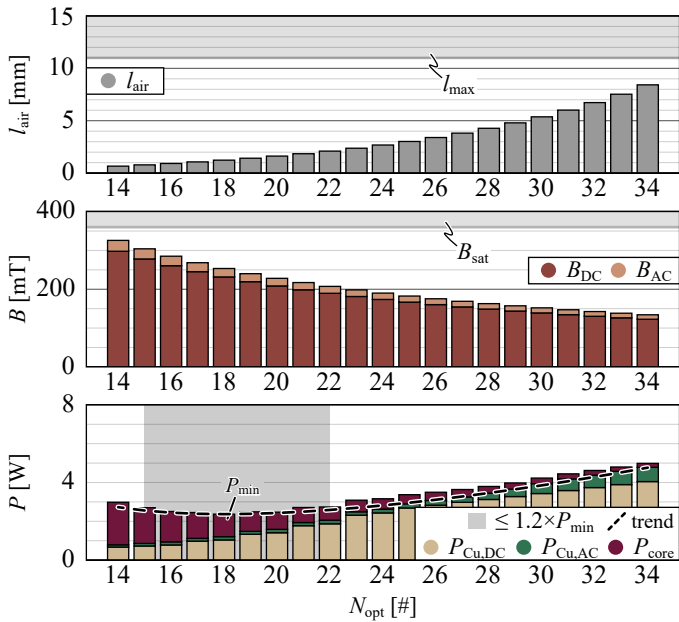


Fig. 2.11: Air-gap length, flux density, and losses for different numbers of turns for the following operating point: $f_s = 375$ kHz, $r = 18$ %. Local minima, P_{min} , and flat ranges A (cf. 2.2.5) are marked for both cases. The dashed trajectory denoted as trend corresponds to application of (2.25).

using i. for the case of 80 kHz a β of 2.63⁸, N_{opt} equal to 22 and $P_{\text{tot,opt}}$ equal to 4.32 W, and ii. for the case of 375 kHz a β of 2.28⁹, N_{opt} equal to 18 and $P_{\text{tot,opt}}$ equal to 2.37 W the analytical solutions of flat range A are denoted as trend. The analytically derived margins of the quasi optimal operation using (2.26), (2.27) are [16.9, 29.1] and [13.5, 24.2] turns, respectively. Finally, the ratio between the core and copper losses varies around the theoretical $2/\beta$ from 0.2 to 2.2. Direct comparison between the two optimizations depicted in Fig. 2.10, 2.11 confirms the initial conclusion, that at higher frequency and lower ripple, the total losses decrease substantially.

2.3.2 Optimization with Respect to f_s and r

Applying the presented local optimization with respect to the number of turns to all the points of (2.28), the contour plots of Fig. 2.12 result. Starting from Fig. 2.12(a) the total losses of each operating point of the optimization are presented. This contour is the equivalent of the analytically calculated result presented in Fig. 2.3(d). Even though, a direct comparison of the two contour plots reveals a similar trend with respect to loss-minimal operation, also significant deviations of the absolute losses can be observed. The main reasons for this difference are, the lower achieved fill factor, the more accurate estimation of the magnetic field inside the winding window, using the mirroring method, the consideration of a single air-gap per limb, instead of a distributed one, and the impact of the temperature on the core losses. Introduced noise, mainly apparent in Fig. 2.12(b), (c), results from the turn's packaging and the measured core loss data.

Fig. 2.12 also presents the global optimum, $P_{\text{gl,opt}} = 2.4$ W, which corresponds to OP₂, and two critical trajectories, i.e., the trajectory of minimum losses for changing frequencies, marked with r_{opt} , and the trajectory of changing ripple, constant frequency ($f = 375$ kHz), and optimal N , marked with r_{375} .

In the course of a closer inspection of Fig. 2.12(a), four characteristic regions are identified.

- Region ① is delimited by two dashed white lines, which illustrate the frequency-dependent changes of the two boundaries of the flat range B for a maximum increase of the losses by 20 % [for a given frequency and

⁸The value corresponds to a core temperature of 89 °C, AC magnetic flux density peak value of 80.2 mT and a DC pre-magnetization of 146 mT.

⁹The value corresponds to a core temperature of 77 °C, AC magnetic flux density peak value of 20.9 mT and a DC pre-magnetization of 233 mT.

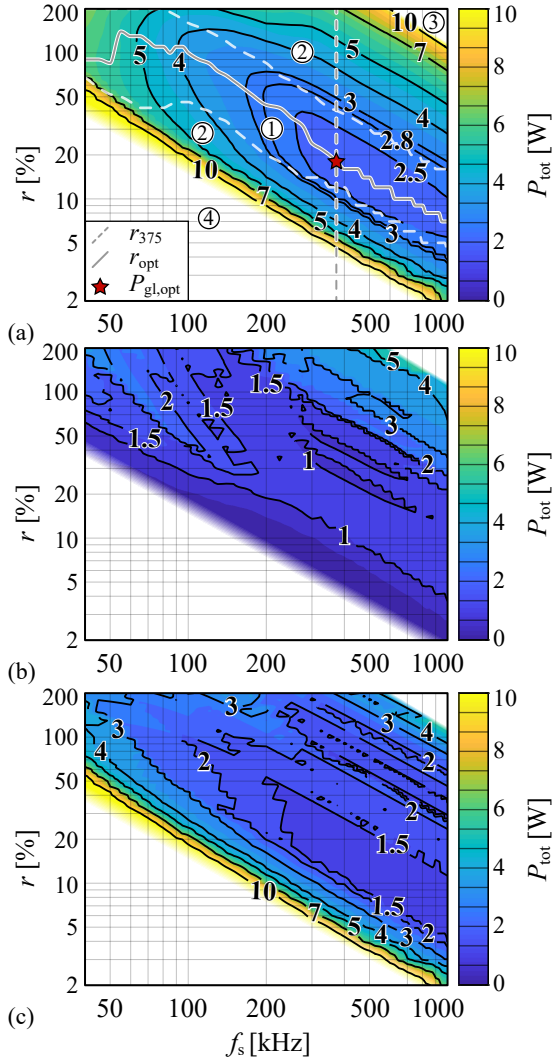


Fig. 2.12: Contour plot of (a) total losses, (b) core losses, and (c) total copper losses, for the $f_s - r$ -plane defined in (2.28). In (a), two trajectories are highlighted: r_{opt} , which corresponds to the minimum losses for changing frequency, and r_{375} , which corresponds to a changing ripple, a constant frequency of 375 kHz, and an optimum number of turns. The global optimum, $P_{\text{gl,opt}} = 2.4$ W, occurs at $f_s = 375$ kHz, $r = 18$ % and is marked with a red star.

with respect to the losses at $r_{\text{opt}}(f_s)$]. The designs within this region are most suitable for realization.

- ▶ Region ② corresponds to suboptimal designs, which are thermally valid, nevertheless, generate unnecessarily high losses.
- ▶ Regions ③ and ④ include invalid designs that will heat above the defined thermal limit, i.e., all temperatures must remain less than 125 °C. Region ③ is limited by AC (copper and core) losses and region ④ by DC copper losses, cf. Figs. 2.12(b), (c).

Fig. 2.13 presents the contours of the corresponding hot-spot temperature inside the coil, T_{hs} , the peak magnetic flux density, and the optimal number of turns, respectively. The hot-spot temperature follows a trend that is identical to the trend of the total losses shown in Fig. 2.12(a) and remains less than 100 °C for $f > 100$ kHz and an assumed ambient temperature of 60 °C. According to Fig. 2.13(b), designs with peak flux densities ranging from 140 mT to 360 mT can result in optimal operation. This confirms the finding that, for increasing ripple, the decrease of the DC flux bias leads to a decrease of the core losses, which can compensate the increase of the AC copper losses within flat range B. Fig. 2.13(c) highlights the fact that with increasing frequency and/or ripple the optimal number of turns decreases in order to lower the impact of the AC copper losses on the total losses. In case of low ripple values, the designs are limited by saturation, leading to a steep increase of the optimal number of turns for decreasing ripple. Finally, Fig. 2.13(c) also highlights the realized inductors and the operating points for experimental verification presented in Section 2.7.

2.3.3 Investigation of r_{opt}

Fig. 2.14 presents the losses and the inductors' characteristic values (L , N , B , and J_{rms}) along the $r_{\text{opt}}(f_s)$ trajectory. The region of low losses, close to the global minimum of 2.4 W, is very flat and starts at 200 kHz. Based on this, operation above 200 kHz to 300 kHz may not provide us with additional benefits on a system level, since the remaining converter losses, e.g., switching losses of semiconductors, will keep increasing. Alternatively, different core material that features higher PF at these frequencies can be considered.

The graphs of L_{opt} and B in Fig. 2.14 confirm the finding of the analysis of Section 2.2 that, with respect to decreasing ripple, the flat range B extends to saturation limited designs. **Fig. 2.15** presents a comparison of the optimal designs to the designs limited by saturation with respect to frequency and

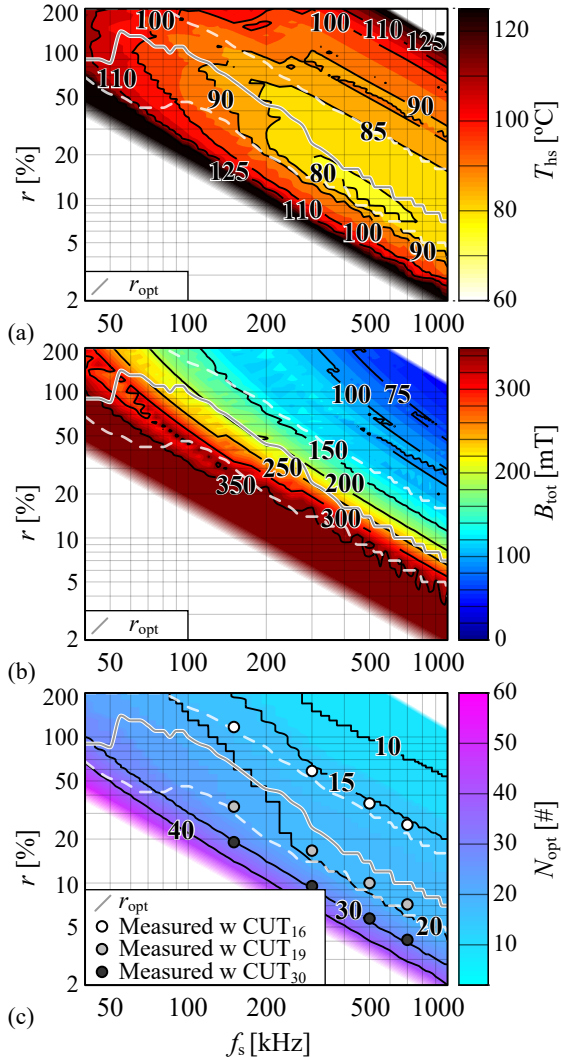


Fig. 2.13: Contour plots of (a) hot-spot temperature inside the coil, (b) peak magnetic flux density, and (c) optimal number of turns. The presented values are used to compute the losses in Fig. 2.12.

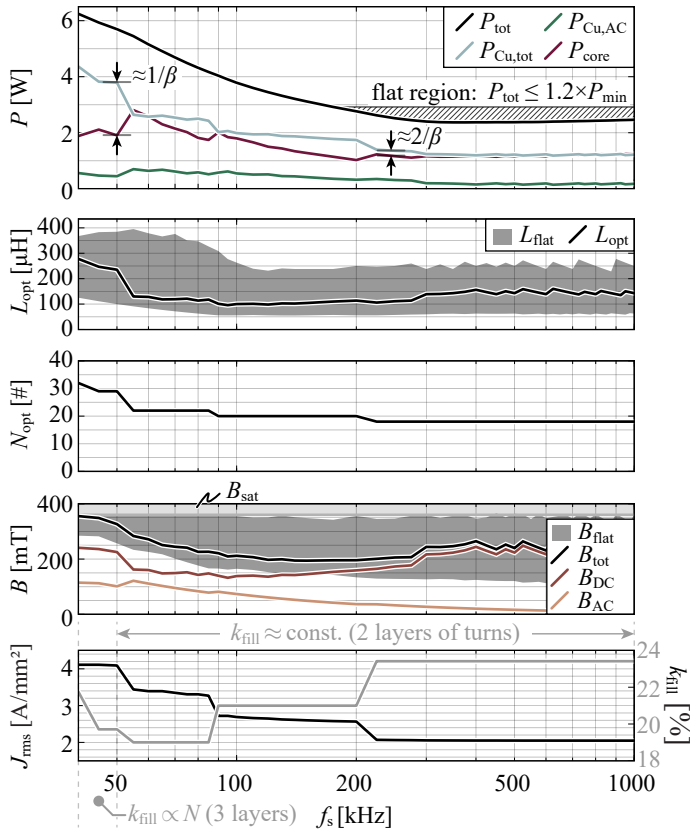


Fig. 2.14: Losses and characteristic values of the corresponding inductor designs along the trajectory r_{opt} shown in Fig. 2.12(a). The result reveals the flat range C, which starts at 200 kHz. The gray regions shown in the graphs of L_{opt} and B denote suboptimal designs according to flat range B that feature an increase of the total losses by less than 20 %.

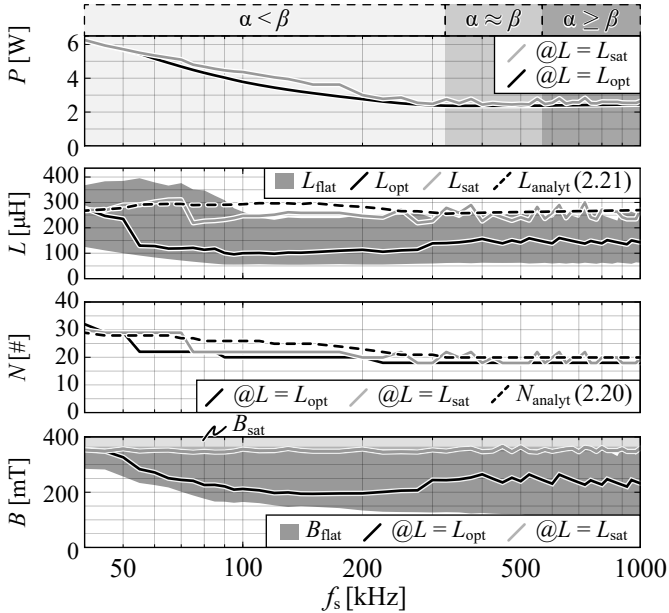


Fig. 2.15: Comparison of the designs along the r_{opt} trajectory to the designs that are marginally limited by saturation in Fig. 2.12(a).

Fig. 2.16(a) depicts the corresponding Steinmetz parameters for the saturation limited designs, which confirm monotonically decreasing losses in case of $\alpha < \beta$ and constant losses for $\alpha \approx \beta$.

Close inspection of the flat region C at frequencies above the frequency featuring the global minimum reveals constant values of N_{opt} , L_{opt} , and AC copper losses and slowly increasing core losses. From (2.5), an increase of the core losses with increasing f_s is expected, since $\alpha > \beta$ applies in this region, cf. Fig. 2.16(a). With regard to the analysis of the AC copper losses, the factors F_r and G_r , used to compute the implications of skin and proximity effects in round wires [60], first need to be investigated. **Fig. 2.17** depicts $F_r(f_s)$ and $G_r(f_s)$ and reveals that, for $d_r = 100 \mu\text{m}$, the losses due to skin effect, $P_{\text{Cu,skin}}$, are negligible in the considered frequency range ($F_r \approx 0.5$) and G_r is proportional to f_s^2 . In addition, the AC magnetic field inside the winding window is proportional to $I_{\text{AC,pk}}$, which for constant L is inversely proportional to f_s , cf. (2.1). Based on the assumption that the proximity losses dominate the AC copper losses (at 375 kHz the ratio between AC to DC

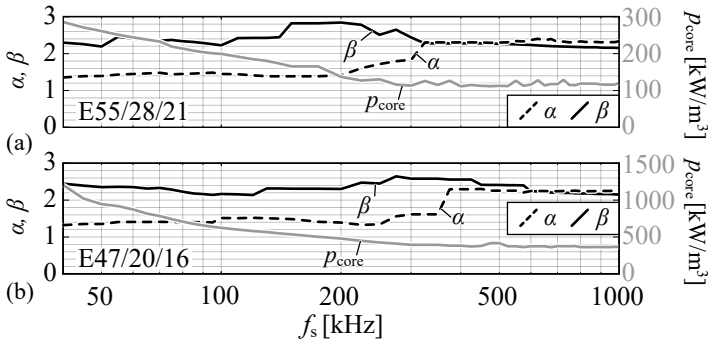


Fig. 2.16: Steinmetz parameters α and β and core losses density, p_{core} , that correspond to the optimal designs along the r_{opt} trajectory of (a) the E55/28/21 core of Fig. 2.12(a) and (b) the E47/20/16 core of Fig. 2.20(c).

resistance is equal to 20.4),

$$P_{\text{Cu,AC}} \approx R_{\text{DC}} \underbrace{G_{\text{r}}}_{\propto f^2} \underbrace{H_{\text{AC,pk}}^2}_{\propto f^{-2}} = \text{const.} \quad (2.29)$$

applies, which explains the constant AC copper losses at high frequencies observed in Fig. 2.14.

The ratio between the copper and core losses fluctuates around the theoretical optimal of $2/\beta$, for $f_s > 50$ kHz. This is attributed to small fluctuations of the fill factor and the integer number of turns. However, according to Fig. 2.14, $2/\beta$ does not apply for $40 \text{ kHz} < f_s < 50 \text{ kHz}$ and the optimal ratio of copper to core losses is found to be approximately $1/\beta$, instead. This result is linked to the copper fill factor, k_f , that results for technically possible arrangements of the conductors inside the core window for different values of N . **Fig. 2.18** illustrates optimal fittings of litz wire with round cross section and for N ranging from 21 to 36 (due to half-plane symmetry only half of the E-core is shown and, in addition, the area occupied by the coilformer is highlighted). It can be observed that k_f ranges from 16.6 % to 24.5 %.

At higher frequencies, the optimal number of turns is close to 20 and the fill factor is approximately constant. However, at lower frequencies, N_{opt} increases and the inductor design enters the region of Fig. 2.18(c), where the wire diameter, d_{wire} , is constant (and comparably small, in order to accommodate three layers of conductors in the core window). Thus, k_f is proportional

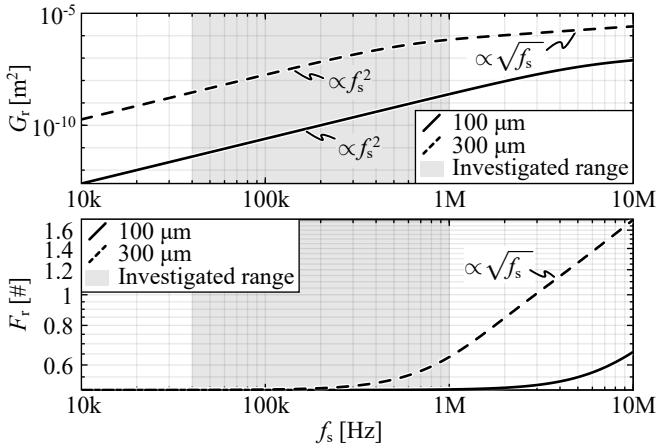


Fig. 2.17: The factors for modeling AC losses due to proximity and skin effects, G_r and F_r , plotted against frequency and for two different single strand diameters of a litz wire, $d_r = 100 \mu\text{m}$ and $d_r = 300 \mu\text{m}$.

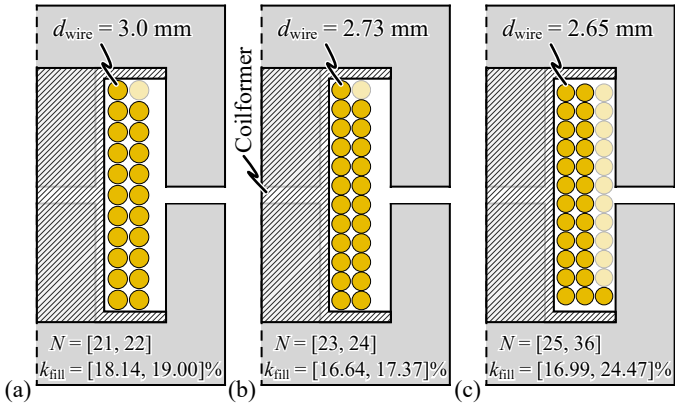


Fig. 2.18: Turn packaging for an E55/28/21 core with coil former and round conductors, for $N \in [21, 36]$.

to N ,

$$k_f = \frac{NA_{\text{wire}}}{A_w}, \quad (2.30)$$

where A_{wire} is the copper cross-section area of the conductor. With this,

$$R_{\text{DC}} = \frac{Nl_{\text{avg}}}{\sigma A_{\text{wire}}} \quad (2.31)$$

results, which gives total losses of

$$P_{\text{tot}} = c_7 N + c_2 N^{-\beta}, \quad (2.32)$$

$$c_7 = \frac{(32f_s^2 I_{\text{DC}}^2 L^2 + c_0 V_0^2) l_{\text{avg}}}{32\sigma A_{\text{wire}} f_s^2 L^2}, \quad (2.33)$$

and, at the optimal number of turns, leads to a ratio of core to copper losses of

$$\left. \frac{P_{\text{core}}}{P_{\text{Cu,tot}}} \right|_{N=N_{\text{opt}}} = \frac{1}{\beta}. \quad (2.34)$$

2.3.4 Trajectory of Constant Frequency, r_{375}

Fig. 2.19 presents the losses and the inductor properties along the trajectory marked with r_{375} in Fig. 2.12(a), i.e., for a constant frequency of $f_s = 375$ kHz. Compared to the losses computed with the analytical model in Section 2.2 and presented in Fig. 2.4(b), substantial differences between the absolute values of the losses are observed that mainly arise from the operating-point dependent Steinmetz parameters. Yet, the trends and the absolute values of the ripple are almost identical and two main findings of the previous Section can be verified. Firstly, the total losses decrease for increasing L (decreasing r) and $L \leq L_{\text{sat}} \approx L_{\text{opt}}$. This is attributed to the AC copper losses, where the decrease of $I_{\text{AC,pk}}$ (and hence the $H_{\text{AC,pk}}$) dominates the minor increase of the optimal number of turns, i.e., N_{opt} , which remains constant for $18\% < r < 34\%$ and decreases only slightly for $34\% < r < 50\%$ (the value of G_r remains constant, due to consideration of constant frequency). Secondly, in accordance to the findings of Section 2.2.5, the value of B_{DC} increases for increasing L (decreasing r) and, with this, also the core losses slightly increase, which compensates the increase of the AC copper losses within flat range B, $11\% < r < 46\%$.

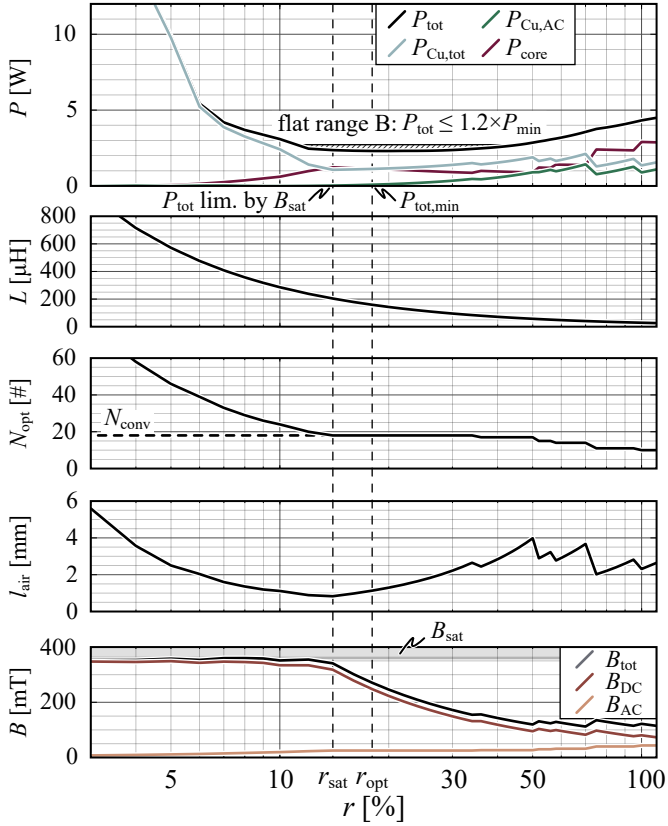


Fig. 2.19: Detailed investigation of the losses and inductor properties determined with the EMT inductor model along the trajectory of varying ripple and constant frequency of $f_s = 375$ kHz, r_{375} , in Fig. 2.12(a). Flat range B, $11\% < r < 46\%$, is highlighted.

2.3.5 Main Findings

With the proposed semi-numerical model, the main findings of Section 2.2, namely optimal region of operation and main design trends, are confirmed, despite the different levels of detail of the employed models. The main difference lies in the absolute value of the total losses, which could lead to a thermally invalid design, if only the analytical approach is considered. In Section 2.5, a direct comparison between the two models is conducted and the obtained result further confirms the above findings.

2.4 Validation with Further Designs

In order to confirm the generality of the above findings, three different cases, for same specifications of Tab. 2.1, are investigated with the EMT inductor model used in Section 2.3:

1. Distributed air gap;
2. Litz wire strand diameter of 300 μm
3. Core E47/20/16 (smaller than E55/28/21).

2.4.1 Distributed Air Gap

For the analysis of the distributed air gap, seven symmetrically distributed air gaps at the center core-limb are considered. The contour plot of the total losses is depicted in **Fig. 2.20(a)**. The basic observations are the following:

- ▶ The impact of the distributed air gap on the global loss minimum, the vicinity of the loss-optimal region, and the optimal frequency is relatively low; specifically, $P_{\text{gl,opt}}$ decreases from 2.4 W to 2.2 W and f_s changes from 375 kHz to 350 kHz.
- ▶ Compared to Fig. 2.12(a), the flat range B is wider, e.g., in comparison to the example analyzed in Section 2.3.4, cf. Fig. 2.19, $10\% < r < 64\%$ applies at $f_s = 375$ kHz, which is due to reduced HF AC copper losses arising from the proximity effect. Accordingly, r_{opt} increases from 20% to 28% and the upper boundary of region ② of Fig. 2.12(a), i.e., a thermal limit of the inductor, is shifted towards higher ripple value.

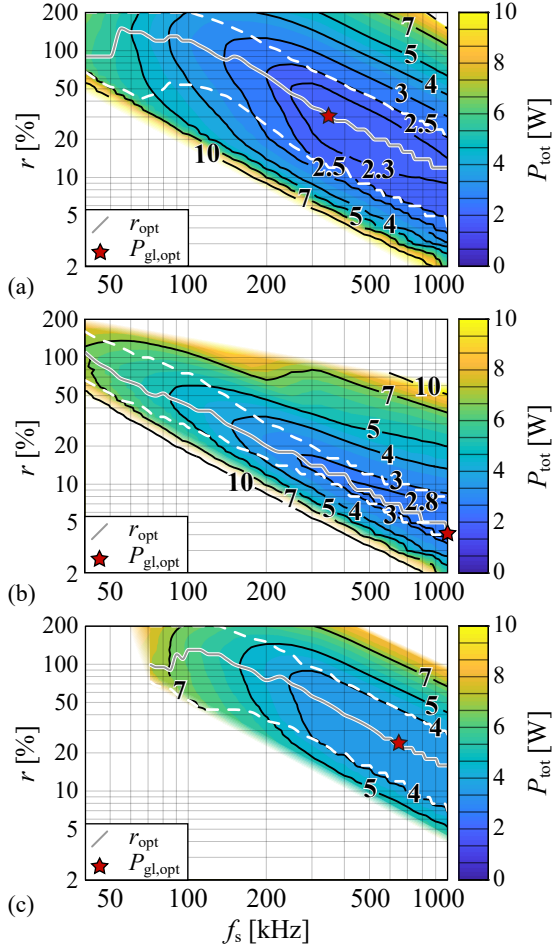


Fig. 2.20: Contour plot of the total losses for three selected cases: (a) distributed air gap, (b) litz wire strand diameter of 300 μm , and (c) core E47/20/16. In each plot, the trajectory of $r_{\text{opt}}(f_s)$ and the global optima, $P_{\text{gl,opt}}$, are highlighted.

On an inductor component level, the additional complexity resulting from the manufacturing of a core with distributed air gap cannot be justified. Nevertheless, on a system level, increased ripple leads to less hard-switching semiconductor losses and, thus, can be beneficial. However, this conclusion may not be valid in case of solid or foil conductors.

2.4.2 Litz Wire Strand Diameter 300 μm

In case the litz wire strand diameter is increased, the absolute value of the losses increases. Interestingly, also the global optimum moves to higher frequencies (cf. **Fig. 2.20(b)**). This is mainly related to the value of G_r , depicted in Fig. 2.17. For a copper wire with a diameter of 300 μm and frequencies greater than 500 kHz, G_r is proportional to $\sqrt{f_s}$. As a result, (2.29) is not constant and the AC copper losses decrease for increasing frequency (the increase of F_r is of minor importance). Hence, the global optimum does not entirely depend on the core losses; in case of $d_r = 300 \mu\text{m}$, it is shifted to 1 MHz, however, the minimum losses are found to be almost constant for $300 \text{ kHz} < f_s < 1 \text{ MHz}$ (below 10 % deviation). Finally, the upper boundary of region ② in Fig. 2.12(a) is shifted towards lower ripple values, due to poor HF performance and related thermal limitations.

2.4.3 Core E47/20/16

The last case analyzed is the next smaller E-core of the series of TDK-EPCOS, E47/20/16, cf. **Fig. 2.20(c)**. For this analysis, forced cooling of 4 m/s air-speed is considered, since consideration of natural convection would significantly limit the valid operating area. With this air-speed and for given losses, the core temperatures are similar to the previously calculated temperatures for the E55/28/21 core.

Compared to Fig. 2.12(a), three characteristic differences are observed:

- ▶ Due to the smaller cross-sectional areas of core window and core, the current and flux densities increase, leading to increased losses, e.g., $P_{\text{gl,opt}}$ rises from 2.4 W to 3.51 W.
- ▶ The loss minimum is shifted towards higher ripple values, because the reduced volume leads to a decrease of the component's energy storage capability, rendering a lower inductance more suitable or, with regard to saturation, necessary.

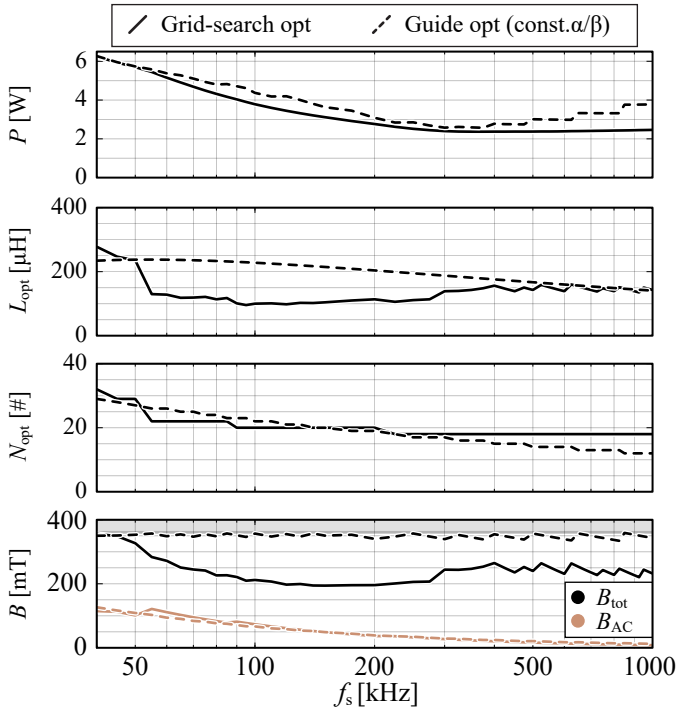


Fig. 2.21: Comparison of losses and inductor properties for optimal designs, determined with a grid-search approach, and designs derived using the proposed “two-equation” guideline. All designs are evaluated with the semi-numerical model.

- The optimal frequency is shifted to a higher value of 650 kHz. This is directly related to the increased optimal ripple, which leads to an increase of $B_{AC, pk}$ and, in turn, extends the frequency range where $\alpha < \beta$ applies towards higher frequencies, cf. **Fig. 2.16(b)**.

2.5 Fast Design Guideline

According to Section 2.3, the results of the detailed models confirm the results of the analytical model. The main difference are different absolute values of copper and core losses. Thus, a guideline using analytical equations is proposed.

For a given frequency, the inductor is close to the optimal design for the following settings:

- ▶ L^* is chosen according to (2.21), in order to set the maximum magnetic flux density to the saturation magnetic flux density;

$$L^* = c_6 f_s^{\frac{\alpha-\beta}{2+\beta}} - \frac{V_0}{4f_s I_{DC}}, \quad (2.35)$$

- ▶ N^* is chosen according to (2.9), in order to achieve a ratio of core to copper losses of $2/\beta$;

$$N^* = \left(\frac{\beta c_2}{2 c_1} \right)^{\frac{1}{2+\beta}}. \quad (2.36)$$

Fig. 2.21 presents a comparison of the designs obtained with this design guideline, evaluated using the EMT inductor model, and the optimal designs that result from the EMT inductor model detailed in Fig. 2.14. Even though, the two approaches return different inductance values, similar losses result for frequencies up to 500 kHz, which is related to the flat characteristic of the loss minimum. Between 40 kHz and 375 kHz, the maximum deviation between the two approaches is equal to 17.8 % and occurs at 120 kHz.

If the operating frequency is not known in advance, the PF can be used to identify the optimal frequency range of the inductor with respect to minimum losses. The PF is defined for a given constant core loss density, $p_{\text{core}} = P_{\text{core}}/V_c$,

$$PF = B_{AC} f_s. \quad (2.37)$$

The consideration of the classical PF , instead of modified versions that consider HF AC losses, is based on the assumption that losses due to the proximity effect are low at the global optimum. Hence, the copper losses are constant with respect to frequency and the CUT performance depends entirely on the performance of the core.

In combination with (2.5),

$$B_{AC} = \frac{c_7}{f_s^{\frac{\alpha}{\beta}}}, \quad c_7 = \left(\frac{p_{\text{core}}}{k_{SE}} \right)^{\frac{1}{\beta}} \Rightarrow PF \propto f_s^{\frac{\beta-\alpha}{\beta}} \quad (2.38)$$

results, i.e., the PF increases for increasing frequency if $\alpha < \beta$ applies (and α is approximately constant). Furthermore, the PF peaks approximately at the

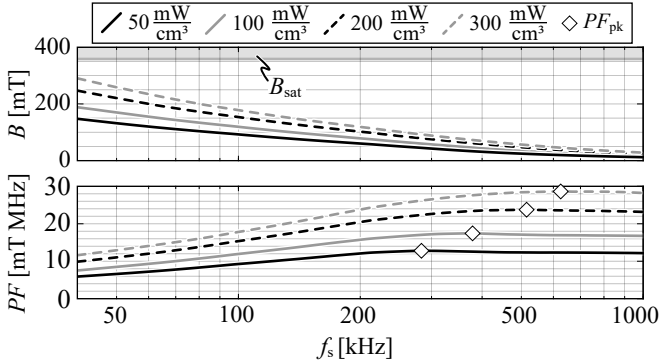


Fig. 2.22: Performance Factor (PF) of N87 ferrite material for four different loss densities, i.e., 50 mW/cm^3 , 100 mW/cm^3 , 200 mW/cm^3 , 300 mW/cm^3 . The peak value of the PF for each value is highlighted.

frequency where α starts to rise significantly, which is close to the frequency where $\alpha = \beta$ applies. The PF data of N87 ferrite material for four different loss densities, ranging from 50 mW/cm^3 to 300 mW/cm^3 , is depicted in **Fig. 2.22**. For $p_{\text{core}} = 50 \text{ mW/cm}^3$, the PF peaks at 285 kHz , which is close to optimal frequency calculated for in Section 2.3 for the inductor realized with the E55/28/21 core (there, $p_{\text{core}} \approx 30 \text{ mW/cm}^3$ applies), even though, the impact of the DC bias on the PF is not considered. For increased loss density, PF peaks at a higher frequency, which confirms the shift of $P_{\text{gl,opt}}$ of E47/20/16 to a higher frequency.

Note that the proposed guideline does not ensure thermal validity, which needs to be verified in a final step.

2.6 Design Space Diversity

According to the results of the previous Sections, the total losses are close to the minimum within relatively wide ranges of N , r , and f_s , cf. Section 2.2.5. In order to narrow the space of suitable designs, further criteria can be taken into account, e.g., partial-load efficiency and cost.

Fig. 2.23 depicts the design space diversity plot, i.e., the characteristic values of all possible designs, for the design settings of Tab. 2.2 and total losses of less than $1.2 \times P_{\text{opt,gl}}$, by taking all three design degrees of freedom into account (f_s , r , and N). Each y-axis represents the value of an individual

variable and, depending on the background color, they are assigned to one of the three groups listed below.

1. Input design variables (light gray)
2. Internally computed variables (gray)
3. Main objectives (dark gray)

The newly defined main objectives are the relative component cost of the inductor, computed with respect to the minimum cost, and the inductor's efficiencies $\eta_{20\%}$, $\eta_{50\%}$, and $\eta_{100\%}$, which result if the buck converter is operated with an output power of 20 %, 50 %, and 100 % of the rated power, respectively. The cost is calculated according to [63], which corresponds to a minimum order quantity of 15'000 pieces.

The result presented in Fig. 2.23 reveals that wide ranges of f_s , r , and N lead to almost minimum losses under full load conditions, however, with respect to cost and partial-load efficiencies, significant performance differences are observed. In order to further investigate this, the multi-objective optimization problem is solved in a grid-search approach by minimizing a cost function,

$$f_{\text{cost,obj},i} = w_1 \frac{P_{100\%,i}}{\max(P_{100\%})} + w_2 \frac{P_{50\%,i}}{\max(P_{50\%})} + w_3 \frac{P_{20\%,i}}{\max(P_{20\%})} + w_4 \frac{\text{cost}_i}{\max(\text{cost})},$$

$$\forall i \in \mathbb{N} \quad \forall i \leq n, \quad (2.39)$$

where i refers to a dedicated design of the calculated design space (which itself comprises of n results),

$$w = [w_1, w_2, w_3, w_4] \quad (2.40)$$

denotes the user-defined optimization weights, and the four objectives are the total losses at full load ($P_{100\%,\text{norm}}$), 50 % load ($P_{50\%,\text{norm}}$) and 20 % load ($P_{20\%,\text{norm}}$) and the cost per component.

Four different scenarios are investigated:

- Scenario 1: $w = [1.0, 0.0, 0.0, 0.0]$, i.e., minimum losses at full load.
- Scenario 2: $w = [0.247, 0.593, 0.16, 0.0]$; this is based on the weighted European efficiency for solar inverters [55],

$$\eta_{\text{Eu}} = 0.03 \eta_{5\%} + 0.06 \eta_{10\%} + 0.13 \eta_{20\%} + 0.10 \eta_{30\%} + 0.48 \eta_{50\%} + 0.20 \eta_{100\%}. \quad (2.41)$$

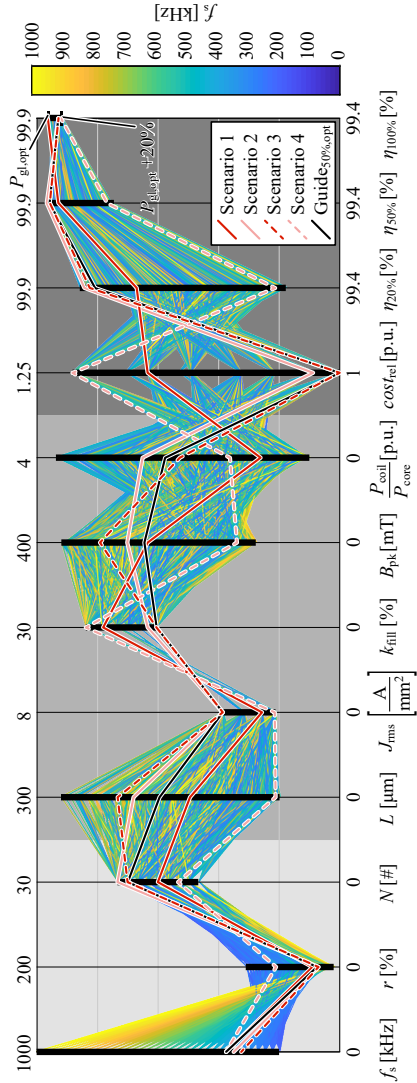


Fig. 2.23: Design space diversity plot for the inductor, computed based on the settings summarized with Tabs. 2.1 and 2.2 and for maximum total losses of $1.2P_{\text{gl,opt}}$, cf. Fig. 2.12(a). The highlighted lines refer to: i. the four scenarios discussed in Section 2.6, ii. a quasi-optimal design at 375 kHz obtained using the proposed guideline of Section 2.5 for L^* at full load and N^* at 50 % partial load.

- ▶ Scenario 3: $w = [0.0, 0.2, 0.2, 0.6]$, i.e., low cost (higher priority) and low partial load losses (lower priority).
- ▶ Scenario 4: Worst-case performance with respect to the additional main objectives (based on programmed logic script).

The *first scenario* shows that exclusive optimization for high efficiency at full load leads to missed opportunities, since both, partial load efficiency and cost, can be improved. Furthermore, with reference to the weights of (2.41), full load efficiency is of limited importance.

The *second scenario* follows the efficiency distribution of (2.41) and achieves a substantial improvement of the partial load efficiencies at the expense of a relatively low increase of the losses at full load, from 2.4 W to 2.72 W. This result is achieved with an increased number of turns and the design enters region ① in Fig. 2.9. Thus, the ratio of core to copper losses is less than $2/\beta$ for operation under full load. This ratio increases for decreasing output power, due to constant core losses and decreasing copper losses, which explains the improved partial-load efficiencies, cf. Section 2.2.5. Furthermore, a decreased cost results, which is unexpected, since scenario 2 does not take cost into consideration. This particular result is related to the fact that copper is an important cost driver and the coincidence that, in the presented case, the increased number of turns leads to a reduced fill factor and, thus, reduced copper mass. Due to this, a very similar result is obtained for the *third scenario*, i.e., increased number of turns, $N > N_{\text{opt}}$, to improve partial-load efficiency and decreased fill factor to lower the cost.

The *fourth scenario* demonstrates the missed opportunities of a bad design, even though, it features approximately similar frequency and losses as the design of scenario 2.

Based on the results of scenarios 2, 3 and in order to achieve improved partial-load efficiency and acceptable full-load efficiency, the design guideline of Section 2.5 is used for the optimal frequency of 375 kHz and for the parameters of Tab. 2.2, nevertheless, this time N is optimized for a partial load of 50 % using (2.9) (L is optimized for the nominal power using (2.21)). The resulting design, referred as $\text{Guide}_{50\%,\text{opt}}$, is depicted in Fig. 2.23.

2.7 Experimental Verification

For the verification of the above-mentioned findings, three Devices Under Test (DUTs) are built, using the E55/28/21 N87 core and litz wire with a strand

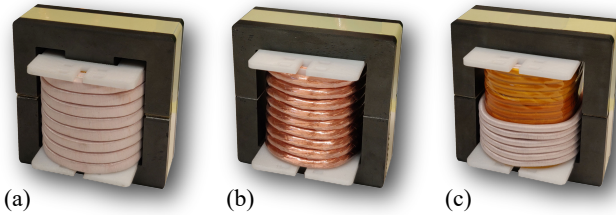


Fig. 2.24: Constructed Devices Under Test (DUTs) for the verification of the findings of Section 2.3. The DUTs employ an E55/28/21 core and litz wires with single-strand diameter of $100\ \mu\text{m}$. The number of turns and inductances of the DUTs are (a) $N = 16$, $L = 57\ \mu\text{H}$, (b) $N = 19$, $L = 200\ \mu\text{H}$, (c) $N = 30$, $L = 350\ \mu\text{H}$.

diameter of $100\ \mu\text{m}$, cf. **Fig. 2.24**. The components differ with regard to N and L :

- ▶ DUT₁: $N = 16$, $L = 57\ \mu\text{H}$;
- ▶ DUT₂: $N = 19$, $L = 200\ \mu\text{H}$;
- ▶ DUT₃: $N = 30$, $L = 350\ \mu\text{H}$.

With this, the selected designs cover wide ranges of frequency (150 kHz to 700 kHz)¹⁰ and ripple, cf. Fig. 2.13(c), to enable a thorough experimental verification of the discussed results. Specifically, DUT₁ and DUT₂ refer to designs with approximately optimal number of turns, however, in case of DUT₁ the AC copper losses and in case of DUT₂ the DC copper losses dominate the total copper losses. Finally, DUT₃ is a suboptimal design, limited by saturation, with dominating DC copper losses. According to the measured impedances of the DUTs, depicted in **Fig. 2.25**, and with a maximum test frequency of 700 kHz, all three components are evaluated well below their self-resonance frequencies.

As opposed to the core losses, the measurement of the copper losses, in case of high frequency effects (i.e., proximity losses), is a challenging task, hence, the total losses of the designed DUTs are measured. Since the modeled core losses result from measured data, cf. Section 2.3, the copper losses can be determined by subtracting the core losses from the total losses.

¹⁰The value of 700 kHz is set as the maximum frequency, since no further improvements are expected above that frequency. Furthermore, the material approaches the maximum limit of its useful operating region (recommended maximum frequency according to [52] is 500 kHz).

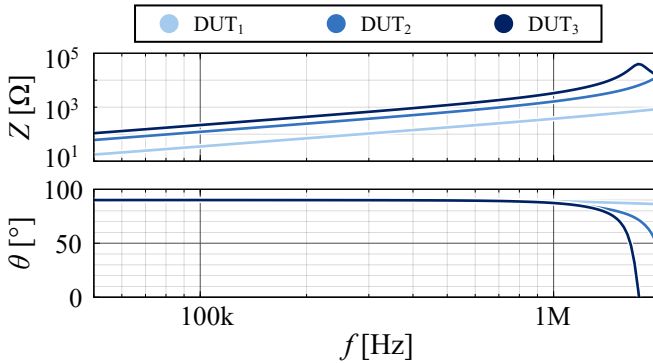


Fig. 2.25: Measured phases and magnitudes of the impedances of the realized DUTs using a 4294A impedance analyzer (by Agilent [64]). All three DUTs feature self-resonance frequencies well above the maximum operating frequency of 700 kHz.

For the measurement of the total losses, a calorimetric setup, depicted in **Fig. 2.26(a)**, is used [31, 65]. It consists of an inner calorimeter chamber and an outer reference chamber, which is used to ensure steady ambient conditions during the experiment. The calorimeter chamber accommodates the DUT and a heating device, i.e., a resistor, an attached heat sink, and fans, to ensure a homogeneous temperature inside the chamber. The employed setup enables measurements at a defined ambient temperature without the need for pre-calibrations [31, 65]. The accuracy of the calorimeter has been assessed by means of reference loss measurements conducted with a 1 k Ω power film resistor (RCH series by Vishay [66]), and two multimeters for measuring DC voltage and current (voltage: Fluke 233 [67], current: Fluke 175 [68]).¹¹ A consecutive measurement of four different losses, i.e., 2 W \rightarrow 5 W \rightarrow 2 W \rightarrow 5 W, reveals maximum and average deviations of 54 mW and 35 mW, respectively, between the calorimetric and the electric measurement. For all four operating points, the resulting deviations, between the two measurement methods, lie within the uncertainty range of the employed multimeters.

For the excitation of the DUTs two sources are employed. The first source is a DC supply that provides the DC current, i.e., 10 A (cf. Tab. 2.1), and the second source is a linear amplifier that provides the AC voltage (up to 3 MHz). The two sources are connected in parallel and decoupled with two filters.

¹¹During this measurement, DUT₁ was placed together with the resistor, in order to emulate the air-flow of the real experiments.

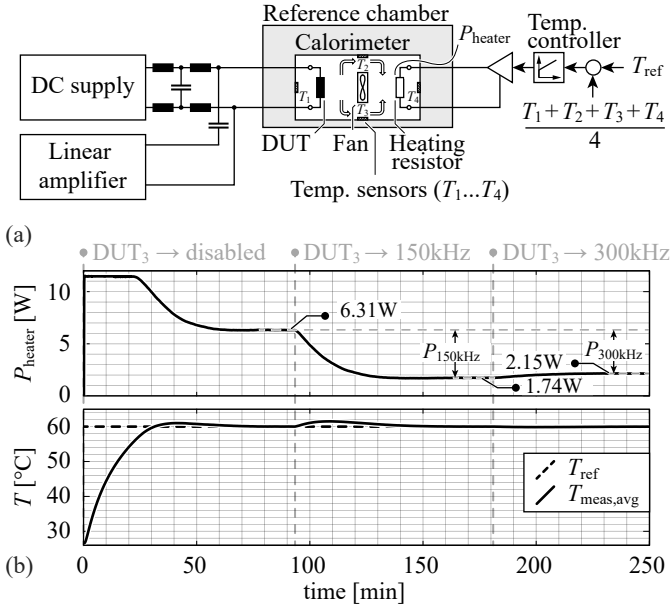


Fig. 2.26: (a) Calorimeter setup used to measure the total losses generated by the Device Under Test (DUT) at the desired ambient temperature. (b) Losses of the heating device and temperature of the calorimeter chamber during the course of two consecutive experiments at 150 kHz and 300 kHz using DUT_3 , cf. Fig. 2.24(c). The losses generated by the heating device during the three phases of steady-state are highlighted.

Fig. 2.26(b) presents the temperature inside the chamber during an experiment in order to illustrate the measurement procedure by way of example. Initially, the DUT is idle and the temperature-controlled heater increases the temperature inside the chamber to a defined value. After the system reaches steady state, the DUT is operated and the heater reduces its power to maintain a constant temperature. Once at steady state, the difference between the heating power before and after the excitation of the DUT corresponds to the losses of the DUT.

For the experimental verification of the findings of Sections 2.2 and 2.3, the EMT model is exactly parameterized according to the corresponding DUT, e.g., the number of strands of the litz wire and the positions of the conductors (inside the core window and on the winding head). The measurements are

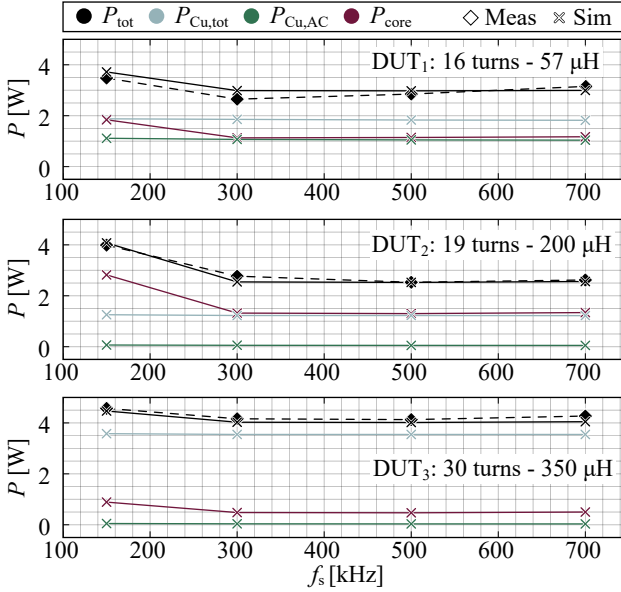


Fig. 2.27: Comparison between the losses estimated using the EMT model (cf. Section 2.3) and the losses using the calorimetric setup of Fig. 2.26(a), for the three DUTs of Fig. 2.24, at a reference (ambient) temperature of 60° . The measurement of the two operating points at 150 kHz and 300 kHz of DUT₃ is shown in Fig. 2.26(b).

conducted at a temperature of $T_{\text{ref}} = 60^\circ\text{C}$. **Fig. 2.27** presents the comparison of measured and calculated total losses for four different operating points per DUT. For the twelve measured operating points, the maximum deviation between calculated and measured results is 12.7% (for DUT₁ and $f_s = 300$ kHz) and the average absolute deviation is 4.85%, i.e., well below 20%, which is a commonly accepted uncertainty value for multi-domain component models. With this, the experimental results confirm the findings of this work.

2.8 Conclusion

In this work, the optimal operation of power inductors in common topologies, i.e., buck/boost switched converters, is analyzed. For the analysis and in order to achieve a comprehensible discussion of the various couplings of design parameters and effects in inductors, the magnetic core (E55/28/21) and the

employed litz wire (100 μm strand diameter) are fixed. The implications of the remaining design degrees of freedom, f_s , r , and N , are investigated with focus on the losses and optimal trends are identified. The analysis is done in two steps, initially with simplified analytical models and, subsequently, with a detailed semi-numerical multi-domain model. The link from the simplified to the detailed model is provided through a step-by-step introduction of different nonlinear effects (e.g., core saturation, impacts of frequency, AC magnetic flux density, and DC bias on the core losses). Experimental results confirm the theoretical findings. The experiments are conducted with an accurate calorimetric method, three different inductors, and within a wide frequency range (150 kHz to 700 kHz).

Around the identified global loss optimum, a very flat characteristic of the losses is observed with respect to all three degrees of freedom. This property enables further potential opportunities with respect to reduced losses at partial load (e.g., 20 % and 50 % of rated load) and reduced cost, which come at the expense of an increase of the full-load losses by 15 % to 20 %. Furthermore, the obtained results enable the compilation of a simple two-equation guideline to achieve designs that feature almost minimal losses for a given frequency. The total losses of the designs obtained using the proposed guideline compared to the designs optimized using the detailed semi-numerical model feature a maximum deviation of 17.8 % within a wide frequency range (40 kHz to 375 kHz).

3

Transient Calorimetric Measurement of Core Losses

This chapter summarizes the most relevant research findings also published in:

- ▶ **P. Papamanolis**, T. Guillod, F. Krismer, and J. W. Kolar, “Transient Calorimetric Measurement of Ferrite Core Losses up to 50MHz,” *IEEE Transactions on Power Electronics*, vol. 36, no. 3, pp. 2548–2563, 2021.
- ▶ **P. Papamanolis**, T. Guillod, F. Krismer, and J. W. Kolar, “Transient Calorimetric Measurement of Ferrite Core Losses,” in *Proc. of the IEEE Applied Power Electron. Conf. and Expo. (APEC)*, New Orleans, LA, USA, 2020.

Motivation

The analysis of Chapter 2 highlighted the importance of accurate core loss data, since the peak performance of the employed power inductors is achieved at frequencies near the peak of the PF of the employed core material. However, to the author’s knowledge, no method exists that achieves reasonable measurement accuracy at very high frequencies, i.e., > 1MHz, which limits the application of the findings of the previous work to lower frequencies. This served as the main motivation behind the work presented in the following.

Executive Summary

In this chapter, an accurate and fast transient calorimetric ferrite core-loss measurement method is proposed. In contrast to electrical measurements, the accuracy of the calorimetric approach is largely independent of the magnetic excitation and operating frequency. However, accurate values of the thermal capacitance and the temperature of the Core Under Test (CUT) are required. Accurate measurement of the specific heat capacity of the core material can be achieved with a Differential Scanning Calorimeter (DSC) or by using the CUT as a DC electric conductor and measuring its thermal response for known Joule heating. Accurate temperature measurements can be realized with NTC temperature sensors. A thorough uncertainty analysis of the presented method is conducted by identifying the impact of each source of uncertainty in the course of a sensitivity analysis. For the considered reference case (R 22.1/13.7/7.9 toroidal core with N₄₉ ferrite material by EPCOS-TDK - 500 kHz/100 mT) the method achieves a total uncertainty with a worst-case value of less than 12 % or, in case of a more realistic approach considering a Gaussian distribution of each source of uncertainty, a mean value of -4.3 % with a 95 % confidence interval of ± 3.2 %. The results are verified by means of FEM simulations and experiments. Furthermore, a step-by-step description of the workflow for preparing and conducting the experiments is provided. The proposed method is tested experimentally and compared to a state-of-the-art electrical loss measurement method for MnZn N87 and N₄₉ ferrite cores of EPCOS-TDK. In addition, it is used to measure the loss-map of the NiZn ferrite material 67 from Fair-Rite for very high frequencies up to 50 MHz, which enables the computation of the material's Steinmetz parameters.

3.1 Introduction

Latest GaN power semiconductors enable very high switching frequencies and efficiencies of power electronics converters. In order to fully utilize the potential of available technologies, the design of power electronic converters is based on multi-objective optimization, e.g., with respect to power density and efficiency, which, however, relies on accurate component models. However, the power semiconductors' switching losses and the magnetic components' core losses are known to be subject to high uncertainties. Accordingly, the accurate knowledge of the switching losses and the losses of magnetic components of the converter circuits up to the MHz range is of great interest. This is particularly challenging for the core losses, whose behavior is highly non-linear, e.g., with respect to frequency, temperature, AC flux density, and DC premagnetization. Such non-linear dependencies apply especially to ferrite

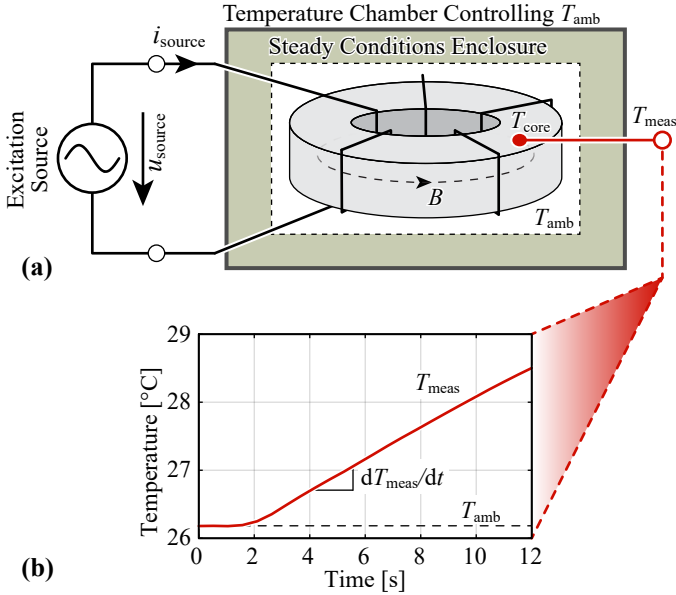


Fig. 3.1: (a) Proposed transient calorimetric core loss measurement setup: Core Under Test (CUT) with temperature sensor, enclosure (to achieve steady ambient conditions), and temperature chamber. (b) Example of the acquired increase of the core temperature over time.

materials, MnZn (20 kHz to 2 MHz) and/or NiZn (1 MHz to 50 MHz), which are best suited for high frequency operation.

The main existing core loss measurement methods can be classified into electrical and calorimetric approaches [69]. Common problems to electrical methods, e.g., poor power factor and limitation to sinusoidal excitation have been resolved in [19, 30, 59, 70–74]. State-of-the-art electrical methods feature partial cancellation of the phase-discrepancy error using an air-core inductor or a high-Q capacitor, in order to ensure adequate accuracy also at high frequencies, i.e., in the MHz range [29, 75]. However, the requirement of precise pre-calibration, elaborate post-processing, and difficulties arising from dealing with parasitics remain as drawbacks.

A steady-state calorimetric measurement [31, 65, 76] presents an alternative approach. However, the time needed for every single measurement is very long, i.e., typically in the range of several tens of minutes, and the realization of such setup is a challenging task. A transient calorimetric measurement

of core losses would drastically reduce the measurement time as shown for power semiconductors in [77]. An adaptation of this method to magnetic components is proposed in [78]. However, the presented approach requires a complex setup with an additional "calorimeter block", which refers to a block of known mass and thermal heat capacity (e.g., copper). The magnetic component is thermally well connected to the block and the total losses (both coil and core losses) can be measured through the rate of rise of the temperature of the copper block. In addition to its complexity, the proposed method requires calibration measurements in order to identify the heat flux leaking through the insulation. A simpler method to identify the core losses in a transient calorimetric approach is introduced in [79], which mainly relies on the correlation between the core losses and the rate of change of the core temperature. However, the method has only been used to measure the relative increase of the core losses, in presence of different levels of DC premagnetization, and has not been evaluated with regard to absolute core loss measurements. Finally, in [80] an effort to measure the absolute core losses using a transient calorimetric approach is presented, however, the work does not provide a detailed investigation of the uncertainties of the method (e.g., with respect to the specific heat capacity of the measured core material, where a constant value is considered) or further verification (e.g., experimental results).

In this chapter, the method presented in [80] is further developed, and a detailed investigation of the measurement uncertainties is introduced. The method is found to achieve a total measurement uncertainty of less than 20% in a wide range of core losses, e.g., $40 \text{ mW} < P_{\text{core}} < 8 \text{ W}$. Accordingly, it is well suited for core loss measurements, in particular at operating points where electrical measurement methods are subject to high uncertainties, e.g., at very high frequencies. The operating principle of the proposed measurement method is detailed in **Section 3.2**. **Section 3.3** presents an analysis of the implications of the individual measurement inaccuracies on the measured core losses, a derivation of the total measurement uncertainty for given specifications, and an investigation of the useful loss-range of the method. The results of the analysis are verified by means of FEM simulations in **Section 3.4**. Finally, **Section 3.5** provides a step-by-step description of the workflow for preparing and conducting the experiments. Furthermore, Section 3.5 presents the experimental results for the investigated transient calorimetric method for two MnZn ferrite materials and a NiZn ferrite material and for frequencies up to 750 kHz and 50 MHz, respectively.

3.2 Experimental Setup and Operating Principle

Fig. 3.1 depicts the setup that consists of the Core Under Test (CUT) and an enclosure that ensures steady ambient conditions (e.g., homogeneous temperature, absence of air-flow) and improves the accuracy of the measurement due to the prevention of forced cooling (cf. Sec. 3.3.2). If the measurement needs to be conducted at an ambient temperature, T_{amb} , that is different than the nominal ambient temperature, a reference temperature chamber, preferably an oven, can be used for that purpose. During the measurements of the presented work, a laboratory oven that uses forced air circulation and achieves a highly stable ambient temperature was employed. Small fluctuations around the reference temperature are of low importance, due to the substantially different time constants between the fluctuations of the temperature of the oven (multiple minutes) and the duration of a single experiment of the proposed method (tens of seconds). Finally, a high accuracy temperature sensor is attached to the core (cf. Fig. 3.1).

3.2.1 Fundamental Measurement Principle

For a given excitation and a negligible heat flux to the ambient, the temperature of the core increases according to

$$P_{\text{core}} = C_{\text{th,core}} \frac{dT_{\text{core}}}{dt} \approx C_{\text{th,core}} \frac{\Delta T_{\text{meas}}}{\Delta t}, \quad (3.1)$$

where $C_{\text{th,core}}$ is the thermal capacitance of the core, T_{core} is the core temperature, and T_{meas} denominates the temperature reading.

According to (3.1), the correlation between the measured losses and the temperature only depends on the thermal capacitance of the core and not on the shape of the core or on the particular waveform of the flux density in the core. Compared to high-accuracy electric measurement procedures, time consuming steps that need to be conducted for each operating point, e.g., calibration of the setup and adaptation of the components for compensation, depending on the operating point [29, 30, 59, 73–75], are avoided.

3.2.2 Equivalent Thermal Network

Fig. 3.2(a) depicts the considered equivalent thermal network of the experimental setup. The CUT is represented by the source of losses, P_{core} , and

its thermal equivalent circuit elements, $R_{\text{th,core}}$ and $C_{\text{th,core}}$. The thermal resistance $R_{\text{th,leak}}$ models the heat leaking from the core to the ambient and to the coil through the mechanisms of thermal conduction, convection, and radiation. The setup employs two temperature sensors, i.e., the Negative Temperature Coefficient (NTC) thermistor,¹ considered with $R_{\text{th,NTC}}$ and $C_{\text{th,NTC}}$ in Fig. 3.2(a), and an IR camera, which, however, is only used for the purpose of verification and is not required for the core loss measurements. A look-up table is used to convert the resistance of the NTC to the measured temperature, $T_{\text{NTC,meas}}$, and a Savitzky-Golay filter, i.e., a filter based on a moving Least Mean Square (LMS) algorithm [81], is applied to decrease the measurement noise for the final temperature, $T_{\text{meas}}(t)$, without distorting the required information.

This network can be simplified based on the following, experimentally supported (cf. Section 3.3), considerations:

- ▶ $R_{\text{th,core}}$ is assumed to be negligible (≈ 0), due to the relatively high thermal conductivities of MnZn and NiZn ferrite core materials ($\lambda \geq 3.5 \text{ W/mK}$, cf. Section 3.3.7).
- ▶ The NTC thermistor is represented by a low-pass filter with a time constant of τ_{NTC} , since $C_{\text{th,NTC}} \ll C_{\text{th,core}}$ applies.
- ▶ $C_{\text{th,core}}$ is assumed to be constant during the course of a single experiment.

Fig. 3.2(b) shows the resulting simplified equivalent circuit, which is used for the thermal analysis. During the heating phase ($t \in [t_{\text{on}}, t_{\text{off}}]$ in **Fig. 3.3**), temperature independent core losses are assumed and the core temperature increases,

$$T_{\text{core}}(t) = T_{\text{amb}} + P_{\text{core}} R_{\text{th,leak}} \left(1 - e^{-\frac{t-t_{\text{on}}}{\tau_{\text{leak}}}} \right), \quad (3.2)$$

$$\tau_{\text{leak}} = R_{\text{th,leak}} C_{\text{th,core}}. \quad (3.3)$$

During the cooling phase ($t > t_{\text{off}}$ in Fig. 3.3), zero core losses apply and the core temperature converges to the ambient temperature,

$$T_{\text{core}}(t) = T_{\text{amb}} + (T_{\text{max}} - T_{\text{amb}}) e^{-\frac{t-t_{\text{off}}}{\tau_{\text{leak}}}}. \quad (3.4)$$

¹From an evaluation of different temperature sensors, also including Resistance Temperature Detector (RTD), and thermocouple sensors, the NTC thermistor has been selected due to its high immunity against induced electrical noise and the comparably fast response.

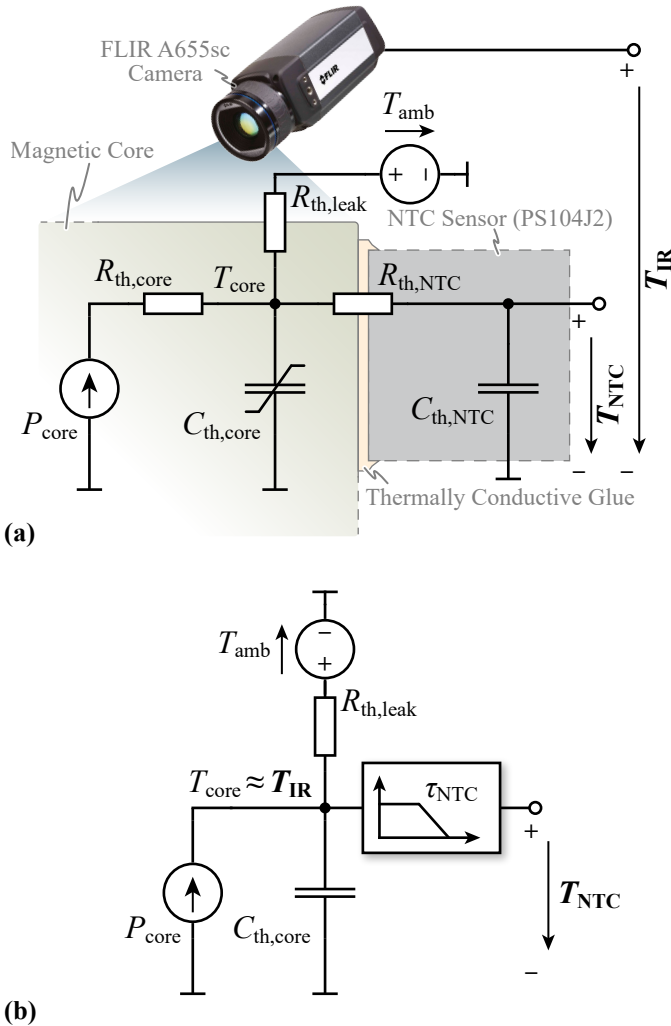


Fig. 3.2: (a) Equivalent circuit of the calorimetric experimental setup, including the Core Under Test (CUT), the attached NTC thermistor, and the high accuracy IR camera; (b) simplified version of the proposed equivalent circuit that is considered in this chapter. The IR camera serves only for model verification and is not required for the measurement of the core losses.

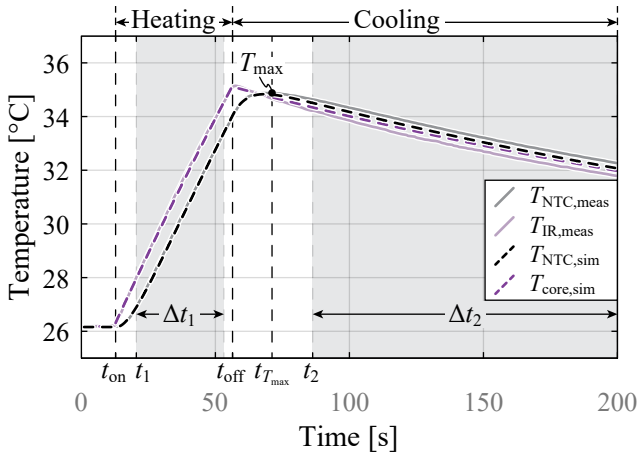


Fig. 3.3: Comparison of the results of a real measurement and a simulation of the thermal equivalent network of Fig. 3.2(b) using a toroidal ferrite core (R 22.1/13.7/7.9, N49) that is subject to a sinusoidal magnetic flux (100 mT, 500 kHz). The core temperature is measured with a NTC thermistor (Littelfuse PS104J2 [82]) and an IR camera (FLIR A655sc [83]) at 30 frames/sec. The component values of the simulated circuit are: $P_{\text{core}} = 1.54 \text{ W}$, $C_{\text{th,core}} = 7.3 \text{ J/K}$, $R_{\text{th,leak}} = 45 \text{ K/W}$, $\tau_{\text{NTC}} = 5.5 \text{ s}$.

According to (3.2) and (3.3), the values of $R_{\text{th,leak}}$ and $C_{\text{th,core}}$ are required for the computation of the core losses. $C_{\text{th,core}}$ depends on the mass of the core and its specific heat capacity, which is a material property that can be acquired in advance using the methods discussed in Section 3.3.1 (or could be specified by the core manufacturer). $R_{\text{th,leak}}$ depends on various factors, including the CUT, the coil, and the ambient conditions, and is estimated after each modification of the experimental setup.

For the estimation of $R_{\text{th,leak}}$, two dedicated temperature values of the cooling phase, i.e., $T_{\text{meas}}(t_2)$ and $T_{\text{meas}}(t_2 + \Delta t_2)$ with $t_2 > t_{\text{off}}$, are required. The resulting equation for $R_{\text{th,leak}}$ is

$$R_{\text{th,leak,est}}(t_2, \Delta t_2) = -\frac{\Delta t_2}{C_{\text{th,core}}} \left[\ln \left(\frac{T_{\text{meas}}(t_2 + \Delta t_2) - T_{\text{amb}}}{T_{\text{meas}}(t_2) - T_{\text{amb}}} \right) \right]^{-1}. \quad (3.5)$$

Finally, P_{core} is estimated using two dedicated temperature values of the waveform acquired during the heating phase, $T_{\text{meas}}(t_1)$ and $T_{\text{meas}}(t_1 + \Delta t_1)$, with $t_{\text{on}} < t_1 < t_1 + \Delta t_1 < t_{\text{off}}$,²

$$P_{\text{core,est}}(t_1, \Delta t_1) = \frac{T_{\text{meas}}(t_1 + \Delta t_1) - T_{\text{meas}}(t_1)}{\left(e^{-\frac{t_1 - t_{\text{on}}}{\tau_{\text{leak}}}} - e^{-\frac{t_1 + \Delta t_1 - t_{\text{on}}}{\tau_{\text{leak}}}} \right)} R_{\text{th,leak}}. \quad (3.6)$$

3.2.3 Validation of the Thermal Equivalent Network

The reference setup specified in **Tab. 3.1** serves for the purpose of validation and employs an R 22.1/13.7/7.9 toroidal core (N49 by EPCOS-TDK) with a coil made of 10 turns of high-frequency litz wire ($180 \times 71 \mu\text{m}$). The CUT is subject to a sinusoidal excitation with a peak flux density of 100 mT at a frequency of 500 kHz, which leads to reasonable core losses of 1.54 W (cf. Section 3.5.1 for further details regarding the selection of a suitable CUT).

Figure 3.3 presents the core temperature measured with an NTC thermistor (Littelfuse, PS104J2 [82]) and an IR camera (FLIR, A655sc [83], 30 frames/sec), for the same excitation. In addition, the temperatures $T_{\text{core,sim}}$ and $T_{\text{NTC,sim}}$ are depicted, as extracted from a simulation of the circuit of

²In an alternative approach, LMS approximations could be used to identify P_{core} and $R_{\text{th,leak}}$, by fitting (3.2) and (3.4), respectively. However, this is computationally more demanding and, due to the noise reduction achieved with the Savitzky-Golay filter [81], the difference between LMS approximation and the described two-points approach is found to be consistently below 1 %.

Tab. 3.1: Specifications and operating conditions for the reference experimental setup.

Parameter	Value
Core material	N49 (EPCOS-TDK)
Core shape	R 22.1 x 13.7 x 7.9
Operat. point	500 kHz/100 mT
$C_{th,core}$	7.3 J/K
$R_{th,leak}$	45 K/W
P_{core}	1.54 W
T_{amb}	26.2 °C

Fig. 3.2. For the implementation of the simulation circuit the values of $C_{th,core}$, $R_{th,leak}$, and τ_{NTC} need to be known. In this regard, $C_{th,core}$ is determined in advance (cf. Section 3.3.1) and $R_{th,leak}$ is estimated with (3.5) during the cooling phase of the measurement. The time constant of the NTC, $\tau_{NTC} = 5.5$ s, is determined such that the difference between simulated and measured waveforms is minimal.

It is found that simulated and measured waveforms match for both measurements, i.e., core and NTC temperatures, with maximum deviations of 0.28 °C and 0.19 °C, respectively. Moreover, the resulting simulated model was further used and successfully reproduced the temperature waveforms of the same experimental setup for different induced core losses, ranging from 0.4 W to 4.5 W, which further verifies the applicability of the considered circuit.

3.3 Measurement Accuracy

Typical sources of uncertainties in calorimetric measurement methods include the measurement accuracy of the employed equipment (e.g., temperature measurement device, DSC, time measurement device) and the impact of temperature on the measured quantities (e.g., generated core losses, specific heat capacity of the material, leaking heat during the experiment). In the course of an uncertainty analysis, the main sources of inaccuracies have been identified and are described in this Section:

- ▶ **Section 3.3.1:** limited accuracy of the *thermal capacitance measurement*, $C_{th,core}$.
- ▶ **Section 3.3.2:** uncertainty of the estimated heat flux arising from the uncertainty of the employed *leakage flux model*, which considers

heat transfer to the ambient and to the coil by means of conduction, convection, and radiation.

- ▶ **Sections 3.3.3 and 3.3.4:** limited dynamic response and accuracy of the *temperature sensor*.
- ▶ **Section 3.3.5:** limited *clock accuracy* of experiment time measurement.
- ▶ **Section 3.3.6:** *temperature dependencies* of P_{core} , $R_{\text{th,leak}}$ and $C_{\text{th,core}}$.
- ▶ **Section 3.3.7:** *temperature gradient in the core* due to non-homogeneous magnetic flux density and finite thermal conductivity of the core.
- ▶ **Section 3.3.8:** implications of *copper losses*.

Tab. 3.2 lists the values of the inaccuracies, ξ , that have been determined for the reference setup specified in Tab. 3.1 and described in Section 3.2.3. Tab. 3.2 further presents the expressions for the linearized sensitivities $\partial P_{\text{core,est}}/\partial \xi$ for the different inaccuracies, which can be used to estimate the boundaries of the uncertainties of the estimated core losses at each operating point (by way of example, the expression for $\partial P_{\text{core,est}}/\partial \delta C_{\text{th,core}}$ is derived in Section 3.3.1). **Tab. 3.3** lists the values of the boundaries determined for the reference setup, using the simplified linearized expressions presented in Tab. 3.2, and, for the purpose of verification, also the corresponding values obtained from a numerical evaluation of the non-linear differential equation of the investigated system. The total measurement uncertainty is finally determined according to Section 3.3.9.

3.3.1 Uncertainty $\delta C_{\text{th,core}}$ of Core's Thermal Capacitance

Accurate knowledge of $C_{\text{th,core}}$ is of high importance, since it directly influences the calculated losses, cf. (3.1). Out of different measurement methods proposed in literature, the Differential Scanning Calorimetry (DSC) [84] features the best trade-off between complexity and accuracy. The basic operating principle of this method relies on the accurate measurement of the heat flow that is provided to a given sample, in order to achieve a defined increase of the sample's temperature, which enables the calculation of its differential specific heat capacity as a function of temperature. The employed DSC 2500, from TA Instruments [85], uses a sapphire sample as reference and provides a maximum measurement accuracy of 2%. Nevertheless, due to the non-ideal

Tab. 3.2: Uncertain parameters and error sources.

Parameter ξ	Description	Range	Linear Sensitivity, $\partial P_{\text{core,est}}/\partial \xi$
$\delta C_{\text{th,core}}$	Uncert. of calc. core thermal capacitance	$\pm 3\%$	$-P_{\text{core}}$
$\delta R_{\text{th,leak}}$	Uncert. of calc. leakage thermal resistance	$\pm 20\%$	$P_{\text{core}} \left(\frac{t_1 - t_{\text{on}}}{\eta_{\text{leak}}} + \frac{\Delta t_1}{2\eta_{\text{leak}} + \Delta t_1} \right)$
$\epsilon_{T_{\text{meas}}}$	Differential temperature meas. uncertainty	$\pm 0.1^\circ\text{C}$	$C_{\text{th,core}}/\Delta t_1$
τ_{NTC}	Time constant of NTC sensor	[3 s, 5.5 s]	cf. (3-13)
$\eta_{T_{\text{core}}}$	Change in core losses due to ΔT_{core}	$-1\%/^\circ\text{C}$	$P_{\text{core}}^2 \frac{\Delta t_1 + 2(t_1 - t_{\text{on}})}{2C_{\text{th,core}}}$
$\epsilon_{I_{\text{meas}}}$	Time meas. error	$\pm 0.0001 \times \Delta t_1$ s	$2P_{\text{core}}/\Delta t_1$
$\eta_{C_{\text{th,core}}}$	Change in $C_{\text{th,core}}$ due to ΔT_{core}	$0.1\%/^\circ\text{C}$	$-P_{\text{core}}^2 \frac{\Delta t_1 + 2(t_1 - t_{\text{on}})}{2C_{\text{th,core}}}$
$\eta_{R_{\text{th,leak}}}$	Change in $R_{\text{th,leak}}$ due to ΔT_{core}	$-1.2\%/^\circ\text{C}$	$P_{\text{core}}^2 \frac{[\Delta t_1 + 2(t_1 - t_{\text{on}})]^2}{2C_{\text{th,core}}(2\eta_{\text{leak}} + \Delta t_1)}$
-	Additional heat from copper losses	-	-
-	Temperature grad. in radial direction, due to non-homogeneous magnetic flux distribution	-	-

Tab. 3.3: Maximum deviations between actual and measured core losses, $\Delta P_{\text{lin}} = \xi(\partial P_{\text{core,est}} / \partial \xi)$, for the reference setup and the operating conditions listed in Tab. 3.1 (core losses are 1.54 W); verification based on numerical results obtained from the system's non-linear differential equation.

ξ	$\Delta P_{\text{lin}} / \text{mW}$ (cf. Tab. 3.2)	$\Delta P / \text{mW}$ (numerical eval. of diff. eq.)
$\delta C_{\text{th,core}}$	± 46.2	$[-41.3, +43.7]$
$\delta R_{\text{th,leak}}$	± 24.47	$[-30.6, +20.8]$
ϵT_{meas}	± 28.91	± 31.3
τ_{NTC}	$[-1.8, +12.4]$	$[-1.5, +12.4]$
ηP_{core}	-86.3	-83.3
ϵt_{meas}	$< \pm 1$	$< \pm 1$
$\eta C_{\text{th,core}}$	-8.6	-7.8
$\eta R_{\text{th,leak}}$	-8.1	-9.3

discoid shape of the employed samples, the measurement accuracy was set to a conservative

$$\delta C_{\text{th,core}} = \pm 3 \%. \quad (3.7)$$

Fig. 3.4 depicts the specific heat capacities of three MnZn ferrite materials (N87, N97, and N49 of EPCOS-TDK) and of one NiZn ferrite material (67 of FairRite). The specific heat capacities of all four materials are temperature dependent, and this is related to different microscopic processes on atomic and molecule level [86, 87]. The abrupt steps for MnZn materials at approximately 225 °C correspond to the Curie temperature [52, 88].

DSCs are commonly used in material science, however, they may be less accessible in power electronics. An alternative, more accessible, way for the measurement of $C_{\text{th,core}}$ is discussed in [89]: a sample of the considered material is used as DC electric conductor ($\rho_{\text{MnZn}} \approx 10 \Omega/\text{m}$ - strongly temperature dependent) and, by means of Joule heating, the thermal response of the core is used to determine $C_{\text{th,core}}$ using (3.1), cf. **Fig. 3.5**. For the sake of completeness, this method has also been applied to the N49 material at three different ambient temperatures, i.e., 30 °C, 55 °C, and 80 °C.

A rectangular block of MnZn N49 ferrite equal to $51.0 \times 11.9 \times 5.1 \text{ mm}^3 / 14.806 \text{ gr}$ is employed. This results in a block resistance, R_{block} , approximately equal to 9.72 k Ω (at 30 °C), 8.43 k Ω (at 55 °C), and 3.07 k Ω (at 80 °C). The block is placed inside an enclosure and the complete setup inside a temperature chamber (cf. Fig. 3.1). For each value of T_{amb} , a constant voltage is applied and the injected DC current is monitored. Due to the temperature

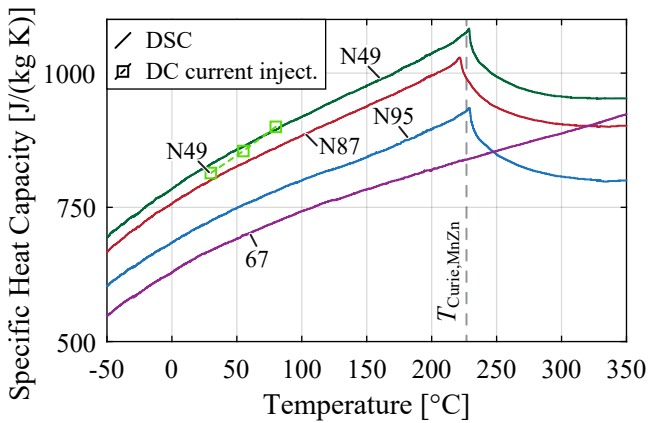


Fig. 3.4: Measured specific heat capacities of N87, N97 and N49 MnZn ferrite materials of EPCOS-TDK and 67 NiZn ferrite material of Fair-Rite using the Differential Scanning Calorimeter (DSC) 2500 of TA instruments. Additionally, for three different temperatures (30 °C, 55 °C, and 80 °C), the specific heat capacity of N49 is measured according to [89], where the ferrite conducts a DC current for generating a defined ohmic power loss in order to heat the core. With known DC losses, temperature rise, and core weight, the specific heat capacity can be calculated.

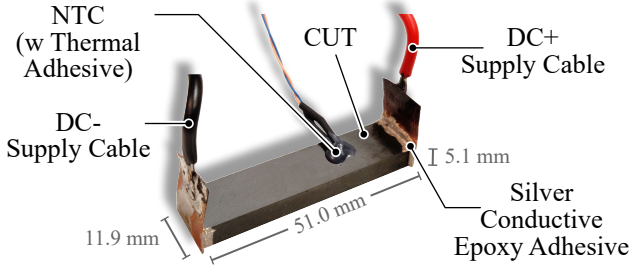


Fig. 3.5: N49 MnZn ferrite sample used as a DC electric conductor, for the estimation of $C_{th,core}$ by means of Joule heating. The rectangular block's volume is $51.0 \times 11.9 \times 5.1 \text{ mm}^3$ and its mass is 14.806 gr. The applied voltage, for all three ambient temperatures (30 °C, 55 °C, 80 °C), is fixed at 58.74 V and the injected average power is equal to 0.355 W, 0.635 W, and 1.124 W, respectively, due to the temperature dependency of ρ_{MnZn} .

dependent conductivity of ferrite material, the value of the injected losses is subject to minor change during the experiment. In such narrow temperature range the injected losses can be averaged. Alternatively, a controller for constant power injection can be used.

Using (3.1) and the averaged injected DC losses, during the heating phase, an initial estimation of $C_{th,core}$ is acquired. Replacement of this value in (3.5) allows for calculation of $R_{th,leak}$ during the cooling phase. Finally, the corrected value of $C_{th,core}$ is calculated using (3.6) and division with the mass of the employed block leads to the calculation of the specific heat capacity. The maximum deviation of the specific heat capacity of MnZn N49 measured with the two proposed methods for the three values of T_{amb} , i.e., 30 °C, 55 °C, 80 °C, is 1.93 %, 0.93 %, and 0.56 %, respectively.

The expression for $\partial P_{core,est} / \partial \delta C_{th,core}$, i.e., the linear sensitivity of the estimated core losses on $\delta C_{th,core}$, can be derived based on the network depicted in Fig. 3.2(b). For this purpose, $C_{th,core}$ is replaced by $C_{th,core}(1 + \delta C_{th,core})$ and

$$\Delta T_{core}(s) = \frac{\frac{P_{core}}{s} - \frac{\Delta T_{core}(s)}{R_{th,leak}}}{sC_{th,core}(1 + \delta C_{th,core})}$$

$$\rightarrow \Delta T_{core}(t) = \mathcal{L}^{-1} \left\{ \frac{P_{core}}{s} \frac{R_{th,leak}}{1 + s\tau_{leak}(1 + \delta C_{th,core})} \right\}, \quad (3.8)$$

results for the increase of the temperature across $C_{\text{th,core}}$. Furthermore, the impact of the NTC temperature sensor on the measurement result, modeled with τ_{NTC} , is neglected, since the corresponding low-pass filter leads to a deviation between the actual and the measured temperature, which can be considered separately, cf. (3.13) in Section 3.3.3. With this, $\Delta T_{\text{core}}(t_1 + \Delta t_1) - \Delta T_{\text{core}}(t_1) = T_{\text{meas}}(t_1 + \Delta t_1) - T_{\text{meas}}(t_1)$ applies and the time-domain function, $\Delta T_{\text{core}}(t)$, can be used to evaluate (3.6). The result is linearized around $\delta_{C_{\text{th,core}}} = 0$,

$$\left. \frac{\partial P_{\text{core,est}}}{\partial \delta_{C_{\text{th,core}}}} \right|_{\delta_{C_{\text{th,core}}} \rightarrow 0} = \frac{P_{\text{core}}}{\tau_{\text{leak}}} \left(t_1 - t_{\text{on}} - \frac{\Delta t_1}{-1 + e^{\frac{\Delta t_1}{\tau_{\text{leak}}}}} \right). \quad (3.9)$$

Due to $\Delta t_1 \ll \tau_{\text{leak}}$, $e^{\Delta t_1/\tau_{\text{leak}}}$ can be approximated by $1 + \Delta t_1/\tau_{\text{leak}}$, and further consideration of $t_1 - t_{\text{on}} \ll \tau_{\text{leak}}$ leads to the expression listed in Tab. 3.2. The other sensitivities are derived in a similar way.

3.3.2 Accuracy of the Modeled Leakage Flux, $\delta_{R_{\text{th,leak}}}$

The calculation of the worst-case uncertainty of $R_{\text{th,leak}}$ is based on (3.5), e.g., in case of the reference experiment,

$$\begin{aligned} C_{\text{th,core}}(25^\circ\text{C}) &= 7.3 \text{ J/K}, & \Delta t_2 &= 115 \text{ s}, \\ T_{\text{meas}}(t_2) &= 34.6^\circ\text{C}, & T_{\text{meas}}(t_2 + \Delta t_2) &= 32.2^\circ\text{C}, \end{aligned} \quad (3.10)$$

apply, cf. Fig. 3.3. With $\delta_{C_{\text{th,core}}} = \pm 3\%$ and $\eta_{C_{\text{th,core}}} = 0.1\%/^\circ\text{C}$, i.e., the given measurement uncertainty and the temperature dependency of $C_{\text{th,core}}$, cf. Tab. 3.2, and for a core temperature between $T_{\text{amb}} + 6.0^\circ\text{C}$ and $T_{\text{amb}} + 8.4^\circ\text{C}$ during $t \in [t_2, t_2 + \Delta t_2]$, a worst-case range of

$$\begin{aligned} &[97\% + 0.1\%/^\circ\text{C} \times 6.0^\circ\text{C}, \\ &103\% + 0.1\%/^\circ\text{C} \times 8.4^\circ\text{C}] C_{\text{th,core}}, \end{aligned} \quad (3.11)$$

applies for the thermal capacitance. In addition, the measurement of the temperature difference is subject to an absolute uncertainty of $\epsilon_{T_{\text{meas}}} = \pm 0.1^\circ\text{C}$ and the uncertainty due to clock accuracy can be neglected, which leads to a minimum value of 38.7 K/W (-14% compared to the nominal value of 45 K/W). On this basis, a conservative uncertainty of $\pm 20\%$ has been considered for $\delta_{R_{\text{th,leak}}}$, cf. Tab. 3.2.

Even though, $R_{\text{th,leak}}$ is subject to a comparably high uncertainty, the impact on the estimated core losses remains low, since the maximum duration

of the core loss measurement, $t_{\text{off}} - t_{\text{on}}$ is typically in the range of 15 s to 30 s, which is much less than the time constant arising from the leakage flux, $\tau_{\text{leak}} \approx 330$ s. Accordingly, the corresponding sensitivity, $\partial P_{\text{core,est}} / \partial \delta_{R_{\text{th,leak}}}$, is small (cf. Tab. 3.3).

3.3.3 Impact of NTC Time Constant, τ_{NTC}

For the temperature measurement, the PS104J2 NTC thermistor of Littelfuse [82] is used. In order to achieve a fast response of the NTC and at the same time mechanical robustness, the temperature sensor is glued to the core using a thermally conductive adhesive (8329TFM-25ML of MG Chemicals). The CUT must be much larger in size than the temperature sensor in order to fulfill $C_{\text{th,NTC}} \ll C_{\text{th,core}}$ (for the case of very small cores, thermal imaging is a valid solution). An uncoated core is preferred, and in case of coating, the coating is carefully locally removed, even though it is found to have a minor impact on the measured response.

The NTC sensor features a dynamic response similar to a first-order low pass filter, cf. Fig. 3.3, with time constants between 3 s and 5.5 s, depending on the investigated CUT. The impact of this transfer function on the measurement result could be compensated by initial identification of the NTC time constant and application of the reciprocal of the sensor's transfer function to the measured temperature waveform. However, the additional effort that arises from the implementation of such a compensation procedure can be avoided by inserting minimum waiting times of at least $2\tau_{\text{NTC}}$ between the beginning of each measurement phase and the actual measurement,

$$t_1 - t_{\text{on}} > 2\tau_{\text{NTC}} \quad \text{and} \quad t_2 - t_{T_{\text{max}}} > 2\tau_{\text{NTC}}, \quad (3.12)$$

which enables small deviations between the actual core losses and the estimated core losses, $\Delta P_{\text{core,NTC}}$.

A detailed inspection of $\Delta P_{\text{core,NTC}}$ reveals a strong non-linear dependency on τ_{NTC} , which renders the use of a linearized sensitivity unsuitable. Instead, $\Delta P_{\text{core,NTC}}$ is directly derived based on the system's differential equation and the resulting expression for the estimated core losses (3.18), cf. Sec. 3.3.9,

$$\Delta P_{\text{core,NTC}} = P_{\text{core}} - P_{\text{core,unc}}(t_1, \Delta t_1) \approx P_{\text{core}} \frac{\tau_{\text{leak}} - t_1 - \frac{\Delta t}{2} - \frac{\tau_{\text{leak}}^2}{\Delta t} e^{-\frac{t_1}{\tau_{\text{NTC}}}}}{\tau_{\text{leak}} - t_1 - \frac{\Delta t}{2}} \frac{\tau_{\text{NTC}}}{\tau_{\text{leak}} - \tau_{\text{NTC}}}, \quad (3.13)$$

using $\epsilon_{T_{\text{meas}}} = \delta_{C_{\text{th,core}}} = \delta_{R_{\text{th,leak}}} = 0$ and a second-order Taylor approximation for $e^{-t/\tau_{\text{leak}}}$. For the reference measurement and $\tau_{\text{NTC}} \in [3 \text{ s}, 5.5 \text{ s}]$,

$\Delta P_{\text{core,NTC}} \in [-1.8 \text{ mW}, 12.4 \text{ mW}]$ results with (3.13), which corresponds to relatively small deviations between -0.12% and 0.81% . It should be pointed out that (3.13) remains approximately valid also in presence of further sources of uncertainties, since all other sources mainly have an impact on the slope of the time-domain characteristic of the core temperature, $T_{\text{core}}(t)$.

3.3.4 Temperature Measurement Accuracy, $\epsilon_{T_{\text{meas}}}$

A custom analog/digital 14-channel interface circuit is employed to process the resistance change of the NTC thermistor. Furthermore, the considered Savitzky-Golay filter reduces eventually present measurement noise. In order to assess the accuracy of this temperature measurement setup, an initial verification has been conducted with a reference temperature measurement. This is composed of a high-accuracy NTC thermistor, MC65F103AN from Amphenol Advanced Sensors [90], which provides an absolute accuracy of $\pm 0.05\text{ }^\circ\text{C}$ at $35\text{ }^\circ\text{C} < T < 39\text{ }^\circ\text{C}$ and $\pm 0.075\text{ }^\circ\text{C}$ at $39\text{ }^\circ\text{C} < T < 42\text{ }^\circ\text{C}$, and the 34410A digital multimeter from Keysight Technologies [91], that provides a resistance reading accuracy, corresponding to an error of 1.1 mK. The result of this reference temperature measurement, $T_{10k,\text{ref}}$ (cf. Fig. 3.6), is compared simultaneously to the measurements obtained from five PS104J2 NTC thermistors that are connected to five channels of the interface circuit, $T_{100k,1..5}$ in Fig. 3.6. All six sensors are closely mounted together, inside an enclosure, and using thermally conductive paste, to achieve high thermal coupling and to limit convection. For the experiment a slow, controlled temperature step from $37\text{ }^\circ\text{C}$ to $45\text{ }^\circ\text{C}$ is conducted inside a laboratory oven (the oven requires a minimum temperature of $T_{\text{amb}} + 10\text{ }^\circ\text{C}$, in order to properly stabilize the temperature).

The measurement results reveal different deviations for absolute temperature values and temperature differences. With regard to the absolute temperature, a maximum deviation of $0.22\text{ }^\circ\text{C}$ is found between $T_{10k,\text{ref}}$ and $T_{100k,4}$, which could be further improved by additional calibration of the interface circuit. However, the absolute temperature is only needed to determine the values of the temperature-dependent variables P_{core} , $C_{\text{th,core}}$, and $R_{\text{th,leak}}$; for an uncertainty of less than $0.5\text{ }^\circ\text{C}$, its impact on the resulting total uncertainty is negligible (cf. $\eta_{P_{\text{core}}}$, $\eta_{C_{\text{th,core}}}$, and $\eta_{R_{\text{th,leak}}}$ listed in Tab. 3.2). The investigated measurement method rather requires a high accuracy of the measured temperature difference, which, for $t_1 = 0$ and a duration of $\Delta t_1 = 2500\text{ s}$, in Fig. 3.6, gives a maximum deviation of 8 mK for the six temperature difference measurements, $T_{\text{meas}}(t_1 + \Delta t_1) - T_{\text{meas}}(t_1)$, i.e., the uncertainties arising from linearity errors of temperature measurement sensors and interface cir-

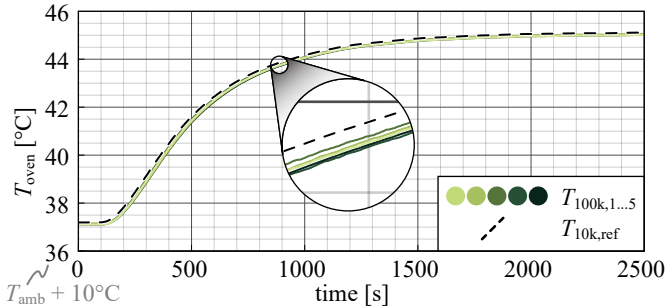


Fig. 3.6: Temperatures of five PS104J2 NTC thermistors from Littelfuse [82], $T_{100k,1...5}$, measured using a custom analog/digital interface circuit and a reference measurement with an MC65F103AN NTC thermistor from Amphenol Advanced Sensors [90], $T_{10k,ref}$, using a 34410A digital multimeter from Keysight Technologies [91]. All sensors are thermally coupled and covered inside an enclosure in order to limit convection; the complete setup is located inside a laboratory oven and during the experiment the reference temperature changes from 37 °C to 45 °C. Due to the overlap of the temperatures of the five PS104J2 NTC thermistors, a magnified ($\times 7.5$) view is added.

cuitry is very small. However, due to missing specifications with regard to temperature difference measurements, the author decided to assign the specified accuracy of the PS104J2 NTC thermistor of ± 0.1 °C to the measured temperature difference,

$$\Delta T_{\text{meas,unc}} = T_{\text{meas}}(t_1 + \Delta t_1) - T_{\text{meas}}(t_1) + \epsilon_{T_{\text{meas}}},$$

$$\epsilon_{T_{\text{meas}}} = \pm 0.1 \text{ } ^\circ\text{C}, \quad (3.14)$$

which allows for a conservative consideration of the corresponding uncertainty.

Accordingly, and with respect to (3.6), the relative uncertainty of the measured core losses decreases for increasing temperature differences and reaches values of less than 2 % for temperatures differences greater than 5 °C.

3.3.5 Clock Accuracy, $\epsilon_{t_{\text{meas}}}$

The considered measurement setup employs a microcontroller that is operated with an oscillator, which features a frequency stability of ± 100 ppm. Accordingly, and with respect to the values given in Tab. 3.2, the uncertainty due to a time measurement error is of low value and low sensitivity and is neglected due to this reason.

3.3.6 Temperature Dependencies ($\eta_{P_{core}}$, $\eta_{C_{th,core}}$, $\eta_{R_{th,leak}}$)

All three fundamental elements of the equivalent circuit in Fig. 3.2 (i.e., P_{core} , $C_{th,core}$, $R_{th,leak}$) are temperature and, hence, in the considered case time dependent. The temperature dependencies of P_{core} and $C_{th,core}$ are properties of the core material, which are especially pronounced for ferrites, and the temperature dependency of $R_{th,leak}$ is due to the heat transfer mechanisms of convection and radiation. The value of $\eta_{P_{core}}$ displayed in Tab. 3.2 is determined based on the *Relative Core Losses versus Temperature* plot of the material's datasheet [92] at $f = 500$ kHz, $B_{pk} = 100$ mT, and for $T \in [25^\circ\text{C}, 40^\circ\text{C}]$. The value of $\eta_{C_{th,core}}$ is determined from the measured specific heat capacity of N49 depicted in Fig. 3.4 and the value of $\eta_{R_{th,leak}}$ is determined based on an evaluation of the temperature dependencies of the thermal leakage flux components due to convection and radiation, considering a horizontally mounted core and using the simplified expressions given in [56].

According to Tab. 3.2, the expressions for computing the linear sensitivities of the measured core losses with respect to $\eta_{P_{core}}$, $\eta_{C_{th,core}}$, and $\eta_{R_{th,leak}}$ are inversely proportional to $C_{th,core}$, which further confirms that an accurate knowledge of $C_{th,core}$ is indispensable to achieve an accurate measurement result.

The sensitivity $\partial P_{core,est}/\partial \eta_{R_{th,leak}}$ is comparably small, since the leakage flux is relatively low during the short measurement time. Accordingly, $\eta_{R_{th,leak}}$ has a minor contribution to the uncertainty of P_{core} and is omitted. Furthermore, also $\eta_{C_{th,core}}$ can be neglected, since $|\eta_{P_{core}}| \gg |\eta_{C_{th,core}}|$ and same absolute values of the sensitivities, $|\partial P_{core,est}/\partial \eta_{P_{core}}| = |\partial P_{core,est}/\partial \eta_{C_{th,core}}|$, apply. Accordingly, only $\eta_{P_{core}}$ is considered in the circuit's differential equation that is examined in Section 3.3.9, which enables a compact and yet accurate solution.

3.3.7 Inhomogeneous Flux Density and Temperature Distribution

The distribution of the flux density over the core cross section has a general impact on the determined core losses. Conversion of the induced flux into flux density is conventionally done by division of the flux by the cross section of the employed core. However, cores (toroids) typically employed for the measurement of core losses cause flux density deviations between the inner and outer radius of 60 % to 70 %. This is attributed primarily to the varying magnetic lengths between the two radii and the current carrying conductors, according to the Biot-Savart law and/or Ampere's law, and secondarily to the impact of the flux density on the relative permeability of ferrite materials.

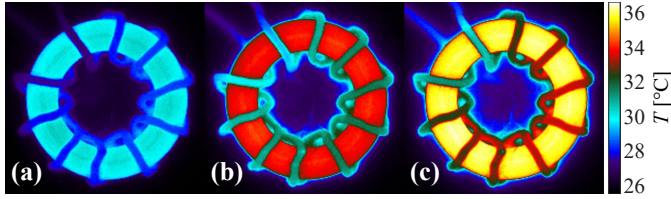


Fig. 3.7: Temperature monitoring of a toroidal ferrite core (R 22.1/13.7/7.9, N49) that is subject to a sinusoidal flux density of 500 kHz and 100 mT, using the FLIR A655sc IR camera. At an ambient temperature of 26.2 °C, the three depicted frames correspond to the temperatures (a) 30 °C, (b) 34 °C, (c) 36 °C. For all temperatures the maximum deviation between the points of lowest and highest temperatures in radial direction of the core is below 0.3 °C (camera resolution: 640 × 480 - pixel dimensions: 0.136 × 0.136 mm²).

This deviation, raised to a typical power of $\beta \approx 2.5$, results in a ratio of the maximum and the minimum losses in radial core direction of more than 3. Therefore, it is advised to consider cores with slim profiles, in order to limit differences in flux density and corresponding loss densities.

Despite the inhomogeneous loss distribution in the CUT, thermal imaging reveals that the temperature gradient inside the core is negligible, cf. **Fig. 3.7**, due to the relatively high thermal conductivity of ferrite [$\lambda \geq 3.5$ W/(mK)]. As a result, and similar to the electric measurement of the core losses, the investigated procedure does not measure the local loss density but rather the total core losses. Furthermore, $R_{\text{th,core}}$ in Fig. 3.2(a) can be omitted.

3.3.8 Impact of Copper Losses

Copper losses in the coil cause additional heating of the core and need to be limited, e.g., to a maximum of one tenth of the core losses, which is found to be easily achieved with proper choice of the CUT design parameters (e.g., core geometry, number of turns, type of conductor). In order to further minimize this effect, a thermally isolating interface tape (≈ 0.3 mm) can be placed between the coil and the core. The impact of the distance between coil and core on the flux distribution inside the core is negligible for core materials with high relative permeabilities, e.g., MnZn ferrite materials with $\mu_r > 1000$. It may become more critical for high frequency NiZn ferrite materials, whose relative permeabilities can be as low as 40. FEM simulations of the high-frequency inductors that are experimentally evaluated in Section 3.5.3 and which employ the NiZn ferrite material 67 of Fair-Rite, however, confirm

that the effect of the winding current on the distribution of the flux density remains negligible.

3.3.9 Total Uncertainty

The total uncertainty of the measured core losses is determined based on the differential equation of the circuit depicted in Fig. 3.2(b),

$$C_{\text{unc}} \frac{dT_{\text{core}}}{dt} = P_{\text{core}} [1 + \eta_{P_{\text{core}}} (T_{\text{core}} - T_{\text{amb}})] - \frac{T_{\text{core}} - T_{\text{amb}}}{R_{\text{unc}}}, \quad (3.15)$$

$$C_{\text{unc}} = C_{\text{th,core}} (1 + \delta_{C_{\text{th,core}}}), R_{\text{unc}} = R_{\text{th,leak}} (1 + \delta_{R_{\text{th,leak}}}), \quad (3.16)$$

which, in accordance to Sections 3.3.1, 3.3.2, and 3.3.6, takes the uncertainties $\delta_{C_{\text{th,core}}}$, $\delta_{R_{\text{th,leak}}}$, and $\eta_{P_{\text{core}}}$ into consideration. Furthermore, the measured temperature is subject to the transient response of the NTC sensor, i.e., for the assumption of $C_{\text{th,NTC}} \ll C_{\text{th,core}}$,

$$T_{\text{meas}} = T_{\text{core}} - \frac{dT_{\text{meas}}}{dt} \tau_{\text{NTC}} \quad (3.17)$$

applies [the corresponding solutions for $T_{\text{core}}(t)$ and $T_{\text{meas}}(t)$ are (A.1) and (A.2) of the Appendix A.1, respectively].

Finally, for the estimation of the core losses according to (3.6), also the temperature measurement uncertainty needs to be considered,

$$P_{\text{core,unc}}(t_1, \Delta t_1) = \frac{T_{\text{meas}}(t_1 + \Delta t_1) - T_{\text{meas}}(t_1) \pm \epsilon_{T_{\text{meas}}}}{\left(e^{-\frac{t_1 - t_{\text{on}}}{\tau_{\text{leak}}}} - e^{-\frac{t_1 + \Delta t_1 - t_{\text{on}}}{\tau_{\text{leak}}}} \right) R_{\text{th,leak}}}, \quad (3.18)$$

leading to a relative total uncertainty of

$$\text{unc}_{\text{meas,\%}}(t_1, \Delta t_1) = 100 \% \times \left| \frac{P_{\text{core,unc}}(t_1, \Delta t_1) - P_{\text{core}}}{P_{\text{core}}} \right|. \quad (3.19)$$

Fig. 3.8 presents a contour plot of the worst-case values of the total uncertainty, $\text{unc}_{\text{meas,\%}}$, obtained for the reference experiment defined in Tab. 3.1, as a function of t_1 and Δt_1 ($t_{\text{on}} = 0$ s is considered). The presented plot is computed with (3.19) and takes the ranges of $\delta_{R_{\text{th,leak}}}$, $\eta_{P_{\text{core}}}$, τ_{NTC} , and $\epsilon_{T_{\text{meas}}}$, listed in Tab. 3.2, into account.³ For an optimal selection of t_1 and Δt_1 , the total uncertainty of the measurement method is below 12 %. In addition, the

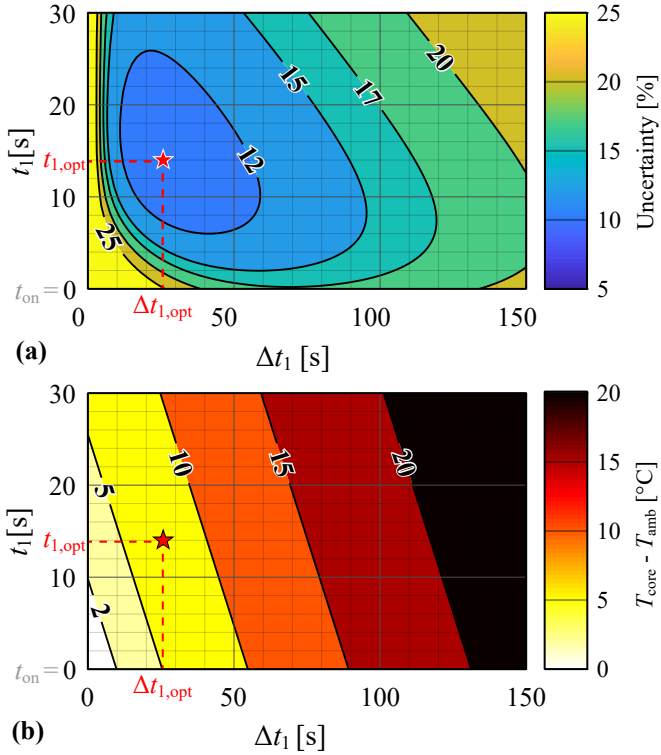


Fig. 3.8: (a) Worst-case total error and (b) increase of the core's temperature with respect to t_1 and Δt_1 (cf. Fig. 3.3), for the specifications of Tab. 3.1, the uncertainties of Tab. 3.2, and the equivalent circuit of Fig. 3.2.

region around the optimal point is substantially flat and is found to occur approximately at

$$t_{1,\text{opt}} \approx 2\tau_{\text{NTC}}, \quad \Delta t_{1,\text{opt}} \approx \min \left(\frac{C_{\text{th,core}}}{P_{\text{core}}} \sqrt{\left| \frac{2\epsilon_{T_{\text{meas}}}}{\eta_{P_{\text{core}}}} \right|}, \Delta t_{1,\text{max}} \right), \quad (3.20)$$

which is detailed in Appendix A.2 and applies if $\epsilon_{T_{\text{meas}}}$ and $\eta_{P_{\text{core}}}$ are dominating sources of uncertainties (the value of $\Delta t_{1,\text{opt}}$ is limited to $\Delta t_{1,\text{max}} = 250$ s in order to prevent unreasonably long measurement times in case of low losses).

Due to the many uncertainty variables that have an influence on $unc_{\text{meas},\%}$, it is unlikely for the worst-case to happen. In a more realistic approach, a Gaussian distribution of each uncertainty is considered such that 95 % of the samples lie within the uncertainty values of Tab. 3.2. Based on a Monte Carlo simulation approach according to [93], featuring 5000 individual simulations, the probability density function of the total uncertainty presented in **Fig. 3.9** is obtained for the settings of the reference experiment and optimal timing values of t_1 and Δt_1 , derived similar to Fig. 3.8. It is found that an approximately Gaussian distribution results for $unc_{\text{meas},\%}$, which is due to the fact that the total uncertainty is approximately proportional to the values of the individual uncertainty variables (except for τ_{NTC} and $\delta_{R_{\text{th,leak}}}$). The negative mean value of $\mu = -4.3\%$ results mainly due to the negative temperature coefficient of the core losses [μ of approximately zero would result if the measured core losses were referred to a core temperature of $T_{\text{meas}}(t_1 + \Delta t_1/2)$]; for a confidence interval of 95 %, $\mu \pm 2\sigma$, the total uncertainty is between -7.4% and -1.1% .

The CUT defined in Tab. 3.1 has been examined with regard to different levels of core losses, ranging from 20 mW to 20 W, in order to determine the range of core losses that lead to a worst-case value of $unc_{\text{meas},\%} < 20\%$ (cf. **Fig. 3.10**). Core loss dependent optimal timing parameters, $t_{1,\text{opt}}(P_{\text{core}})$ and $\Delta t_{1,\text{opt}}(P_{\text{core}})$, have been used in this plot to enable a meaningful assessment of the achievable total uncertainty. According to the results, the method is valid from 40 mW up to 8 W, which corresponds to a value of 200 for the ratio of maximum to minimum core losses.

In case of low losses, the core temperature increases slowly and, due to the limitation of $\Delta t_{1,\text{opt}}$ to $\Delta t_{1,\text{max}}$, according to (3.20), a reduced temperature

³The implemented computation takes $2^5 = 32$ combinations of uncertainty values into account. Each of these values is selected such that, in case of a standalone consideration, minimum (most negative) or maximum (most positive) contribution to the total uncertainty results. With regard to $\delta_{C_{\text{th,core}}}$, $\delta_{R_{\text{th,leak}}}$, $\eta_{P_{\text{core}}}$, and $\epsilon_{T_{\text{meas}}}$, this is achieved by using the minimum and maximum boundary values of these four uncertainties. In case of τ_{NTC} , the minimum and maximum uncertainties need to be obtained numerically from (3.13) for each combination of t_1 and Δt_1 , due to the nonlinear characteristic of (3.13).

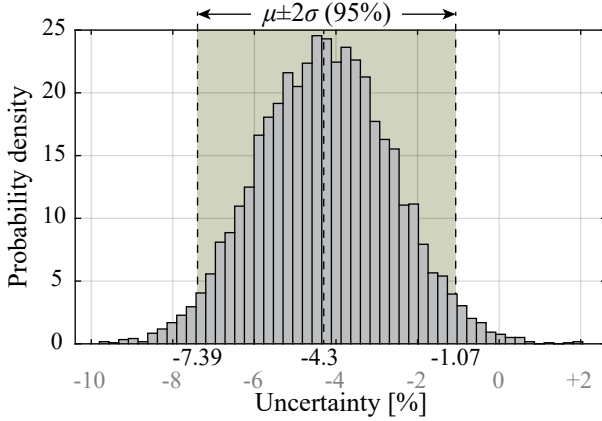


Fig. 3.9: Distribution of the total uncertainty resulting from a Monte Carlo simulation of the uncertainties of Tab. 3.2 and for the specifications presented in Tab. 3.1. The uncertainties are assumed to follow a Gaussian distribution.

difference is measured. As a consequence, the corresponding increase of the uncertainty is mainly related to the temperature measurement error, $\epsilon_{T_{\text{meas}}}$. In addition, with $\Delta t_{i,\text{opt}}$ approaching τ_{leak} , also the impact of $\delta R_{\text{th,leak}}$, i.e., the uncertainty of $R_{\text{th,leak}}$, on the total uncertainty becomes more relevant.

In case of high losses, the core temperature increases quickly. Accordingly, the increase of the total uncertainty is mainly due to the increased uncertainties arising from the temperature dependency of the core losses, $\eta_{P_{\text{core}}}$, and the time constant of the NTC temperature sensor, τ_{NTC} . The two uncertainties are contradictory to each other, since the first one requires small values of t_1 and Δt_1 , in order to limit the temperature increase, and the second one needs $t_1 > 2\tau_{\text{NTC}}$ in order to overcome the delay error introduced by the transfer function of the NTC.

The extreme cases of core losses close to 40 mW or 8 W correspond to operating points of limited interest, i.e., insignificant introduced heat in case of low losses, which is not of practical relevance, and potential thermal runaway in case of high losses. Nevertheless, these values confine the absolute measurement limits of the specific core. Measurements of higher or lower absolute core losses are feasible for larger or smaller cores, due to the increased or decreased values of the thermal capacitance, $C_{\text{th,core}}$.

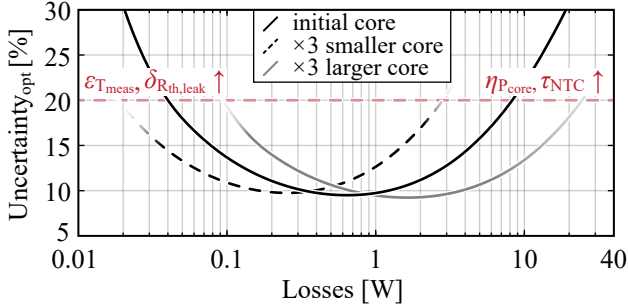


Fig. 3.10: Evaluation of the measurement uncertainty for a wide range of losses, i.e., between 20 mW and 20 W, for the specifications of Tab. 3.1. For each value of P_{core} the optimal selection of t_1 and Δt_1 (cf. Fig. 3.3) is considered. Moreover, the same curve for a core of three times larger volume and a core of three times smaller volume is depicted.

3.4 FEM Simulation

Section 3.2.2 details an equivalent circuit that correctly reproduces the measurement results. However, the physical validity of the circuit has not been investigated, e.g., other circuits could give similar waveforms, too. In addition, certain parameters, e.g., $R_{\text{th,core}}$, depend on 3D phenomena related to the field pattern. For both these reasons, a 3D FEM simulation (COMSOL Multiphysics software [94]) of the core losses and the temperature distribution of the experimental setup is performed and the results are presented in this Section.

The model is solved in a two-step process, starting from a frequency domain Magnetic Field (MF) problem, followed by a Heat Transfer (HT) problem in the time-domain. Critical dependencies, i.e., core loss density with respect to magnetic flux and temperature, specific heat capacity with respect to temperature, and the dependencies of different cooling mechanisms (convection and radiation) on temperature are taken into consideration. On the contrary, dependencies of less impact, e.g., temperature dependency of the core permeability and hence of the magnetic field pattern, are excluded (cf. Fig. 3.11). Solving both, MF and HT, problems in the time domain would lead to unrealistic computation times, due to the substantially different time constants of the two problems, i.e., microseconds for the MF problem and

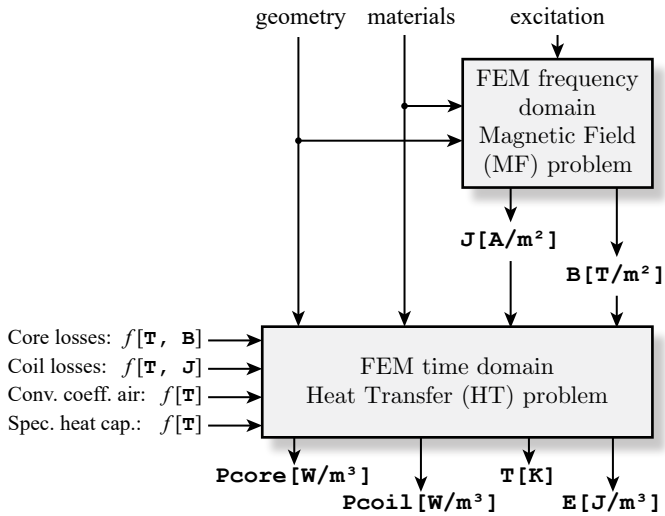


Fig. 3.11: Flowchart of the realized FEM model. The model is split into two subsequent problems, one in the frequency and one in the time domain. This results in a significant decrease of the computational effort, by preserving only the critical model dependencies.

seconds for the HT problem. The implemented model corresponds to the experiment specified in Tab. 3.1 and considers the waveforms of Fig. 3.3, i.e., it features a toroidal core (R 22.1/13.7/7.9) made of N49 MnZn ferrite material with 10 turns of high-frequency litz wire ($180 \times 71 \mu\text{m}$) that is subject to a sinusoidal flux with a frequency of 500 kHz and an average flux density of 100 mT. The loss data for the simulations are taken from the *Magnetic Design Tool* of EPCOS-TDK [95] and for the convection mechanism, natural convection is considered. The specific heat capacity data is taken from the DSC measurement of Fig. 3.4.

The resulting temperature progression over time, shown in **Fig. 3.12(a)**, is in good agreement with the core temperature behavior of the simulated circuit, $T_{\text{core,sim}}$, of Fig. 3.3. **Fig. 3.12(b)** depicts the change of the core losses over time and reveals the high ratio of core to copper losses. Finally, **Fig. 3.12(c)** presents the energy distribution of the losses generated in the core and the coil, $E_{\text{losses,core}}$ and $E_{\text{losses,coil}}$, the thermal energy stored in the core, $E_{\text{stored,core}}$, and the thermal energy transferred to the ambient, $E_{\text{stored,other}}$. During the heating phase, most of the energy stays inside the core and during the cooling phase the energy is slowly passed to the ambient. However, even during the heating phase, a substantial amount of energy is leaking to the ambient, which confirms that the estimation of the core losses needs to take $R_{\text{th,leak}}$ into account.

Fig. 3.13 presents important values of the simulated component for the time instant of t_{off} , cf. Fig. 3.12. As discussed in Section 3.3.7, Fig. 3.13(a) and (b) reveal a gradient of the flux density in radial direction and an even more substantial gradient of the core loss density, due to the raise to the power of β , with a ratio of maximum to minimum loss density of 3.8 [cf. Fig. 3.13(b)]. However, the impact on the core temperature gradient is negligible [$T_{\text{core,max}}(t_{\text{off}}) - T_{\text{core,min}}(t_{\text{off}}) < 0.3 \text{ }^\circ\text{C}$, cf. Fig. 3.13(c)], which further confirms the assumption of $R_{\text{th,core}} \approx 0$. Accordingly, the stored thermal energy features a nearly homogeneous distribution, since the change in the specific heat capacity of N49 is negligible for ΔT_{core} of $0.3 \text{ }^\circ\text{C}$ [cf. Fig. 3.13(d)].

A comparison between the core losses estimated with (3.5), (3.6), and (3.20), using $C_{\text{th,core}}$ at $T_{\text{core}} = T_{\text{amb}}$ and the instantaneous losses at t_{on} , results in a deviation of 9 %. Nevertheless, the comparison between the same calculation, using $C_{\text{th,core}}$ at $T_{\text{core}} = T_{\text{mid}}$ (cf. Fig. 3.12) and the instantaneous losses at t_{mid} , results in a deviation of only 2 %. With this, the FEM simulation results confirm the validity of both, the equivalent circuit and the uncertainty analysis. Finally, comparison between the extraction of losses using the temperature waveform measured on the inner, middle, and outer circumference results in a maximum deviation of 0.8 %, for the simulated maximum instantaneous tem-

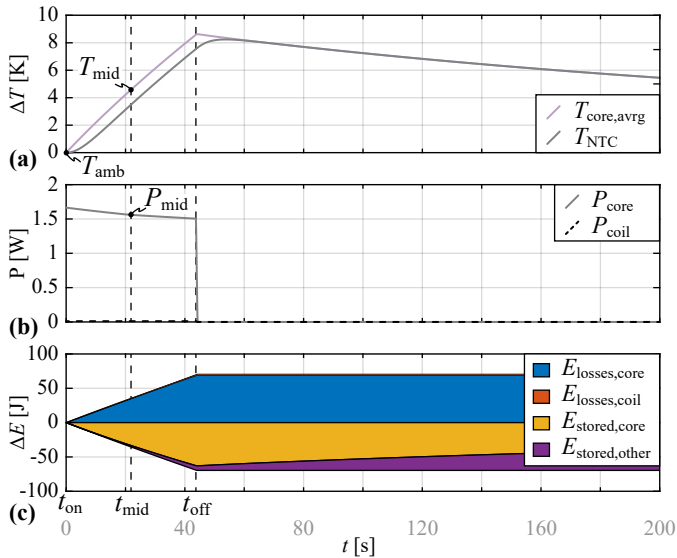


Fig. 3.12: Waveforms of the Heat Transfer (HT) FEM simulation in the time domain for the specifications of Tab. 3.1. (a) Temperature change of the magnetic core and the NTC; (b) generated core and coil losses; (c) distribution of the generated losses and the stored thermal energy over time.

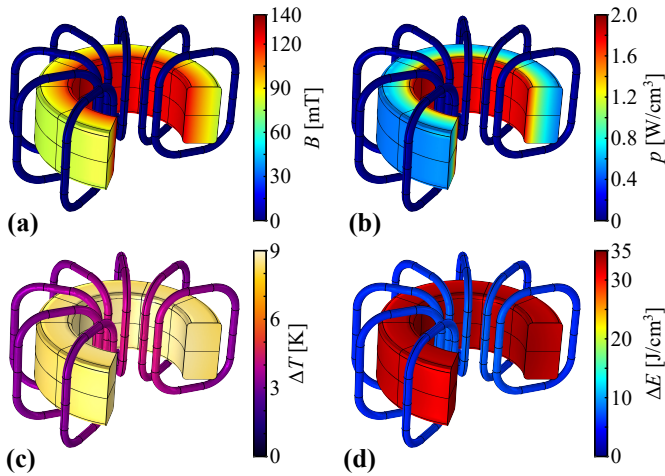


Fig. 3.13: FEM simulation results of a toroidal ferrite core (R 22.1/13.7/7.9, N49) with 10 turns (high frequency litz wire, $180 \times 71 \mu\text{m}$), for the specifications of the experiment of Fig. 3.3/Tab. 3.1, i.e., 500 kHz/100 mT and average core losses equal to 1.54 W. The depicted result corresponds to the instant $t = t_{\text{off}}$. Distributions of: (a) flux density, (b) loss density, (c) temperature difference, (d) density of the stored thermal energy (as compared to the ambient condition).

perature difference of $0.3\text{ }^{\circ}\text{C}$, since the instantaneous deviation corresponds to a temperature offset and the temperature differences measured over time are almost identical at inner and outer circumference.

3.5 Experimental Verification

3.5.1 Workflow of the Core Loss Measurements

The workflow of the complete experiment consists of three main parts, i.e., selection of the CUT, conducting the measurements, and post-processing the acquired data.

Selection of a suitable CUT

The selection of the CUT features two main degrees of freedom, i.e., the core volume, Vol_{core} (which translates into magnetic core length, core cross-section, average turn length, and wire diameter) and the number of turns, N . The requirement of negligible coil losses, defined with $P_{\text{core}} \geq k_{\text{loss}}P_{\text{coil}}$, where $k_{\text{loss}} \gg 1$ is the minimum acceptable ratio between P_{core} and P_{coil} , sets a lower boundary for Vol_{core} . At the other end of the scale, the maximum allowed voltage in the setup, e.g., due to insulation and safety reasons and/or equipment limitations, defines an upper boundary for the the product of $Vol_{\text{core}}N$ (assuming a core cross section that is proportional to $Vol_{\text{core}}^{2/3}$). Both boundaries need to be evaluated with respect to the desired measurement ranges, e.g., minimum to maximum peak flux density and frequency.

In case of cores made of NiZn materials, which feature low relative permeability (i.e. commonly below 300), it is advised to experimentally verify whether the flux distribution is equal, by measuring the voltage induced in a single turn sensing winding when moving it along the circumference of the magnetic core. In addition, it is mentioned in literature that cores of same NiZn materials but different sizes perform differently [96], therefore, the same core should be used for all considered frequencies.

Finally, it is important to consider a core with a thin profile (i.e., a relatively small value of $d_{\text{out}} - d_{\text{in}}$), in order to mitigate the error caused by the gradient of loss density in radial direction, cf. Section 3.3.7, and to ensure that the maximum measurement frequency is less than the self-resonance frequency of the component, which limits the maximum number of turns for a given core.

Conducting the experiments

The experimental setup is implemented according to Section 3.2. In case of large cores, two NTC sensors can be used (on the inner and outer circumference of the toroid) in order to monitor the homogeneity of the temperature distribution. The type of excitation is independent of the core loss measurement method, hence, any flux waveform can be applied to the CUT and also an additional winding for DC premagnetization can be employed.

After a change in the experimental setup (e.g., reference temperature update, different core size) and during the first experiment, both the heating and the cooling phase are required for the extraction of P_{core} and $R_{\text{th,leak}}$ according to (3.6) and (3.5), respectively. For subsequently acquired measurement points, it is sufficient to record only the heating phase, since $R_{\text{th,leak}}$ remains constant.

Post-processing

In a first step, a Savitzky-Golay filter is applied to the measured temperature, in order to decrease the measurement noise without distorting the required information, as shown in **Fig. 3.14(a)**. The extraction of P_{loss} is based on (3.6) and employs the timing parameters defined with (3.20). Under the valid assumption of $\tau_{\text{NTC}} \ll \tau_{\text{leak}}$, the increase of the temperature difference $T_{\text{meas}}(t) - T_{\text{amb}}$ can be considered a low-pass filtered response of a ramp function. Hence, the intersection of the asymptote that results after convergence of $T_{\text{meas}}(t) - T_{\text{amb}}$ with the time axis yields an estimate for τ_{NTC} (assuming that $t_{\text{on}} = 0$) as explained with **Fig. 2.47(b)** in [97]. The estimation of $R_{\text{th,leak}}$ uses (3.5), $t_2 = t_{T_{\text{max}}} + 2\tau_{\text{NTC}}$, and a measurement duration, Δt_2 , that corresponds approximately to $|\Delta T_2| \geq 30|\epsilon_{T_{\text{meas}}}| = 3^\circ\text{C}$ to achieve sufficient accuracy of $\delta_{R_{\text{th,leak}}}$. Analysis similar to **Fig. 3.8** for the extraction of $t_{2,\text{opt}}$ and $\Delta t_{2,\text{opt}}$ is possible.

3.5.2 Measurement Results for MnZn Ferrite Cores

Fig. 3.14 depicts measured temperatures and core losses for ferrite N87 and N49 (EPCOS-TDK) that have been obtained with a setup according to **Fig. 3.1**. The two CUTs are R 41.8/26.2/12.5 (N87) and R 22.1/13.7/7.9 (N49) toroidal cores, having excitation coils with 15 and 10 turns, respectively, which are made of high-frequency litz wire ($180 \times 71 \mu\text{m}$). Moreover, the temperature is measured according to Section 3.3.3, by averaging of the temperatures measured by two sensors glued on the inner and outer circumference, respectively. In order to verify the accuracy of the measurement, electrical measurements are conducted as an alternative to the proposed method, employing capacitive

compensation of the inductive behavior as described in [73] and shown in **Fig. 3.15**. For this concept, in addition to the capacitive compensation, a sense winding directly connected to a high input impedance voltage probe is used, to exclude the influence of the copper losses in R_{coil} . Finally, a high accuracy measurement of the circuit current, i_{meas} , allows for calculation of the core losses of the CUT using

$$P_{\text{CUT}} = I_{\text{meas,rms}} V_{\text{meas,rms}}. \quad (3.21)$$

For each measured point an error analysis has been conducted for both methods in order to verify the accuracies of the measurements.

The average absolute deviation between the two methods for all measurements is less than 5.0 % and the maximum absolute deviation is below 13.0 %, both of which confirm the validity of the method. More interestingly, the proposed method is successfully applied to a wide range of losses between 45 mW to 4.5 W. Finally, it can be observed that with increasing frequency the uncertainty range of the electrical measurements, even for the case of capacitive compensation of the reactive power, starts exceeding the one of the proposed method, mainly due to the error introduced by the measurement equipment. This confirms the significance of the transient calorimetric method especially for measurements of NiZn ferrite cores in the MHz range.

3.5.3 Measurement Results for NiZn Ferrite Cores

For the measurement of NiZn ferrite cores, the core R 21/13/6.4 with material 67 (Fair-Rite, manufacturer no: 5967000601) has been used. Due to its thin profile, a single NTC sensor glued on the middle circumference is used. The measurement circuit employed is depicted in **Fig. 3.16**. The input signal, which is generated with the waveStation 2052 signal generator from Teledyne LeCroy [99], is amplified with the AR 150A100D RF power amplifier [100]. A custom made impedance matching transformer, realized with a R 32/19/9.5 toroidal core with material 67 (Fair-Rite, manufacturer no: 5967001701) and a turns ratio of 12:3 is used in order to increase the load impedance on the primary side (i.e., RF amplifier side) and provide galvanic isolation between the amplifier and the core loss measurement circuit. For each considered CUT, resonance matching capacitors of type MC from Cornell Dubilier Electronics [101] with mica dielectric are used. The specific capacitors are suitable for RF applications in the MHz range. The proposed circuit is required to achieve sufficient impedance matching for the amplifier and, with this, stable operation, and is not relevant for the proposed transient calorimetric measurement

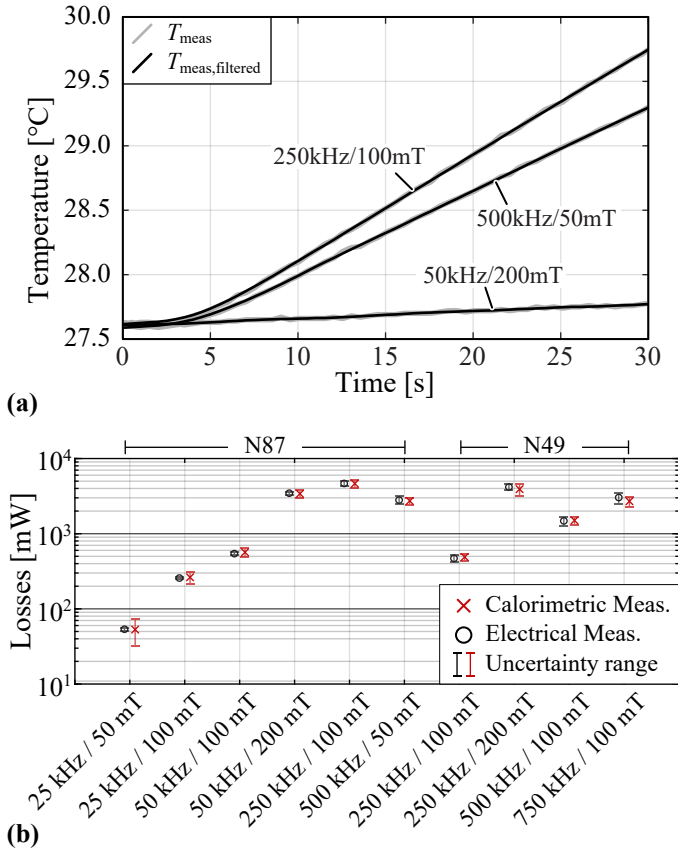


Fig. 3.14: (a) Comparison of waveforms of three different measurements of Ferrite N87, before and after application of the Savitzky-Golay filter; (b) comparison of the accuracies achieved with the proposed calorimetric method and the electric method described in [73] for two different DUTs, i.e., R 41.8/26.2/12.5 - N87 and R 22.1/13.7/7.9 - N49, and for ambient temperature between 26 °C and 28 °C.

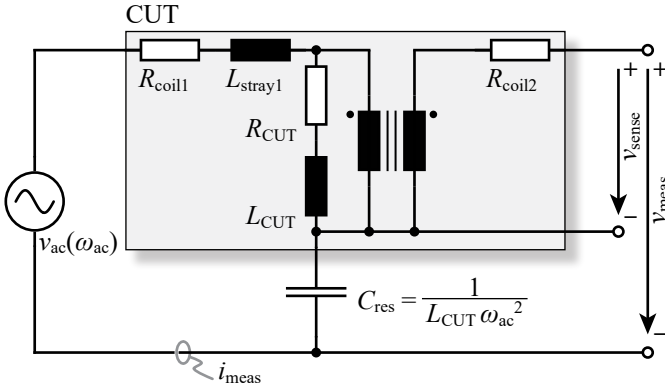


Fig. 3.15: Electrical circuit according to [73], used for the purpose of experimental verification, cf. Fig. 3.14(b). Examples of the same setup can be also found in [19, 59]. For the measurements, the following equipment from Teledyne LeCroy was used: PPO18-1 passive probe (v_{meas}), ADP305 differential probe (v_{sense}), AP015 current probe (i_{meas}) all together connected to HDO4054A oscilloscope [98].

method. Hence, provided that the required voltage, V_{CUT} , is applied to the CUT, operation directly at the resonant frequency is not required. Finally, a sensing winding is used to monitor the flux in the core, since the low relative permeability of the 67, $\mu_r \approx 40$, leads to low coupling (cf. Section 3.5.1).

For the acquirement of the loss-data of Fair-Rite 67 NiZn material, the same core has been used during the complete measurement procedure. However, depending on the measured frequency range, the number of turns has been adapted in order to limit the required rms voltage to values of less than 120 V. Voltage measurement in this frequency range, i.e., 5 MHz to 50 MHz, requires a careful selection of the equipment. In case of the discussed experiments, the *PHV 1000-RO* passive probe (by PMK) has been used, since the selected probe can measure two to three times higher voltages at 50 MHz than other state-of-the-art high frequency passive probes, i.e., up to 150 V_{rms} . However, it has a parasitic input capacitance of 8 pF, which at this frequency range leads to non-negligible currents through the probe and also affects the resonance frequency of the circuit. Nevertheless, in case of the proposed method, this impact is of minor relevance. In order to ensure flat response of the probe at the complete frequency range, compensation of the probe individually for each measured frequency is important.

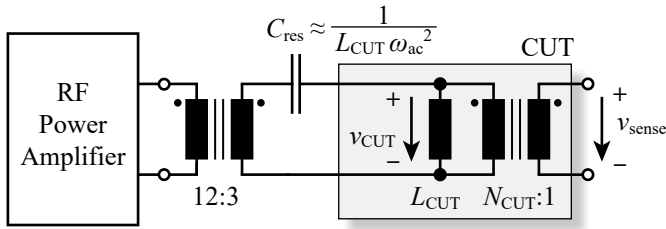


Fig. 3.16: Electrical circuit employed for the measurement of core losses of Fair-Rite 67 NiZn material. The setup is required only in order to achieve a better impedance matching for the $50\ \Omega$ output of the RF amplifier and not directly for the transient calorimetric measurement method.

In **Fig. 3.17** the measured impedances of the CUT for different numbers of turns are depicted. The abrupt change of the cores' behavior at 60 MHz is in consistency with the real and imaginary relative permeability values of the material's datasheet [96]. According to this result, core loss measurements up to 50 MHz are clearly feasible, since no resonance issues exist and at 50 MHz the phase angle is still greater than 89.3° .

Fair-Rite 67 NiZn is a permivar material, i.e., in case high enough magnetic field or strong enough mechanical shock is applied to the core, it will change its magnetic properties in an irreversible way [102]. Therefore, when measuring such material, it is advised to repeat the initial measurements, i.e., impedance measurement and/or first loss-measurement points, after all the points of interest have been measured, in order to confirm that the material was not over-stressed by accident and hence preserves its initial properties and the measurements are valid.

The complete measured loss-map of the material at 25°C is shown in **Fig. 3.18**. According to the results, the maximum frequency for practical use is 20 MHz, since above this frequency the value of α (Steinmetz equation) increases abruptly. This is consistent with the small signal imaginary part of the permeability shown in the material's data sheet [96]. Steinmetz parameters of $k = 1.36 \times 10^{-10}$, $\alpha = 1.4$, and $\beta = 2.4$ provide a good approximation of the measured losses in the frequency range between 5 MHz and 20 MHz, with a maximum and average error of 17% and 4.5%, respectively. Above 20 MHz, different Steinmetz parameters are required due to the increase of α .

Due to the nature of the proposed method, the measurement uncertainty is independent of the type of excitation, e.g., the worst-case uncertainty

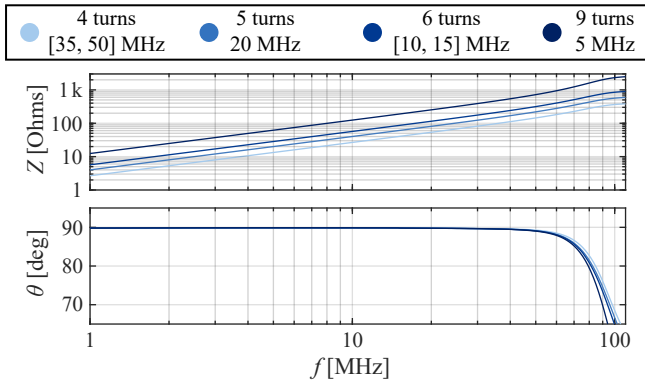


Fig. 3.17: Impedance measurement, using the high precision impedance analyzer 4294A from Agilent, of the R 21/13/6.4 Fair-Rite 67 NiZn core for different numbers of turns. For the coil a flat-wire, 3.175 mm \times 0.137 mm, is used.

for the challenging measurements at 50 MHz is below 15%. Overall, the measurements of Fig. 3.18 feature a maximum and an average worst-case uncertainty of 19.8% and 13.3%, respectively.

3.6 Conclusion

This chapter presents a transient calorimetric method for measuring the losses of ferrite cores independent of the type of excitation, with or without premagnetization. The method relies upon the correlation between the measured rate of rise of the core temperature over time, the core's thermal capacitance and the introduced losses. Accurately measured specific heat capacities of four commonly used ferrite core materials, using a Differential Scanning Calorimeter (DSC), are provided. The main sources of inaccuracy are analyzed and, with this, the total measurement uncertainty is evaluated. The analytical findings are supported based on a proposed thermal equivalent circuit, FEM simulations, and thermal imaging using a high resolution IR camera. In addition, a step-by-step description of the workflow for conducting the experiments is given.

The method is initially applied to commonly used N87 and N49 MnZn ferrite materials of EPCOS-TDK, and the results of thermal measurement are verified by electrical measurements. For all measurements, the deviations

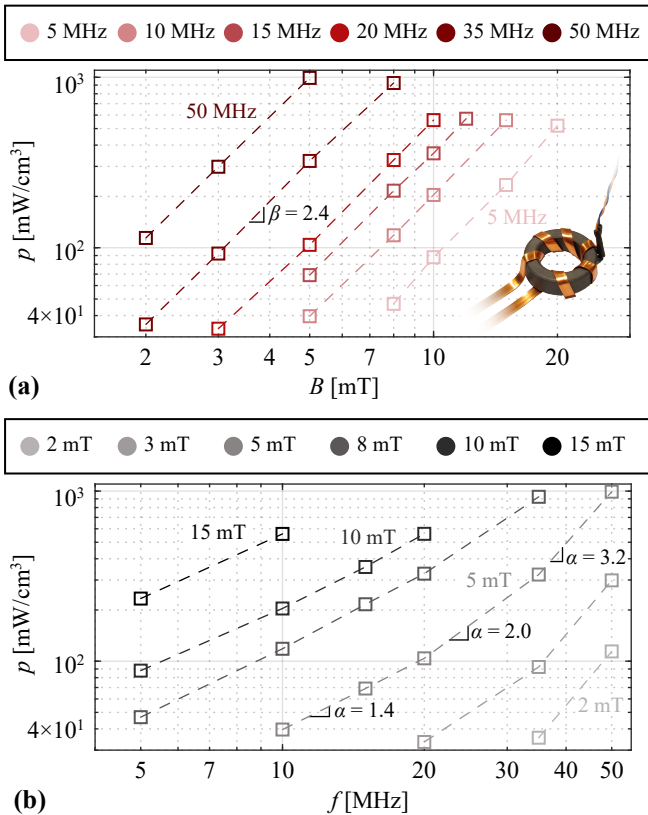


Fig. 3.18: Measured loss density of Fair-Rite 67 at 25°C (a) with respect to magnetic flux and (b) with respect to frequency. The losses are measured using a R 21/13/6.4 (manufacturer no: 5967000601) magnetic core. The fitted Steinmetz parameters, $k = 1.36 \times 10^{-10}$, $\alpha = 1.4$, and $\beta = 2.4$, result in a maximum and an average error of 17% and 4.5%, respectively, and are valid for frequencies up to 20 MHz. Above this frequency, different Steinmetz parameters are required due to the increase in α . The measurements feature a maximum and an average worst-case measurement uncertainty of 19.8% and 13.3%, respectively.

between the measured and the reference values are below 13 %, which is within the typical tolerance of cores produced in different batches and also within the commonly accepted accuracy for the execution of a complete component optimization. Finally, the method is applied to the 67 NiZn material of Fair-Rite for frequencies up to 50 MHz. With total measurement uncertainties of less than 20 %, the transient calorimetric method demonstrates its great strength compared to electrical methods, which would be very difficult to realize at these high frequencies. Based on the acquired loss-map, Steinmetz parameters are provided that accurately describe the material up to 20 MHz.

PART 2

**Universal EV Charger
Mains Interfaces**

4

Universal 3-Phase / 1-Phase PFC Rectifier System

This chapter summarizes most relevant research findings also published in:

- ▶ **P. Papamanolis**, D. Bortis, F. Krismer, D. Menzi, and J. W. Kolar, “New EV Battery Charger PFC Rectifier Front-End Allowing Full Power Delivery in 3-Phase and 1-Phase Operation,” *MDPI Electronics*, vol. 10, no. 17, pp. 2069, 2021.
- ▶ **P. Papamanolis**, F. Krismer, and J. W. Kolar, “22 kW EV Battery Charger Allowing Full Power Delivery in 3-Phase as well as 1-Phase Operation,” in *Proc. of the IEEE Energy Conversion Congress and Expo. (ECCE Asia)*, Busan, South Korea, 2019.

Motivation

Private charging of EVs will further dominate the share of employed charging methods in the near future. Moreover, with the increase of EV battery capacities, charging at high powers, i.e., > 10 kW, becomes necessary. However, LV mains infrastructures differ as for example USA features a 1-phase, 240 V, 60 Hz grid, whereas Europe features a 3-phase, 400 V, 50 Hz grid. Accordingly, a globally applicable charging system would be preferable. Motivated by this challenge, this chapter proposes a simple universal solution, that will allow interoperability and cost-efficient production lines.

Executive Summary

A new universal front-end PFC rectifier topology of a battery charger for Electric Vehicles (EVs) is proposed, which allows fast charging at rated and/or full power level in case of 3-phase (Europe) as well as 1-phase (USA) mains supply. In this regard, a conventional 3-phase PFC rectifier would facilitate only $1/3$ of the rated power in case of 1-phase operation. The new topology is based on a two-level six-switch (2LB6) 3-phase boost-type PFC rectifier, which is extended with a diode bridge-leg and additional windings of the Common-Mode (CM) chokes of the EMI filter. Besides this extension of the power circuit, the general design of the new converter is explained, and the generated Differential Mode (DM) and Common Mode (CM) EMI disturbances are investigated for 3-phase and 1-phase operation, resulting in guidelines for the EMI filter design. The EMI performance (CISPR 11 class-B QP) is experimentally verified for 1-phase and 3-phase operation at an output power of 4.5 kW, using a full-scale hardware prototype that implements the proposed extensions for a 2LB6 3-phase boost-type PFC rectifier and that is designed for output power levels of 22 kW and 19 kW in case of 3-phase and 1-phase operation, respectively. Compared to a conventional 2LB6 PFC rectifier, the volume of the extended system increases from 2.7 dm^3 to 3.4 dm^3 , of which 0.5 dm^3 are due to the additional DC-link capacitance for buffering the power pulsation with twice the mains frequency occurring for 1-phase operation.

4.1 Introduction

The internationally increasing sales figures of Electric Vehicles (EVs) results in a demand for universal front-end PFC rectifier topologies of EV chargers that facilitate full power operation in presence of 3-phase and 1-phase mains. For example, in Europe, a charging power of 22 kW is accessible from the 3-phase mains with a line-to-line rms voltage of 400 V and a maximum phase current of 32 A [3]. In the USA, the three-wire split-phase system, which basically represents a 1-phase mains, provides similarly high power of 19.2 kW with an rms voltage of 240 V and a maximum current of 80 A [103].

In the context of economy of scale it can be preferable that both, i.e., 3-phase and 1-phase operation, are covered using the same power circuit, especially a universal ac/dc front-end. Different reasons for potential cost reductions are listed below.

- Reduced development effort since only a single product needs to be designed and tested.

- ▶ Product certification, e.g., as described in [104], which often is a time-consuming process for automotive supply equipment, needs to be conducted for only one product instead of two.
- ▶ Reduction of the number of different components, in particular magnetic components.
- ▶ Only a single production line is needed to manufacture the EV charger.

For these reasons, it is expected that, up to a certain production volume, the total cost of the presented converter structure is lower than the total cost of two separate EV chargers (in case of very high production volumes, a lower total cost may be achieved with separate EV chargers for 3-phase and 1-phase operation, since a separate realization facilitates the independent optimization with regard to the specific requirements).

A straight-forward realization can be achieved with three individual 1-phase PFC AC/DC converter modules, as described e.g., in [105–108], which requires three individual isolated DC/DC converters. Alternatively, according to **Fig. 4.1(a)**, the front-end of an EV charger (which comprises an AC/DC converter and a DC/DC converter with galvanic isolation [109]) can be realized with a conventional 3-phase boost-type PFC rectifier that readily enables 1-phase operation, cf. **Fig. 4.1(b)**, whereas the unused bridge-leg, e.g., of phase b in **Fig. 4.1(b)**, can be employed to buffer the Low Frequency (LF) power pulsation at the DC-link, as detailed in [110]. However, the maximum power in case of 1-phase operation is limited to approximately 1/3 of the nominal 3-phase power, since the power components of the rectifier stage in each phase are only rated for the current occurring for nominal 3-phase operation [111, 112].

These state-of-the-art approaches are the starting point for investigating whether a conventional 3-phase PFC rectifier can be extended such that 1-phase operation is feasible at full power. This potentially offers advantages concerning circuit complexity, realization effort, and manufacturing costs. The resulting PFC rectifier has been introduced in [113]. In the following, a systematic design procedure is presented, based on a detailed stress comparison, between the two types of operation. Furthermore, the guidelines for the EMI filter design of [113] are further developed, including FEM simulations for each of the proposed realizations of the 4-phase CM choke, as well as, experimental measurements. Finally, a full-scale hardware prototype allows for experimental verification, revealing the viability of the proposed concept.

To start with, **Section 4.2** describes the extension of a 3-phase two-level six-switch (2LB6) PFC rectifier topology with respect to full power 1-phase

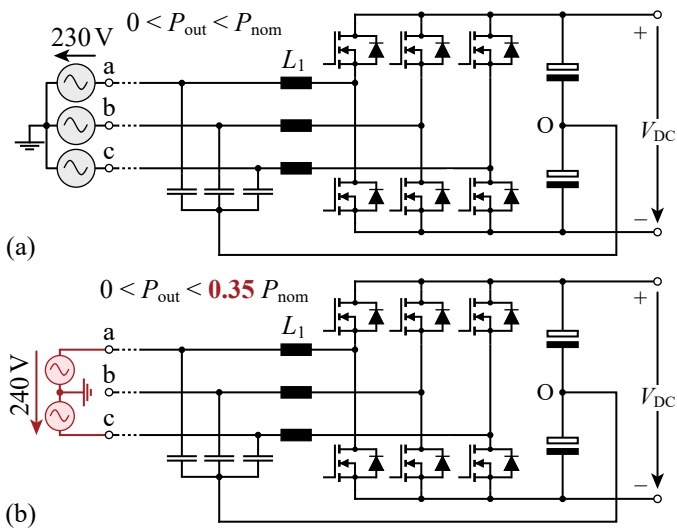


Fig. 4.1: Block diagrams of conventional boost-type 3-phase AC/DC converters for different operating conditions: **(a)** operation from 3-phase mains; **(b)** operation from 1-phase mains [110–112].

Tab. 4.1: Specifications of the EV charger.

Parameter	Description	3-phase	1-phase
P_{nom}	Nominal power	22 kW	19.2 kW
$V_{\text{AC,rms}}$	Grid input voltage (rms)	3×230 V	240 V
$I_{\text{AC,rms}}$	Grid input current (rms)	32 A	80 A
$I_{\text{ph,rms}}$	Phase current (rms)	32 A	26.67 A
f_{in}	Grid frequency	50 Hz	60 Hz
V_{DC}	Output voltage	750 V	750 V
f_{s}	Switching frequency	48 kHz	

operation. The proposed extension can also be applied to multilevel 3-phase AC/DC converters whose power stages do not require a connection to the DC-link midpoint (e.g., a flying capacitor converter). **Section 4.3** details the design of the power circuit, i.e., the derivation of the analytical expressions used to calculate the component stresses and presents a design guideline, which clarifies specific design requirements. **Section 4.4** investigates conducted EMI in case of 3-phase and 1-phase operation. The EMI equivalent circuits derived in this context enable the identification of most critical operating conditions (3-phase or 1-phase) for Differential Mode (DM) and Common Mode (CM) disturbances and facilitate the compilation of guidelines for the EMI filter design. **Section 4.5** presents the experimental verification of the theoretical considerations at an output power of 4.5 kW, using a full-scale hardware prototype that implements the proposed extensions for a 2LB6 3-phase boost-type PFC rectifier. The measurement results confirm that the EMI filter complies with CISPR 11 Class-B QP regulations in case of 3-phase and 1-phase operation.

4.2 Modifications for 1-Phase Operation

This Section summarizes the 3 extensions that are applied to the 2LB6 3-phase PFC rectifier depicted in Fig. 4.1, in order to gain 1-phase operating capability at full power. Starting from the power stage, these are listed below.

- ▶ DC-side unfolder (passive diode bridge-leg) for the return current.
- ▶ DC-side relay to enable DC-side CM filtering with a CM filter capacitor for 1-phase and 3-phase operation.

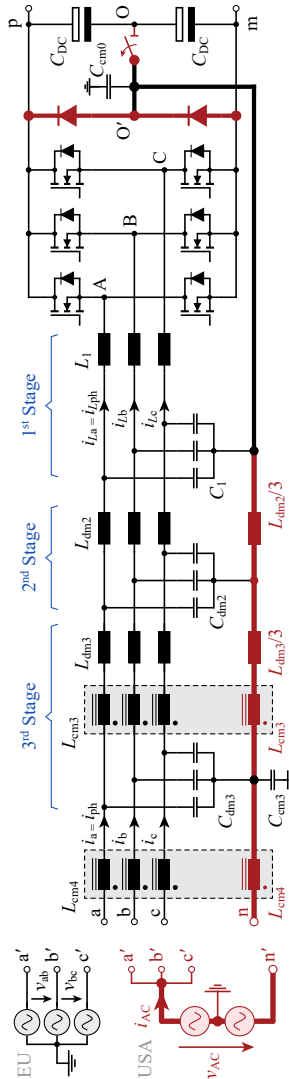


Fig. 4.2: Proposed two-level six-switch (2LB6) 3-phase boost-type PFC AC/DC converter with three-stage EMI filter. Compared to a conventional 2LB6 rectifier topology, the additional components, highlighted with red color, allow full / rated power delivery also for 1-phase operation, otherwise, the 1-phase rating would be limited to 1/3 of the rated 3-phase power (cf. Fig. 4.1(b)). The relay contact is closed in 3-phase operation and open in 1-phase operation, cf. Sec. 4.2.

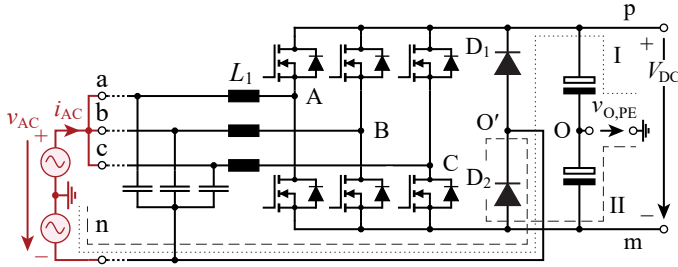


Fig. 4.3: Illustration of the voltage loops (I and II) used to estimate $v_{O,PE}$ under 1-phase operation. Both loops encompass PE, O', O, and the currently conducting rectifier diode. The voltage drop caused by the EMI filter is neglected.

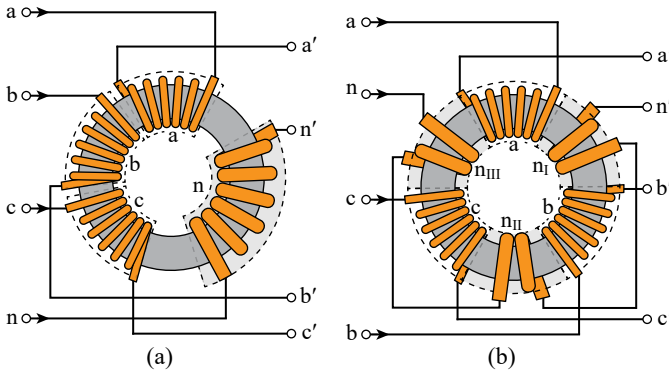


Fig. 4.4: Two different constructions of a 4-phase CM choke with toroidal core and 6 turns per phase: (a) the winding of the 4th phase is not split apart; (b) the winding of the 4th phase is split into three parts that are connected in series.

- Modified EMI filter: 4-phase CM chokes; no CM chokes in the filter stages directly connected to the switching stage.

Fig. 4.2 depicts the resulting converter topology. A detailed explanation is presented in [113].

Tab. 4.1 lists the main converter specifications, which reveal similar output power levels and similar phase voltages in case of 3-phase and 1-phase operation. Accordingly, similar component stresses are expected for the two modes of operation. The three half-bridges of the PFC rectifier can be operated in parallel during 1-phase operation in order to equally share the mains current, advantageously with interleaving, which, however, requires all 3 phases a, b, c of the rectifier for drawing the input current. Hence, the 3-phase PFC rectifier needs to be equipped with a conductor for the return current. This conductor could be directly connected to the DC-link midpoint, O, in Fig. 4.1. However, this solution would lead to very high DC-link capacitances, since both, the upper and the lower DC-link capacitor would only be charged during every second mains half cycle in an alternating manner. For this reason, the rectifier is extended by a passive diode bridge-leg that is realized with low-cost Si diodes and acts as unfolder. Compared to the direct connection to the DC-link midpoint, the LF rms current of the DC-link reduces from 44 A to 18 A. The return conductor is connected to the AC input of this unfolder bridge-leg as shown in Fig. 4.2. The resulting topology resembles a typical interleaved totem pole PFC rectifier [114].

In the 2LB6 3-phase PFC rectifier shown in Fig. 4.1, the star-point formed with the DM EMI filter capacitors is connected back to the midpoint, O. This connection enables a low-impedance current path for CM EMI disturbances and stabilizes the electric potential of the midpoint with respect to earth at high frequencies [115, 116]. In addition, one or more CM EMI filter capacitors can be installed at the DC side, e.g., between O and PE, in order to further decrease the level of CM EMI noise applied to the EMI filter [117]. However, during 1-phase operation, the rectifier diodes of the unfolder change their states at every zero-crossing of the phase current. The voltage between O and PE, $v_{O,PE}$, can be determined based on the voltage loops I and II depicted in **Fig. 4.3**. Depending on the conducting diode, i.e., D_1 or D_2 , loop I or II is valid, respectively. Hence, should the voltage drop across the EMI filter be neglected at mains frequency,

$$v_{O,PE} \approx \begin{cases} -v_{AC}(t)/2 - V_{DC}/2 \quad \forall i_{AC} < 0 \text{ (loop I)}, \\ -v_{AC}(t)/2 + V_{DC}/2 \quad \forall i_{AC} > 0 \text{ (loop II)}. \end{cases} \quad (4.1)$$

results. According to (4.1), $v_{O,PE}$ is subject to a voltage step of V_{DC} at every zero-crossing of the phase current, cf. Fig. 4.2, which leads to an increase of the EMI noise floor, e.g., as described in [118, 119]. For this reason, no filter capacitor should be connected between O and PE in 1-phase operation. However, since the voltage between the midpoint of the unfold, O', and earth, is not subject to such voltage step, $v_{O',PE} \approx -v_{AC}/2$, a filter capacitor, C_{cmo} , can be placed between O' and PE to attenuate CM EMI noise. Accordingly, a relay is installed between O and O', which is in the on-state during 3-phase operation and in the off-state during 1-phase operation in order to keep C_{cmo} effective for 3-phase and 1-phase operation.

In a last step, the EMI filter needs to be modified, which, in particular, requires the 3-phase CM chokes to be extended. These CM chokes are intended to handle a small magnetizing current, because the sum of the phase currents, $i_a + i_b + i_c$, is approximately zero during 3-phase operation. However, during 1-phase operation the sum of the phase currents is equal to the return current and the cores of the 3-phase CM chokes would saturate. Accordingly, all CM chokes must feature a 4th winding for the return current. **Fig. 4.4(a)** depicts a straightforward realization of this CM choke with a single 4th winding. This construction is cost-effective because it requires only 4 dedicated windings but it introduces an asymmetry that can be critical regarding mixed-mode EMI noise [120, 121]. An assessment of the implications of this asymmetry on the components' stray inductances is presented in Appendix B.1 for a selected design example, for which an acceptable ratio of 1.41 for maximum to minimum stray inductance is obtained. Apart from that, the construction of Fig. 4.4(a) enables a PCB layout that is of low complexity and features a high fill factor, since it requires a minimum number of separators between the windings. A more symmetric construction is depicted in **Fig. 4.4(b)** where the 4th winding is split up into three parts that are connected in series. This construction is more complex to realize than that of Fig. 4.4(a) and limited to numbers of turns that are a multiple of three. Both constructions have in common that the cross-section of the wire of the 4th winding is three times larger than that of each wire of the three phases. With this, same LF winding losses occur during 1-phase operation in all 4 windings. Initially, it was intended to realize both CM chokes based on the more symmetric construction depicted in Fig. 4.4(b), however, it turned out that the construction with a single 4th winding features a lower number of connections and enables a PCB layout with less overlapping conductors. Thus, lower parasitic capacitances due to interconnections result. In order to verify the proper operation of both configurations, L_{cm3} is based on Fig. 4.4(b) and L_{cm4} on Fig. 4.4(a).

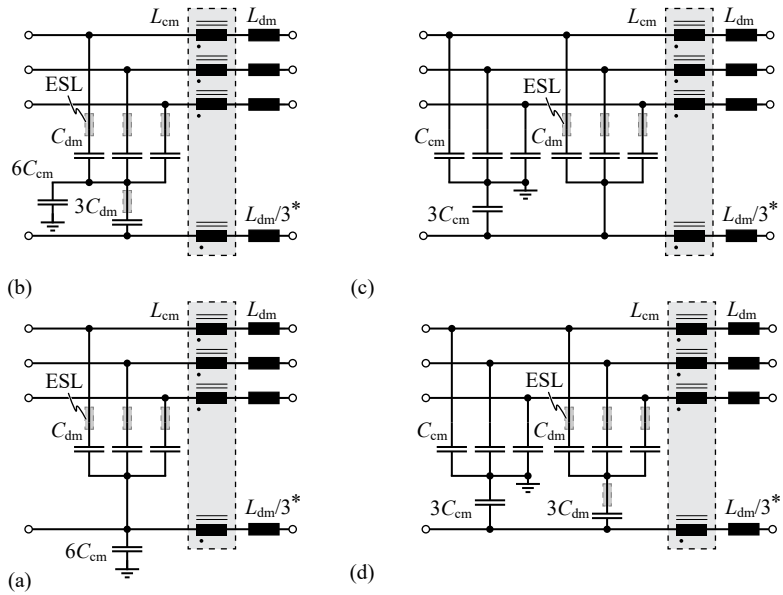


Fig. 4.5: (a)-(d) Proposed structures for a single stage of the EMI filter that are effective in 1-phase as well as 3-phase operation. $L_{dm}/3$ (marked with an *) is included for symmetry reasons and may be omitted.

The resulting EMI filter structures, shown in **Figs. 4.5(a)–(d)**, effectively attenuate the generated DM and CM EMI noise for operation with 3-phase as well as 1-phase mains. In all four structures, a low impedance return path for the CM noise of the switching stage is provided through one or more CM capacitors, PE, and C_{cmo} (cf. Fig. 4.2).

Fig. 4.5(a) depicts the realization of a filter stage with the lowest component count, which comes at the costs of a disturbed symmetry (with regard to the placement of the CM capacitor) and an increased parasitic inductance in series to the CM capacitor that arises from the Equivalent Series Inductances (ESLs) of the DM capacitors. Fig. 4.5(b) presents an alternative structure that achieves symmetry, due to the additional DM capacitor between the return conductor and the star-point of the DM capacitors of the three phases. A drawback of this structure is the increased volume, since X-rated DM capacitors, typically in the μF range, are bulky components. Fig. 4.5(c) depicts a structure with only three DM capacitors and with a CM filter part that is symmetric and achieves improved HF performance, due to the reduced parasitic inductances in series to the CM capacitors. Finally, Fig. 4.5(d) shows the most symmetrical structure, which, however, requires four bulky DM capacitors.

The filter stages directly connected to the switching stage, e.g., the 1st filter stage, do not comprise a CM choke, cf. Fig. 4.2. The reason is that a 4-phase CM choke, during 3-phase operation (where the relay is in the on-state), would short circuit the zero sequence voltage inherently generated by the 2LB6 topology (cf. v_{cm} in Fig. 4.8(a)). Instead of that, the CM choke is placed close to the mains-side interface of the EMI filter where it is fully effective, i.e., L_{cm4} in Fig. 4.2. Furthermore, in anticipation of the detailed analytical investigation conducted in Sec. 4.4, a second CM choke is placed in the 3rd filter stage (L_{cm3}), together with a CM EMI filter capacitor between the two CM chokes.

The DM part of the EMI filter can remain unchanged because the DM EMI filter components are similarly effective for both, 3-phase and 1-phase operation. The DM filter components $L_{\text{dm2}}/3$ and $L_{\text{dm1}}/3$ in the return path are only used for the reason of symmetry and could be omitted.

The presented extension can be applied to any conventional multilevel 3-phase AC/DC converter that can be implemented without connection to the DC-link midpoint (e.g., a flying capacitor converter). A possible extension of AC/DC converters with inherent utilization of the midpoint (e.g., T-type converter) is presented in Appendix B.5.

4.3 Design of Main Power Stage

This Section aims for a systematic design of the converter that takes into consideration whether 3-phase or 1-phase operation is more critical for the design of a power component. In this regard, suitable values of switching frequency and inductor current ripple are determined in Subsection 4.3.1 and the selection or design of the power components is presented in Subsection 4.3.2. The expressions used to calculate the currents in the power components and the losses for 3-phase and 1-phase operation are well known; for the reason of completeness, the expressions used in the course of the converter design are compiled in Appendix B.2 and B.3.

4.3.1 Switching frequency and current ripple

In order to obtain a compact EMI filter, it is sufficient to limit the switching frequencies that are considered during the design process to a set of discrete values, $f_s \in \{24, 36, 48, 72, 144\}$ kHz [122]. From these, $f_s = 48$ kHz has been considered, since this choice provides acceptable switching losses and a compact design of the boost inductor [123, 124].

The value of the current ripple has been determined such that, in case of 1-phase operation, the diode bridge-leg is not subject to parasitic HF switching operations around the zero crossing of the phase current, due to the superimposed HF ripple. Since the three phases are modulated with interleaved carriers during 1-phase operation, the HF ripple of the current in the rectifier diodes only contains harmonic components at $3f_s$ and multiples thereof (cf. Sec. 4.4). Furthermore, the superimposed HF ripple leads to a total current in the return path that is limited by an upper and a lower envelope. In our case, the lower envelope is of interest, because it enables the derivation of a condition for L_1 such that parasitic HF oscillations of the diode bridge-leg AC-side voltage are avoided. The expression for the lower envelope of the return current can be estimated with the mains current fundamental component and the amplitude of the spectral component at $3f_s$, calculated from the Fourier series of the rectangular waveform of the switch-node voltage,

$$i_{D,env}(t) = \underbrace{\frac{\sqrt{2}P}{V_{AC,rms}} \sin(2\pi f_m t)}_{\text{LF term}} - \underbrace{\left[\frac{V_{DC}}{9f_s \frac{L_1}{3} \pi^2} \sin(3\pi d(t)) \right]}_{\text{ampl. of spectral comp. at } 3f_s}. \quad (4.2)$$

According to (4.2), parasitic HF switching of the diode bridge-leg is avoided if the gradient of the LF term is greater than the gradient of the amplitude

of the 3rd harmonic at $t \rightarrow 0$. For output power levels greater than 2.5 kW, this condition leads to $L_1 = 150 \mu\text{H}$, which translates into a peak-to-peak current ripple of 60 %. In case the specifications require operation at lower power, low-power MOSFETs or IGBTs can be placed in parallel to the diodes, to clamp the path of the current around zero-crossings.

4.3.2 Power components

Using the provided expressions of Appendix B.2, B.3 all currents can be calculated for 3-phase and 1-phase operation; **Tab. 4.2** lists the obtained results. The comparison of the listed values reveals slightly higher values of $I_{\text{ph,rms}}$ and $I_{\text{ph,avg}}$ in case of 3-phase operation, which is due to the higher output power of 22 kW. However, 1-phase operation leads to a higher peak value of the phase current and a higher HF rms value of the inductor current, since the durations with large current ripples are longer than for 3-phase operation. Furthermore, the DC-link capacitors are subject to high LF rms currents during 1-phase operation. These results, in combination with (B.6), (B.10), and (B.33), allow to directly draw the conclusion that 3-phase operation is more relevant for the selection of the MOSFETs and 1-phase operation is important for the design of the DC-link capacitor. The selected power components are listed in **Tab. 4.3**. A single *1EDI60N12AF* gate driver (by *Infineon*) is employed for each pair of parallel MOSFET devices with separate gate resistors. Moreover, for the relay on the DC-side (cf. Section 4.2), two parallel *IMo6DGR* relays from *TE* have been employed. Such configuration is possible, since the relays are only used as disconnectors and are not intended to switch any current.¹

With regard to the design of the boost inductor, both operating modes need to be considered, since 3-phase operation leads to higher copper losses (higher value of $I_{\text{ph,rms}}$) and 1-phase operation causes higher core losses and is more critical with regard to a saturation of the magnetic core (higher values of $I_{\text{ph,pk}}$ and $I_{L\text{ph,rms,HF}}$). In order to ensure that the defined values for peak flux density and current density are maintained, the area product of (B.12) is modified,

$$(A_c A_w)_{\min} = \max \left(\frac{L_1 I_{\text{ph,pk}}}{B_{\text{pk}}} \right) \max \left(\frac{I_{\text{ph,rms}}}{k_f J_{\text{rms}}} \right). \quad (4.3)$$

¹In case interoperability is not considered, i.e., possibility of operation in Europe and in the USA, the relay can be omitted (1-phase operation), or replaced by a hardwired connection (3-phase operation).

Tab. 4.2: Components' current stresses for 3-phase and 1-phase operation.

Parameter	Description	3-phase	1-phase
$I_{\text{ph,rms}}$	rms value of $i_{\text{ph}}(t)$	32 A	27 A
$I_{\text{ph,avg}}$	average value of $ i_{\text{ph}}(t) $	29 A	24 A
$I_{\text{ph,pk}}$	peak value of $ i_{\text{ph}}(t) $	50 A	57 A
$I_{L\text{ph,rms,HF}}$	rms value of the HF components of $i_{L\text{ph}}(t)$	5.1 A	6.0 A
$I_{C_{\text{DC,rms}}}$	rms value of the LF current in the DC-link cap.	≈ 0	18 A

In order to evaluate (4.3), the values for B_{pk} and J_{rms} need to be defined. With regard to the current density, a typical value of $J_{\text{rms}} = 4 \text{ A/mm}^2$ is used. However, the value of the peak flux density depends on the selected core material. In this work, the core of the boost inductor is made of the iron-powder material KoolMu, since this features a compact design, due to a high useful flux density, and a smooth transition to saturation in case of overcurrent conditions. However, the practically useful peak flux density is lower than the material's saturation flux density of 1 T, since the permeability of the material and, with this, the resulting inductance decrease for increasing magnetic flux density. Therefore, $B_{\text{pk}} \approx 500 \text{ mT}$ is used, which, for the finally chosen material with an initial relative permeability of $\mu_r = 60$, tolerates a decrease to $\mu_r = 26$. With this, $(A_c A_w)_{\text{min}} = 23 \text{ cm}^4$ results. This area product serves as initial value for selecting a suitable core. The final inductor design is conducted with the multi-domain inductor optimization algorithm outlined in [32] that takes nonlinear effects and coupled electro-thermal effects into account and results in an area product of 25.2 cm^4 . **Tab. 4.4** lists the resulting inductor design. This inductor design features an initial inductance of $170 \mu\text{H}$ at zero current and tolerates a decrease of the inductance to $100 \mu\text{H}$ at 45 A (the maximum of the LF phase current in case of 3-phase operation) and $80 \mu\text{H}$ at 57 A .

Tab. 4.5 summarizes the estimated losses for all main power components and for 3-phase and 1-phase operation. The sum of all semiconductor losses is 214 W for 3-phase operation and 239 W for 1-phase operation, due to the additional losses in the diodes. Therefore, the cooling system is dimensioned based on 1-phase operation. For the cooling system a pin-fin heat sink design is considered, which is known to outperform conventional plate-fin heat sinks [125]. The selection of the heat sink has been a two-step process. First, an online tool that considers lateral airflow [126] has been used to preselect a suitable heat sink. In a second step, the thermal resistance of the cooling

Tab. 4.3: Selected power components.

Parameter	Value
Power MOSFETs (per switch)	two parallel <i>C2Moo4o12oD</i> devices (<i>Wolfspeed/Cree</i>)
Power diodes (per diode)	three parallel <i>VS-8oAPF1o</i> devices (<i>Vishay</i>)
Boost inductors	summarized in Tab. 4.4
DC-link capacitors	14 <i>ESMR451VSN471MR4oS</i> devices (2×7 parallel) (450 V, 470 μ F, $ESR_C \approx 160$ m Ω at 60 $^\circ$ C, $I_{C,rms,max} = 2.66$ A rated at 120 Hz; <i>United Chemi-Con</i>)

Tab. 4.4: Design parameters of the boost inductor L_1 .

Parameter	Value
Magnetic core	KoolMu ($\mu_r = 60$) $5 \times E 4o/2o$
Number of turns (N)	15
Initial inductance ($L(I_L = 0)$)	170 μ H
Inductance at peak current ($L(I_L = 57$ A))	80 μ H
Core volume (V_c)	90000 mm ³
Core cross-section (A_c)	915 mm ²
Area of the core window (A_w)	258.3 mm ²
Height of the core window (h_w)	29.8 mm
Average turn length (l_{avg})	214.3 mm
Copper fill factor (k_f)	55 %
Conductor diameter (d_w)	3.0 mm
Steinmetz par. (k_{SE} , α , β)	5.21, 1.36, 2.78

system (comprised of the selected heat sink and the the fans used for the final system) has been measured in the course of an experiment, in order to ensure that the achieved thermal resistance is sufficiently small. The calculated losses for the boost inductor reveal a slightly higher value of 92 W in case of 1-phase operation compared to 80 W for 3-phase operation, which is due to substantially higher HF copper and core losses. With the additional losses in the DC-link capacitor of 15 W, the estimated total losses for 1-phase operation are 339 W and, with this, approximately 15 % higher than the estimated total losses for 3-phase operation (294 W).² This increase of the losses can be lowered by reducing the DC-link voltage, e.g., to $1/2 \times 750$ V, which is in

²Consideration of the conduction losses of the EMI filter further extends the losses difference between the two operating modes, due to the additional current in the return path.

Tab. 4.5: Estimated losses of the main power components for 3-phase and 1-phase operation.

Parameter	Description	3-phase	1-phase
$P_{M,c}$	MOSFET cond. losses	94.7 W	66.3 W
$P_{M,sw}$	MOSFET switch. losses	119.6 W	101.3 W
$P_{D,c}$	Diode cond. losses	-	71.7 W
$P_{L_1,Cu,LF}$	Boost induct. LF copper losses	8.0 W	5.6 W
$P_{L_1,Cu,HF}$	Boost induct. HF copper losses	2.1 W	2.9 W
$P_{L_1,core}$	Boost induct. core losses	16.5 W	22.1 W
$P_{C_{DC}}$	DC-link cap. losses	-	15 W

principle feasible, because the maximum swing of the input voltage applied to the active bridge-legs of the rectifier reduces from $2 \times \sqrt{2} \times 230 \text{ V} = 650 \text{ V}$ for 3-phase operation to $\sqrt{2} \times 240 \text{ V} = 340 \text{ V}$ for 1-phase operation. However, for this, the system needs to be further extended, which includes two output-side DC/DC converters with galvanic isolation. The respective modifications and possible loss reductions are explained in Appendix B.4.

Figs. 4.6(a) and **Fig. 4.7(a)** depict simulated waveforms for 3-phase and 1-phase operation, respectively. The circuit simulations have been used to verify the component stresses calculated in this Section. It can be seen that the DC-link voltage shows a peak-to-peak voltage ripple of 42 V in 1-phase operation, due to the power pulsation with twice the mains frequency.³

4.4 Generated EMI Noise and Filtering

This Section provides individual analyses of the EMI noise components that occur in case of 3-phase and 1-phase operation. According to the CISPR 16 regulations, the generated EMI noise is measured with a test receiver, using average or Quasi-Peak (QP) detectors, and the noise level is expressed in dB μ V. The circuit models of the detectors are nonlinear systems that include diodes and, as a result, an analytic calculation of the generated noise is hardly possible. Therefore, [128] proposes an approximation, that neglects correlations between individual frequency components. For the defined receiver bandwidth (RBW) of 9 kHz (according to CISPR 16 regulations), the

³In the final EV charger application, the realized AC/DC converter will be connected to a DC/DC converter stage with galvanic isolation, which continuously adapts to the changing DC-link voltage and provides a constant output voltage [127].

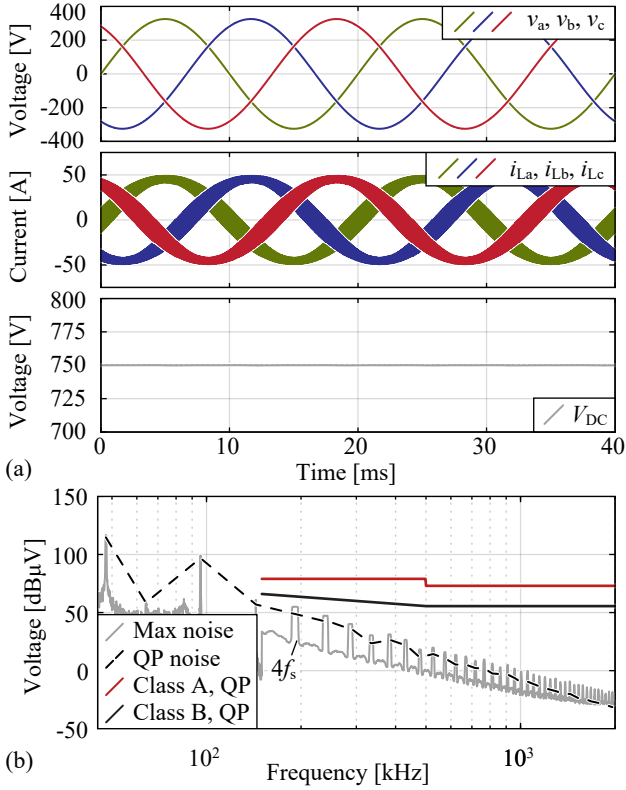


Fig. 4.6: Simulation results for the proposed 22 kW EV charger and/or AC/DC converter specified in Tab. 4.1, with the EMI filter of Fig. 4.2 and the filter component values of Tab. 4.7. (a) Main waveforms and (b) conducted EMI for 3-phase operation.

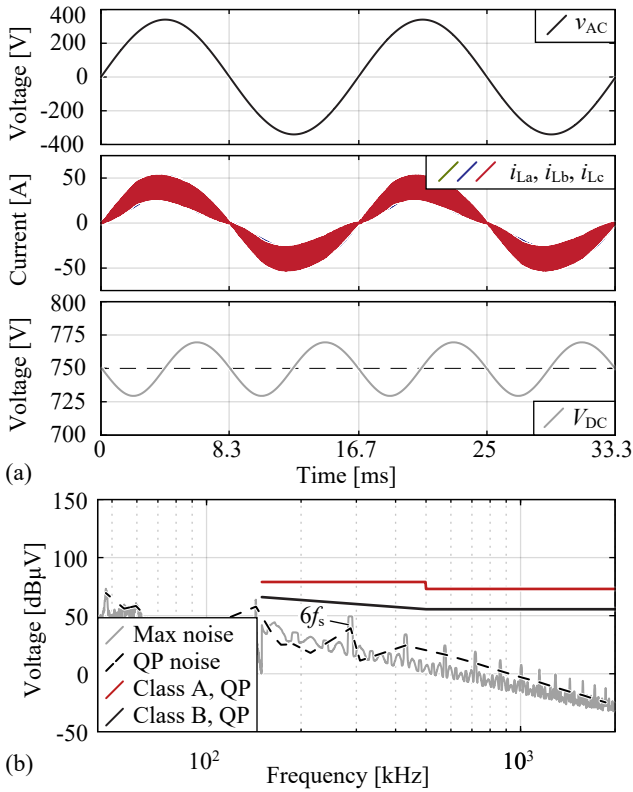


Fig. 4.7: Simulation results for the proposed 19.2 kW EV charger and/or AC/DC converter specified in Tab. 4.1, with the EMI filter of Fig. 4.2 and the filter component values of Tab. 4.7. (a) Main waveforms and (b) conducted EMI for 1-phase operation.

generated noise is determined based on the spectrum of a single mains period and using:

$$\max_{\text{noise}}(f) = 20 \log_{10} \left(\frac{1}{1\mu\text{V}} \sum_{\xi=f-\frac{\text{RBW}}{2}}^{\xi=f+\frac{\text{RBW}}{2}} V_{\text{sim}}(\xi) \right), \quad (4.4)$$

where $V_{\text{sim}}(\xi)$ denotes the spectrum of the simulated voltage at the HF output of the Line Impedance Stabilization Network (LISN), which is terminated with a resistance of 50Ω . This concept, i.e., (4.4), will be employed in the following for both, the DM and the CM component of the EMI noise.

4.4.1 Conducted EMI for 3-Phase Operation

In case of 3-phase operation, the relay contact in Fig. 4.2 is closed. With this, the HF EMI model shown in Fig. 4.8(a) results. The EMI noise source is modeled with one CM source and three DM sources,

$$v_{\text{cm}} = \frac{v_{\text{AO}} + v_{\text{BO}} + v_{\text{CO}}}{3}, \quad v_{\text{dm},i} = v_{i\text{O}} - v_{\text{cm}} \quad \forall i \in \{A,B,C\}. \quad (4.5)$$

Furthermore, Fig. 4.8(a) considers the three parasitic capacitances $C_{\text{par,sw}}$ between the switch-nodes and PE, because these capacitances are found to have a substantial impact on the effective CM attenuation of the EMI filter.⁴

For the design of the DM part of the filter, each stage of the DM filter, k , is considered to achieve an attenuation of

$$\text{Att}_{k,\text{dB}} = 20 \log_{10} (\omega^2 C_k L_k), \quad (4.6)$$

for frequencies much greater than the corner frequency. The dashed red line in Fig. 4.8(a) highlights a path of HF DM EMI noise.

The CM part of the EMI filter is commonly assessed with the equivalent circuit for EMI CM noise depicted in Fig. 4.8(b). The respective derivation of the CM EMI model is conducted in the style of [131, 132]. In a first step, the first filter stage is considered, which is not symmetric, i.e., the inductor $L_1/3$ is only present in the upper vertical path; the lower vertical path of the first filter stage does not contain a filter component. For this reason, the CM

⁴Due to the grounded heat sink, the value of $C_{\text{par,sw}}$ can be approximated by the total surface of the metallic backplates of the low-side MOSFETs and the thickness and the permittivity of the interface material [129, 130], which for two parallel MOSFETs (TO-247 packages) per switch leads to $3C_{\text{par,sw}} = 225 \text{ pF}$.

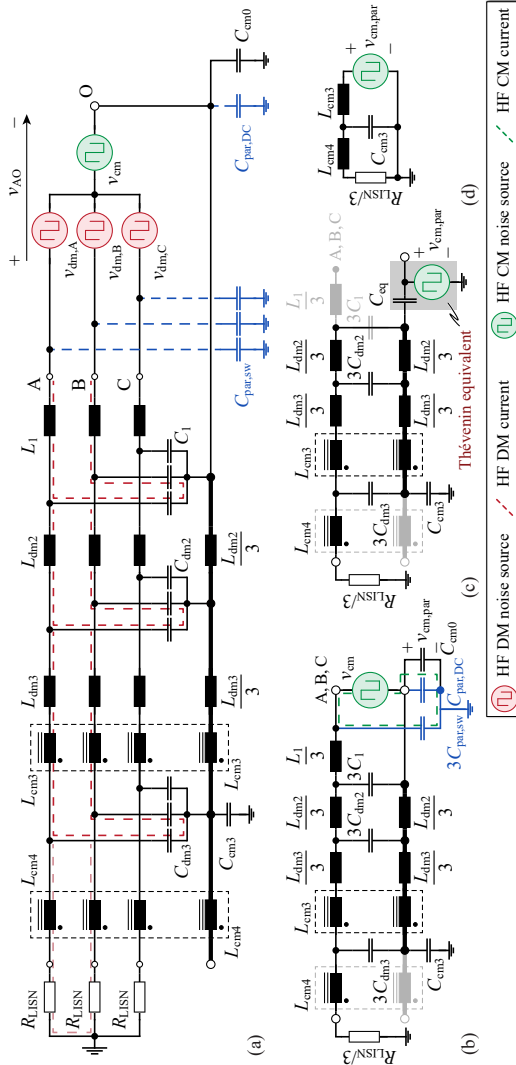


Fig. 4.8: (a) HF equivalent circuit of the 2LB6 converter shown in Fig. 4.2, for 3-phase operation; (b) CM equivalent circuit; (c)-(d) effective CM equivalent circuit, derived in the style of [131, 132].

noise current will prefer the lower path of the first filter stage and $L_1/3$ can be replaced by an open circuit. Furthermore, the capacitance $3C_1$ features a very low impedance for the CM noise current and is approximated by a short circuit. Moreover, the CM noise source can be replaced by its Thévenin equivalent source, cf. **Fig. 4.8(c)**, with

$$C_{\text{eq}} = 3C_{\text{par,sw}} + C_{\text{par,DC}} + C_{\text{cmo}}, \quad (4.7)$$

$$v_{\text{cm,par}} = -v_{\text{cm}} \frac{3C_{\text{par,sw}}}{C_{\text{eq}}}. \quad (4.8)$$

According to (4.7) and (4.8), the effective CM noise voltage, $v_{\text{cm,par}}$, can be decreased by increasing the value of C_{cmo} . However, the impedance between the voltage source $v_{\text{cm,par}}$ and the CM equivalent circuit of the EMI filter decreases for increasing value of C_{cmo} , too. A respective analysis reveals that, due to the high CM impedance of L_{cm_3} in the considered frequency range, $f \in [150 \text{ kHz}, 30 \text{ MHz}]$, even the parasitic capacitances $3C_{\text{par,sw}} + C_{\text{par,DC}}$ feature a sufficiently low impedance such that $C_{\text{eq}}|_{C_{\text{cmo}} \rightarrow 0}$ can be approximated by a short circuit for $f > \approx 400 \text{ kHz}$. Based on this consideration, **Fig. 4.8(c)** can be further simplified to the structure depicted in **Fig. 4.8(d)**, which, together with (4.8), reveals the increase of the CM attenuation for an increasing capacitance of C_{cmo} and highlights the impact of the remaining EMI filter components, L_{cm_3} , C_{cm_3} , and L_{cm_4} , on the CM attenuation of the EMI filter.

4.4.2 Conducted EMI of 1-Phase Operation

The DM equivalent circuit is depicted in **Fig. 4.9(a)**. Due to the interleaved modulation of the three active bridges of the PFC rectifier, ideally, only the multiples of the switching frequency that are equal to $(3k+3)f_s$, $k \in \mathbb{N}_0$, are common to all three phases and appear in the LISN. The remaining HF harmonics circulate between the three phases and, in case of an ideally symmetric filter, do not lead to significant voltages at the LISN.

Without consideration of $C_{\text{par,sw}}$, the equivalent circuit for the filtering of the harmonics with ordinal numbers of $(3k+3)$, $k \in \mathbb{N}_0$, depicted in **Fig. 4.9(b)**, is similar to **Fig. 4.8(b)**, except that the neutral conductor is also connected to the LISN. Due to this reason, the magnetizing inductance of L_{cm_4} is not effective. As a result, only the DM filter components and the stray inductances of L_{cm_3} and L_{cm_4} are effective. The parallel path through C_{cmo} and C_{cm_3} is ineffective, since, in case of a current through C_{cm_3} , also the magnetizing inductances of L_{cm_3} and L_{cm_4} would become effective. The circuit of **Fig. 4.9(b)** serves for the evaluation of DM EMI noise in 1-phase operation.

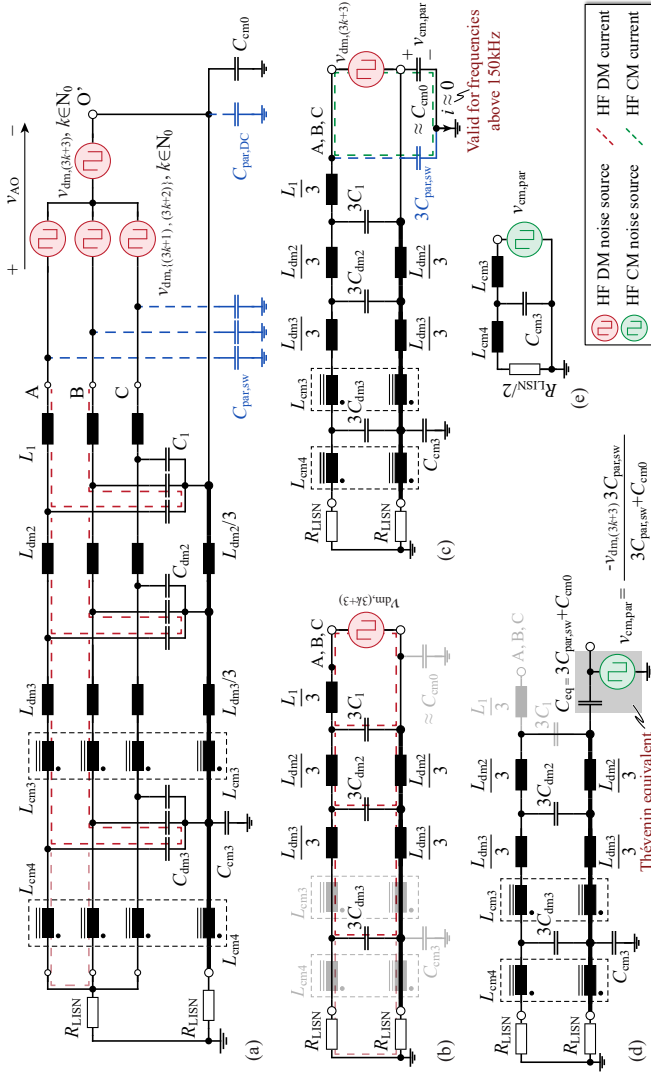


Fig. 4.9: (a) HF equivalent circuit of the 2LB6 converter shown in Fig. 4.2, for 1-phase operation; the conduction paths of the HF current harmonics at $(3k + 1)f_s$ and $(3k + 2)f_s$, $k \in \mathbb{N}_0$, are highlighted; (b) DM 1-phase equivalent circuit considering the HF current harmonics at $(3k + 3)f_s$, $k \in \mathbb{N}_0$; (c)-(e) CM equivalent circuit considering $C_{par,sw} > 0$.

Tab. 4.6: EMI generated noise and filter attenuation.

Source	Operation	CISPR Freq. [kHz]	Max Noise* [dB μ V]	Filter Att.** [dB]	Class B Limit [dB μ V]
$v_{dm,\{A,B,C\}}$	3-phase	192	162	116	
$v_{cm,par}$	3-phase	192	118	71	63.9
$v_{dm,(3k+3)}$	1-phase	288	162.3	150	
$v_{cm,par}$	1-phase	288	126	73	60.3

* Obtained from numerical calculations and (4.4).

** Calculated for the component values listed in Tab. 4.7.

With regard to the CM EMI noise in 1-phase operation, two main sources are identified. First, the LF switching of the mains rectifier diodes causes CM EMI noise, which is greatly reduced by proper placement of C_{cmo} . The second source of CM noise is the effective switched voltage, $v_{dm,(3k+3)}$, $k \in \mathbb{N}_0$, that generates displacement currents through the parasitic capacitances, $C_{par,sw}$. The derivation of the equivalent filter circuit is identical to that of 3-phase operation presented in Sec. 4.4.1, cf. Fig. 4.9(c)–(e), only the load resistance is different, i.e., $R_{LISN}/2$ instead of $R_{LISN}/3$.

4.4.3 Basic Design Guideline for the EMI Filter

The design of the EMI filter is a three-step procedure. In a first step, DM and CM attenuations required for 3-phase and 1-phase operation are determined in order to identify the most critical mode of operation. Thereafter, the number of filter stages for the calculated attenuation is defined. With this information, the components of the EMI filter can be designed in a last step.

For the investigated EMI filter, the number of filter stages for attenuating DM and CM EMI noise has been set to $n_{dm} = 3$ and $n_{cm} = 2$, respectively. These are typical values that are commonly used for PFC rectifiers with similar specifications [133].

According to the discussion presented in Sec. 4.4.1 and 4.4.2, the four networks depicted in Figs. 4.8(a), 4.8(d), 4.9(b), and 4.9(e) need to be considered in order to assess whether 3-phase or 1-phase operation is more critical with respect to the required DM and/or CM attenuation. The noise voltages are calculated for each equivalent circuit, based on (4.4). The spectra of the noise voltages feature envelopes that decrease with a slope of at least -20 dB/dec and each L - C -filter stage of the EMI filter ideally provides an attenuation

that increases with 40 dB/dec in the relevant frequency range. In addition, the specified spectrum of allowable conducted EMI emissions decreases with -20 dB/dec for $150 \text{ kHz} < f < 500 \text{ kHz}$. For these reasons, the first significant spectral component that enters this frequency range is found to be most critical with regard to the required attenuation of the EMI filter (3-phase and 1-phase operation, as well as DM and CM noise, must be considered separately, since different EMI models apply). **Tab. 4.6** lists the obtained relevant spectral components. Since interleaved PWM carriers are used in case of 1-phase operation, the corresponding relevant harmonic components result at 288 kHz instead of 192 kHz. Due to this, and because the levels of the two DM voltage components are nearly equal for 3-phase and 1-phase operation (162 dB μ V vs. 162.3 dB μ V), it is found that 3-phase operation, i.e., the network of Fig. 4.8(a), is decisive for the design of the DM filter, leading to a minimum required attenuation of the DM EMI noise of

$$\begin{aligned} Att_{dm,min,dB}(192 \text{ kHz}) &= \\ &= (162 \text{ dB}\mu\text{V} - 64 \text{ dB}\mu\text{V}) + 18 \text{ dB} = 116 \text{ dB}, \quad (4.9) \end{aligned}$$

The additional safety margin of +18 dB accounts for an approximately 50 % inductance drop of the inductors L_1 and L_{dm3} at peak current, due to the employed magnetic powder cores, i.e., -12 dB of attenuation, plus approximately 6 dB for further component tolerances. With this, a rather conservative safety margin is considered.

A different result is obtained for the CM components, since the CM noise voltage for 3-phase operation is substantially less than for 1-phase operation (118 dB μ V vs. 126 dB μ V). Thus, 1-phase operation, i.e., the network of Fig. 4.9(e), is found to be relevant for the design of the CM filter. Accordingly, the minimum attenuation of the CM EMI noise is

$$\begin{aligned} Att_{cm,min,dB}(288 \text{ kHz}) &= \\ &= (126 \text{ dB}\mu\text{V} - 60 \text{ dB}\mu\text{V}) + 7 \text{ dB} = 73 \text{ dB}, \quad (4.10) \end{aligned}$$

which considers component tolerances.

Furthermore, certain practical aspects are considered in the course of the filter design. In this context, the attenuations of the different filter stages are partitioned such that smaller filter components with improved HF performances, i.e., with self-resonance frequencies that are deep in the MHz range, are located towards the mains. With regard to the DM filter, the attenuations at 192 kHz are set to 67 dB, 25 dB, and 18 dB for the 1st, 2nd, and 3rd filter stage, respectively. With this, a better HF performance of the EMI filter

can be achieved, because a decreased attenuation of a filter stage reduces the required values of inductance and capacitance, which results in smaller components that feature improved HF properties. The final values of the EMI filter components have been optimized to minimize the total volume.⁵ With the capacitances that result from the volume optimization of the DM filter, the total reactive power consumption does not exceed 770 VA (3.5 % of 22 kW) at 50 Hz and this is below the typical limit of 5 % to 10 % of the rated power [134, 135]. With regard to the CM filter, the attenuation of the first filter stage, composed of L_{cm3} and C_{cm3} , is set to 38 dB at 288 kHz and the attenuation of the second filter stage, i.e., L_{cm4} and $R_{LISN}/2$, to 35 dB. With L_{cm4} , the EMI filter features increased CM impedance at the interface to the mains such that the filter effectively attenuates CM noise also in presence of the relatively low effective resistance of the LISN of 16.7 Ω or 25 Ω , cf. [117, 133]. With regard to the CM filter capacitances, two considerations have been taken into account, i.e., the maximum total capacitance to PE, $C_{cm0} + C_{cm1}$, is limited by reason of the maximum allowable touch current and the ratio of C_{cm3}/C_{cm0} has been optimized to achieve maximum CM attenuation for a given value of L_{cm3} . The filter components have been selected such that the EMI regulations are fulfilled and stable operation is achieved without the need of damping networks, to avoid increased costs due to the additional components.

The resulting filter component values are listed in **Tab. 4.7**. As a result of this design approach, the switching frequency is located between the resonance frequencies of stages two and three of the DM filter, cf. Fig. 4.10(a). For this reason, L_{dm2} employs a ferrite N97 core, in order to maintain a constant inductance with respect to the inductor current, to avoid that the resonance frequency of the second stage approaches the switching frequency. The DM filter inductors L_{dm3} and, in the return path, $L_{dm3}/3$ are realized with cores made of iron-powder (KoolMu), to achieve low inductor volumes. The DM filter capacitors are film capacitors that feature low losses at 50 Hz. Nevertheless, their parasitic equivalent series inductance (ESL) can be critical in terms of EMI performance and needs to be considered.

The CM filter chokes employ cores made of nanocrystalline material that features very high permeability. However, the permeability decreases with increasing frequency. For this reason, the permeability at the relevant frequency of 288 kHz has been used to design the CM choke. Furthermore, each CM choke can be subject to local saturation of the core, due to the DM currents, which causes a reduction of the CM inductance for increasing

⁵The final attenuation of stage three is 25 dB, due to the stray inductance of the subsequent CM choke, L_{cm3} .

Tab. 4.7: EV charger: Values of the EMI Filter Components.

Parameter	Description	Value
L_1^*	Inductance of 1 st filter stage	150 μ H
C_1	Capacitance of 1 st filter stage	10 μ F
L_{dm2}	DM filter ind., 2 nd filter stage	3.5 μ H
C_{dm2}	DM filter cap., 2 nd filter stage	3.3 μ F
L_{dm3}^{**}	DM filter ind., 3 rd filter stage	5.5 μ H
C_{dm3}	DM filter cap., 3 rd filter stage	2.2 μ F
L_{cm3}^{***}	CM filter ind., 3 rd filter stage	1.6 mH (1.2 mH)
C_{cm3}	CM filter cap., 3 rd filter stage	20 nF
L_{cm4}^{***}	CM filter ind., 4 th filter stage	1.0 mH (0.75 mH)
C_{cm0}	CM filter cap., DC-side	15 nF
C_{DC}	Capacitor of split DC-link	3.3 mF

* Corresponds to the initially defined theoretical value and to the value considered for the calculated / simulated attenuations
** This results from the series connection of $L_{dm3} = 2.5 \mu$ H with the stray inductance of L_{cm3} , which is equal to 3 μ H (cf. Tab. B.1)
*** The provided value corresponds to 192 kHz and the value in the parenthesis to 288 kHz

power [136]. However, a respective analysis reveals that the total peak flux density in the core, due to CM and DM currents, is only 250 mT, i.e., well below the saturation flux density of the material of 1 T. Accordingly, the designed CM chokes are found to be rather thermally limited by the LF copper losses (only these are relevant, since L_{cm3} and L_{cm4} are subject to relatively low HF excitations) than by the flux density.

The design of the PCB is conducted according to commonly known design guidelines [117, 137, 138]. The position and the orientation of each filter component has been carefully selected to minimize magnetic and/or capacitive couplings. In addition, no copper planes are present below the magnetic components and the input and output terminals of the CM chokes do not overlap.

Tab. 4.6 shows the achieved attenuations for all sources. As expected, the rms value of the noise voltage generated by $v_{dm,(3k+3)}$ (line 3 in Tab. 4.6) is highly attenuated such that the corresponding filtered noise amplitude is well below the regulated limits, which is addressed to the interleaved operation and the additional DM inductors in the return path that are present to provide symmetry (the total boxed volume of these DM inductors is 42 cm³ or 1.2 % of the overall converter volume).

Fig. 4.6(b) and **Fig. 4.7(b)** depict simulated spectra of conducted EMI, which verify the validity of the presented analytic considerations ('max. noise' in Figs. 4.6(b) and 4.7(b) denotes the maximum estimation according to (4.4)). In addition, the absence of frequency multiples equal to $\{3k+1, 3k+2\}$, $k \in \mathbb{N}_0$, in 1-phase operation is depicted.

4.4.4 Experimental Evaluation of the EMI Filter

The transfer function of the ideal DM part of the filter (line-to-neutral), i.e., frequency-independent capacitors and inductors without parasitic components, for 3-phase operation is shown with the dashed line in **Fig. 4.10(a)** for $f \in [1\text{kHz}, 30\text{MHz}]$. In the same figure, the solid black line depicts the transfer function of the filter as calculated with the individually measured impedance characteristics of each component, using the Agilent 4294A impedance analyzer [64]. With this, the impacts of the components' self-parasitics are identified [139], which already have an effect at frequencies as low as 500 kHz. Finally, the solid red curve denotes the transfer function of the assembled EMI filter, measured with the *Bode100* network analyzer (*Omicron Lab* [140]), which reveals a decreased attenuation due to the close placement of the different components (leading to couplings [141]) and additional parasitics introduced by the PCB. The 4-phase CM choke would saturate during the measurement of the filter's DM transfer function, since the measurement is only conducted for a single phase, e.g., phase a in Fig. 4.10(a). In order to avoid this, the windings of phases B and C of $L_{cm,3}$ and $L_{cm,4}$ are shorted together, which, however, increases their effective stray inductances (e.g., by a factor of 1.5 for a symmetrical CM choke, cf. Appendix B.1). The equivalent measured circuit is depicted in **Fig. 4.11(a)**. The input of the measurement device is configured to high-impedance (high-Z), which is a worst-case consideration, since, at the frequency of interest (192 kHz), the last effective component of the measured filter is a capacitor.

According to Fig. 4.10(a), the measured attenuation does not exceed 100 dB in the frequency range from 140 kHz to 3.7 MHz, which is partly addressed to the limitation of the dynamic range of the network analyzer. However, 100 dB marks a very high attenuation; as a consequence, parasitic couplings (capacitive and magnetic) have a strong impact, e.g., as elaborated in [137]. For this reason, the maximum achieved attenuations of EMI filters are typically between 80 dB and 100 dB [142]. Furthermore, implications of parasitic couplings on the attenuation particularly apply to the investigated compact converter, since the components of the EMI filter had to be placed close to each other. Above 4 MHz, the measurement is expected to become decreas-

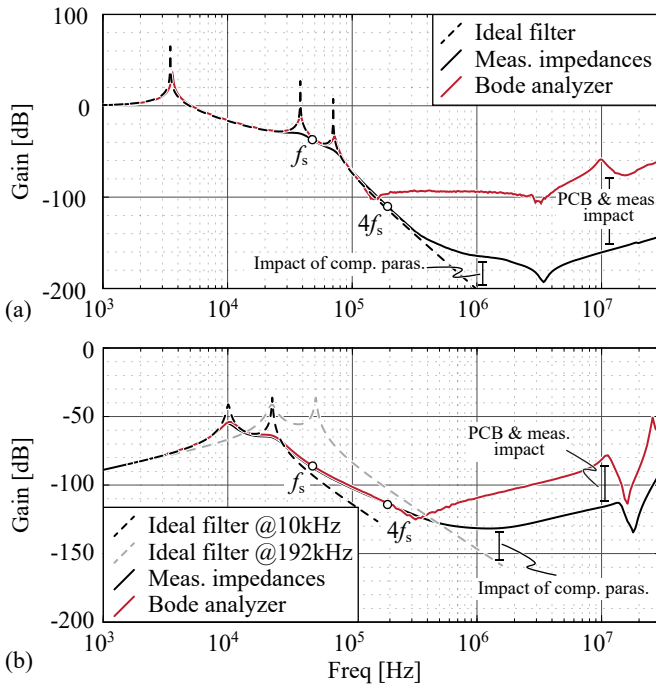


Fig. 4.10: Comparison of (a) DM and (b) CM filter transfer functions: i. calculated for ideal components (dashed lines), ii. calculated based on individually measured impedance characteristics for each filter component (solid black lines), and iii. measured directly on the PCB using the *Bode100* network analyzer from *OmicronLab* (solid red lines).

ingly useful, since the implications of the parasitics of the measurement setup become increasingly pronounced. Hence, an EMI measurement is conducted to verify the performance of the realized filter. Alternatively, EMI behavioral models could be employed [143, 144].

According to the derivation of the CM equivalent circuits presented in Section 4.4, two main conduction paths are present for the EMI CM noise, either through the first filter stage of the EMI filter, $L_1/3-3C_1$, or through the capacitive voltage divider (4.8) that is formed by the parasitic capacitances to the heat sink, $3C_{\text{par,sw}}$. Due to the large values of L_1 and C_1 , cf. Tab. 4.7, the CM EMI noise is found to prefer the path via the parasitic capacitances to the heat sink. For this reason, the transfer function of the CM part of the

EMI filter is measured for the four phases being shorted together (on input and output sides) and with an additional input side capacitive voltage divider realized with ceramic capacitors (230 pF to emulate $C_{\text{par,sw}}$ and 15 nF for C_{cmo} ; $C_{\text{par,DC}}$ is neglected due to $C_{\text{cmo}} \gg C_{\text{par,DC}}$). Since the last component at the output side of the filter, L_{cm4} , is inductive, the output is terminated with an effective load resistance of 25Ω , which denotes the effective resistance of the LISN in case of 1-phase operation,

$$R_{\text{LISN,eff}} = \begin{cases} 1/3 R_{\text{LISN}} & \text{for 3-phase operation,} \\ 1/2 R_{\text{LISN}} & \text{for 1-phase operation,} \end{cases} \quad (4.11)$$

cf. Fig. 4.8(d) and Fig. 4.9(e). The impedances of C_{dm2} , L_{dm2} , and L_{dm3} are comparably small; therefore, the equivalent circuit depicted in **Fig. 4.11(b)** results. Due to the frequency-dependency of the nanocrystalline cores, which are used for the 4-phase CM chokes, the ideal transfer functions consider the values of L_{cm3} and L_{cm4} at two frequencies, i.e., 10 kHz and 192 kHz. At 10 kHz the permeability and, thus, the inductances are five times higher than at 192 kHz. Due to the small capacitance values of $C_{\text{par,sw}}$ and C_{cmo} , decreasing CM attenuation results for $f < 10$ kHz.

Similar to Fig. 4.10(a), the ideal transfer functions (dashed lines) are initially compared to the one calculated based on the components' measured impedances (solid black line). This comparison reveals a difference at 192 kHz, which results from the increased impedance of the real CM chokes, due to increased core losses at this frequency (e.g., the impedance phase angle of L_{cm3} is 35° at 192 kHz). In addition, the resonances at 10 kHz and 23 kHz are well damped due to the core losses of the realized CM chokes. The figure further depicts the measured transfer function of the realized filter (solid red line), which reveals an unmodeled resonance at $f = 320$ kHz that decreases the CM attenuation of the EMI filter by 20 dB at 1 MHz. A further investigation of this resonance reveals that this effect is related to a parasitic capacitive coupling between the components of the 2nd filter stage (L_{dm2} , $C_{\text{dm,2}}$) and L_{cm4} , in combination with the high CM attenuation of more than 120 dB achieved at this frequency (this parasitic coupling capacitance is in the range of 1 pF). Accordingly, it is found that the CM attenuation can be further improved by placing an electrically conductive shielding plate between $C_{\text{dm,2}}$ and L_{cm4} , which is connected to PE.

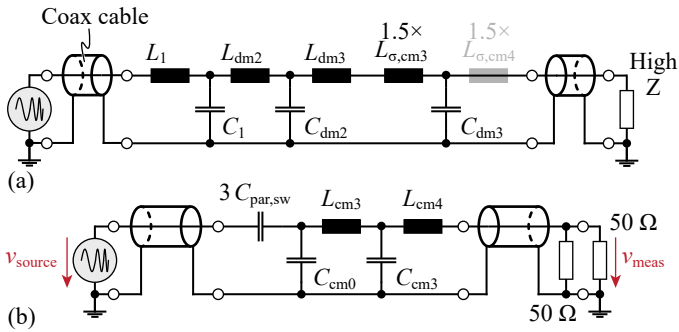


Fig. 4.11: Equivalent filter circuits for the measurements of the (a) DM and (b) CM transfer functions shown in Fig. 4.10(a), (b).

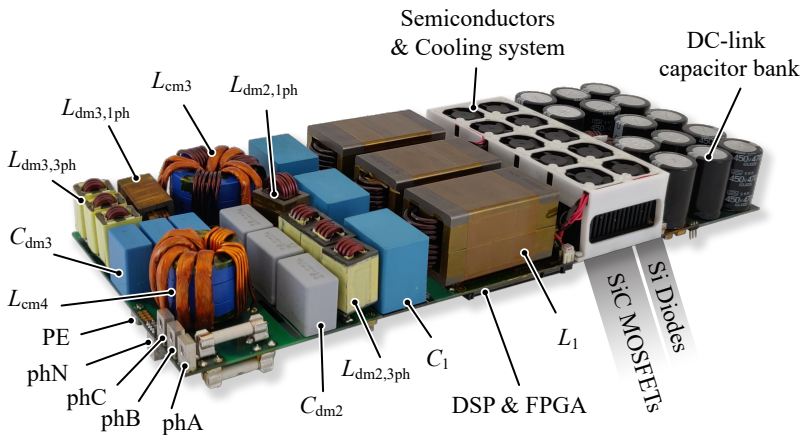


Fig. 4.12: Realized EV charger mains interface designed for a rated power of 22 kW, that allows for rated/full power delivery in both 3-phase and 1-phase operation. The boxed volume of the system is 3.4 dm^3 . The realized hardware has been tested with an output power of 4.5 kW.

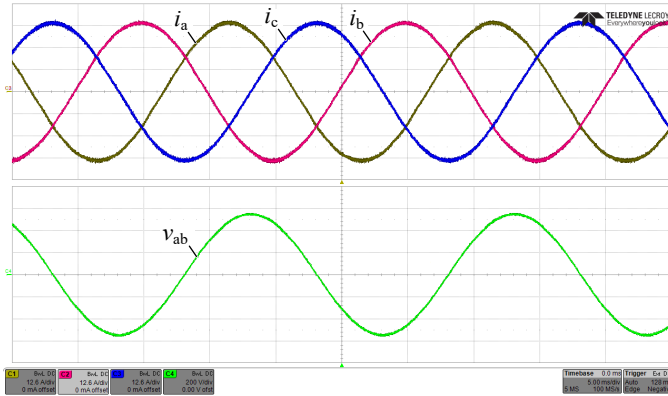


Fig. 4.13: AC waveforms of the three input current, i_a , i_b , i_c , and line-to-line voltage, v_{ab} , in 3-phase inverter operation at 20 kW / 230 V / 50 Hz. The measurement is acquired using the *HDO6104* oscilloscope from *Teledyne Lecroy* [147].

4.5 Experimental Results

Fig. 4.12 depicts the realized hardware, which is designed for a DC-link voltage of 750 V and for output power levels of 22 kW and 19 kW in case of 3-phase and 1-phase operation, respectively. The boxed volume of the hardware is 3.4 dm³. **Fig. 4.13** shows 3-phase operation at 20 kW, which validates the thermal feasibility of the hardware. The measured efficiency at this power level is 97.9 %.

The EMI measurements are conducted with the *ESPI Test Receiver* [145] and *ENV216* single-phase Line Impedance Stabilization Networks (LISN) [146] (one per phase), both manufactured by *Rohde & Schwarz*. The measurements employ the peak detector, which, compared to the QP detector, is much faster and provides a worst-case result of the noise spectrum. The experimental setup is realized according to the guideline presented in [128]. For the measurements, a grounded metal plate has been placed below the hardware, to emulate a hardware enclosure. However, the plate has a minor impact and is only effective in case of 1-phase operation, where the measured noise decreases by ≈ 3 dB for frequencies greater than 20 MHz.

The maximum rms value of the phase current of the employed LISN is 16 A, which limits the power in 1-phase operation to approximately 4 kW. Therefore, in the following, the main findings of this work are verified by measuring the EMI generated by the realized hardware at a power output of 4.5 kW for

both, 3-phase and 1-phase operation (during the 1-phase measurements, the employed LISNs were thermally monitored, to ensure safe operation). Since all parts of the power stage (e.g., SiC MOSFETs, heat sink, inductors, capacitors, PCB tracks) are designed for the full power levels specified in Tab. 4.1 (despite the limited power level of the EMI test), the hardware comprises parasitic components and exhibits the EMI filter attenuation characteristic of a final high power system.

With regard to the HF equivalent circuits depicted in Fig. 4.8 and Fig. 4.9, the generated EMI noise voltages mainly depend on the voltages at the switch-nodes and, therefore, on the DC-link voltage and the modulation index [148]. This has been analyzed in the course of further circuit simulations that have been conducted for two different DC-link voltages (375 V and 750 V), same modulation indices of $M = 0.867$, and same output DC currents of 29.3 A. The resulting DM and CM components are shown in **Fig. 4.14** (grey curve: $V_{DC} = 750$ V; black curve: $V_{DC} = 375$ V). Both, DM and CM characteristics increase by ≈ 6 dB if the DC-link voltage increases by a factor of two. Accordingly, it is important to test the EMI performance of the rectifier at the rated DC-link voltage of 750 V.

In theory, the EMI noise voltages are independent of the output power. However, in a practical system, different implications may disturb this property:

- ▶ The influence of the switched currents on the switching speeds of the employed SiC MOSFETs, in particular during turn-off [149]. With increasing currents, the switching speeds increase and, with this, also the EMI noise in the higher frequency ranges increases. With regard to the setup at hand, a worst-case scenario with constant rise and fall times of 20 ns for all drain-source voltages during switching has been considered. With this, the envelope of the simulated EMI noise spectrum decays with -20 dB/decade for $f < 16$ MHz.
- ▶ The inductors, which are realized with powder cores, feature inductances that decrease with increasing currents. Accordingly, the efficacy of the filter decreases for higher inductor currents [150].
- ▶ The HF current components in the commutation loops depend on the load current and the associated magnetic fields can lead to induced voltages in the EMI filter components that increase the EMI noise.
- ▶ Increased power leads to increased temperatures of the EMI filter components. However, this effect is disregarded, since the resulting tolerances are below 5 %.

The impact of the output power on the EMI noise has been analyzed in the course of further circuit simulations. The simulation considers typical values of the parasitic loop inductances ($40 \text{ nH} \pm 20 \%$) in the three commutations loops of the 2LB6 PFC rectifier to model their impact on the EMI noise. Reverse recovery effects have been disregarded, since these are comparably low in case of SiC MOSFETs [148]. The hardware is realized such that the EMI filter components that are closest to the mains (and, thus, most sensitive to induced voltages) are placed as far away from the switching stage as possible. With this, the implications of voltages induced by the HF magnetic fields generated by the commutation loops on the filtered EMI noise are negligible. As a result, the impact of non-linear filter inductances on the EMI performance remains. The simulation results presented in Fig. 4.14 consider boost inductors that feature the inductance characteristic, $L_1(i)$, which results for the employed powder cores, cf., Tab. 4.4. This figure reveals a slight increase of the DM noise (by less than 2 dB) and a negligible change of the CM noise. Accordingly, only a minor impact of the load current on the EMI performance is expected as, e.g., also shown in Fig. 9 in [151]. Overall, this Section provides a proof of the proposed concept, i.e., the effective attenuation of the generated noise of the proposed topology for same output power in case of 3-phase and 1-phase operation.

4.5.1 3-Phase Operation

Fig. 4.15 shows measured waveforms of v_{ab} and the three phase currents of the converter during 3-phase rectifier operation, at an output power of 4.5 kW and for an rms line-to-neutral voltage of 230 V. The rms current per phase is 6.5 A with a Total Harmonic Distortion (THD) of 3.2%. The waveforms are recorded using the *HDO6104* oscilloscope from *Teledyne Lecroy*. The EMI measurement result for the same operating condition is shown in **Fig. 4.16**. According to this result, the converter successfully complies with the CISPR 11 Class B QP regulations. Furthermore, Fig. 4.16 reveals that the measured EMI noise decreases with approximately -20 dB/dec for increasing frequency.

A direct comparison to the simulated results depicted in Fig. 4.6 reveals increased EMI noise also in the lower frequency range, i.e., for frequencies close to 288 kHz. Furthermore, a steeper decrease would be expected. However, according to Fig. 4.10, the self-parasitics of the components, couplings between components, and the interconnections on the PCB lower the DM and CM attenuations of the EMI filter. In case of the DM characteristic, deviations are already found at frequencies close to 200 kHz, due to the already very high attenuation of 100 dB. In the course of a deeper analysis, the EMI noise

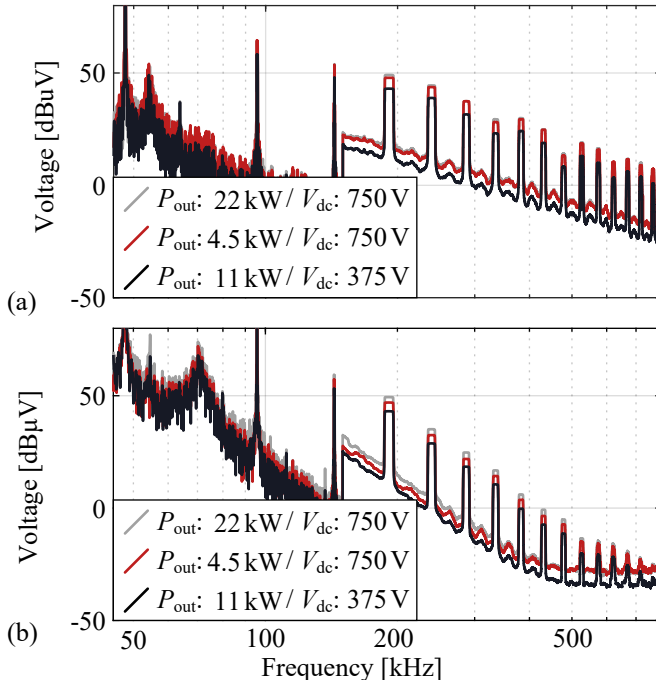


Fig. 4.14: (a) Simulated DM and (b) CM EMI noise components obtained for different operating conditions. The black curve represents rated operation, the red curve refers to the condition during the conducted EMI measurements, and the grey curve represents operation with half of the rated DC-link voltage (which, for same converter currents, implies half of the rated output power).

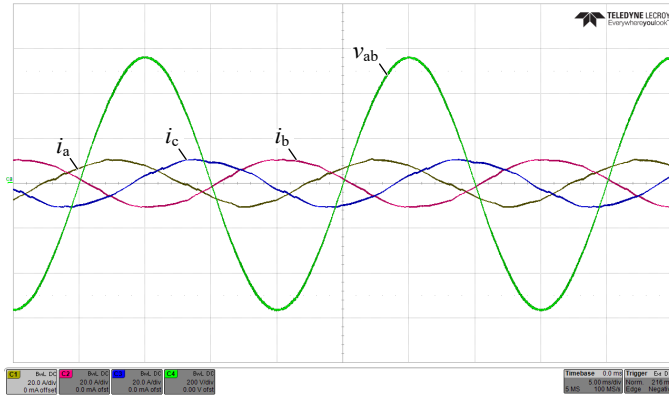


Fig. 4.15: AC waveforms of the three input current, i_a , i_b , i_c , and line-to-line voltage, v_{ab} , in 3-phase operation at 4.5 kW / 230 V / 50 Hz. The measurement is acquired using the *HDO6104* oscilloscope from *Teledyne Lecroy* [147].

envelope has been estimated based on a combination of circuit simulations and measured attenuation characteristics; the grey curve in Fig. 4.16 presents the obtained results. For this, the unfiltered QP EMI noise spectra generated at the switch-nodes (DM and CM) have been estimated with a circuit simulation. Each spectrum is multiplied with the corresponding, i.e., DM or CM, measured filter characteristic, to obtain the DM and CM spectra at the LISNs. Finally, the absolute values of the DM and CM voltage components at the LISN have been added, which estimates the result of the least desirable superposition of the two voltage components (this simplified approach neglects the conversion of DM components into CM components and vice versa). The estimated envelope of the EMI noise confirms the measured increase of the EMI noise, which is found to be mainly related to the deviations between the ideal and the measured attenuation characteristic of the DM part of the EMI filter, that are present for frequencies as low as 200 kHz, cf. Section 4.4.4.

4.5.2 1-Phase Operation

Fig. 4.17 depicts the boost inductor currents of the three phases, together with the switch-node voltage of phase a, during 1-phase operation at 4.5 kW. The magnified view of ten switching periods highlights the interleaved operation of the three currents and the balanced sharing of the LF component of the grid current. The measured total input current (rms value of 18.8 A) and

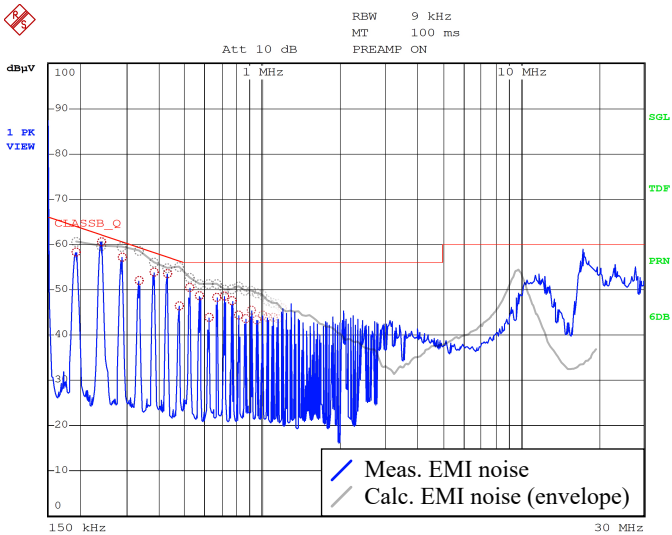


Fig. 4.16: EMI measurement for 3-phase operation at 4.5 kW / 230 V / 50 Hz (cf. Fig. 4.15). The measured noise reveals compliance with the CISPR 11 Class B QP limits. For the measurement a Peak detector is employed that, potentially, overestimates the measured noise compared to a QP detector, nevertheless, is faster. The employed equipment is three *ENV216* single-phase Line Impedance Stabilization Networks (LISN) from *Rohde & Schwarz* (one per phase) and an *ESPI Test Receiver* from the same manufacturer.

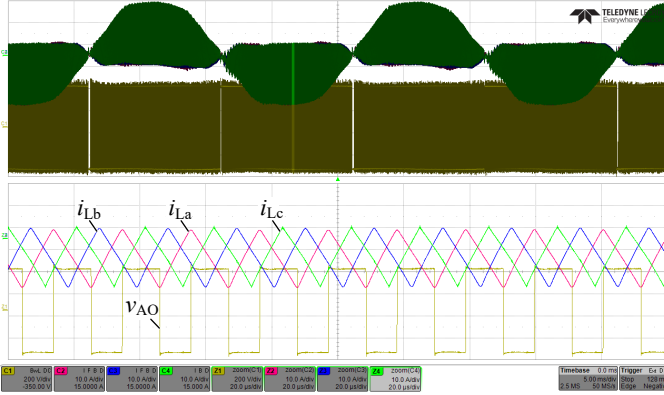


Fig. 4.17: Waveforms of the boost inductor currents, i_{La} , i_{Lb} , i_{Lc} , and the switch-node voltage of phase a, v_{AO} , of the three phases in 1-phase operation at 4.5 kW / 240 V / 50 Hz. The measurement is acquired using the *HDO6104* oscilloscope from *Teledyne Lecroy* [147]. The top part of the figure depicts the envelopes of i_{La} , i_{Lb} , i_{Lc} , and v_{AO} . The marked (brightened) narrow time interval in the middle of the top part refers to the magnified presentation of the waveforms given in the bottom part of this figure.

the phase voltage (rms value of 240 V) are shown in **Fig. 4.18**.⁶ Around the zero-crossings, a LF ringing can be observed in the current, which is attributed to the transition between Continuous Conduction Mode (CCM) and Discontinuous Conduction Mode (DCM). The resulting THD of the current is 6.9 %, which is a typical value for a totem pole configuration at 20 % partial load operation [114, 152, 153] (a reduction of the THD can be achieved with the concepts proposed in [154, 155]). Furthermore, new EV charger designs typically require bidirectional operation; in that case the LF bridge-leg is actively operated, which resolves the aforementioned issue.

In **Fig. 4.19**, the measured EMI noise of the 1-phase operation is shown. Due to the interleaved modulation of the three phases, only multiples of three times the switching frequency are seen, e.g., $6f_s$, $9f_s$. In comparison to the simulated EMI spectra depicted in Fig. 4.7 and Fig. 4.14, a steeper decrease of the EMI noise would be expected. In order to provide further verification, the envelope of the QP EMI noise has been estimated for 1-phase operation using the same procedure that has been applied for 3-phase operation (grey

⁶For the experiment an AC frequency of 50 Hz, instead of 60 Hz, is considered, to allow for a direct comparison of the waveforms obtained for 3-phase and 1-phase operation.

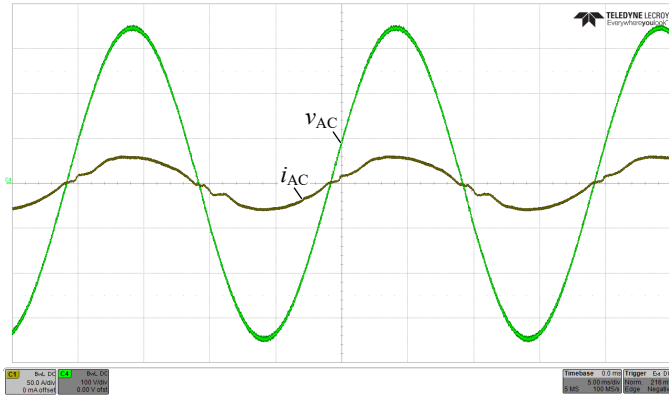


Fig. 4.18: Waveforms of input current, i_{AC} , and the grid voltage, v_{AC} , in 1-phase operation at 4.5 kW / 240 V / 50 Hz. The measurement is acquired using the HDO6104 oscilloscope from Teledyne Lecroy [147].

curve in Fig. 4.19). The estimated envelope predicts similar emissions of the conducted EMI noise up to 3 MHz and reveals that the characteristic of the EMI noise at frequencies below 3 MHz is mainly defined by the characteristic of the DM attenuation of the EMI filter. Compared to the 3-phase operation, the 1-phase operation leads to an increased noise floor, which originates from the displacement currents in the parasitic capacitances between the plus and minus nodes of the DC-link and PE that are due to the DC-side voltage step at every zero-crossing of the mains current, cf. Sec 4.2 and Fig. 4.3. Finally, at 17.8 MHz, a noise peak can be observed, that exceeds the limits by 3 dB. At these frequencies the generated noise is typically linked to CM disturbances. However, corresponding hardware improvements, to ensure compliance in this very high frequency range, would only be reasonable for a final system with a final enclosure.

4.6 Conclusion

The proposed universal 3-phase/1-phase front-end AC/DC converter of a 22 kW EV charger facilitates fast charging in countries providing 3-phase 400 V/32 A or 1-phase 240 V/80 A mains connections. This is expected to enable a more economic production of EV chargers both for on-board and off-board (charging stations) applications for both geographical regions.

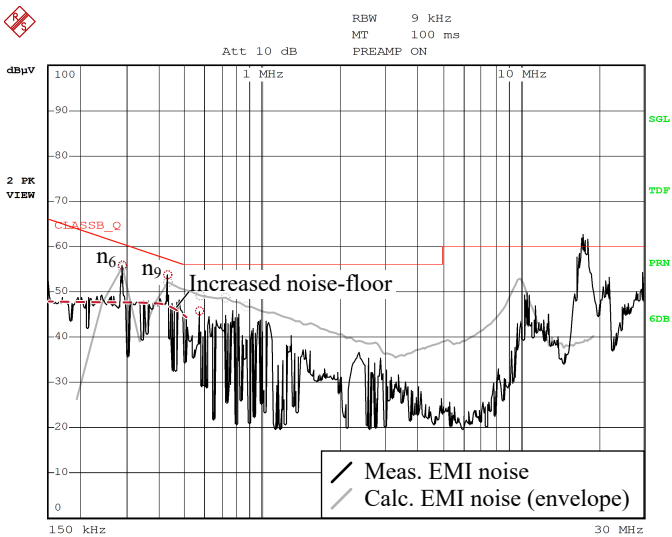


Fig. 4.19: EMI measurement for 1-phase operation at 4.5 kW / 240 V / 50 Hz (cf. Fig. 4.18). The measured noise reveals compliance with the CISPR 11 Class B QP limits. For the measurement a Peak detector is employed that, potentially, overestimates the measured noise compared to a QP detector, nevertheless, is faster. The employed equipment is three *ENV216* single-phase Line Impedance Stabilization Networks (LISN) from *Rohde & Schwarz* (one per phase) and an *ESPI Test Receiver* from the same manufacturer.

For a 3-phase two-level six-switch (2LB6) converter topology, this is achieved with a modified power stage that provides a return path for the current in case of 1-phase operation, through a dedicated return conductor and a diode bridge-leg, and a novel EMI filter structure that features 4-phase Common Mode (CM) chokes, which do not saturate in case of 3-phase or 1-phase operation. The proposed modifications can be directly applied to multilevel 3-phase rectifier topologies that do not require a connection to the DC-link midpoint (e.g., flying capacitor converters). The extension to a three-level T-type converter is outlined in Appendix B.5.

The stresses of the main power components (semiconductors, boost inductor, DC-link capacitors) are analyzed for the 2LB6 topology for 3-phase and 1-phase operation and, based on the results, a design guideline of the power stage is presented. Furthermore, the conducted EMI noise is analyzed and the efficacies of the filter components are discussed for both operating modes, which enables the compilation of a guideline for the design of the EMI filter.

The discussed solution is validated with circuit simulations and a prototype is designed based on common practical considerations for an output power of 22 kW (3-phase operation) and 19 kW (1-phase operation). The boxed volume of the realized prototype is 3.4 dm^3 . Due to the current limitations of the employed LISNs, EMI measurements are conducted at a reduced output power of 4.5 kW, which is justified by the fact that the characteristic of the noise source is mainly defined by the DC-link voltage level and the modulation index, and not the processed current. The measurement results confirm the findings of this work, i.e., the EMI filter complies with CISPR 11 Class B QP regulations under 3-phase and 1-phase operation.

The versatility of the proposed solution comes at an increase of the converter volume from 2.7 dm^3 to 3.4 dm^3 , mostly due to the additional capacitance of the DC-link (plus 0.5 dm^3), but also due to the losses of the diode bridge-leg, hence, a slightly larger cooling system and the increased volume of the EMI filter. In return, the proposed solution features low complexity and the modifications are of low cost.

5

Conclusion and Outlook

The rapidly emerging market of EVs mandates the need of compact, efficient and inexpensive on-board EV chargers. In this regard, the highly invested research field of power semiconductors contributed with the arrival of the Wide-BandGap (WBG), i.e., SiC and GaN switches, that have essentially pushed the performance barriers of power electronic converters even further. This is why, despite their technological youth and their, potentially, increased cost, industry has already started adopting them (e.g., [156]).

Power semiconductors represent the most expensive and lossy component of an EV charger, nevertheless, with such a technological breakthrough magnetic components have turned into the potential bottleneck of the complete system performance, and further research is required in order follow the emerging trend.

In this work, two challenging aspects of EV chargers were examined. First, the optimal operation of power inductors, that are fundamental components of power electronic converters, was investigated with respect to key system parameters. Moreover, promising HF NiZn 67 material from Fair-Rite was measured for frequencies up to 50 MHz, using an innovative new transient calorimetric method. The measurements featured a maximum worst-case uncertainty of 20 %. As a second step, a new concept of a universal EV charger mains interface that allows full power delivery both in a 3-phase and a 1-phase mains and that is EMI compliant for both grids was developed, aiming for a more cost-efficient and simple production line of on-board EV chargers.

5.1 Results of the Thesis

The main achievements of this thesis are summarized in the following. In particular:

PART 1 - Magnetic Components

► **Minimum Loss Operation of Power Inductors**

In a first step, the optimal operation of inductors employed in common topologies, i.e., buck/boost converters, is investigated. During the analysis, all design degrees of freedom are narrowed down to the number of turns; the rest, e.g., core shape, core material, type of coil are considered fixed, in order to minimize the numerous involved implications. The component operation with respect to key system parameters, i.e., the switching frequency and the current ripple is investigated and the optimal region is identified in the proximity of the region where Steinmetz parameters, α , β become equal in value.

The analysis is done in a systematic approach, separated in two steps. First, using simple analytical equations, and, second, using more detailed/accurate semi-numerical models. Compared to a typical brute-force optimization, the followed approach allows for better insight, identification of certain trends, and understanding of critical nonlinearities, e.g., core saturation and impact of DC premagnetization on the core losses.

► **Design Guidelines for Power Inductors**

The losses around the optimal region are found to be substantially flat, with respect to all three considered degrees of freedom. This behavior provides the designer with different opportunities, e.g., improved partial load performance and reduced cost, in the expense of only 15% - 20% increased total losses. According to the above findings, important trends with respect to optimal operation of inductors are identified, and a simple two-equation guideline is provided, that directly leads to quasi-optimal inductor designs, for given core/coil parameters.

► **Transient Calorimetric Measurement of Core Losses**

In the previous analysis, the importance of the accuracy of the employed core data is highlighted, nevertheless, at high frequencies, i.e., > 1 MHz, no reliable method exists, in order to acquire such data. Motivated by that, a novel transient calorimetric measurement method of core losses, whose accuracy is independent of the applied excitation, is proposed. The method is fast and simple to employ. For the method, accurate knowledge of the material's specific heat capacity is required and two methods are proposed, in order to achieve that. The measurement uncertainties, namely:

1. the uncertainty of the calculated core thermal capacitance,
2. the uncertainty of the calculated thermal leakage resistance,
3. the uncertainty of the measured differential temperature,
4. the uncertainty of the time constant of the NTC sensor,
5. the impact of the temperature change on the core losses during the measurement,
6. the error of the time measurement,
7. the impact of the temperature change on the core's thermal capacitance during the measurement,
8. the impact of the temperature change on the leakage thermal resistance during the measurement,
9. the additional heat due to the copper losses,
10. the temperature gradient in the core caused by the non-homogeneous flux density distribution in the radial direction,

are analyzed, including a thorough sensitivity analysis, and confirmed by means of FEM simulations. The practical applicability is verified by direct comparison with a state-of-the-art electrical method, for frequencies up to 750 kHz, where the uncertainty of the electrical method is within reasonable limits. Finally, a simple guideline in order to optimally apply the proposed method is provided.

► **Core Loss Measurements up to 50 MHz**

The proposed method is employed for the measurement of NiZn 67 material from Fair-Rite. The material is measured for frequencies ranging between 5 MHz - 50 MHz and for a temperature of 25 °C. The measurements feature a maximum worst-case uncertainty of approximately 20 %. Based on the measurements, Steinmetz parameters are provided that, compared to the measured values, feature an average error of 4.5 % for frequencies up to 20 MHz. According to the measurements, the material achieves a PF of 210 kHz T at 34 MHz, which highlights its great potentials at high frequencies, e.g., compared to MnZn N87 material from EPCOS-TDK, which achieves a PF of just 32 kHz T at 750 kHz. Nevertheless, exploitation of these potentials is challenging, as will be further discussed in Section 5.2.

► **Universal EV Chargers**

In the second part, a universal topology for a PFC rectifier mains interface of EV chargers is proposed that allows for operation at rated power for both 1-phase and 3-phase mains. The topology connects to LV mains and focuses on the EV charging application. It is based on economical and simple modifications applied on the conventional two-level six-switch (2LB6) 3-phase PFC rectifier, i.e., an additional diode bridge-leg for the return current during 1-phase operation and a novel EMI filter structure that incorporates a 4-phase CM choke. According to the proposed modifications, component over-dimensioning is limited. An extension of the proposed concept to multilevel topologies is introduced, in case increased power density and/or efficiency is desired. The stress on the power components is analyzed for each operation, i.e., 1-phase / 3-phase mains connection, and comprehensive guidelines are proposed.

► **EMI Challenges**

An analysis of the generated conduction EMI is conducted for each operation. The analysis is general and can be further applied to conventional 3-phase and 1-phase topologies. The generated noise is separated into DM and CM components and all different sources, resulting from the two operating modes are discussed. Based on the results, a filter design guideline is presented, together with a final filter design.

► **Hardware Prototype**

A 22 kW hardware prototype is presented that fully confirms the proposed concept, and achieves a power density of 6.4 kW/dm^3 and a peak efficiency of 98.2 % at 15 kW. Compared to a conventional 3-phase topology that limits 1-phase operation to $1/3$ of the rated power, the increase in volume is approximately 0.7 dm^3 (26 %), i.e., from 2.7 dm^3 to 3.4 dm^3 . Out of the total 0.7 dm^3 of additional volume, 0.5 dm^3 is attributed to the additional DC-link capacitance requirement in order to process the inherent power fluctuation with twice the mains frequency occurring in case of 1-phase operation at rated power, hence, is unavoidable. The converter successfully complies with the CISPR 11 Class B QP EMI regulations for operation at 4.5 kW.

5.2 Future Trends and Research Areas

WBG semiconductors unlocked new potentials with respect to operation of power converters in the MHz range, in an effort to achieve unprecedented performances mostly with respect to volumetric/gravimetric power densities. The application of EV chargers could benefit from that, since especially with respect to on-board chargers, the need for efficient, light, and compact converters is essential. In this work, this need was addressed mostly from a magnetics perspective, in an effort to analyze the potentials of magnetic components, and especially inductors. This was done initially based on the optimization of standard technologies, and, moreover, based on the measurements of emerging HF materials (NiZn). During the course of this work many challenges were faced, nevertheless, the basis for some key topics was successfully set, and further research into these topics should follow.

PART 1 - Magnetic Components

► Minimum Loss Operation of Power Inductors

Despite being a fundamental topic, operation of inductors with respect to main system parameters was, to the author's knowledge, never systematically analyzed before in literature. Power inductors represent an essential component of power electronic systems, nevertheless, there is still fundamental knowledge missing. Understanding of inductors is critical for maximizing their performance, especially, in order to be able to follow the new trends set by the evolution of semiconductors. Pushing the performance barriers further using smart design techniques, e.g., distributed air-gaps and optimal conductor placement, improved the performance substantially. However, there is still room for improvement also in more basic design choices.

In a first step, the findings of the presented work can be further generalized to different core shapes, core materials, and types of coil. Moreover, investigation of the impact of an AC modulation and an extension of the analytical solutions in order to take such impact into consideration will be of great importance.

A thorough investigation/comparison between different levels of detail of modeling, e.g., analytical, semi-numerical, numerical, will allow to classify each model with respect to its potentials. A first step towards this direction was conducted in this work, and allowed for a better

understanding of the component nonlinearities, and provided a simple two-equation quasi-optimal design guideline.

Using the results of such work, a sensitivity analysis, with respect to different design parameters, can further broaden the understanding of power inductors and, based on this, push even further the performance barriers. Such parameters can be the geometrical core parameters, the geometrical coil parameters, as well as, main material parameters. This analysis can lead to design modifications, where an insensitive parameter is sacrificed for the benefit of other more sensitive parameters.

As a final extension of the above analysis, the impact of the core shape can be investigated, with respect to the generated core losses, the coil losses, and the heat extracting capabilities and more suitable core shapes can result.

► **Transient Calorimetric Measurement of Core Losses**

The understanding of ferromagnetism and its associated losses is limited, especially, for electrical engineers. In this regard, direct collaboration between power electronics engineers and material scientists is considered essential. A first effort towards this direction was conducted in this work by introducing the DSC into power electronics. Such collaboration may accelerate further understanding of the main loss mechanisms of magnetic cores; and generalized loss models may result.

Nevertheless, currently data-based semi-empirical models correspond to the state-of-the-art, hence, accurate measurement of the generated losses is critical. The proposed transient calorimetric solution overcomes most limitations introduced by the electrical methods, however, there is still room for improvement. Leakage heat can be mitigated by reduction of the core emissivity, e.g., by different colors of the core, and/or by conducting the measurement in vacuum, even though this will introduce challenges for measurements at elevated temperatures. A solution to this could be the continuous excitation of the CUT with a certain flux density in vacuum, for continuous heating of the core, e.g., between 25 °C - 100 °C, and based on the local slope of the temperature, the extraction of the core losses for each temperature value. Comparison between this approach and the initially proposed one would be of great interest.

Since the proposed method, heavily relies on accurate knowledge of the thermal capacitance of the measured core, a reasonable next step is

the measurement of the specific heat capacities of numerous magnetic core materials of interest. Moreover, this can be realized in collaboration with well-known manufacturers of magnetic cores, in an effort to highlight the importance of such data, so as to introduce it in the core material datasheets.

With practice, further challenges will arise, nevertheless, the fundamentals of the proposed method are well defined. Therefore, at this point different further measurements are also an interesting future step. Further application to different materials, as well as, extension to RF core materials is required. Moreover, measurement of core losses under DC premagnetization can be introduced, e.g., using the circuit configuration proposed in [157]. With continuous measurements the interesting irreversible behavior of permivar materials can be analyzed and classified, with respect to the conditions under which such transition takes place. Moreover, the currently not fully understood impact of the core size of the employed NiZn material on the generated losses can also be further investigated.

A potential application of the transient calorimetric method can be the measurement of core losses of unusual magnetic configurations, where the flux density is not clearly imposed. Such configurations can be Inductive Power Transfer (IPT) systems [158] or magnetic shielding of air-core transformers [159].

The proposed measurement method can be also employed, not only for component characterization, but also for the component monitoring. Permanently attached temperature sensors on magnetic components may allow the health monitoring of the material/component, further enhanced with a digital twin. This can be further useful for permivar materials, where such monitoring could identify the irreversible transition of such components which can lead to an increase of the generated losses by up to four times.

As a final point, during the course of the thesis, the PFs of different core materials were measured, including the PF of NiZn 67 from Fair-Rite. Based on this measurements, doubts were raised regarding the common statement that magnetic core materials represent that bottleneck of power electronic systems. NiZn 67 material can operate at 50 MHz (features a performance peak at 34 MHz), however, to the author's knowledge, no publications exist, in which WBG power semiconductors operate optimally at such frequency levels. Moreover, existing control units might not be able to operate robustly at such speeds, as well.

In this regard, a natural next project, based on the presented work, is once adequate data has been acquired, a final design of a NiZn-based boost inductor employed in a conventional converter topology, featuring state-of-the-art WBG semiconductors. Such project can be substantially challenging, e.g., with respect to component coupling for frequencies in the MHz range, hence, further consideration of the design process might be required; nevertheless, a significant insight on the performance benefits and limitations of the further pursuit of HF power electronics can be gained.

PART 2 - Universal EV Charger Mains Interface

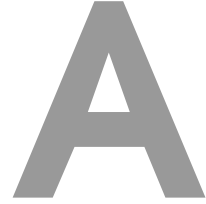
► **Extension to multilevel topologies**

The universal mains interface proposed corresponds to an initial proof of concept. This can be further directly applied to multilevel topologies that do not require a midpoint connection, e.g., flying capacitor converters, and also, based on the proposed modifications to a three-level T-type converter. This can be especially useful, in case increased power density and/or efficiency is required.

► **Further applications**

Moreover, the proposed concept can be extended to different applications where high power (i.e., > 8 kW) is required and access to 3-phase LV mains in the USA is not possible, e.g., medical applications [160] and residential DC distribution systems [161]. Furthermore, inverter applications, e.g., for natural gas power generators [162] or solar panels, can also benefit from such concept. The DC grid concept proposed by *SolarEdge*, features local "Power Optimizers", i.e., MPPT tracking DC/DC converter modules per solar panel [163], and a central high power inverter. Also in that case, the proposed concept could be applied.

Appendices



Transient Calorimetric Measurement of Core Losses

A.1 Derivation of Total Measurement Uncertainty

In this chapter, the resulting expressions of the derivation of the total uncertainty equation employed in Section 3.3.9 are provided.

The solution of the differential equation (3.15) is:

$$T_{\text{core}}(t) = -\frac{T_{\text{amb}}}{P_{\text{core}}\eta P_{\text{core}}R_{\text{unc}} - 1} + \frac{P_{\text{core}}R_{\text{unc}} \left(e^{\frac{(P_{\text{core}}\eta P_{\text{core}}R_{\text{unc}} - 1)t}{R_{\text{unc}}C_{\text{unc}}}} + \eta P_{\text{core}}T_{\text{amb}} - 1 \right)}{P_{\text{core}}\eta P_{\text{core}}R_{\text{unc}} - 1}. \quad (\text{A.1})$$

Solution of the differential equation (3.17), taking solution (A.1) into account (cf. Tab. 3.2):

$$T_{\text{meas}}(t) = \frac{e^{-\frac{t}{\tau_{\text{NTC}}}}}{(P_{\text{core}}\eta_{P_{\text{core}}}R_{\text{unc}} - 1)} \frac{1}{\left[C_{\text{unc}}R_{\text{unc}} + (P_{\text{core}}\eta_{P_{\text{core}}}R_{\text{unc}} - 1) \tau_{\text{NTC}} \right]} \left((P_{\text{core}}\eta_{P_{\text{core}}}R_{\text{unc}} - 1) P_{\text{core}}R_{\text{unc}}\tau_{\text{NTC}} + e^{\frac{t}{\tau_{\text{NTC}}}} \left\{ C_{\text{unc}}P_{\text{core}}R_{\text{unc}}^2 e^{\frac{(P_{\text{core}}\eta_{P_{\text{core}}}R_{\text{unc}} - 1)t}{C_{\text{unc}}R_{\text{unc}}}} + [C_{\text{unc}}R_{\text{unc}} + (P_{\text{core}}\eta_{P_{\text{core}}}R_{\text{unc}} - 1) \tau_{\text{NTC}}] [(\eta_{P_{\text{core}}}T_{\text{amb}} - 1) P_{\text{core}}R_{\text{unc}}\tau_{\text{NTC}} - T_{\text{amb}}] \right\} \right). \quad (\text{A.2})$$

A.2 Derivation of Optimal Measurement Times

It is found that nearly minimum total uncertainty can be achieved with

$$t_{1,\text{opt}} \approx 2\tau_{\text{NTC}}, \quad (\text{A.3})$$

which mainly mitigates the uncertainty that arises from the time constant of the NTC. With regard to the measurement duration, Δt_1 , the evaluation of all sensitivities listed in Tab. 3.2, based on the values given in Tab. 3.1, reveals that $\epsilon_{T_{\text{meas}}}$ and $\eta_{P_{\text{core}}}$ are dominating sources of time-dependent uncertainties.¹ Summation of these two uncertainties and minimization with respect to Δt_1 provides an approximation of $\Delta t_{1,\text{opt}}$,

$$unc_{\Delta t_1}(\Delta t_1) \approx \left| \eta_{P_{\text{core}}} \right| \frac{P_{\text{core}}^2 (\Delta t_1 + 2(t_1 - t_{\text{on}}))}{2 C_{\text{th,core}}} + \left| \epsilon_{T_{\text{meas}}} \right| \frac{C_{\text{th,core}}}{\Delta t_1}, \quad (\text{A.4})$$

$$\frac{\partial unc_{\Delta t_1}(\Delta t_{1,\text{opt}})}{\partial \Delta t_{1,\text{opt}}} = 0 \Rightarrow \Delta t_{1,\text{opt}} = \frac{C_{\text{th,core}}}{P_{\text{core}}} \sqrt{\left| \frac{2\epsilon_{T_{\text{meas}}}}{\eta_{P_{\text{core}}}} \right|}. \quad (\text{A.5})$$

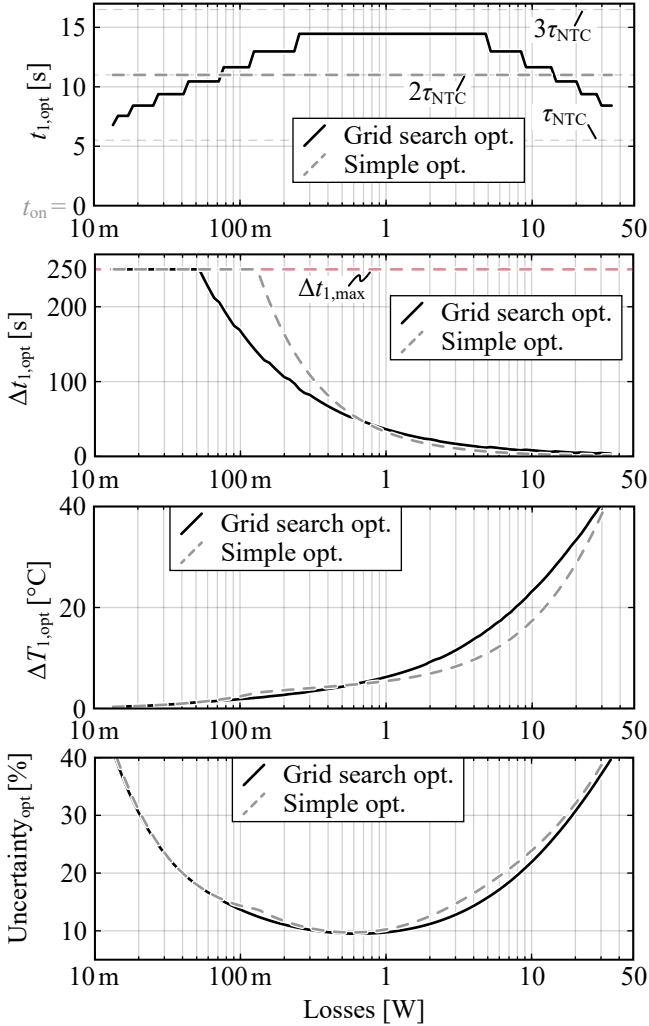


Fig. A.1: Comparison of the results obtained with a numerically expensive grid-search approach and the presented simplification, for the optimal selection of t_1 (A.3) and Δt_1 (A.5) (cf. Fig. 3.3), which is required for the estimation of the measured core losses using (3.6). For the complete range of losses $t_{1,\text{opt}}$ stays within τ_{NTC} and $3\tau_{\text{NTC}}$, hence confirming (3.20). The maximum deviation of the measurement uncertainty between the two approaches is below 14 %.

Fig. A.1 presents a comparison between $t_{1,\text{opt}}$ and $\Delta t_{1,\text{opt}}$ determined with a grid-search and the simplified expressions, for the range of losses considered in Fig. 3.10. The result for the achieved measurement uncertainty reveals an average deviation of less than 14 %. However, long measurement durations at low losses cause a violation of the initial assumption that $\Delta t_1 \ll \tau_{\text{leak}}$ applies. Accordingly, the results for accurate and simplified values of $\Delta t_{1,\text{opt}}$ differ substantially at low losses. Still, the impact on the total error is low, since the resulting uncertainty maps are highly flat at these loss-levels.

¹If the uncertainty due to $\eta_{P_{\text{core}}}$ is excessively greater than the uncertainty arising from $\epsilon_{T_{\text{meas}}}$ at the tested operating point, it is found that the corresponding loss density is very high.

B

Universal 3-Phase / 1-Phase PFC Rectifier System

B.1 Asymmetric Construction of the 4-Phase CM Choke: Implications on Stray Induc- tance

In order to assess the asymmetry of the construction of the CM choke depicted in Fig. 4.4(a), 2D Finite Element Method (FEM) simulations of both constructions are conducted using COMSOL Multiphysics software for the example of L_{cm3} , i.e., 6 turns per phase on three stacked nanocrystalline cores featuring a relative permeability of $\mu_r = 9\,000$, outer and inner diameters of 48.4 mm and 23.9 mm, respectively, and a total height of 36.6 mm. Six different inductances are examined:

1. Three inductances of phase a:
 - (a) For phase b being shorted: $L_{\sigma,a}|_{v_b=0}$
 - (b) For phase c being shorted: $L_{\sigma,a}|_{v_c=0}$
 - (c) For phases b and c being shorted: $L_{\sigma,a}|_{v_b=v_c=0}$
2. Three inductances of phase b for separate and simultaneous short-circuits across phases a and c: $L_{\sigma,b}|_{v_a=0}$, $L_{\sigma,b}|_{v_c=0}$, and $L_{\sigma,b}|_{v_a=v_c=0}$.

Tab. B.1 lists the computed results for a frequency of 192 kHz (this value refers to the EMI noise harmonic with the lowest frequency that is subject to EMI limitations in case of the investigated system) and **Figs. B.1(a)** and **(b)**

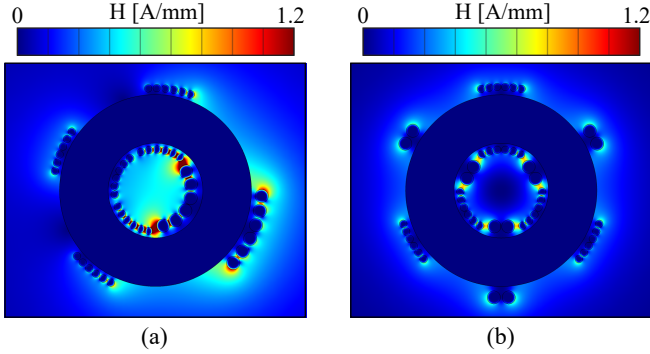


Fig. B.1: 2D FEM simulation of 4-phase CM chokes of the designs depicting the magnetic stray fields of two different constructions of a 4-phase CM choke obtained with 2D FEM simulations for the normalized case $i_a = i_b = i_c = i_n/3 = 1A$: **(a)** asymmetric construction and **(b)** symmetric construction shown in Fig. 4.4(a) and Fig. 4.4(b), respectively.

Tab. B.1: FEM simulated and measured stray inductances.

Constr.	Phase	Condition	Variable	Sim.	Meas.
Fig. 4.4(a)	a	shorted b	$L_{\sigma,a} _{v_b=0}$	3.87 μH	4.41 μH
		shorted c	$L_{\sigma,a} _{v_c=0}$	5.02 μH	6.20 μH
		shorted b, c	$L_{\sigma,a} _{v_b=v_c=0}$	3.40 μH	4.03 μH
	b	shorted a	$L_{\sigma,b} _{v_a=0}$	3.98 μH	4.43 μH
		shorted c	$L_{\sigma,b} _{v_c=0}$	3.98 μH	4.38 μH
		shorted a, c	$L_{\sigma,b} _{v_a=v_c=0}$	2.70 μH	2.95 μH
Fig. 4.4(b)	a	shorted b	$L_{\sigma,a} _{v_b=0}$	4.71 μH	5.86 μH
		shorted c	$L_{\sigma,a} _{v_c=0}$	4.71 μH	6.01 μH
		shorted b, c	$L_{\sigma,a} _{v_b=v_c=0}$	3.53 μH	4.52 μH
	b	shorted a	$L_{\sigma,b} _{v_a=0}$	4.71 μH	6.00 μH
		shorted c	$L_{\sigma,b} _{v_c=0}$	4.71 μH	5.80 μH
		shorted a, c	$L_{\sigma,b} _{v_a=v_c=0}$	3.53 μH	4.40 μH

show the simulated magnetic field strengths. In case of complete symmetry,

$$L_{\sigma,a|v_b=0} = L_{\sigma,a|v_c=0} = L_{\sigma,b|v_a=0} = L_{\sigma,b|v_c=0} = 2L_{\sigma} \quad (\text{B.1})$$

and

$$L_{\sigma,a|v_b=v_c=0} = L_{\sigma,b|v_a=v_c=0} = 1.5L_{\sigma} \quad (\text{B.2})$$

apply. According to the simulation results listed in Tab. B.1, (B.1) and (B.2) hold true for the symmetric construction of Fig. 4.4(b) whereas the asymmetric construction of Fig. 4.4(a) reveals deviations of up to 30 %, which is between $L_{\sigma,a|v_b=0}$ and $L_{\sigma,a|v_c=0}$.

The simulated results are validated with impedance measurements, using a high-precision impedance analyzer Agilent 4294A [64]. The measurement results are consistent with the simulations, with a maximum deviation of 20 %, which is attributed to inaccuracies of the simplified 2D FEM simulations, due to unmodeled effects. The measured inductances of the symmetric construction agree with (B.1) and (B.2) and the measured inductances of the asymmetric construction are subject to a maximum deviation of 41 %. In view of typical component tolerances, this deviation is considered to be of minor relevance, in particular, if dedicated DM filter inductors are connected in series that are reducing the overall asymmetry. However, the asymmetric construction is subject to an increased magnetic stray field, cf. Fig. B.1(a). For this reason, additional shielding may be necessary (even though this was not needed in case of the hardware presented in this work).

B.2 Power Components' Stresses in 3-Phase Operation

In order to enable the calculation of the currents in the different power components for 3-phase operation, the duty cycle functions need to be calculated. The latter are directly related to the mains phase voltages that are applied to the AC port of the rectifier, which, in 3-phase operation, are given with

$$v_{\{a,b,c\}} = \sqrt{2} \times V_{AC,rms} \sin \left(2\pi f_m t + \begin{pmatrix} 0 \\ -120^\circ \\ 120^\circ \end{pmatrix} \right), \quad (\text{B.3})$$

as shown in **Fig. B.2(a)** for a selected phase-to-neutral voltage, e.g., v_a . The calculation of the expressions for the duty cycles is based on two assumptions.

First, it is assumed that the power stage of the rectifier does not generate a LF CM component and, second, that the voltage drops due to EMI filter and boost inductor are negligible at mains frequency. The resulting duty cycle, e.g., for phase a, is calculated according to [164] and

$$d_{3\text{ph,a}}(t) = 0.5 + M \sin(2\pi f_m t), \quad M = \frac{\sqrt{2}V_{\text{AC,rms}}}{V_{\text{DC}}}, \quad (\text{B.4})$$

results, which is shown in **Fig. B.2(b)** (M is the modulation index). According to Tab. 4.1 and (B.4), the duty cycles utilize the range between 13 % and 87 %.

It is to be noted that (B.4) neglects that the input current controller of the PFC rectifier needs to modify the duty cycle of each half-bridge in order to generate a fundamental inductor voltage drop and/or to achieve that every phase current is proportional to the corresponding phase-to-neutral voltage, e.g.,

$$i_a(t) = \sqrt{2}I_{\text{ph,rms}} \sin(2\pi f_m t) \quad (\text{B.5})$$

in case of phase a. Thus, the presented design is limited to $f_s \gg f_m$ where this impact on the duty cycle function is negligible. Expressions (B.4) and (B.5) serve as the basis for the computation of the component stresses, e.g., the rms currents in the semiconductors.

B.2.1 Semiconductors

The shown expressions for the semiconductor losses are based on the assumptions that the current ripple in the boost inductor can be neglected and that the rms currents in all phases are equal. In case of 3-phase operation, the DC-side unfold bridge-leg is unused and only the MOSFETs generate conduction and switching losses. The total conduction losses of all six MOSFETs over a mains period can be calculated with

$$P_{\text{M,c}} = 3I_{\text{ph,rms}}^2 R'_{\text{ds,on}}, \quad R'_{\text{ds,on}} = \frac{R_{\text{ds,on}}}{N_{\text{M}}}. \quad (\text{B.6})$$

In (B.6), $R'_{\text{ds,on}}$ denotes the on-state resistance per switch, i.e., for N_{M} parallel devices. Equation (B.6) yields the conduction losses of the MOSFETs in case of 3-phase and 1-phase operation, since either the low-side or the high-side MOSFET of each bridge conducts the current of the connected boost inductor.

The local switching losses, i.e., the switching losses during one switching period, are calculated based on a second-order polynomial approxima-

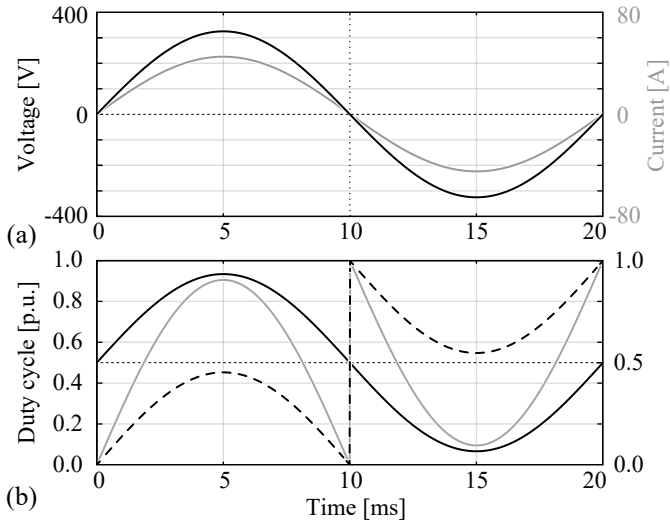


Fig. B.2: (a) Phase-to-neutral voltage (black line) and phase current (gray line) of a selected phase, e.g., phase a, for 3-phase operation. (b) Change of duty cycle over time for three different operating modes: 3-phase operation (solid black line), 1-phase operation and $V_{DC} = 750$ V (dashed line), 1-phase operation and $V_{DC} = 375$ V (solid gray line).

tion [165],

$$e_{M,sw}(t) = k_{A_{chip}} \left(k_{sw,o} + k_{sw,1} \frac{i_a(t)}{k_{A_{chip}}} + k_{sw,2} \left(\frac{i_a(t)}{k_{A_{chip}}} \right)^2 \right), \quad (B.7)$$

where $k_{A_{chip}}$ refers to the ratio of the chip areas of the employed device and the device for which the switching losses have been measured for; $k_{A_{chip}}$ is approximated by the inverse ratio of the corresponding on-state resistances,

$$k_{A_{chip}} = \frac{R_{ds,on}^*}{R_{ds,on}/N_M}. \quad (B.8)$$

There, $R_{ds,on}^*$ denotes the nominal on-state resistance of the device whose switching losses are known.¹ The total switching losses can be approximately calculated from the average energy dissipated within a mains period, $T_m = f_m^{-1}$.

$$P_{M,sw} = f_m E_{M,sw}, \quad E_{M,sw} = \frac{1}{T_m} \int_0^{T_m} e_{M,sw}(t) dt. \quad (B.9)$$

The evaluation of (B.9) leads to the final expression for the switching losses,

$$P_{M,sw} = 3f_s k_{A_{chip}} \left(k_{sw,o} + k_{sw,1} \frac{I_{ph,avg}}{k_{A_{chip}}} + k_{sw,2} \left(\frac{I_{ph,rms}}{k_{A_{chip}}} \right)^2 \right), \quad (B.10)$$

which are calculated with the average absolute value,

$$I_{ph,avg} = I_{ph,rms} \frac{2\sqrt{2}}{\pi}, \quad (B.11)$$

and the rms value of the current in each phase.

B.2.2 Boost inductor

The first step of the design of the boost inductor is the selection of a suitable core. Based on this, the number of turns, N , the wire diameter, d_w , and the losses can be calculated in a second step.

¹In the presented case, this is the C2Moo25120D device (Wolfspeed/Cree). The measured device features $R_{ds,on}^* = 25 \text{ m}\Omega$ and employs a 3-pin TO-247 package. It is of the same generation as the device employed in this work. The switching losses shown in [166] are used in this work.

For defined values of inductance, L_1 , peak flux density in the core, B_{pk} , maximum rms current density in the conductor, J_{rms} , and fill factor, k_f , a suitable core can be found based on the area product, which refers to the minimum required value of the product of core cross-section, A_c , and core window area, A_w [167], of a core,

$$(A_c A_w)_{\min} = \frac{L_1 I_{ph,pk}}{B_{pk}} \frac{I_{ph,rms}}{k_f J_{rms}}. \quad (B.12)$$

However, besides the above mentioned values and $I_{ph,rms}$, also the peak current, $I_{ph,pk}$, is needed to evaluate (B.12). A respective derivation reveals

$$I_{ph,pk} = \begin{cases} \frac{f_s L_1 I_{ph,rms}^2}{M^2 V_{DC}} + \frac{V_{DC}}{8 f_s L_1} & \forall L_1 < L_{lim3p}, \\ \sqrt{2} I_{ph,rms} + \frac{(1 - 4M^2) V_{DC}}{8 f_s L_1} & \forall L_1 \geq L_{lim3p}, \end{cases} \quad (B.13)$$

$$L_{lim3p} = \frac{1}{f_s} \frac{M^2 V_{DC}}{\sqrt{2} I_{ph,rms}}, \quad (B.14)$$

which takes into account that, due to the inductor current ripple, the peak of the total current and the peak of the LF mains current do not necessarily occur at the same time. With known values of A_c and A_w , the number of turns and the diameter of the conductor can be calculated,

$$N = \left\lceil \frac{L_1 I_{ph,pk}}{A_c B_{pk}} \right\rceil, \quad d_w = \sqrt{\frac{4}{\pi} \frac{k_f A_w}{N}}. \quad (B.15)$$

Subsequently, the losses can be calculated. This calculation considers three main loss components: LF and HF conduction losses and HF core losses:

$$P_{L1} = 3 (P_{Cu,LF} + P_{Cu,HF} + P_{core}). \quad (B.16)$$

LF copper losses

The LF copper losses of each boost inductor are calculated with

$$P_{Cu,LF} = I_{ph,rms}^2 R_{L1,DC}, \quad R_{L1,DC} = \frac{N l_{avg}}{\sigma k_f \frac{A_w}{N}}, \quad (B.17)$$

which assumes that the LF rms inductor current and the input rms current of the converter are equal (l_{avg} is the average turn length and σ the conductivity).

HF copper losses

The calculation of the HF copper losses,

$$P_{\text{Cu,HF}} = I_{L_{\text{ph,rms,HF}}}^2 R_{L_{1,\text{AC}}}, \quad (\text{B.18})$$

assumes that all spectral HF current components are concentrated at the switching frequency, i.e., $R_{L_{1,\text{AC}}}$ is the AC resistance of the inductor at the switching frequency and $I_{L_{\text{ph,rms,HF}}}$ is the rms value of all HF components of the inductor current. $I_{L_{\text{ph,rms,HF}}}$ is calculated by averaging the square of the time-dependent local HF rms current, $i_{L_{\text{ph,rms,HF}}}(t)$, over one mains period. The local HF rms current refers to the HF rms current during one switching period and is calculated with the local HF peak current,

$$i_{L_{\text{ph,rms,HF}}}(t) = \frac{i_{L_{\text{ph,pk,HF}}}(t)}{\sqrt{3}}, \quad i_{L_{\text{ph,pk,HF}}}(t) = \frac{1}{2} \frac{V_{\text{DC}}(1-d)}{L_1} \frac{d}{f_s}, \quad (\text{B.19})$$

which can be calculated in a straightforward manner, since the first filter stage does not feature a CM choke and because the capacitors of the first filter stage are connected to the midpoint, O. Based on (B.19), an overall HF rms inductor current of

$$I_{L_{\text{ph,rms,HF}}} = \frac{1}{2\sqrt{3}} \frac{V_{\text{DC}}}{f_s L_1} \sqrt{0.0625 - 0.25M^2 + 0.375M^4} \quad (\text{B.20})$$

results.

The AC resistance is calculated according to [54],

$$R_{L_{1,\text{AC}}} = 2 (F_r + H_{w,\text{norm}}^2 G_r) R_{L_{1,\text{DC}}}, \quad (\text{B.21})$$

where F_r and G_r refer to the scaling factors due to skin and proximity effects;² $H_{w,\text{norm}}$ denotes the magnetic field that leads to the proximity effect and is normalized with respect to the inductor current. For $d_w \geq 32^{\frac{1}{3}}\delta$ [54] (δ is the skin depth),

$$F_r = \frac{d_w}{8\delta}, \quad G_r = \frac{\pi^2 d_w^3}{4\delta}, \quad \delta = \frac{1}{\sqrt{\mu_r \mu_0 \mu_o f_s \sigma \pi}} \quad (\text{B.22})$$

apply, which, for the considered solid copper wire is fulfilled at $f_s = 48$ kHz ($\delta = 0.35$ mm). The value of $H_{w,\text{norm}}$ is calculated under the assumption of a

²The presented factors correspond to values compatible with the peak value of the current. For rms currents, an additional factor of 2 is needed.

distributed air gap on the outer and the inner core limbs (approximation for powder core). With this,

$$H_{w,\text{norm}} = \frac{N}{2\sqrt{3}h_w} \quad (\text{B.23})$$

results.

HF magnetic core losses

The core losses are calculated based on the assumption of a sinusoidal (instead of triangular) shape of the magnetic flux density with same peak value, B_{pk} . Accordingly, the local core losses can be calculated with the Steinmetz Equation,

$$p_{\text{core}}(t) = V_c k_{\text{SE}} f_s^\alpha (B_{\text{pk}}(t))^\beta, \quad B_{\text{pk}}(t) = \frac{L_1 i_{L,\text{ph,pk,HF}}(t)}{NA_c}, \quad (\text{B.24})$$

which is slightly overestimating the core losses that result for triangular currents [50,168]. Due to the raise of the flux density to the power of β , the average core losses are calculated by means of numerical integration,

$$P_{\text{core}} = \frac{2}{T_m} \int_0^{\frac{T_m}{2}} p_{\text{core}}(t) dt. \quad (\text{B.25})$$

B.3 Power Components' Stresses in 1-Phase Operation

Similar to 3-phase operation, the function of the duty cycle needs to be determined before the currents in the different power components can be calculated. According to Fig. 4.3, the mains voltage,

$$v_{\text{AC}} = \sqrt{2} \times 240 \text{ V} \sin(2\pi f_m t), \quad (\text{B.26})$$

is equal to the local average of the voltage between each switch-node (A, B, C in Fig. 4.3) and either the minus terminal of the DC-link, m, if D_2 conducts ($i_{\text{AC}} > 0$) or the plus terminal, p, if D_1 conducts ($i_{\text{AC}} < 0$). The resulting duty cycle for 1-phase operation is equal to

$$d_{\text{1ph}}(t) = \begin{cases} M \sin(2\pi f_m t), & 2\pi f_m t \in [0, \pi), \\ 1 + M \sin(2\pi f_m t), & 2\pi f_m t \in [\pi, 2\pi). \end{cases} \quad (\text{B.27})$$

B.3.1 Semiconductors and boost inductor

The calculation of the MOSFETs' conduction and switching losses and the losses in the boost inductor is identical to Appendix B, however, different expressions apply to $I_{\text{ph,pk}}$ and $I_{L\text{ph,rms,HF}}$,

$$I_{\text{ph,pk}} = \begin{cases} \frac{\left(2\sqrt{2}I_{\text{ph,rms}}f_sL_1 + MV_{\text{DC}}\right)^2}{8f_sL_1M^2V_{\text{DC}}} & \forall L_1 < L_{\text{limp}}, \\ \sqrt{2}I_{\text{ph,rms}} + \frac{(M - M^2)V_{\text{DC}}}{2f_sL_1} & \forall L_1 \geq L_{\text{limp}}, \end{cases} \quad (\text{B.28})$$

$$L_{\text{limp}} = \frac{1}{f_s} \frac{(2M^2 - M)V_{\text{DC}}}{2\sqrt{2}I_{\text{ph,rms}}}. \quad (\text{B.29})$$

$$I_{L\text{ph,rms,HF}} = \frac{1}{12\sqrt{2}\pi} \frac{V_{\text{DC}}M}{f_sL_1} \sqrt{12\pi + M(-64 + 9M\pi)}, \quad (\text{B.30})$$

which are derived for the duty cycle function $d_{\text{ph}}(t)$, instead of $d_{3\text{ph}}(t)$. In addition, the diode bridge-leg generates conduction losses, i.e.,

$$P_{\text{D,c}} = (3I_{\text{ph,rms}})^2 r'_d + 3I_{\text{ph,avg}}V_f, \quad (\text{B.31})$$

where V_f denotes the current independent forward voltage drop of each diode and r'_d refers to the total differential resistance of N_{D} diodes that are operated in parallel,

$$r'_d = \frac{r_d}{N_{\text{D}}}. \quad (\text{B.32})$$

B.3.2 Electrolytic capacitors of the DC-link

The computation of the losses in the electrolytic DC-link capacitors only takes the LF component of the capacitor current into consideration, since ceramic capacitors are located close to the power semiconductors and effectively keep the HF current components away from the electrolytic capacitors. Commonly available electrolytic capacitors cannot provide operating voltages of 750 V. Accordingly, the DC-link employs N_{C} parallel branches of electrolytic capacitors where each branch contains two capacitors that are connected in series. Furthermore, the calculation of the capacitor losses is based on the assumption that each capacitor has the same Equivalent Series Resistance, ESR_{C} . With this, the losses of all electrolytic capacitors are:

$$P_{\text{C,DC}} = I_{\text{C,DC,rms}}^2 \frac{2ESR_{\text{C}}}{N_{\text{C}}}, \quad I_{\text{C,DC,rms}} = \frac{1}{\sqrt{2}} \frac{P_{\text{nom}}}{V_{\text{DC}}}. \quad (\text{B.33})$$

Tab. B.2: Losses in 1-phase operation at half and full DC-link voltage.

V_{DC}	$P_{M,c}$	$P_{M,sw}$	$P_{D,c}$	$P_{L_1,Cu,LF}$	$P_{L_1,Cu,HF}$	$P_{L_1,core}$	$P_{C_{DC}}$
375 V	66 W	38 W	72 W	5.6 W	0.6 W	5.3 W	15 W
750 V	66 W	101 W	72 W	5.6 W	2.9 W	22.1 W	15 W

B.4 Power Components' Stresses in 1-Phase Operation at Half DC-link Voltage

In case of 1-phase operation of the PFC rectifier shown in Fig. 4.2, the DC-link voltage can be reduced, which expectedly leads to lower core losses in the boost inductors and lower switching losses. The reduction of V_{DC} is possible due to the diode bridge-leg that acts as unfold circuit, such that the full DC-link voltage can be utilized to follow the mains voltage during half a mains period [13] (in comparison, the discussed 3-phase PFC rectifier can only utilize half of V_{DC} to follow the mains voltage during half a mains period, as the DC-link voltage midpoint serves as virtual reference point for the AC voltage formation). However, the reduction of the DC-link voltage from $V_{DC} = 750$ V to, e.g., half of this value, imposes the same voltage change to the input of a directly series connected power converter. **Fig. B.3** depicts a solution that prevents supplied converters from being subject to a wide input voltage range. The additional relay circuitry connects the two capacitor banks of the DC-link and two isolated DC/DC converters either in series (3-phase operation) or in parallel (1-phase operation). With this, the same input voltages are applied to the DC/DC converters and the same LF rms currents are achieved in the two DC-link capacitors, C_{DC} , in case of full and half DC-link voltage, $V_{DC} = 750$ V and $V_{DC} = 375$ V, respectively.

The losses of the main power components for 1-phase operation at half DC-link voltage can be calculated with the equations of Appendix B.3. **Tab. B.2** lists the results for 1-phase operation at half and full DC-link voltage, which reveal a substantial reduction of the switching losses and the losses in the boost inductor (due to reduced HF conduction and core losses). This leads to total losses of 226 W, i.e., less than for 3-phase operation, where total losses of 294 W result, cf. Sec. 4.3.2.

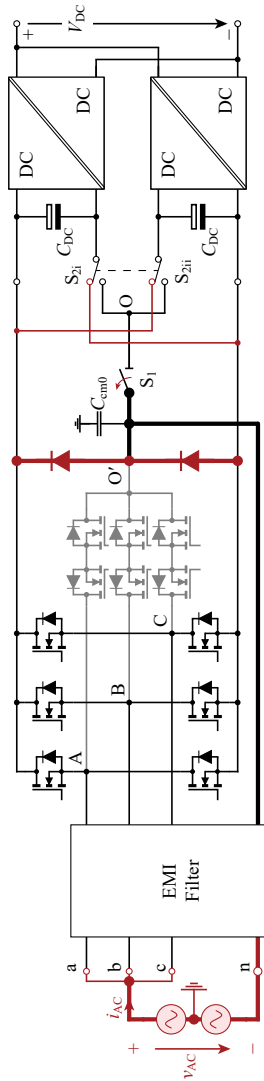


Fig. B.3: Proposed extension of a T-type rectifier, shown for 1-phase operation with $V_{DC} = 375$ V. In case of 3-phase operation, the relay contact S_1 is closed and $S_{2\{i,ii\}}$ change their positions such that the two DC-link capacitors are connected in series and withstand the full DC-link voltage of 750 V.

B.5 Extension to Three-Level Converters with Inherent Utilization of the DC Midpoint

A direct extension of converters with inherent utilization of the DC midpoint (e.g., T-type converter) by a diode bridge-leg according to Fig. 4.2 would lead to very high LF rms currents in the DC-link capacitors in case of three-level operation and 1-phase AC input, because each capacitor of the split DC-link, C_{DC} , would only be charged every second mains half period, i.e., in an alternating manner [169]. A practical solution to mitigate this undesirable property is to change the operating mode of the converter depending on the type of mains supply:

- ▶ Three-level operation for 3-phase mains connection (middle leg enabled, $V_{DC} = 750$ V).
- ▶ Two-level operation for 1-phase AC input (middle leg disabled, $V_{DC} = 375$ V).

In this regard, the DC-link voltage is reduced to 375 V during 1-phase operation in order to achieve similar cores losses (and ripple currents) in the PFC inductors and similar switching losses in both operating modes listed above. The circuit shown in **Fig. B.3**, which realizes the modifications listed below, can be used to achieve constant input voltages for series-connected DC/DC converters:

- ▶ A relay circuit for series/parallel reconfiguration of the DC-link capacitors and the subsequent DC/DC converters is provided.
- ▶ The middle power switches of the T-type converter are connected to the switch-node of the diode rectifier, O' , since the electrical potential of O' is always defined (the node O is floating during 1-phase operation).

With this circuit, the input voltages of the DC/DC converters are equal to 375 V, independent of whether 3-phase or 1-phase operation applies. Furthermore, the LF rms current in each capacitor of the DC-link in 1-phase operation is equal to the one of the 2LB6 converter operating in 1-phase mode (cf. Fig. 4.2).

Bibliography

- [1] IEA, *Global EV Outlook 2020*. Paris, 2020. [Online]. Available: <https://www.iea.org/reports/global-ev-outlook-2020>
- [2] I. T. Forum, *ITF Transport Outlook 2017*, 2017, DOI: 10.1787/9789282108000-en. [Online]. Available: <https://www.oecd-ilibrary.org/content/publication/9789282108000-en>
- [3] “Plugs, socket-outlets, vehicle connectors and vehicle inlets – conductive charging of electric vehicles,” *IEC 62196*, 2004.
- [4] M. C. Falvo, D. Sbordone, I. S. Bayram, and M. Devetsikiotis, “EV charging stations and modes: international standards,” in *Proc. of the International Symposium on Power Electronics, Electrical Drives, Automation and Motion*, Ischia, Italy, June 2014, DOI: 10.1109/SPEEDAM.2014.6872107.
- [5] “A brief history of battery swapping,” (accessed January 05, 2021). [Online]. Available: <https://www.nio.com/blog/brief-history-battery-swapping>
- [6] “Volkswagen lets its charging robots loose,” (accessed December 31, 2020). [Online]. Available: <https://www.volkswagenag.com/en/news/stories/2019/12/volkswagen-lets-its-charging-robots-loose.html>
- [7] “Electric vehicle fast charging challenges,” (accessed January 2, 2021). [Online]. Available: https://www.infineon.com/dgdl/Infineon-Electric_Vehicle_Fast_Charging_Challenges-Article-v01_00-EN.pdf?fileId=5546d462696dbf120169b9f185334b35
- [8] C. Chen, F. Shang, M. Salameh, and M. Krishnamurthy, “Challenges and advancements in fast charging solutions for EVs: a technological review,” in *Proc. of the IEEE Transportation Electrification Conf. and Expo. (ITEC)*, Long Beach, CA, USA, June 2018, DOI: 10.1109/ITEC.2018.8450139.
- [9] “Top 5 challenges of fast charging for electric vehicles,” (accessed December 31, 2020). [Online]. Available: <https://www.ionenergy.co/resources/blogs/fast-charging-for-electric-vehicles/>
- [10] “The challenges of AC and DC charging may be slowing EV adoption,” (accessed December 31, 2020). [Online]. Available: <https://www.allaboutcircuits.com/news/challenges-ac-dc-charging-slowing-electric-vehicle-adoption/>

- [11] “The future of EV charging may be at 50kW, not the ‘Gasoline Thinking’ of 250kW,” (accessed December 31, 2020). [Online]. Available: <https://www.forbes.com/sites/bradtempleton/2020/07/09/the-future-of-ev-charging-may-be-at-50kw-not-the-gasoline-thinking-of-250kw/?sh=203ba8817535>
- [12] E. Paffumi, M. De Gennaro, and G. Martini, “European-wide study on big data for supporting road transport policy,” *Case Studies on Transport Policy*, vol. 6, no. 4, pp. 785–802, 2018, DOI: 10.1016/j.cstp.2018.10.001.
- [13] J. A. Azurza, G. Zulauf, P. Papamanolis, S. Hobi, S. Mirić, and J. W. Kolar, “Three levels are not enough: scaling laws for multilevel converters in AC/DC applications,” *IEEE Trans. Power Electron.*, vol. 36, no. 4, pp. 3967–3986, 2021, DOI: 10.1109/TPEL.2020.3018857.
- [14] T. Friedli, M. Hartmann, and J. W. Kolar, “The essence of three-phase PFC rectifier systems—part II,” *IEEE Trans. Power Electron.*, vol. 29, no. 2, pp. 543–560, 2014, DOI: 10.1109/TPEL.2013.2258472.
- [15] M. K. Ranjram, C. Zhang, and D. J. Perreault, “A two-stage universal input charger with wide output voltage range,” in *Proc. of the IEEE Energy Conversion Congress and Expo. (ECCE USA)*, Oct. 2019, pp. 4685–4692, DOI: 10.1109/ECCE.2019.8913317.
- [16] L. Gu, G. Zulauf, A. Stein, P. A. Kyaw, T. Chen, and J. M. R. Davila, “6.78-MHz wireless power transfer with self-resonant coils at 95% DC–DC efficiency,” *IEEE Trans. Power Electron.*, vol. 36, no. 3, pp. 2456–2460, 2021, DOI: 10.1109/TPEL.2020.3014042.
- [17] J. Xu, L. Gu, Z. Ye, S. Kargarrazi, and J. Rivas-Davila, “Cascode GaN/SiC power device for MHz switching,” in *Proc. of the IEEE Applied Power Electronics Conf. and Expo. (APEC)*, Mar. 2019, DOI: 10.1109/APEC.2019.8721931.
- [18] J. W. Kolar, D. Bortis, and D. Neumayr, “The ideal switch is not enough,” in *Proc. of the 28th IEEE International Symposium on Power Semiconductor Devices and ICs (ISPSD)*, Prague, Czech Republic, 2016, DOI: 10.1109/ISPSD.2016.7520767.
- [19] A. J. Hanson, J. A. Belk, S. Lim, C. R. Sullivan, and D. J. Perreault, “Measurements and performance factor comparisons of magnetic materials at high frequency,” *IEEE Trans. Power Electron.*, vol. 31, no. 11, pp. 7909–7924, 2016, DOI: 10.1109/TPEL.2015.2514084.

-
- [20] “Soft Ferrites and Accessories - Data Handbook 2013 - Ferroxcube,” (accessed Sep. 1, 2020). [Online]. Available: <https://www.ferroxcube.com/en-global/download/download/11>
- [21] R. M. Burkart, “Advanced modeling and multi-objective optimization of power electronic converter systems,” Ph.D. dissertation, ETH Zurich, Zurich, Switzerland, 2016.
- [22] C. P. Steinmetz, “On the law of hysteresis,” *Proc. of the IEEE*, vol. 72, no. 2, pp. 197–221, 1984, DOI: 10.1109/PROC.1984.12842.
- [23] E. C. Snelling, *Soft ferrites, properties and applications*. Butterworths, 2nd edition, 1988.
- [24] S. A. Mulder, “Fit formulae for power loss in ferrites and their use in transformer design,” in *Proc. of the Int. Conf. on Power Conversion and Intelligent Motion (PCIM)*, Nuremberg, Germany, 1993.
- [25] J. Li, T. Abdallah, and C. R. Sullivan, “Improved calculation of core loss with nonsinusoidal waveforms,” in *Proc. of the IEEE Industry Applications Society Annual Conf. (IAS)*, Chicago, IL, USA, Oct. 2001, DOI: 10.1109/IAS.2001.955931.
- [26] K. Venkatachalam, C. R. Sullivan, T. Abdallah, and H. Tacca, “Accurate prediction of ferrite core loss with nonsinusoidal waveforms using only Steinmetz parameters,” in *Proc. of the IEEE Workshop on Computers in Power Electronics*, Mayaguez, Puerto Rico, USA, June 2002, DOI: 10.1109/CIPE.2002.1196712.
- [27] J. Muhlethaler, J. Biela, J. W. Kolar, and A. Ecklebe, “Core losses under the DC bias condition based on Steinmetz parameters,” *IEEE Trans. Power Electron.*, vol. 27, no. 2, pp. 953–963, 2012, DOI: 10.1109/TPEL.2011.2160971.
- [28] Yehui Han, G. Cheung, An Li, C. R. Sullivan, and D. J. Perreault, “Evaluation of magnetic materials for very high frequency power applications,” in *Proc. of the IEEE Power Electronics Specialists Conf. (PESC)*, Rhodes, Greece, June 2008, DOI: 10.1109/PESC.2008.4592628.
- [29] F. Zhu, Q. Li, and F. C. Lee, “Improved partial cancellation method for high frequency core loss measurement,” in *Proc. of the IEEE Applied Power Electronics Conf. and Expo. (APEC)*, Anaheim, CA, USA, March 2019, DOI: 10.1109/APEC.2019.8722221.

- [30] M. Mu, F. C. Lee, Q. Li, D. Gilham, and K. D. T. Ngo, "A high frequency core loss measurement method for arbitrary excitations," in *Proc. of the IEEE Applied Power Electronics Conf. and Expo. (APEC)*, Fort Worth, TX, USA, March 2011, DOI: 10.1109/APEC.2011.5744590.
- [31] T. Kleeb, B. Dombert, S. Araújo, and P. Zacharias, "Loss measurement of magnetic components under real application conditions," in *Proc. of the IEEE European Conference on Power Electronics and Applications (EPE-ECCE Europe)*, Lille, France, Sep. 2013, DOI: 10.1109/EPE.2013.6631895.
- [32] P. Papamanolis, T. Guillod, F. Krismer, and J. W. Kolar, "Minimum loss operation and optimal design of high-frequency inductors for defined core and litz wire," *IEEE Open Journal of Power Electron.*, vol. 1, pp. 469–487, 2020, DOI: 10.1109/OJPEL.2020.3027452.
- [33] P. Papamanolis, T. Guillod, F. Krismer, and J. W. Kolar, "Transient calorimetric measurement of ferrite core losses up to 50MHz," *IEEE Trans. Power Electron.*, vol. 36, no. 3, pp. 2548–2563, 2021, DOI: 10.1109/TPEL.2020.3017043.
- [34] Z. Liu, F. C. Lee, Q. Li, and Y. Yang, "Design of GaN-based MHz totem-pole PFC rectifier," *IEEE Trans. Emerg. Sel. Topics Power Electron.*, vol. 4, no. 3, pp. 799–807, 2016, DOI: 10.1109/JESTPE.2016.2571299.
- [35] Z. Liu, B. Li, F. C. Lee, and Q. Li, "Design of CRM AC/DC converter for very high-frequency high-density WBG-based 6.6kW bidirectional on-board battery charger," in *Proc. of the IEEE Energy Conversion Congress and Expo. (ECCE USA)*, Milwaukee, WI, USA, Feb. 2016, DOI: 10.1109/ECCE.2016.7855024.
- [36] T. M. Undeland, J. Lode, R. Nilssen, W. P. Robbins, and N. Mohan, "A single-pass design method for high-frequency inductors," *IEEE Industry Applications Magazine*, vol. 2, no. 5, pp. 44–51, 1996, DOI: 10.1109/2943.532154.
- [37] M. Bogs and W. Holubarsch, "Design principles for high frequency power transformer materials," *Le J. de Physique IV*, vol. 7, no. C1, pp. 117–118, 1997, DOI: 10.1051/jp4:1997136.
- [38] F. Forest, E. Laboure, T. Meynard, and M. Arab, "Analytic design method based on homothetic shape of magnetic cores for high-frequency transformers," *IEEE Trans. Power Electron.*, vol. 22, no. 5, pp. 2070–2080, 2007, DOI: 10.1109/TPEL.2007.904251.

-
- [39] M. Mogorovic and D. Dujic, "Sensitivity analysis of medium-frequency transformer designs for solid-state transformers," *IEEE Trans. Power Electron.*, vol. 34, no. 9, pp. 8356–8367, 2019, DOI: 10.1109/TPEL.2018.2883390.
- [40] T. Guillod and J. W. Kolar, "Medium-frequency transformer scaling laws: derivation, verification, and critical analysis," *IEEE CPSS Trans. Power Electron. and Appl.*, vol. 5, no. 1, pp. 18–34, 2020, DOI: 10.24295/CPSST-PEA.2020.00003.
- [41] J. Biela and J. W. Kolar, "Pareto-optimal design and performance mapping of telecom rectifier concepts," in *Proc. of the Int. Conf. on Power Conversion and Intelligent Motion (PCIM)*, Nuremberg, Germany, 2010.
- [42] A. Stupar, T. Friedli, J. Miniböck, M. Schweizer, and J. W. Kolar, "Towards a 99% efficient three-phase buck-type PFC rectifier for 400V DC distribution systems," in *Proc. of the IEEE Applied Power Electronics Conf. and Expo. (APEC)*, Fort Worth, TX, USA, March 2011, DOI: 10.1109/APEC.2011.5744644.
- [43] Q. Li, M. A. E. Andersen, and O. C. Thomsen, "Research on power factor correction boost inductor design optimization – efficiency vs. power density," in *Proc. of the IEEE International Conf. on Power Electronics (ICPE - ECCE Asia)*, Jeju, South Korea, June 2011, DOI: 10.1109/ICPE.2011.5944650.
- [44] U. Badstuebner, A. Stupar, and J. W. Kolar, "Sensitivity of telecom dc-dc converter optimization to the level of detail of the system model," in *Proc. of the IEEE Applied Power Electronics Conf. and Expo. (APEC)*, Fort Worth, TX, USA, March 2011, DOI: 10.1109/APEC.2011.5744655.
- [45] J. Muhlethaler, M. Schweizer, R. Blattmann, J. W. Kolar, and A. Ecklebe, "Optimal design of LCL harmonic filters for three-phase PFC rectifiers," *IEEE Trans. Power Electron.*, vol. 28, no. 7, pp. 3114–3125, 2013, DOI: 10.1109/TPEL.2012.2225641.
- [46] A. Stupar, J. A. Taylor, and A. Prodic, "Posynomial models of inductors for optimization of power electronic systems by geometric programming," in *Proc. of the IEEE Workshop on Control and Modeling for Power Electronics (COMPEL)*, Trondheim, Norway, June 2016, DOI: 10.1109/COMPEL.2016.7556660.

- [47] K. Watanabe, F. Campelo, Y. Iijima, K. Kawano, T. Matsuo, T. Mifune, and H. Igarashi, "Optimization of inductors using evolutionary algorithms and its experimental validation," *IEEE Trans. Magn.*, vol. 46, no. 8, pp. 3393–3396, 2010, DOI: 10.1109/TMAG.2010.2044986.
- [48] T. Sato, K. Watanabe, H. Igarashi, T. Matsuo, T. Mifune, K. Kawano, M. Suzuki, Y. Uehara, and A. Furuya, "3-D optimization of ferrite inductor considering hysteresis loss," *IEEE Tans. Magn.*, vol. 49, no. 5, pp. 2129–2132, 2013, DOI: 10.1109/TMAG.2013.2241413.
- [49] K. Booth and J. Bandler, "Space mapping for codesigned magnetics: optimization techniques for high-fidelity multidomain design specifications," *IEEE Power Electronics Magazine*, vol. 7, no. 2, pp. 47–52, 2020, DOI: 10.1109/PEL.2020.2985188.
- [50] J. Leicht, A. Moses, and S. Zurek, "Hysteresis loss component under non-sinusoidal flux waveforms," *Journal of Magnetism and Magnetic Materials*, vol. 320, no. 20, pp. e608 – e610, 2008, DOI: 10.1016/j.jmmm.2008.04.017.
- [51] T. Komma, "Allgemein gültiger Entwurfsalgorithmus für magnetische Komponenten in Schaltnetzteilen mit unterschiedlichen Topologien und Schaltfrequenzen bis 2 MHz (in German)," Ph.D. dissertation, Dresden University of Technology, Dresden, Germany, 2004.
- [52] "EPCOS Data Book 2013 - Ferrites and Accessories," (accessed Sep. 1, 2020). [Online]. Available: <https://www.tdk-electronics.tdk.com/download/519704/069c210d0363d7b4682d9ff22c2ba503/ferrites-and-accessories-db-130501.pdf>
- [53] D. Bortis, D. Neumayr, and J. W. Kolar, " $\eta\rho$ -Pareto optimization and comparative evaluation of inverter concepts considered for the GOOGLE Little Box Challenge," in *Proc. of the IEEE Workshop on Control and Modeling for Power Electronics (COMPEL)*, Trondheim, Norway, June 2016, DOI: 10.1109/COMPEL.2016.7556767.
- [54] M. Leibl, "Three-phase PFC rectifier and high-voltage generator for X-ray systems," Ph.D. dissertation, ETH Zurich, Zurich, Switzerland, 2017.
- [55] R. Hotopp, *Private Photovoltaik-Stromerzeugungsanlagen im Netzparallelbetrieb: Planung, Errichtung, Betrieb, Wirtschaftlichkeit, Fachberatung regenerativer Energien.* (in German). RWE Energie, 1991.

- [56] V. C. Valchev and A. Van den Bossche, *Inductors and Transformers for Power Electronics*. CRC Press, 2005, DOI: 10.1201/9781420027280.
- [57] W. G. Hurley and W. H. Wölfle, *Transformers and Inductors for Power Electronics: Theory, Design and Applications*. John Wiley & Sons Inc., 2013, DOI: 10.1002/9781118544648.
- [58] “MATLAB v. 9.5.” (MathWorks Inc, Natick Massachusetts, United States). [Online]. Available: <https://www.mathworks.com>
- [59] M. Mu, Q. Li, D. J. Gilham, F. C. Lee, and K. D. T. Ngo, “New core loss measurement method for high-frequency magnetic materials,” *IEEE Trans. Power Electron.*, vol. 29, no. 8, pp. 4374–4381, 2014, DOI: 10.1109/TPEL.2013.2286830.
- [60] J. Ferreira, “Analytical computation of AC resistance of round and rectangular litz wire windings,” *IEE Proc. B – Electric Power Applications*, vol. 139, no. 1, p. 21, 1992, DOI: 10.1049/ip-b.1992.0003.
- [61] M. Antivachis, D. Wu, D. Bortis, and J. W. Kolar, “Analysis of double-bridge inverters for drive systems with open-end winding motors,” *IEEE Trans. Emerg. Sel. Topics Power Electron. - Early Access*, 2020, DOI: 10.1109/JESTPE.2020.3017085.
- [62] M. Antivachis, J. A. Anderson, D. Bortis, and J. W. Kolar, “Analysis of a synergetically controlled two-stage three-phase DC/AC buck-boost converter,” *IEEE CPSS Trans. Power Electron. and Appl.*, vol. 5, no. 1, pp. 34–53, 2020, DOI: 10.24295/CPSSTPEA.2020.00004.
- [63] R. Burkart and J. W. Kolar, “Component cost models for multi-objective optimizations of switched-mode power converters,” in *Proc. of the IEEE Energy Conversion Congress and Expo. (ECCE USA)*, Denver, CO, USA, Sep. 2013, DOI: 10.1109/ECCE.2013.6646971.
- [64] “Agilent 4294A - Precision Impedance Analyzer 40Hz to 110MHz.” (accessed Oct. 16, 2020). [Online]. Available: <http://literature.cdn.keysight.com/litweb/pdf/5968-3808E.pdf>
- [65] P. Papamanolis, F. Krismer, and J. W. Kolar, “Minimum loss operation of high-frequency inductors,” in *Proc. of the IEEE Applied Power Electronics Conf. and Expo. (APEC)*, San Antonio, TX, USA, March 2018, DOI: 10.1109/APEC.2018.8341255.

- [66] “Power Resistor, for Mounting onto a Heatshink Thick Film Technology,” (accessed Oct. 16, 2020). [Online]. Available: <https://www.vishay.com/docs/50006/rch.pdf>
- [67] “Fluke 233 Remote Display Digital Multimeter,” (accessed Oct. 16, 2020). [Online]. Available: <https://www.fluke.com/en/product/electrical-testing/digital-multimeters/fluke-233>
- [68] “Fluke 175 True-RMS Digital Multimeter,” (accessed Oct. 16, 2020). [Online]. Available: <https://www.fluke.com/en/product/electrical-testing/digital-multimeters/fluke-175>
- [69] B. Carsten, “Waveforms for stimulating magnetic cores,” *Presentation at the PSMA Magnetics Committee / IEEE PELS High Frequency Magnetics Workshop*, March 2017.
- [70] V. J. Thottuvelil, T. G. Wilson, and H. A. Owen, “High-frequency measurement techniques for magnetic cores,” in *Proc. of the IEEE Power Electronics Specialists Conf. (PESC)*, Toulouse, France, June 1985, DOI: 10.1109/PESC.1985.7070975.
- [71] B. Carsten, “Fast, accurate measurement of core loss at high frequencies,” in *Proc. of the Int. Conf. on Power Conversion and Intelligent Motion (PCIM)*, Nuremberg, Germany, March 1986.
- [72] J. Zhang, G. Skutt, and F. C. Lee, “Some practical issues related to core loss measurement using impedance analyzer approach,” in *Proc. of the IEEE Applied Power Electronics Conf. and Expo. (APEC)*, Dallas, TX, USA, March 1995, DOI: 10.1109/APEC.1995.469075.
- [73] Z. Daming, S. Birlasekaran, S. T. Tang, and H. P. Cheng, “Ferrite core loss measurement with arbitrary wave excitation,” in *Proc. of the IEEE International Conf. on Power System Technology (PowerCon)*, Singapore, Nov. 2004, DOI: 10.1109/ICPST.2004.1460058.
- [74] C. R. Sullivan, “Survey of core loss test methods,” (accessed Oct. 16, 2020). [Online]. Available: <http://sites.dartmouth.edu/power-magnetics/files/2017/03/Survey-of-Core-Loss-Test-Methods-Sullivan.pdf>
- [75] D. Hou, M. Mu, F. C. Lee, and Q. Li, “New high-frequency core loss measurement method with partial cancellation concept,” *IEEE Trans. Power Electron.*, vol. 32, no. 4, pp. 2987–2994, 2017, DOI: 10.1109/TPEL.2016.2573273.

- [76] C. Xiao, G. Chen, and W. G. H. Odendaal, "Overview of power loss measurement techniques in power electronics systems," *IEEE Trans. Ind. Appl.*, vol. 43, no. 3, pp. 657–664, 2007, DOI: 10.1109/TIA.2007.895730.
- [77] D. Rothmund, D. Bortis, and J. W. Kolar, "Accurate transient calorimetric measurement of soft-switching losses of 10-kV SiC MOSFETs and diodes," *IEEE Trans. Power Electron.*, vol. 33, no. 6, pp. 5240–5250, 2018, DOI: 10.1109/TPEL.2017.2729892.
- [78] J. K. Bowman, R. F. Cascio, M. P. Sayani, and T. G. Wilson, "A calorimetric method for measurement of total loss in a power transformer," in *Proc. of the IEEE Power Electronics Specialists Conf. (PESC)*, Cambridge, MA, USA, June 1991, DOI: 10.1109/PESC.1991.162742.
- [79] T. Komma and H. Gueldner, "A method of determining core losses caused by a DC flux-density bias," in *Proc. of the Int. Conf. on Power Conversion and Intelligent Motion (PCIM)*, Nuremberg, Germany, May 2002.
- [80] V. Loyau, M. LoBue, and F. Mazaleyrat, "Comparison of losses measurement in a ferrite with two calorimetric methods," *IEEE Trans. Magn.*, vol. 46, no. 2, pp. 529–531, 2010, DOI: 10.1109/TMAG.2009.2032860.
- [81] A. Savitzky and M. J. E. Golay, "Smoothing and Differentiation of Data by Simplified Least Squares Procedures," *Analytical Chemistry*, vol. 36, no. 8, p. 1627–1639, 1964, DOI: 10.1021/ac60214a047.
- [82] "PS104J2 - PS Series," (accessed Oct. 16, 2020). [Online]. Available: <https://www.littelfuse.com/products/temperature-sensors/lead-thermistors/interchangeable-thermistors/standard-precision-ps/ps104j2.aspx>
- [83] "High-Resolution Science Grade LWIR Camera - FLIR A655sc," (accessed Oct. 08, 2019). [Online]. Available: <https://www.flir.com/products/a655sc/>
- [84] G. W. H. Höhne, W. F. Hemminger, and H.-J. Flammersheim, *Differential Scanning Calorimetry*. Springer, 2003, DOI: 10.1007/978-3-662-03302-9.
- [85] "DSC 2500 - Discovery DSC Series," (accessed Nov. 12, 2019). [Online]. Available: <https://www.tainstruments.com/dsc-2500/>

- [86] M. Kostryukova, "Specific heat of nickel-zinc system ferrites in the low-temperature region," *Journal of Experimental and Theoretical Physics*, vol. 40, no. 6, pp. 1638–1643, 1961.
- [87] N. W. Grimes, "On the specific heat of compounds with spinel structure," in *Proc. of the Royal Society of London. Series A, Mathematical and Physical Sciences*, London, UK, June 1974, DOI: 10.1098/rspa.1974.0082.
- [88] S. Ziemniak, L. Anovitz, R. Castelli, and W. Porter, "Magnetic contribution to heat capacity and entropy of nickel ferrite (NiFe_2O_4)," *Journal of Physics and Chemistry of Solids*, vol. 68, no. 1, pp. 10 – 21, 2007, DOI: 10.1016/j.jpcs.2006.07.015.
- [89] D. Neumayr, D. Bortis, J. W. Kolar, S. Hoffmann, and E. Hoene, "Origin and quantification of increased core loss in MnZn ferrite plates of a multi-gap inductor," *IEEE CPSS Trans. Power Electron. and Appl.*, vol. 4, no. 1, pp. 72–93, 2019, DOI: 10.24295/CPSSTPEA.2019.00008.
- [90] "NTC Thermistors | Epoxy Type," (accessed Oct. 16, 2020). [Online]. Available: <https://amphenol-sensors.com/en/thermetrics/ntc-thermistors/epoxy/3334-type-65?highlight=WyJtYzY1Il0=>
- [91] "Keysight Technologies - 34410A and 34411A Multimeters," (accessed Oct. 16, 2020). [Online]. Available: <https://www.keysight.com/us/en/assets/7018-01326/data-sheets/5989-3738.pdf>
- [92] "SIFERRIT material N49," (accessed Oct. 16, 2020). [Online]. Available: <https://www.tdk-electronics.tdk.com/download/528856/cf394eea3fae828c345f46dc297b76ab/pdf-n49.pdf>
- [93] T. Guillod, F. Krismer, and J. W. Kolar, "Magnetic equivalent circuit of MF transformers: modeling and parameter uncertainties," *Springer Nature, Electrical Engineering*, vol. 100, no. 4, pp. 2261–2275, 2018, DOI: 10.1007/s00202-018-0701-0.
- [94] "COMSOL Multiphysics® v. 5.4." (COMSOL AB, Stockholm, Sweden). [Online]. Available: www.comsol.com
- [95] "Ferrite Magnetic Design Tool," (accessed Jan. 13, 2020). [Online]. Available: <https://www.tdk-electronics.tdk.com/en/180490/design-support/design-tools/ferrite-magnetic-design-tool>
- [96] "67 Material Data Sheet," (accessed Oct. 16, 2020). [Online]. Available: <https://www.fair-rite.com/67-material-data-sheet/>

- [97] M. Gopal, *Control Systems: Principles and Design*. McGraw-Hill Education, India, 2002.
- [98] “HDO4054A,” (accessed Oct. 16, 2020). [Online]. Available: <https://teledynelecroy.com/oscilloscope/hdo4000a-high-definition-oscilloscopes/hdo4054a>
- [99] “Arbitrary Waveform Generators - WaveStation 2052,” (accessed Oct. 16, 2020). [Online]. Available: <https://teledynelecroy.com/wavestation/detail.aspx?modelid=6865&capid=131&mid=1043>
- [100] “150A100D,” (accessed Oct. 16, 2020). [Online]. Available: <https://www.arworld.us/post/150A100D.pdf>
- [101] “Types MC and MCN Multilayer RF Capacitors,” (accessed Oct. 16, 2020). [Online]. Available: <https://www.cde.com/resources/catalogs/MC.pdf>
- [102] J. de Lau, “Influence of chemical composition and microstructure on high-frequency properties of Ni-Zn-Co ferrites,” Ph.D. dissertation, Technische Hogeschool Eindhoven, Eindhoven, Netherlands, 1975, DOI: 10.6100/IR73051.
- [103] “SAE surface vehicle recommended practice J1772, SAE electric vehicle conductive charge coupler,” *SAE J1772*, 2009.
- [104] R. Byczek, “EVSE testing and global certifications – what manufacturers need to know,” (accessed August 17, 2021). [Online]. Available: <https://www.intertek.com/blog/2020-10-02-evse/>
- [105] “RFM - Power Tablet™ 3-Phase AC to 48V converter,” (accessed October 30, 2018). [Online]. Available: <http://www.vicorpower.com/industries-computing/RFM.html>
- [106] J. Schmenger, S. Endres, S. Zeltner, and M. März, “A 22 kW on-board charger for automotive applications based on a modular design,” in *Proc. of the IEEE Conf. on Energy Conversion (CENCON)*, Johor Bahru, Malaysia, Oct. 2014, DOI: 10.1109/CENCON.2014.6967467.
- [107] J. Lu, K. Bai, A. R. Taylor, G. Liu, A. Brown, P. M. Johnson, and M. McAmmond, “A modular-designed three-phase high-efficiency high-power-density EV battery charger using dual/triple-phase-shift control,” *IEEE Trans. Power Electron.*, vol. 33, no. 9, pp. 8091–8100, 2018, DOI: 10.1109/TPEL.2017.2769661.

- [108] K. Yoo, K. Kim, and J. Lee, "Single- and three-phase PHEV onboard battery charger using small link capacitor," *IEEE Trans. on Ind. Electron.*, vol. 60, no. 8, pp. 3136–3144, 2013, DOI: 10.1109/TIE.2012.2202361.
- [109] X. Wang, C. Jiang, B. Lei, H. Teng, H. K. Bai, and J. L. Kirtley, "Power-loss analysis and efficiency maximization of a silicon-carbide MOSFET-based three-phase 10-kW bidirectional EV charger using variable-DC-bus control," *IEEE J. Emerg. Sel. Topics Power Electron.*, vol. 4, no. 3, pp. 880–892, 2016, DOI: 10.1109/JESTPE.2016.2575921.
- [110] H. Zhao, Y. Shen, W. Ying, S. S. Ghosh, M. R. Ahmed, and T. Long, "A single- and three-phase grid compatible converter for electric vehicle on-board chargers," *IEEE Trans. Power Electron.*, vol. 35, no. 7, pp. 7545–7562, 2020, DOI: 10.1109/TPEL.2019.2956653.
- [111] BRUSA Elektronik AG, "NLG664 - On Board Fast Charger," in *NLG664 Datasheet*, May 2018.
- [112] K. Stengert, "On-board 22 kW fast charger 'NLG6'," in *Proc. of the World Electric Vehicle Symposium and Exhibition (EVS27)*, Barcelona, Spain, Nov. 2013, DOI: 10.1109/EVS.2013.6914854.
- [113] P. Papamanolis, F. Krismer, and J. W. Kolar, "22 kW EV battery charger allowing full power delivery in 3-phase as well as 1-phase operation," in *Proc. of the IEEE International Conf. on Power Electronics (ICPE - ECCE Asia)*, Busan, South Korea, May 2019, DOI: 10.1109/APEC.2018.8341255.
- [114] X. Gong, G. Wang, and M. Bhardwaj, "6.6kW three-phase interleaved totem pole PFC design with 98.9% peak efficiency for HEV/EV onboard charger," in *Proc. of the IEEE Applied Power Electronics Conf. and Expo. (APEC)*, Anaheim, CA, USA, Mar. 2019, DOI: 10.1109/APEC.2019.8722110.
- [115] J. W. Kolar, U. Drogenik, J. Miniböck, and H. Ertl, "A new concept for minimizing high-frequency common-mode EMI of three-phase PWM rectifier systems keeping high utilization of the output voltage," in *Proc. of the IEEE Applied Power Electronics Conf. and Expo. (APEC)*, New Orleans, LA, USA, Feb. 2000, DOI: 10.1109/APEC.2000.826153.
- [116] D. Dong, X. Zhang, F. Luo, D. Boroyevich, and P. Mattavelli, "Common-mode EMI noise reduction for grid-interface converter in low-voltage DC distribution system," in *Proc. of the IEEE Applied Power Electronics Conf. and Expo. (APEC)*, Orlando, FL, USA, Feb. 2012, DOI: 10.1109/APEC.2012.6165859.

- [117] M. Hartmann, H. Ertl, and J. W. Kolar, "EMI filter design for a 1 MHz, 10 kW three-phase/level PWM rectifier," *IEEE Trans. Power Electron.*, vol. 26, no. 4, pp. 1192–1204, 2011, DOI: 10.1109/TPEL.2010.2070520.
- [118] K. Shi, M. Shoyama, and S. Tomioka, "Common mode noise reduction in totem-pole bridgeless PFC converter," in *Proc. of the IEEE International Power Electronics and Application Conf. and Expo. (PEAC)*, Shanghai, China, Feb. 2014, DOI: 10.1109/PEAC.2014.7037943.
- [119] B. Zhang, Q. Lin, J. Imaoka, M. Shoyama, S. Tomioka, and E. Takegami, "Conducted noise prediction for zero-crossing issue in totem-pole bridgeless PFC converter," in *Proc. of the IEEE International Telecommunications Energy Conf. (INTELEC)*, Broadbeach, QLD, Australia, Oct. 2017, DOI: 10.1109/INTLEC.2017.8214169.
- [120] S. Qu and D. Chen, "Mixed-mode EMI noise and its implications to filter design in offline switching power supplies," *IEEE Trans. Power Electron.*, vol. 17, no. 4, pp. 502–507, 2002, DOI: 10.1109/TPEL.2002.800965.
- [121] M. Jin and M. Weiming, "A new technique for modeling and analysis of mixed-mode conducted EMI noise," *IEEE Trans. Power Electron.*, vol. 19, no. 6, pp. 1679–1687, 2004, DOI: 10.1109/TPEL.2004.836630.
- [122] J. W. Kolar, F. Krismer, Y. Lobsiger, J. Muhlethaler, T. Nussbaumer, and J. Minibock, "Extreme efficiency power electronics," in *Proc. of the International Conf. on Integrated Power Electronics Systems (CIPS)*, Nuremberg, Germany, March 2012.
- [123] D. O. Boillat, F. Krismer, and J. W. Kolar, "Optimization and comparative evaluation of multiloop control schemes for controllable ac sources with two-stage LC output filters," *IEEE Trans. Power Electron.*, vol. 31, no. 10, pp. 7353 – 7368, 2016, DOI: 10.1109/TPEL.2015.2510022.
- [124] F. Krismer, J. Böehler, J. W. Kolar, and G. Pammer, "New series-resonant solid-state DC transformer providing three self-stabilized isolated medium-voltage input ports," in *Proc. of the IEEE International Conf. on Power Electronics (ICPE - ECCE Asia)*, Busan, South Korea, May 2019.
- [125] S. Kanyakam and S. Bureerat, "Multiobjective optimization of a pin-fin heatsink using evolutionary algorithms," *Journal of Electronic Packaging*, vol. 134, no. 2, 2012, DOI: 10.1115/1.4006514.

- [126] “Thermal Resistance Calculator – Round Pin Heat Sink,” (accessed May 08, 2021). [Online]. Available: <https://myheatsinks.com/calculate/thermal-resistance-round-pin/>
- [127] Infineon Technologies AG, “Comprehensive solutions for fast EV charging design,” Jan. 2019. [Online]. Available: https://infineoncommunity.com/register_for_ev_charging_whitepaper_presentation_ID1048?ic=00d1003
- [128] M. L. Heldwein, “EMC filtering of three-phase PWM converters,” Ph.D. dissertation, ETH Zurich, Zurich, Switzerland, 2008.
- [129] Y. Xie, C. Chen, Z. Huang, T. Liu, Y. Kang, and F. Luo, “High frequency conducted EMI investigation on packaging and modulation for a SiC-based high frequency converter,” *IEEE J. Emerg. Sel. Topics Power Electron.*, vol. 7, no. 3, pp. 1789–1804, 2019, DOI: 10.1109/JESTPE.2019.2919349.
- [130] B. Zhang and S. Wang, “A survey of EMI research in power electronics systems with wide-bandgap semiconductor devices,” *IEEE J. Emerg. Sel. Topics Power Electron.*, vol. 8, no. 1, pp. 626–643, 2020, DOI: 10.1109/JESTPE.2019.2953730.
- [131] H. Ye, Z. Yang, J. Dai, C. Yan, X. Xin, and J. Ying, “Common mode noise modeling and analysis of dual boost PFC circuit,” in *Proc. of the IEEE Int. Telecom. Energy Conf. (INTELEC)*, Chicago, IL, USA, Sep. 2004, DOI: 10.1109/INTLEEC.2004.1401526.
- [132] S. Wang, P. Kong, and F. C. Lee, “Common mode noise reduction for boost converters using general balance technique,” *IEEE Trans. Power Electron.*, vol. 22, no. 4, pp. 1410–1416, 2007, DOI: 10.1109/TPEL.2007.900503.
- [133] D. O. Boillat, F. Krismer, and J. W. Kolar, “EMI filter volume minimization of a three-phase, three-level T-type PWM converter system,” *IEEE Trans. Power Electron.*, vol. 32, no. 4, pp. 2473–2480, 2017, DOI: 10.1109/TPEL.2016.2617085.
- [134] M. L. Heldwein, T. Nussbaumer, and J. W. Kolar, “Differential mode EMC input filter design for three-phase ac-dc-ac sparse matrix PWM converters,” in *Proc. of the IEEE Power Electronics Specialists Conf. (PESC)*, Aachen, Germany, June 2004, DOI: 10.1109/PESC.2004.1355757.

- [135] M. Silva, N. Hensgens, J. Oliver, P. Alou, Ó. García, and J. A. Cobos, “New considerations in the input filter design of a three-phase buck-type PWM rectifier for aircraft applications,” in *Proc. of the IEEE Energy Conversion Congress and Expo. (ECCE USA)*, Phoenix, AZ, USA, Sep. 2011, DOI: 10.1109/ECCE.2011.6064325.
- [136] R. West, “Common mode inductors for EMI filters require careful attention to core material selection,” in *PCIM Mag.*, July 1995.
- [137] Shuo Wang, F. C. Lee, D. Y. Chen, and W. G. Odendaal, “Effects of parasitic parameters on EMI filter performance,” *IEEE Trans. Power Electron.*, vol. 19, no. 3, pp. 869–877, 2004, DOI: 10.1109/TPEL.2004.826527.
- [138] L. Rossetto, S. Buso, and G. Spiazzi, “Conducted EMI issues in a 600-W single-phase boost PFC design,” *IEEE Trans. Ind. Appl.*, vol. 36, no. 2, pp. 578–585, 2000, DOI: 10.1109/28.833776.
- [139] R. Wang, D. Boroyevich, H. F. Blanchette, and P. Mattavelli, “High power density EMI filter design with consideration of self-parasitic,” in *Proc. of the IEEE Applied Power Electronics Conf. and Expo. (APEC)*, Orlando, FL, USA, Feb. 2012, DOI: 10.1109/APEC.2012.6166141.
- [140] “Vector Network Analyzer.” (accessed Dec. 22, 2020). [Online]. Available: https://www.picotest.com/images/download/Bode-100_Product_Brochure_V7-2002.pdf
- [141] R. Wang, H. Fortin Blanchette, M. Mu, D. Boroyevich, and P. Mattavelli, “Influence of high-frequency near-field coupling between magnetic components on EMI filter design,” in *Proc. of the IEEE Applied Power Electronics Conf. and Expo. (APEC)*, Long Beach, CA, USA, Mar. 2013, DOI: 10.1109/APEC.2013.6520496.
- [142] S. Wang, F. Lee, and W. Odendaal, “Improving the performance of boost PFC EMI filters,” in *Proc. of the IEEE Applied Power Electronics Conf. and Expo. (APEC)*, Miami Beach, FL, USA, Feb. 2003, DOI: 10.1109/APEC.2003.1179240.
- [143] H. Bishnoi, P. Mattavelli, R. Burgos, and D. Boroyevich, “EMI behavioral models of DC-fed three-phase motor drive systems,” *IEEE Trans. Power Electron.*, vol. 29, no. 9, pp. 4633–4645, 2014, DOI: 10.1109/TPEL.2013.2284436.

- [144] B. Sun, R. Burgos, and D. Boroyevich, "Common-mode EMI un-terminated behavioral model of wide-bandgap-based power converters operating at high switching frequency," *IEEE J. Emerg. Sel. Topics Power Electron.*, vol. 7, no. 4, pp. 2561–2570, 2019, DOI: 10.1109/JESTPE.2018.2888604.
- [145] "R & S ESPI Test Receiver." (accessed Dec. 22, 2020). [Online]. Available: https://www.rohde-schwarz.com/us/product/esp-productstartpage_63493-8645.html?change_c=true
- [146] "R & S ENV216 Two-Line V-Network." (accessed Dec. 22, 2020). [Online]. Available: https://www.rohde-schwarz.com/us/product/env216-productstartpage_63493-9775.html?change_c=true
- [147] "HDO6104A," (accessed Dec. 22, 2020). [Online]. Available: <https://teledynelecroy.com/oscilloscope/hdo6000a-high-definition-oscilloscopes/hdo6104a>
- [148] I. Laird, X. Yuan, J. Scoltock, and A. J. Forsyth, "A design optimization tool for maximizing the power density of 3-phase DC–AC converters using silicon carbide (SiC) devices," *IEEE Trans. Power Electron.*, vol. 33, no. 4, pp. 2913–2932, 2018, DOI: 10.1109/TPEL.2017.2705805.
- [149] A. Charalambous, X. Yuan, and N. McNeill, "High-frequency EMI attenuation at source with the auxiliary commutated pole inverter," *IEEE Trans. Power Electron.*, vol. 33, no. 7, pp. 5660–5676, 2018, DOI: 10.1109/TPEL.2017.2743041.
- [150] Y. Liu, K. Y. See, and K.-J. Tseng, "Conducted EMI prediction of the PFC converter including nonlinear behavior of boost inductor," *IEEE Trans. Electromagn. Compat.*, vol. 55, no. 6, pp. 1107–1114, 2013, DOI: 10.1109/TEMC.2013.2254120.
- [151] T. Ibuchi, R. Kamikomaki, and T. Funaki, "Experimental evaluation on time variation of conducted noise spectrum for a PFC converter," in *Proc. of the International Symposium on Electromagnetic Compatibility*, Tokyo, Japan, May 2014, DOI: 10.34385/proc.18.13A2-A2.
- [152] K. Zhu, M. O'Grady, J. Dodge, J. Bendel, and J. Hostetler, "1.5 kW single phase CCM totem-pole PFC using 650V SiC cascodes," in *Proc. of the IEEE Workshop on Wide Bandgap Power Devices and Applications (WiPDA)*, Fayetteville, AR, USA, Nov. 2016, DOI: 10.1109/WiPDA.2016.7799915.

- [153] J. Sun, N. N. Strain, D. J. Costinett, and L. M. Tolbert, "Analysis of a GaN-based CRM totem-pole PFC converter considering current sensing delay," in *Proc. of the IEEE Energy Conversion Congress and Expo. (ECCE USA)*, Baltimore, MD, USA, Sep. 2019, DOI: 10.1109/ECCE.2019.8912203.
- [154] K. De Gusseme, D. de Sype, A. Van den Bossche, and J. Melkebeek, "Sample correction for digitally controlled boost PFC converters operating in both CCM and DCM," in *Proc. of the IEEE Applied Power Electronics Conf. and Expo. (APEC)*, Miami Beach, FL, USA, Feb. 2003, DOI: 10.1109/APEC.2003.1179243.
- [155] K. De Gusseme, D. Van de Sype, A. Van den Bossche, and J. Melkebeek, "Digital control of boost PFC converters operating in both continuous and discontinuous conduction mode," in *Proc. of the IEEE Power Electronics Specialists Conf. (PESC)*, Aachen, Germany, June 2004, DOI: 10.1109/PESC.2004.1355488.
- [156] "STMicroelectronics SiC Module - Tesla Model 3 Inverter," 2018, (accessed Jan. 07, 2021). [Online]. Available: https://www.systemplus.fr/wp-content/uploads/2018/06/SP18413-STM_SiC_Module_Tesla_Model_3_Inverter_sample-2.pdf
- [157] C. A. Baguley, U. K. Madawala, and B. Carsten, "A new technique for measuring ferrite core loss under DC bias conditions," *IEEE Trans. Magn.*, vol. 44, no. 11, pp. 4127–4130, 2008, DOI: 10.1109/TMAG.2008.2002862.
- [158] R. Bosshard and J. W. Kolar, "Multi-objective optimization of 50kW/85kHz IPT system for public transport," *IEEE Trans. Emerg. Sel. Topics Power Electron.*, vol. 4, no. 4, pp. 1370–1382, 2016, DOI: 10.1109/JESTPE.2016.2598755.
- [159] P. Czyz, T. Guillod, F. Krismer, and J. W. Kolar, "Exploration of the design and performance space of a high frequency 166kW/10kV SiC solid-state air-core transformer," in *Proc. of the IEEE International Power Electronics Conference (IPEC -ECCE Asia)*, Niigata, Japan, May 2018, DOI: 10.23919/IPEC.2018.8507746.
- [160] "AN-SERIES - High Frequency APR X-ray Generator," (accessed Jan. 07, 2021). [Online]. Available: <https://radiologyimagingssolutions.com/wp-content/uploads/2020/07/ANTHEM.pdf>

- [161] D. Dong, F. Luo, X. Zhang, D. Boroyevich, and P. Mattavelli, "Grid-interface bidirectional converter for residential DC distribution systems – Part 2: AC and DC interface design with passive components minimization," *IEEE Trans. Power Electron.*, vol. 28, no. 4, pp. 1667–1679, 2013, DOI: 10.1109/TPEL.2012.2213614.
- [162] "GENERAC - Residential Standby Generators 20/22 kW," (accessed Jan. 07, 2021). [Online]. Available: https://www.generac.com/generacorporate/media/library/content/all-products/generators/home-generators/guardian-series/16kw-7036/20-and-22kw-spec-sheet-generac-new_2.pdf
- [163] "Power Optimizer," (accessed Jan. 07, 2021). [Online]. Available: <https://www.solaredge.com/sites/default/files/se-p-series-commercial-add-on-power-optimizer-datasheet.pdf>
- [164] N. Mohan, T. M. Undeland, and W. P. Robbins, *Power Electronics: Converters, Applications, and Design, 3rd Edition*. John Wiley & Sons Inc., 2002.
- [165] G. Deboy, O. Haerberlen, and M. Treu, "Perspective of loss mechanisms for silicon and wide band-gap power devices," *IEEE CPSS Trans. Power Electron. and Appl.*, vol. 2, no. 2, pp. 89–100, 2017, DOI: 10.24295/CPSST-PEA.2017.00010.
- [166] F. Krismer, E. Hatipoglu, and J. W. Kolar, "Novel isolated bidirectional integrated dual three-phase active bridge (D3AB) PFC rectifier," in *Proc. of the IEEE International Conf. on Power Electronics (ICPE - ECCE Asia)*, Niigata, Japan, May 2018, DOI: 10.23919/IPEC.2018.8507362.
- [167] C. McLyman, *Transformer and Inductor Design Handbook*. CRC Press, 2017, DOI: 10.1201/9780203913598.
- [168] M. Albach, T. Durbaum, and A. Brockmeyer, "Calculating core losses in transformers for arbitrary magnetizing currents - a comparison of different approaches," in *Proc. of the IEEE Power Electronics Specialists Conf. (PESC)*, Baveno, Italy, June 1996, DOI: 10.1109/PESC.1996.548774.
- [169] J. Chen and C. Wang, "Topology and voltage-balance control of a single-phase double T-type seven-level inverter," *IEEE J. Emerg. Sel. Topics Power Electron.*, vol. 9, no. 1, pp. 1075–1087, 2021, DOI: 10.1109/JESTPE.2020.2968799.

Curriculum Vitae

Personal Information

Name Panteleimon Papamanolis
Date of Birth July 19, 1989
Place of Birth Athens, Greece
Citizen of Greece
Contact papamanolis@lem.ee.ethz.ch
pant.papamanolis@gmail.com
+41 78 820 17 10



Education

2016 – 2021 Doctorate - Power Electronic Systems Laboratory (PES)
Swiss Federal Institute of Technology - ETH Zurich
Zurich, Switzerland
2014 – 2016 MSc, Master of Science in Robotics, Systems and Control
Swiss Federal Institute of Technology - ETH Zurich
Zurich, Switzerland
2007 – 2013 MSc / BSc, Diploma in Electrical and Computer Engineering
National Technical University of Athens - NTUA
Athens, Greece

Work Experience

2016 – 2021 Scientific Assistant - PES
Swiss Federal Institute of Technology - ETH Zurich
Zurich, Switzerland
2015 Intern - Power Electronics Engineer
ABB Corporate Research Center - CRC
Baden - Dättwil, Switzerland

